https://ntrs.nasa.gov/search.jsp?R=19900010207 2020-03-19T23:02:18+00:00Z

NASA CR- 183457

NUMERICAL AND EXPERIMENTAL ANALYSIS OF A THIN LIQUID FILM ON A ROTATING DISK RELATED TO DEVELOPMENT OF A SPACECRAFT ABSORPTION COOLING SYSTEM

Amir Faghri, Ph.D.

Brage Golding Distinguished Professor

Department of Mechanical and Materials Engineering

Wright State University

Dayton, Ohio 45435

Theodore D. Swanson, P.E.

Thermal Management Group

NASA Goddard Space Flight Center

Greenbelt, Maryland 20771

September, 1989

(NASA-CR-183457) NUMERICAL AND EXPERIMENTAL ANALYSIS OF A THIN LIQUID FILM ON A ROTATING DISK RELATED TO DEVELOPMENT OF A SPACECRAFT ABSORPTION COOLING SYSTEM (NASA) 335 p CSCL 20D G3/34

N90-19523

Unclas 0257102

Forward

The information in this report was assembled for NASA Goddard Space Flight Center under contract no. NAG5-956. The work was carried out at the Department of Mechanical and Materials Engineering at Wright State University. Dr. Wilbur Hankey, Dr. Muhammad Rahman, Mr. Scott Thomas and Mr. Joseph Schmalhofer provided technical assistance to the authors for the completion of this report at different stages.

The various tasks described in this report dealt with numerical and experimental analysis of a thin liquid film on a rotating and stationary disk related to the development of an absorber unit for a high capacity spacecraft absorption cooling system. The idea that was focused upon in this report was the creation of an artificial gravity by the use of a centrifugal field. The basic phenomena related to the fluid flow and heat transfer on rotating systems that have been reported during this effort can be applied to other areas of space systems as well.

TABLE OF CONTENTS

I. ONE-DIMENSIONAL COMPUTATION OF THIN LIQUID FILM FLOWS

1.1 Summary 1
1.2 Introduction 2
1.3 Fluid Flow Analysis 7
1.4 Heat Transfer Analysis 17
1.5 Numerical Solution Procedure 20
1.6 Results and Discussion 24
1.7 Conclusions 34

II. EXPERIMENTAL MEASUREMENT OF FILM HEIGHT AND VISUALIZATION OF FLOW

2.1 Summary 37
2.2 Introduction 38
2.3 Experimental Setup 44
2.4 Error Analysis 51
2.5 Results and Discussion ..... [illegible]
2.5.1 Liquid Film Thickness Measurements ..... [illegible]
2.5.2 Flow Visualization ..... [illegible]
2.6 Conclusions ..... [illegible]

III. TWO DIMENSIONAL COMPUTATION OF THE FREE SURFACE FLOW OF A THIN LIQUID FILM USING "PRESSURE OPTIMIZATION METHOD"

3.1 Summary 85
3.2 Introduction 86
3.3 Problem Formulation 88
3.4 Numerical Solution Procedure 96
3.5 Results and Discussion 104
3.5.1 Falling Film 104
3.5.2 Film Flow Under Zero Gravity 111
3.5.3 Horizontal Film Flow in the Presence of Gravity ..... [illegible]
3.6 Conclusions ..... [illegible]

[illegible] OF HEAT TRANSFER IN [illegible]-DIMENSIONAL THIN FILM F[illegible]

[illegible] 7
[illegible] 8
[illegible]

ORIGINAL PAGE IS
OF POOR QUALITY

Table of Contents (continued)

V. DEVELOPMENT OF A NEW COMPUTATIONAL METHODOLOGY FOR THE FREE SURFACE FLOWS USING A PERMEABLE WALL

5.1 Summary....172
5.2 Introduction....173
5.3 Governing Equations....177
5.4 Numerical Solution Procedure....181
5.5 Discussion of Results....187
5.5.1 Film Flows in the Absence of Gravity....187
5.5.2 Film Flows Involving a Hydraulic Jump....196
5.6 Conclusions....203

VI. ANALYSIS OF FLUID FLOW AND HEAT TRANSFER IN A THIN LIQUID FILM IN THE PRESENCE AND ABSENCE OF GRAVITY

6.1 Summary....205
6.2 Introduction....206
6.3 Equations of Motion....210
6.4 Analysis of Flow Using One-Dimensional Uniform Velocity...213
6.4.1 Flow Under Zero Gravity....214
6.4.2 Flow in the Presence of Gravity....221
6.4.3 Characteristic Behavior of the Flow....226
6.4.4 Application of Results to Micro-Gravity....228
6.5 Analysis of Flow and Heat Transfer using Parabolic Velocity Distribution....229
6.5.1 Plane Flow Under Zero Gravity....231
6.5.2. Radial Flow Under Zero Gravity....232
6.5.3 Plane Flow in the Presence of Gravity....234
6.5.4 Radial Flow in the Presence of Gravity....239
6.5.5 Analysis of Heat Transfer....241
6.6 Conclusions....245

VII. COMPARISON OF THEORETICAL PREDICTION AND EXPERIMENTAL DATA

7.1 Summary....247
7.2 Introduction....248
7.3 Equations of Motion....253
7.4 Flow on a Stationary Disk....255
7.5 Flow on a Rotating Disk....269
7.6 Conclusions....276

REFERENCES....278

Appendix A EQUIPMENT SPECIFICATIONS....282
Appendix B DESIGN OF THE ROTATING DISK ASSEMBLY....287
Appendix C ERROR ANALYSIS....297
Appendix D EXPERIMENTAL DATA....308

LIST OF FIGURES

1.1 The generalized coordinate system.....5

1.2a The coordinate system for plane flow.....6

1.2b The coordinate system for radial flow.....6

1.3 Dimensionless liquid height versus dimensionless distance for plane flow with Fr_{in} = 10.0, Fr_{out} = 1.0, Re_{in} = 75.0, $\hat{\xi}_{in}$ = 0.0, $\hat{\xi}_{out}$ = 100.0 as the solution marches in time.....25

1.4 Dimensionless liquid height versus dimensionless distance for plane flow with $\hat{\xi}_{in}$ = 0.0, $\hat{\xi}_{out}$ = 100.00.....27

1.5 Dimensionless liquid height versus dimensionless distance for plane and radial flow with $\hat{\xi}_{in}$ = 0.0 (plane), $\hat{\xi}_{in}$ = 10.0 (radial), $\hat{\xi}_{out}$ = 100.0 for different values of the inlet Reynolds number in zero g...29

1.6 Dimensionless liquid height versus dimensionless distance for radial flow with $\hat{\xi}_{in}$ = 10.0, $\hat{\xi}_{out}$ = 100.0.....30

1.7 Dimensionless liquid height versus dimensionless distance for radial flow with Re_{in} = 50.0, $\hat{\xi}_{in}$ = 10.0, $\hat{\xi}_{out}$ = 100.0 for different values of the Rossby number in one g and zero g.....32

1.8 Nusselt number versus the dimensionless distance for plane and radial flow with Fr_{in} = 10.0, $\hat{\xi}_{in}$ = 0.0 (plane), $\hat{\xi}_{in}$ = 10.0 (radial), $\hat{\xi}_{out}$ = 100.0 under one g.....33

1.9 Nusselt number versus the dimensionless distance for radial flow with Fr_{in} = 10.0, Re_{in} = 50.0, $\hat{\xi}_{in}$ = 10.0, $\hat{\xi}_{out}$ = 100.0, under one g.....35

2.1 Experimental setup of the rotating disk unit.....46

2.2 Liquid film height measurement.....48

List of Figures (continued)

2.3 Film thickness versus radial location for different flow rates (stationary disk).....56

2.4 Film thickness versus radial location in the supercritical region for different flow rates (stationary disk).....58

2.5 Film thickness versus radial location for different flow rates (55 ± 2 RPM).....59

2.6 Film thickness versus radial location for different flow rates (100 ± 2 RPM).....61

2.7 Film thickness versus radial location for different flow rates (200 ± 2 RPM).....63

2.8 Film thickness versus radial location for different flow rates (300 ± 2 RPM).....64

2.9 Film thickness versus radial location for different rotational speeds (7.0 ± 0.3 LPM).....65

2.10 Film thickness versus radial location for different rotational speeds (11.0 ± 0.3 LPM).....66

2.11 Film thickness versus radial location for different rotational speeds (15.0 ± 0.3 LPM).....67

2.12 Stationary disk, 7.0 LPM, supercritical region highlighted.....69

2.13 Stationary disk, 7.0 LPM, subcritical region highlighted.....69

2.14 Stationary disk, 3.0 LPM.....71

2.15 Stationary disk, 4.0 LPM.....71

2.16a Roller for 3.0-6.0 LPM.....72

2.16b Roller for 7.0-8.0 LPM.....72

2.16c Roller for 9.0-15.0 LPM.....72

2.17 Stationary Disk, 5.0 LPM 74

List of Figures (continued)

2.18 Rotating disk, 7.0 LPM, 55 RPM.....74
2.19 Rotating disk, 7.0 LPM, 100 RPM.....75
2.20 Rotating disk, 7.0 LPM, 150 RPM.....75
2.21 Rotating disk, 7.0 LPM, 200 RPM.....76
2.22 Rotating disk, 7.0 LPM, 250 RPM.....76
2.23 Rotating disk, 7.0 LPM, 300 RPM.....77
2.24 Rotating disk, 7.0 LPM, 350 RPM.....77
2.25 Rotating disk, 13.0 LPM, 55 RPM.....80
2.26 Rotating disk, 13.0 LPM, 100 RPM.....80
2.27 Rotating disk, 13.0 LPM, 150 RPM.....81
2.28 Rotating disk, 13.0 LPM, 200 RPM.....81
2.29 Rotating disk, 13.0 LPM, 250 RPM.....82
2.30 Rotating disk, 13.0 LPM, 300 RPM.....82
2.31 Rotating disk, 13.0 LPM, 350 RPM.....83
3.1 The coordinate system on a grid cell.....90
3.2 Flow systems in present investigation.....93
3.3 Film height in a developing falling film flow.....108
3.4 Friction coefficient in a developing falling film flow.....109
3.5 Film height for plane flow under zero gravity.....113
3.6 Velocity profile for plane flow under zero gravity (case 2P).....114
3.7 Wall shear stress and friction coefficient for plane flow under zero gravity.....115
3.8 Film height for radial flow under zero gravity.....117
3.9 Velocity profile for radial flow under zero gravity.....118
3.10 Friction coefficient for radial flow under zero gravity.....120
3.11 Film height for plane and radial horizontal flow.....122

List of Figures (continued)

3.12 Supercritical and subcritical film height for plane horizontal flow 123
4.1 Flow systems in present investigation.....133
4.2 The coordinate system on a grid cell.....136
4.3 Film height in a developing falling film flow.....147
4.4 Nusselt number in falling film flow adjacent to an isothermal surface 148
4.5 Nusselt number in falling film flow adjacent to a uniformly heated surface.....149
4.6 Film height for plane flow and radial flow under zero gravity.....154
4.7 Nusselt number for plane flow along an isothermal surface under zero gravity.....155
4.8 Nusselt number for plane flow along a uniformly heated surface under zero gravity.....156
4.9 Nusselt number for radial flow along an isothermal surface under zero gravity.....158
4.10 Nusselt number for radial flow along a uniformly heated surface under zero gravity.....159
4.11 Film height for plane horizontal flow.....161
4.12 Nusselt number for plane horizontal flow on an isothermal surface..162
4.13 Nusselt number for plane horizontal flow on a uniformly heated surface 163
4.14 Film height for radial horizontal flow.....164
4.15 Nusselt number for radial horizontal flow on an isothermal surface.165
4.16 Nusselt number for radial horizontal flow on a uniformly heated surface.....166

List of Figures (continued)

5.1 The coordinate and flow systems in the present investigation.....178

5.2 The film height variation for plane flow under zero gravity.....189

5.3 Penetration through the free surface for plane flow under zero gravity 190

5.4 Computed results for plane film flow under zero gravity (Re = 50)..191

5.5 Velocity vectors for plane and radial film flows under zero gravity 192

5.6 Computed results for radial film flow under zero gravity (Re_{in} = 34) 193

5.7 Computed results for plane hydraulic jump (Re = 355, Fr_{in} = 9).....198

5.8 Velocity vectors for plane hydraulic jump.....199

5.9 Computed results for radial hydraulic jump (Re_{in} = 50, Fr_{in} = 11)..201

5.10 Velocity vectors for radial hydraulic jump.....202

6.1 Schematic of the physical problem.....211

6.2 Film height for plane and radial flows under zero gravity.....218

6.3 Analytical film height for radial flow under zero gravity.....219

6.4 Analytical solution for plane and radial flows over a plate in the presence of gravity (uniform velocity).....224

6.5 Analytical solution for horizontal flow over a plate in the presence of gravity (parabolic velocity).....236

6.6 Froude number distribution for plane flow over a plate in the presence of gravity.....238

6.7 Comparison of predicted film height with a previous result for plane flow in the presence of gravity.....240

6.8 Comparison of predicted Nusselt number for heating without evaporation adjacent to a constant flux wall.....243

ORIGINAL PAGE IS
OF POOR QUALITY

List of Figures (continued)

7.1 The coordinate system used for two dimensional numerical computation 254

7.2 Comparison of experiment with one-dimensional numerical prediction for stationary disk (flow rate = 7 lpm) 257

7.3 Comparison of experiment with one-dimensional numerical prediction for stationary disk (flow rate = 1[illegible] lpm).....258

7.4 Film height distribution over a stationary disk at flow rate of 7 lpm 262

7.5 Film height distribution over a stationary disk at flow rate of 9 lpm 263

7.6 Film height distribution over a stationary disk at flow rate of 1[illegible] lpm 264

7.7 Velocity vectors for thin film flow adjacent to a stationary disk (flow rate = 11 lpm).....268

7.8 Comparison of experiment with numerical solution of rotating disk (flow rate = 11 lpm, rpm = 100).....271

7.9 Comparison of experiment with numerical solution of rotating [illegible] (flow rate = 9 lpm, rpm = 51[illegible]) .....

7.10 Comparison of experiment with numerical solution of rotating [illegible] (flow rate = 12 lpm, rpm = 20[illegible]) .....

7.11 Comparison of experiment with numerical solution [illegible] (flow rate = [illegible] lpm, rpm = [illegible]) .....

[illegible]

List of Figures (continued)

7.1 The coordinate system used for two-dimensional numerical computation 254

7.2 Comparison of experiment with one-dimensional numerical prediction for stationary disk (flow rate = 7 lpm).....257

7.3 Comparison of experiment with one-dimensional numerical prediction for stationary disk (flow rate = 11 lpm).....258

7.4 Film height distribution over a stationary disk at flow rate of 7 lpm 262

7.5 Film height distribution over a stationary disk at flow rate of 9 lpm 263

7.6 Film height distribution over a stationary disk at flow rate of 11 lpm 264

7.7 Velocity vectors for thin film flow adjacent to a stationary disk (flow rate = 11 lpm).....268

7.8 Comparison of experiment with numerical solution of rotating disk (flow rate = 11 lpm, rpm = 100).....271

7.9 Comparison of experiment with numerical solution of rotating disk (flow rate = 9 lpm, rpm = 54.7).....273

7.10 Comparison of experiment with numerical solution of rotating disk (flow rate = 13 lpm, rpm = 200).....274

7.11 Comparison of experiment with numerical solution of rotating disk (flow rate = 7 lpm, rpm = 300).....275

B.1 Side view #1 of motor, spindle, and disk assembly.....288

B.2 Collar design.....290

B.3 Side view #2 and top view of motor and spindle.....292

B.4 Aluminum disk.....293

Two page 9

List of Figures (continued)

B.5 Ceramic disk.....294

B.6 Electrical diagram for the rotating disk unit.....295

C.1 Typical mean h" and standard deviation versus number of data points for subcritical flow.....302

C.2 Typical mean h" and standard deviation versus number of data points for supercritical flow.....303

LIST OF TABLES

3.1 Boundary conditions for plane flow and radial flow.....91

3.2 Flow conditions and free surface specifications.....94

3.3 Summary of computed optimum profiles and normalized RMS error in pressure.....106

4.1 Flow parameters and free surface geometry.....145

7.1 Comparison of calculated and measured film height at outlet for a stationary disk.....260

D.1. Experimental data for the stationary disk.....309

D.2. Experimental data for the rotating disk: 55 RPM.....311

D.3. Experimental data for the rotating disk: 100 RPM.....313

D.4. Experimental data for the rotating disk: 200 RPM.....315

D.5. Experimental data for the rotating disk: 300 RPM.....317

NOMENCLATURE

A Optimization parameter in free surface equation, or flow parameter (defined by eqn. 6.14)

an Optimization parameter in free surface equation

bn Optimization parameter in free surface equation

C Optimization parameter in free surface equation, or wave speed, or Courant number $(\Delta\tau/\Delta\hat{\xi})\ (1 + Ro^{-1})$

c_f Friction coefficient, $\tau_w/(0.5\ \rho W^2)$

C_p Constant pressure specific heat, J/kg-K

D Optimization parameter in free surface equation

Fr Froude number, $W/\sqrt{g\delta}$

g Acceleration due to gravity, m/s^2

g_s Average gravitational acceleration on earth, m/s^2

h Heat transfer coefficient, W/m^2K

i Index for iteration number

k Index for wall location in z-direction

K Thermal conductivity, W/m-K

L Length of the plate, m

n Normal outward direction, or nodal point in time

$\vec{n}$ Unit vector normal to free surface

Nu Nusselt number, $(h/K)\ (\nu^2/g)^{1/3}$

Nu^* Nusselt number in terms of film height, $h\delta/K$

p Difference between static and ambient pressures, Pa

q Heat flux, W/m^2

Q Volumetric flow rate (per unit width, if plane flow), m^3/s

Q_{loss} Volumetric flow rate for the penetration through the free surface, m^3/s

Nomenclature (continued)

r Radial coordinate or coordinate along the plate (section I)

R Riemann invariant, or dimensionless radius defined by eqns. (6.45) and (6.50)

$\hat{R}$ Radius of curvature, m

R1 Dimensionless radius, defined by equations (6.22) and (6.26)

Re Reynolds number, $W\delta/\nu$

Re^* Reynolds number in terms of plate length, $W_{in}L/\nu$ or $W_{in}r_o/\nu$

Ro Rossby number, $\bar{u}/\omega r$

t Time, s

$\vec{t}$ Unit tangent vector at the free surface

T Temperature, K

u Velocity in the θ-direction, m/s

v Component of velocity in y-direction, m/s

v_{loss} y-component of velocity associated with penetration through the free surface, m/s

V Dimensionless velocity in the r-direction, W/W_{in}

$\vec{V}$ Velocity vector, m/s

w Component of velocity in z-direction, m/s

W Average velocity at a radial (or z-) location, m/s

We Weber number, $\rho W_{in}^2 L/\sigma$ or $\rho W_{in}^2 r_o/\sigma$

x Coordinate orthogonal to the r- and z-directions in plane flow

y Coordinate normal to the plate

z Coordinate along the plate (section VI) or coordinate along the main flow direction in a boundary-fitted system (section III-V, VII)

Nomenclature (continued)

Greek symbols

α Thermal diffusivity, m^2/s

β Flow parameter (defined by eqn. 6.54), or artificial viscosity coefficient

δ Film thickness, m

δ_B Thickness of momentum boundary layer, m

δ^+ Dimensionless film thickness, δ/δ_{in}

δ_B^+ Dimensionless boundary layer thickness, δ_B/δ_{in}

δ^* Film height corresponding to $Fr = 1$, m

Δ Increment, or dimensionless film height, δ/δ_{in}

Δz Grid size in the z-direction, m

η Dimensionless coordinate across film thickness, y/δ

θ Coordinate orthogonal to the r- and z-directions in radial flow

λ $\lambda = 0$ for plane flow, $\lambda = 1$ for radial flow

μ Dynamic viscosity, Ns/m^2

ν Kinematic viscosity, m^2/s

ξ Dimensionless distance, z/L or $(r - r_{in})/(r_{out} - r_{in})$

$\hat{\xi}$ Dimensionless coordinate parallel to the plate, r/δ_{in}

ξ_1 Optimization parameter in free surface equation

ρ Density, kg/m^3

τ Shear stress, or dimensionless time, tW_{in}/δ_{in}

$\underline{\underline{\tau}}$ Stress tensor, N/m^2

σ Surface tension, N/m

ω Angular velocity, radian/s

Nomenclature (continued)

Subscripts

b	Mixed mean (bulk) condition
c	Cartesian component of velocity
e	Condition on the free surface
fd	Fully-developed
in	Condition at entrance
out	Condition at exit
r	Component in radial direction
sat	Saturation condition
w	Condition on solid wall
$\hat{\xi}$	derivative with respect to $\hat{\xi}$
τ	derivative with respect to τ
ϕ	Component in angular direction
0	at the initial time

Superscript

*	Critical condition in the flow

Section I

ONE-DIMENSIONAL COMPUTATION OF THIN LIQUID FILM FLOWS

1.1 SUMMARY

The flow of a thin liquid film with a free surface along a horizontal plate which emanates from a pressurized vessel is examined numerically. In one g, a hydraulic jump was predicted in both plane and radial flow, which could be forced away from the inlet by increasing the inlet Froude number or Reynolds number. In zero g, the hydraulic jump was not predicted. The effect of solid-body rotation for radial flow in one g was to "wash out" the hydraulic jump and to decrease the film height on the disk. The liquid film height under one g and zero g was equal under solid-body rotation because the effect of centrifugal force was much greater than that of the gravitational force. The heat transfer to a film on a rotating disk was predicted to be greater than that of a stationary disk because the liquid film is extremely thin and is moving with a very high velocity.

1.2 INTRODUCTION

The study of thin liquid films has been performed by many researchers in the past due to the high heat transfer rates that can be achieved. Even though the heat transfer to thin films falling down a vertical plate is quite high, much better heat transfer rates can be realized when the film is generated by the impingement of a liquid jet onto a surface that is perpendicular to the jet. This is due to the fact that in most cases the film velocities are greater than those of a falling film. Since it is difficult to examine the entire flow field from the impinging jet to the perpendicular thin film, it is proposed to study only the thin film. This is accomplished by the following mechanism: the liquid is pressurized in a container and emanates from a slot which generates the thin film on a horizontal plate. With this situation, the height and mean velocity of the film will be known boundary conditions, which will aid in determining the characteristics of the film downstream. After the structure of the liquid film has been examined, the amount of heat that can be transferred to it can be found. Furthermore, in this study it is also desired to understand the effects of centrifugal force and zero gravity on the flow field. If the film is generated on a spinning disk, it is expected that the film will accelerate and become thinner, since the centrifugal force acts in the main direction of the flow. This acceleration of the liquid film will increase the amount of heat that can be transferred from the spinning disk to the film. The effect of zero g on the flow is also examined to determine the nature of the liquid film height when the gravitational field across the film is not present. The combined effects of centrifugal acceleration and a zero g environment on the fluid characteristics and heat transfer to a

thin film are not known at present. It is felt, however, that this fundamental research will become important in the future because of programs like the Space Station where improved heat exchangers will be needed. This research will also be instrumental in the development of an absorber unit for a spacecraft vapor-absorption heat pump system, which was the motivation for the present work.

Many investigations have been carried out concerning thin liquid films created by impinging jets and/or spinning disks because of the numerous applications where the improved heat or mass transfer is desirable. Sparrow and Gregg (1959) analytically determined the condensate thickness on a rotating disk in a large vessel of quiescent saturated vapor. Watson (1964) analysed a free-falling jet which impinges on a horizontal plane using a similarity solution. Chaudhury (1964) used a similarity solution to analyse the heat transfer in the thin liquid layer on a horizontal plate on which a liquid jet impinges. Aroesty et al. (1967) studied the use of thin films under centrifugal force as an aid to blood oxygenation. The flow of a liquid film on a rotating disk was examined by Matsumoto et al. (1973) in connection with the atomization of a liquid for spray drying and the promotion of chemical reactions or absorption between gases and liquids. Rauscher et al. (1973) analysed the laminar flow of a thin film on a rotating disk by employing the asymptotic expansion technique. Eliseev (1983) examined the spatial stability of liquid films on a rotating disk by the asymptotic expansion technique. The study of thin films in regard to spin coating deposition of thin solid films was carried out by Jenekhe (1984). Needham and Merkin (1987) theoretically studied thin axisymmetric liquid films on a horizontally rotating disk to determine the

criteria for stability of the film. Katto and Yokoya (1988) analyzed the existing experimental data for the critical heat flux of a disk heater cooled by an impinging liquid jet and gave an equation correlating the data.

The motivation of the present work is the study of thin liquid films which will be used in space-based centrifugal heat exchangers and vapor absorption heat pumps. Since a falling film cannot be achieved in a zero g environment, it is natural to consider the possibility of using the artificial gravity created by the centrifugal force on a rotating disk to generate a thin film.

In the present study, the governing equations and boundary conditions are presented for two situations of a thin liquid layer emanating from a pressurized vessel and traveling along a horizontal plate with a constant initial height and uniform initial velocity as shown in Fig. 1.1. The first case is when the liquid flows along a channel with a constant width, which is shown in Fig. 1.2a. This situation is the same as open channel flow, but since the liquid height is very thin the effect of viscosity must be accounted for. The second case, which is shown in Fig. 1.2b, is when the liquid originates between two parallel disks, and then spreads out radially over the bottom disk in a free surface thin film because the diameter of the upper disk is much smaller than that of the lower disk. This situation is similar to a jet of liquid impinging onto the center of a horizontal disk, except that the height and the mean velocity of the liquid film are known at a specific radial location. In the case of radial flow, the rotational acceleration will be modeled as solid-body rotation, where

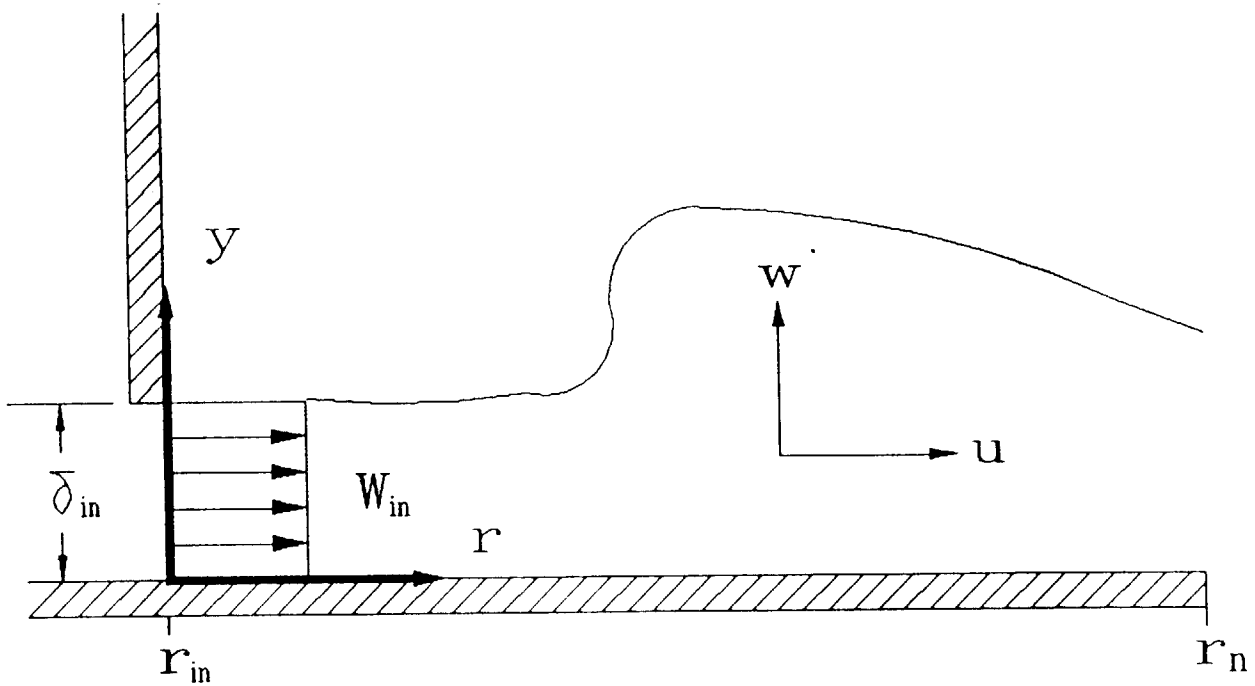

Figure 1.1. The generalized coordinate system

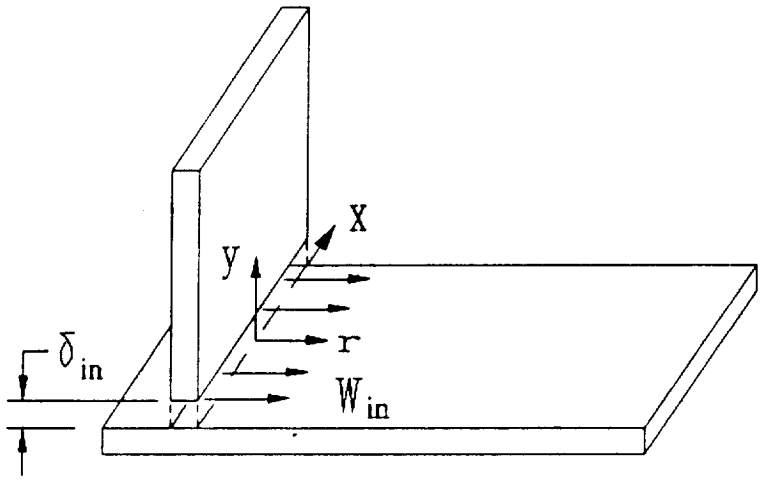

Figure 1.2a. The coordinate system for channel flow

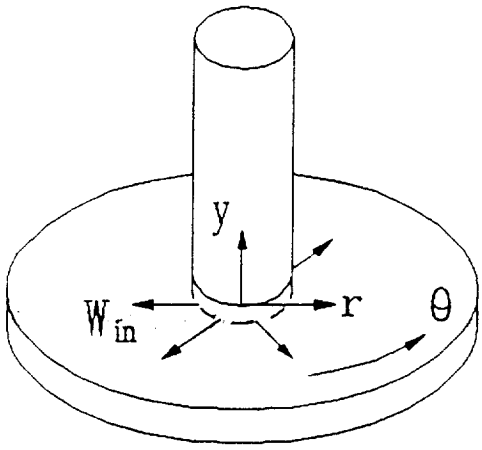

Figure 1.2b The coordinate system for radial flow

the centrifugal forces act only in the radial direction.

It is desired to numerically solve for the liquid height at any distance down the length of the plate for different Froude numbers and Reynolds numbers specified at the inlet. The heat transfer from the plate will also be studied for the case of simple heating with no evaporation at the free surface. Since the inlet Froude number may be greater than unity, it is possible that a hydraulic jump will occur at some point in the computational domain. A hydraulic jump is when the flow suddenly changes from supercritical ($Fr > 1$) to subcritical ($Fr < 1$) flow, which is accompanied by a sudden increase in the liquid height. This is analogous to the shock wave in gas dynamics when the flow changes from supersonic ($M > 1$) to subsonic ($M < 1$) flow in a very short distance. The similarity between the hydraulic jump and the shock wave in gas dynamics suggests using the familiar approach of modeling the flow as a transient phenomenon and allowing the solution to march in time to achieve the desired steady-state results. To the authors' knowledge, this approach has not been applied to this type of problem before. It should be emphasized that conventional numerical techniques that are applied to 2- or 3-dimensional problems cannot be used directly to solve this particular problem because the location of the free surface is unknown prior to the start of the calculations.

1.3 FLUID FLOW ANALYSIS

The conservation of mass, momentum, and energy in the general coordinate system can be expressed in the following compact form for a thin incompressible liquid film with constant properties.

$$\nabla \cdot \vec{V} = 0 \tag{1.3.1}$$

$$\rho \frac{D\vec{V}}{Dt} = - \nabla p + \mu \nabla^2 \vec{V} + \rho \vec{g} \tag{1.3.2}$$

$$\frac{DT}{Dt} = a \nabla^2 T \tag{1.3.3}$$

In the general coordinate system given in Fig. 1.1, the direction that is parallel to the plate in the main direction of the flow will be denoted by r and the direction that is normal to the plate will be denoted by z. The velocity vector $\vec{V}$ has three components; w, v, and u, where w is in the r-direction and v is in the y-direction. The component of velocity in the x-direction, as shown in Fig. 1.2a, is set equal to zero for plane flow. The component of velocity in the θ-direction, as shown in Fig. 1.2b, is equal to u for radial flow.

Several assumptions are made in order to reduce the complexity of the governing equations. Any changes in the variables with respect to the θ- or x-directions are set to zero. In the gravitational field, $\vec{g}$, only the component across the film thickness, g_y, is considered. The boundary layer assumptions are imposed on the governing equations, which neglect the diffusion terms in the main direction of the flow based on an order-of-magnitude analysis. At the free surface, the effects of interfacial shear stress and the surface tension are assumed to be zero. It should be noted that the effect of surface tension may be significant near the inlet and outlet of the domain and in the hydraulic jump region. The pressure in the liquid film is defined as the difference between the

actual pressure and the atmospheric pressure, so at the free surface the pressure is equal to zero. For the case of radial flow, it is assumed that the velocity component in the θ-direction is $u = \omega r$, i.e., solid-body rotation. By an order-of-magnitude analysis, this assumption is valid for small values of the Rossby number ($Ro < 1$).

The boundary and initial conditions for the governing equations in fixed coordinates are those on the flat plate and on the free surface of the liquid.

$$y = 0: \quad w = 0, \quad u = \omega r, \quad v = 0$$

$$y = \delta: \quad v = \frac{\partial \delta}{\partial t} + w\frac{\partial \delta}{\partial r}, \quad p = 0, \quad \frac{\partial w}{\partial y} = 0$$

$$r = r_1: \quad w = w_{in}, \quad v = 0, \quad \delta = \delta_{in}$$

$$t = 0: \quad w = w_0, \quad v = 0$$

The boundary condition involving v at the free surface is the kinematic condition for time-dependent problems. The boundary condition involving $\partial w/\partial y$ at $y = \delta$ corresponds to neglecting the interfacial shear stress at the free surface.

The continuity equation and the conservation of momentum equations in the r- and y-directions can be integrated with respect to the y-direction across the thin liquid layer by using Leibniz's rule and the kinematic condition at the free surface. Due to the boundary-layer assumptions, the conservation of momentum equation in the y-direction results in a balance between the pressure gradient and the gravitational force. This equation is then substituted into the r-direction momentum equation. It is assumed

that the velocity in the main direction of the flow is constant across the thin film, so that

$$\int_0^{\delta} w^2 \, dy = W^2 \delta$$

It should be noted that this is not a major assumption. For example, for a parabolic velocity profile, the left-hand side is equal to $6W^2\delta/5$. The resulting one-dimensional time-dependent equations in the general coordinate system are given in the following form:

$$\frac{1}{r^{\lambda}} \frac{\partial}{\partial r} (r^{\lambda} W \delta) + \frac{\partial \delta}{\partial t} = 0 \qquad (1.3.4)$$

$$\frac{\partial}{\partial t} (W\delta) + \frac{\partial}{\partial r} \left[W^2 \delta + \frac{1}{2} g \delta^2 \right] = \lambda \delta \left[r\omega^2 - \frac{W^2}{r} \right] - \frac{1}{\rho} \mu \frac{\partial w}{\partial y} \Big|_{y = 0} \qquad (1.3.5)$$

To properly assign the boundary conditions of the flow, the characteristic behavior of the flow will be examined. The governing equations can be cast in the characteristic form by the following analysis.

The governing equations (1.3.4 and 1.3.5) can be rearranged by subtracting W continuity equation from the momentum equation.

$$\frac{1}{\delta} \frac{\partial \delta}{\partial t} + \frac{W}{\delta} \frac{\partial \delta}{\partial r} + \frac{\partial W}{\partial r} = - \frac{\lambda W}{r}$$

$$\frac{\partial W}{\partial t} + W \frac{\partial W}{\partial r} + (g\delta) \frac{1}{\delta} \frac{\partial \delta}{\partial r} = r\omega^2 \left[1 - \frac{\tau_w}{\delta \rho r \omega^2} \right]$$

The characteristic form of the equations are obtained by linearizing the continuity and momentum equations:

$$\left[\frac{\partial}{\partial t} + W_{in}\frac{\partial}{\partial r}\right]\frac{\delta}{\delta_{in}} + \frac{\partial}{\partial r}(W) = S_1$$

$$\left[\frac{\partial}{\partial t} + W_{in}\frac{\partial}{\partial r}\right]W + a_{in}^2 \frac{\partial}{\partial r}\left(\frac{\delta}{\delta_{in}}\right) = S_2$$

where

$$a_{in}^2 = g\delta_{in}$$
$$S_1 = -\frac{\lambda W}{r}$$
$$S_2 = r\omega^2\left[1 - \frac{\tau_w}{\delta\rho r\omega^2}\right]$$

These two equations can be represented by the following characteristic equation.

$$\frac{\partial R_i}{\partial t} + c_i \frac{\partial R_i}{\partial r} = S_i$$

The Reimann invariants and the physical wave speeds are given in the following table.

R_i	c_i	S_i
$W + a_{in}(\delta/\delta_{in})$	$W_{in} + a_{in}$	$a_{in}S_1 + S_2$
$W - a_{in}(\delta/\delta_{in})$	$W_{in} - a_{in}$	$-a_{in}S_1 + S_2$

An examination of the characteristics reveals that the first invariant will always propagate downstream. The direction of propagation for the second invariant depends upon whether the flow is supercritical or subcritical. For supercritical flow (i.e., Fr > 1), the second invariant propagates downstream, so the boundary conditions on W and δ will both be assigned at the inlet of the flow field. For subcritical flow (i.e., Fr < 1), the second invariant propagates upstream, so the boundary conditions must be assigned at the inlet and the outlet of the flow field.

The following assumption is made to simplify the governing equations so that the film height can be eliminated from the equations.

$$\frac{\partial \delta}{\partial t} \simeq 0$$

This assumption results in the following quasi - steady governing equations:

$$r^{\lambda} W \delta = \frac{Q}{(2\pi)^{\lambda}} = \text{constant} \tag{1.3.6}$$

$$\delta \frac{\partial W}{\partial t} + \frac{\partial}{\partial r}\left[W^2 \delta + \frac{1}{2} g \delta^2\right] = \lambda \delta \left[r\omega^2 - \frac{W^2}{r}\right] - \frac{1}{\rho}\mu \left.\frac{\partial w}{\partial y}\right|_{y = 0} \tag{1.3.7}$$

By using this assumption, it is understood that the unsteady solutions with respect to time are not precisely accurate, but the accuracy of the steady-state solution is not affected.

The following analysis for the skin friction coefficient is given since the shear stress at the wall is not known. When the boundary layer on the plate is much smaller than the film thickness, i.e., developing flow, it is assumed that the boundary layer is the same as when there is a uniform far-field boundary. Therefore, when $\delta > \delta_B$, where δ_B is the Blasius boundary layer thickness, the Blasius skin friction coefficient will be employed to approximate the shear stress term. When the boundary layer reaches the free surface (i.e., $\delta = \delta_B$), a parabolic velocity profile is used to approximate the shear stress term. The Blasius boundary layer thickness is given by

$$\frac{\delta_B}{(r - r_{in})} = \frac{5.0}{\sqrt{\frac{W(r - r_{in})}{\nu}}}$$

The Blasius skin friction coefficient is as follows:

$$c_f = \frac{0.664}{\sqrt{\frac{W(r - r_{in})}{\nu}}}$$

The Blasius skin friction coefficient can also be presented in terms of the Blasius boundary layer thickness.

$$c_f(\text{Blasius}) = \frac{3.32}{\left[\frac{W\delta_B}{\nu}\right]}$$

For $\delta = \delta_B$, it is assumed that the velocity profile is parabolic.

$$w = \frac{3W}{\delta}\left[y - \frac{y^2}{2\delta}\right] \qquad (1.3.8)$$

The coefficient of skin friction is

$$c_f(\text{parabolic}) = \frac{\tau_w}{\frac{1}{2}\rho W^2} = \frac{\mu \frac{\partial w}{\partial y}\Big|_{y=0}}{\frac{1}{2}\rho W^2} = \frac{6}{\left[\frac{W\delta}{\nu}\right]}$$

The two skin friction coefficients match when

$$c_f\ (\text{Blasius}) = c_f\ (\text{parabolic})$$

or

$$\frac{\delta}{\delta_B} = 1.81$$

The value of the skin friction will be determined in the following manner.

$$\delta_B = \frac{5.0(r - r_{in})}{\sqrt{\frac{W(r - r_{in})}{\nu}}}$$

$$0 < \frac{\delta}{\delta_B} < 1.81 \qquad c_f = \frac{6}{\left[\frac{W\delta}{\nu}\right]}$$

$$\frac{\delta}{\delta_B} > 1.81 \qquad c_f = \frac{0.664}{\sqrt{\frac{W(r - r_{in})}{\nu}}}$$

The governing equations are nondimensionalized in the following manner

to simplify the analysis and to generalize the results.

$$\frac{W}{W_{in}} = V \qquad \frac{\delta}{\delta_{in}} = \delta^{+} \qquad \frac{r}{\delta_{in}} = \hat{\xi} \qquad t\frac{W_{in}}{\delta_{in}} = \tau$$

$$\frac{W_{in}^2}{g\delta_{in}} = Fr_{in}^2 \qquad \frac{W_1\delta_{in}}{\nu} = Re_{in} \qquad \frac{W_{in}}{\omega r_{in}} = Ro_{in}$$

$$\frac{\delta_B}{\delta_{in}} = \delta_B^{+} = \text{dimensionless boundary layer thickness}$$

The Reynolds number of the flow was chosen to nondimensionalize the governing equations instead of the Ekman number because the Reynolds number is needed when the flow is stationary.

After eliminating the dimensionless film height from the momentum equation with the continuity equation, the dimensionless governing equation is as follows:

$$V_{\tau} + V\hat{\xi}^{\lambda}G_{\hat{\xi}} = H \tag{1.3.9}$$

where

$$G = \frac{V}{\hat{\xi}^{\lambda}} + \frac{\hat{\xi}_{in}^{\lambda}}{2Fr_{in}^2}\left[\frac{1}{V\hat{\xi}^{\lambda}}\right]^2 - \beta V\hat{\xi} \tag{1.3.10}$$

and

$$H = \lambda\left[\frac{\hat{\xi}}{(\xi_{in}Ro_{in})^2} - \frac{V^2}{\hat{\xi}}\right] - 3\frac{V^3}{Re_{in}}\left[\frac{\hat{\xi}}{\xi_{in}}\right]^{2\lambda} \quad \text{for} \quad 0 < \frac{\delta^{+}}{\delta_B^{+}} < 1.81 \tag{1.3.11}$$

or

$$H = \lambda\left[\frac{\hat{\xi}}{(\hat{\xi}_{in}\ Ro_{in})^2} - \frac{V^2}{\hat{\xi}}\right] - \frac{0.332V^{5/2}}{\sqrt{Re_{in}\ (\hat{\xi} - \hat{\xi}_{in})}}\left[\frac{\hat{\xi}}{\hat{\xi}_{in}}\right]^{\lambda} \quad \text{for } \frac{\delta^+}{\delta_B^+} > 1.81 \quad (1.3.12)$$

where the dimensionless boundary layer thickness is given by

$$\delta_B^+ = 5.0\sqrt{\frac{(\hat{\xi} - \hat{\xi}_{in})}{VRe_{in}}} \quad (1.3.13)$$

The dimensionless initial and boundary conditions are given as follows:

$$V(0,\hat{\xi}) = 1$$

$$V(\tau,\hat{\xi}_{in}) = 1$$

These conditions correspond to a constant velocity across the region at the initial time and a constant inlet velocity at all times. Since the steady-state results are the only concern due to the constraints made on the mathematical modeling ($\partial\delta/\partial t \simeq 0$), the specification of the initial condition is required only for the numerical iteration scheme.

An artificial viscosity term ($\beta V_{\hat{\xi}}$) is included in the governing equation to dampen numerical oscillations in the solution (Anderson et al., 1984). The oscillations are commonly referred to as the Gibb's phenomenon, which occurs near a double-valued point in the solution, such as a hydraulic jump or a shock wave. This term reduces the numerical

oscillations in the immediate vicinity of the hydraulic jump, but does not affect the numerical solution elsewhere in the domain.

1.4 HEAT TRANSFER ANALYSIS

It is desired to find the amount of heat transferred from the plate or disk to the liquid when the plate is heated. This analysis assumes that the velocity of the thin film is approximated by the similarity profile presented in equation (1.3.8). The temperature profile across the thin film is assumed to be a quadratic function, with the coefficients determined by the boundary conditions imposed at the surface of the plate and the free surface. The boundary conditions are a constant heat flux at the plate and the free surface of the liquid film is adiabatic, which corresponds to simple heating with no evaporation at the free surface. The boundary conditions are given as:

$$\left.\frac{\partial T}{\partial y}\right|_{y = \delta} = 0 \qquad (1.4.1)$$

$$-K \left.\frac{\partial T}{\partial y}\right|_{y = 0} = q \qquad (1.4.2)$$

The temperature distribution across the thin film is

$$T = T_w - \frac{q}{K} y + \frac{q}{2K\delta} y^2 \qquad (1.4.3)$$

The mixed-mean temperature of the film is given by the following equation

$$T_b = \frac{1}{W\delta} \int_0^{\delta} wT \, dy = T_w - \frac{2}{5} \frac{q\delta}{K} \tag{1.4.4}$$

The heat transfer coefficient is defined by

$$h = \frac{q}{(T_w - T_b)} = \frac{5}{2} \frac{K}{\delta} \tag{1.4.5}$$

Therefore, the heat transfer coefficient can be found in terms of the liquid film height.

The modified Nusselt number is defined in the following manner:

$$Nu = \frac{h}{K} \left[\frac{\nu^2}{g}\right]^{1/3} = \frac{2.5}{\delta} \left[\frac{\nu^2}{g}\right]^{1/3} \tag{1.4.6}$$

This definition has been used previously in the literature concerning thin falling films. For a zero g situation, the Nusselt number is defined in terms of the liquid film thickness:

$$Nu^* = \frac{h\delta}{K} = 2.5 \tag{1.4.7}$$

For practical applications, the mixed-mean temperature of the fluid should be known. Therefore, the following analysis is given to find the mixed-mean temperature for the case of simple heating with no evaporation at the free surface for plane and radial flow. This analysis follows the same pattern as was accomplished for the momentum equation of the problem. The conservation of energy will be integrated across the thin film in order

to find the mixed-mean temperature.

The conservation of energy equation is

$$\rho C_p \left[\frac{\partial T}{\partial t} + w\frac{\partial T}{\partial r} + v\frac{\partial T}{\partial y}\right] = \frac{K}{r^{\lambda}} \frac{\partial}{\partial r}\left[r^{\lambda}\frac{\partial T}{\partial r}\right] + K\frac{\partial^2 T}{\partial y^2} \qquad (1.4.8)$$

The assumption is made that the diffusive term in the r-direction is zero.

$$\frac{\partial T}{\partial t} + w\frac{\partial T}{\partial r} + v\frac{\partial T}{\partial y} = a\frac{\partial^2 T}{\partial y^2} \qquad (1.4.9)$$

The conservation of energy equation is integrated across the thickness of the film by using Leibniz's rule and the kinematic condition at the free surface. Since the steady-state solution of the fluid velocity will be known from the fluid mechanics analysis, the steady solution of the conservation of energy equation will be found. The continuity equation (1.3.6) and the conservation of energy equation are

$$r^{\lambda} W\delta = \frac{q}{(2\pi)^{\lambda}} = \text{constant}$$

$$\frac{\partial T_b}{\partial r} = \frac{(2\pi r)^{\lambda} a}{q}\left[\left.\frac{\partial T}{\partial y}\right|_{\delta} - \left.\frac{\partial T}{\partial y}\right|_{0}\right] \qquad (1.4.10)$$

Implementing the heat flux boundary conditions corresponding to simple heating with no evaporation at the free surface results in the following equation.

$$\frac{\partial T_b}{\partial r} = \frac{(2\pi r)^{\lambda} q}{Q\rho C_p} \tag{1.4.11}$$

This equation can be integrated directly to determine the difference in the mixed-mean temperature between the inlet and any point in the r-direction.

$$T_b - T_{b,in} = \frac{\pi^{\lambda} q r}{Q\rho C_p} \left[r - \frac{r_{in}^2}{r} \right]^{\lambda} \tag{1.4.12}$$

1.5 NUMERICAL SOLUTION PROCEDURE

Due to the similarity between the hydraulic jump and the shock wave in gas dynamics, the MacCormack explicit method (Anderson et al., 1984), which is quite often used for the solution of compressible flow problems, will be used in the present numerical analysis of this incompressible film flow. Since it is an explicit method, the unknown variables are found in terms of known quantities, as opposed to implicit methods which must solve a matrix equation to obtain the solution of the problem.

The governing equation for the present problem is equation (1.3.9):

$$V_{\tau} + V\hat{\xi}^{\lambda} G_{\hat{\xi}} = H$$

The forward-predictor finite-difference equation for the governing equation is forward in time and space.

$$V_k^{\overline{n+1}} = V_k^n \left[1 - \hat{\xi}_k^{\lambda} \frac{\Delta\tau}{\Delta\xi} \left[G_{k+1}^n - G_k^n \right] \right] + \Delta\tau H_k^n \tag{1.5.1}$$

The finite-difference equation based on the predicted solution using a forward-time, backward-space differencing scheme is:

$$(V_k^{\overline{n+1}})' = V_k^{\overline{n+1}} \left[1 - \hat{\xi}_k^{\lambda} \frac{\Delta\tau}{\Delta\xi} \left[G_k^{\overline{n+1}} - G_{k-1}^{\overline{n+1}}\right]\right] + \Delta\tau H_k^{\overline{n+1}}$$

The corrected solution is the arithmetic average of the past and predicted solutions.

$$V_k^{n+1} = \frac{1}{2}\left[V_k^n + (V_k^{\overline{n+1}})'\right]$$

$$V_k^{n+1} = \frac{1}{2}\left\{V_k^n + V_k^{\overline{n+1}} \left[1 - \hat{\xi}_k^{\lambda} \frac{\Delta\tau}{\Delta\xi} \left[G_k^{\overline{n+1}} - G_{k-1}^{\overline{n+1}}\right]\right] + \Delta\tau H_k^{\overline{n+1}}\right\} \qquad (1.5.2)$$

Since the forward-predictor velocity is in terms of a forward-space approximation, an outlet boundary condition on the velocity is needed. For the case of one g, it is assumed that the Froude number at the outlet is unity, which is a common boundary condition when a liquid falls over an edge because the liquid accelerates from a subcritical velocity to a supercritical velocity through the critical velocity. It was experimentally observed, however, that for thin films the surface tension greatly alters this boundary condition. The Froude number at the inlet and the dimensionless velocity at the outlet are related as follows:

$$V_{out} = \left[\frac{\hat{\xi}_{in}}{\hat{\xi}_{out}}\right]^{\lambda/3} Fr_{in}^{-2/3} \qquad (1.5.3)$$

For the zero g case and when the Rossby number is Ro < 1, the slope of the dimensionless velocity at the last node is set equal to the slope at the next to last node for the outlet boundary condition.

The solution of the governing equation using MacCormack's method proceeds as follows:

- The parameters pertaining to the numerical domain and the inlet and outlet boundary conditions are specified.

- The initial velocity distribution is input to the program.

- The variables G and H are computed using the velocity profile at the old time step.

- The velocity distribution at the midpoint time step is calculated in terms of the velocity, G, and H at the old time step. An outlet boundary condition is needed in this step because of the forward-space approximation.

- The variables G and H are computed again by using the velocity profile at the midpoint time step.

- The velocity distribution at the new time step is calculated. The inlet boundary condition is used in this step because of the backward-space approximation.

- The values of the velocity distribution at the new time step are used as the initial velocity profile for the next iteration.

- The process is repeated until steady values are reached.

In explicit schemes, the magnitude of the time step is chosen based upon a Courant number, which is defined for the present problem in the following manner.

$$C = \frac{\Delta\tau}{\Delta\xi}\left[\frac{w + r\omega}{w}\right] = \frac{\Delta\tau}{\Delta\xi}\left(1 + Ro^{-1}\right)$$

In this study, the grid size was set to a specific value and the time step was varied to avoid convergence difficulties. The largest time step that did not lead to a divergent solution was then used in the calculations. The following table is a general guideline which was used to determine the time step size.

Flow situation	**Courant number, C**
Plane flow	< 1.0
Radial flow	**< 0.5**
Radial flow with rotation	< 0.1

One hundred grids were used in the plane flow calculations. For radial flow, 500 grids were used because the governing equation was very lightly damped, so that the numerical oscillations were excessive with only 100 grids. There was no significant change (< 0.1 percent) in the numerical

results when the aforementioned grid specifications were reduced by one-half to check the grid independence of the solution.

1.6 RESULTS AND DISCUSSION

The thicknesses of free surface films in plane and radial flow have been calculated numerically. In addition, the Nusselt number was calculated for simple heating with no evaporation at the free surface with water as the working fluid. The results of the one-dimensional quasi-steady governing equation of fluid motion are given in Figs. (1.3 - 1.7). The heat transfer results are shown in Fig. 1.8 for plane and radial flow in one g and in Fig. 1.9 for radial flow with solid-body rotation.

Figure 1.3 shows the solution for channel flow as it progresses in time. It can be seen that the supercritical portion of the flow develops very quickly while the subcritical region and the exact location of the hydraulic jump takes more time to reach the steady state. The Gibb's phenomenon can easily be noticed in the transient solutions of the governing equation, but the oscillations become more damped in the steady solution. Due to the assumptions pertaining to the governing equations, the transient solutions of the problem are not accurate, but the steady solutions should be acceptable. In the following figures, only the steady-state solutions are given. It is clear that the velocity profile in the immediate vicinity of the hydraulic jump is not a good representation of the flow field due to the transient nature of the jump. However, this does not affect the numerical results in the supercritical or subcritical regions as well as the location of the jump. In order to capture the

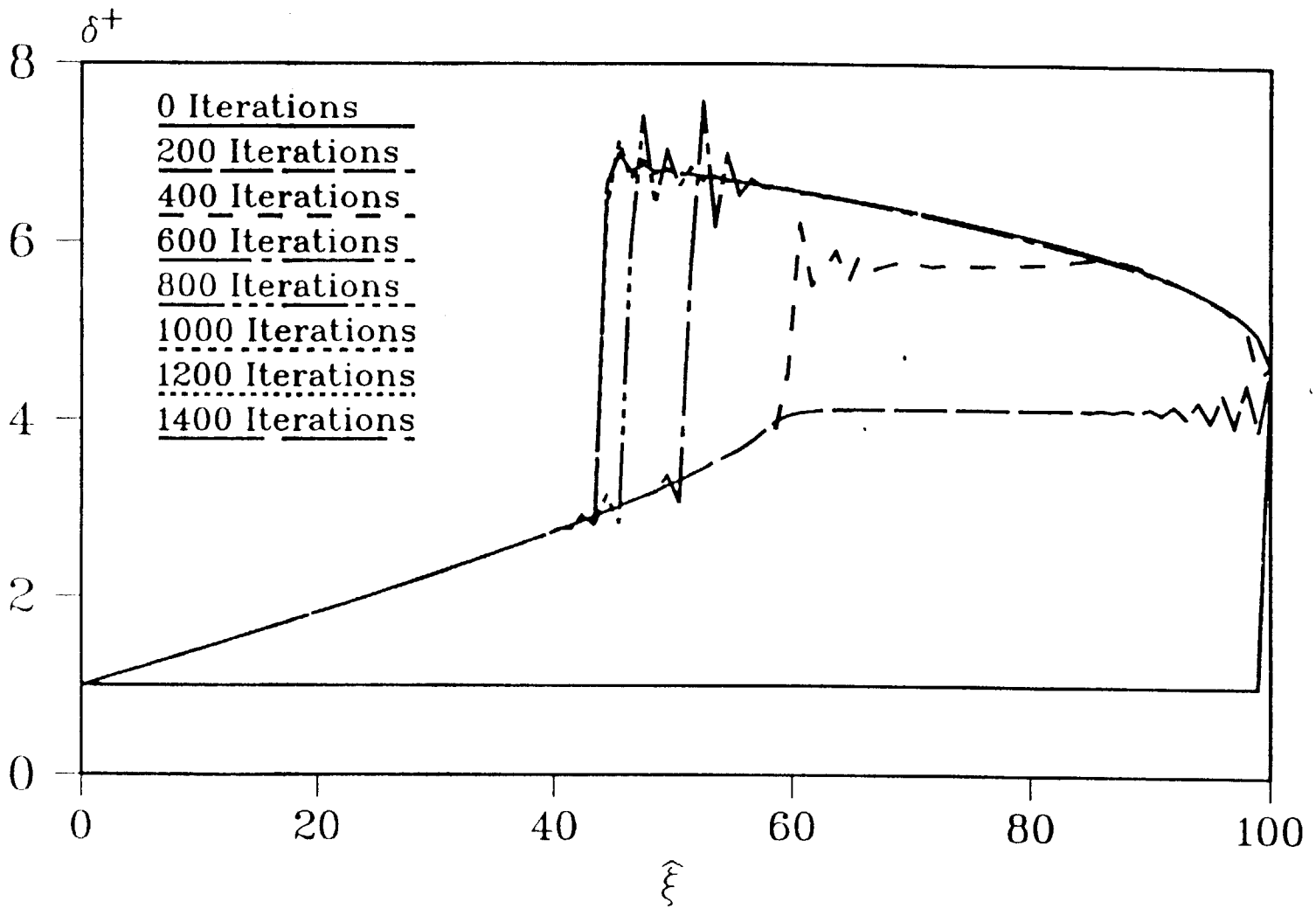

Figure 1.3. Dimensionless liquid height versus dimensionless distance for plane flow with Fr_{in}=10.0, Fr_{out}=1.0, Re_{in}=75.0, $\hat{\xi}_{in}$=0.0, $\hat{\xi}_{out}$=100.0 as the solution marches in time

details of the jump, a two-dimensional model using body-fitting coordinates is needed.

As can be seen in Fig. 1.3, the film thickness increases along the plate as the fluid travels away from the inlet of the region. The fluid is prevented from rolling back due to the action of gravity by the momentum of the fluid in the main direction of the flow. The reason that the film thickness increases with distance in the supercritical region is that the friction at the interface between the fluid and the plate slows the fluid, which translates into an increase in the film thickness due to continuity.

The effects of changing the inlet Reynolds number and the inlet Froude number in plane flow are presented in Fig. 1.4. The graphs in the left-hand column of the legend show the dimensionless liquid height when the Froude number is held at Fr_{in} = 10.0 and the Reynolds number is varied for Re_{in} = 25.0, 50.0, and 75.0. By increasing the inlet Reynolds number, the location of the hydraulic jump moves downstream and the dimensionless height of the liquid at all points in the domain decreases. Physically, increasing the Reynolds number can be interpreted as increasing the inertial forces on the fluid, so one would intuitively expect that the velocity of the fluid would increase as the Reynolds number increases. This increase in the fluid velocity is correlated to a decrease in the film thickness through the continuity equation.

The graphs in the right-hand column of the legend in Fig. 1.4 present the dimensionless liquid film height when the Reynolds number is constant at Re_{in} = 100.0 and the Froude number is varied for Fr_{in} = 5.0, 7.0, and

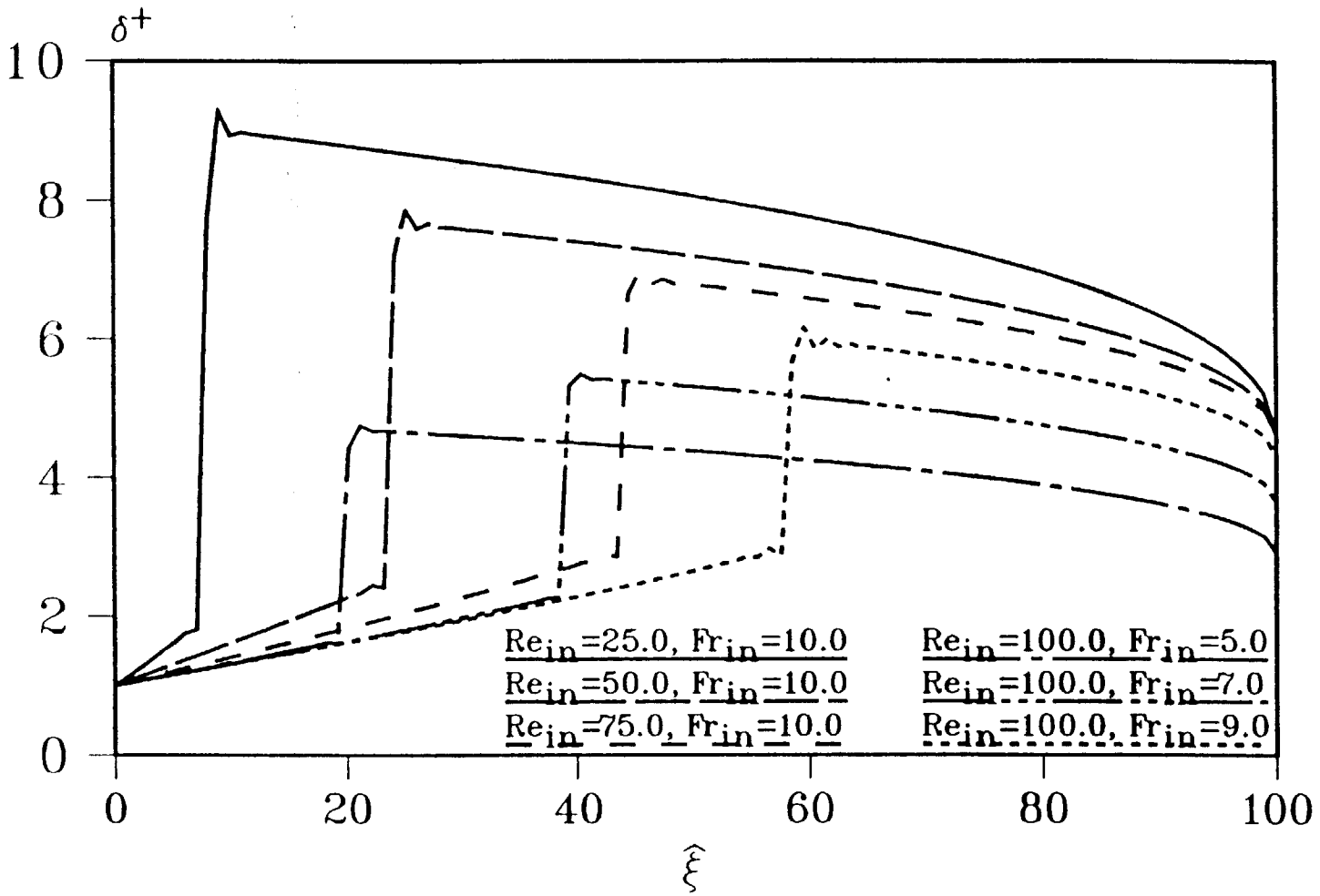

Figure 1.4. Dimensionless liquid height versus dimensionless distance for plane flow with $\hat{\xi}_{in}$=0.0, $\hat{\xi}_{out}$=100.0

9.0. The location of the hydraulic jump moves downstream when the inlet Froude number increases, which has been seen in qualitative experiments. The dimensionless height of the liquid in the supercritical region generally lies along the same line because the viscous forces are not changing in this case. Increasing the Froude number can be thought of as decreasing the effect of the gravitational force, so by increasing the inlet Froude number, the flow approaches the zero g case. In the zero g situation, as shown in Fig. 1.5 for plane and radial flow, the hydraulic jump does not occur because the flow at all points in the domain is supercritical, since the Froude number approaches infinity in zero g. In Fig. 1.5, the dimensionless film height decreases as the Reynolds number increases because the inertial forces on the film flow are greater.

In Fig. 1.6, the inlet Froude number and the inlet Reynolds number in radial flow are varied parametrically. When the inlet Froude number is held constant and the Reynolds number is increased, the behavior of the flow is similar to plane flow in that the film thickness decreases and the hydraulic jump moves downstream. The film thickness in the supercritical region, however, decreases below the initial thickness downstream from the inlet at high Reynolds numbers. This is due to the increase in the flow area downstream as the flow spreads out radially. After this initial decrease in the film thickness, the film height increases in the supercritical region even though the flow is spreading out radially. This is due to the fact that the frictional effect is greater than the effect due to the increase in the flow area. The friction at the plate slows down the flow and increases the film thickness. As shown by Rahman et al. (1989), the liquid film height in the supercritical region may or may not

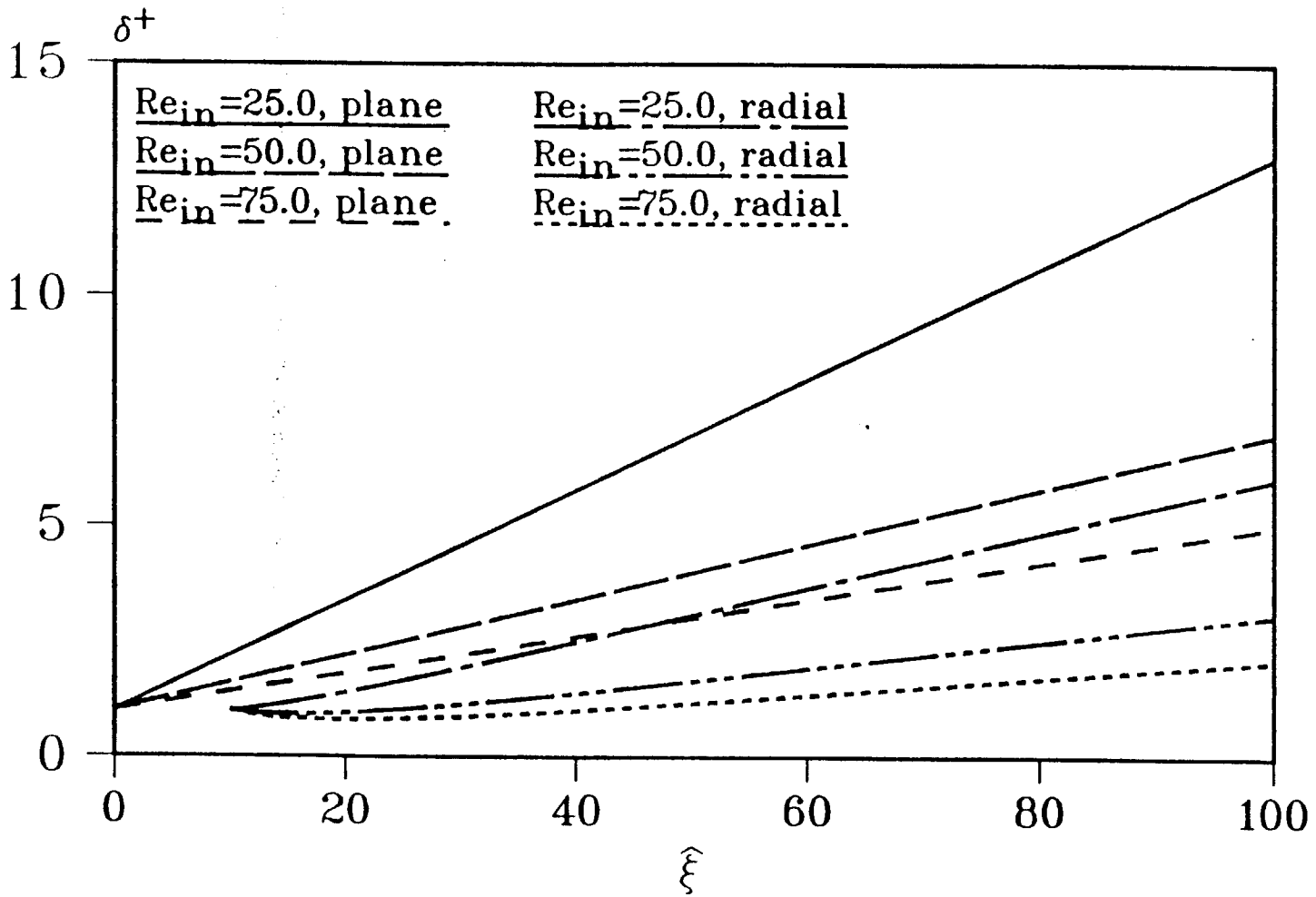

Figure 1.5. Dimensionless liquid height versus dimensionless distance for plane and radial flow with $\hat{\xi}_{in}$=0.0 (plane), $\hat{\xi}_{in}$=10.0 (radial), $\hat{\xi}_{out}$=100.0 for different values of the inlet Reynolds number in zero g

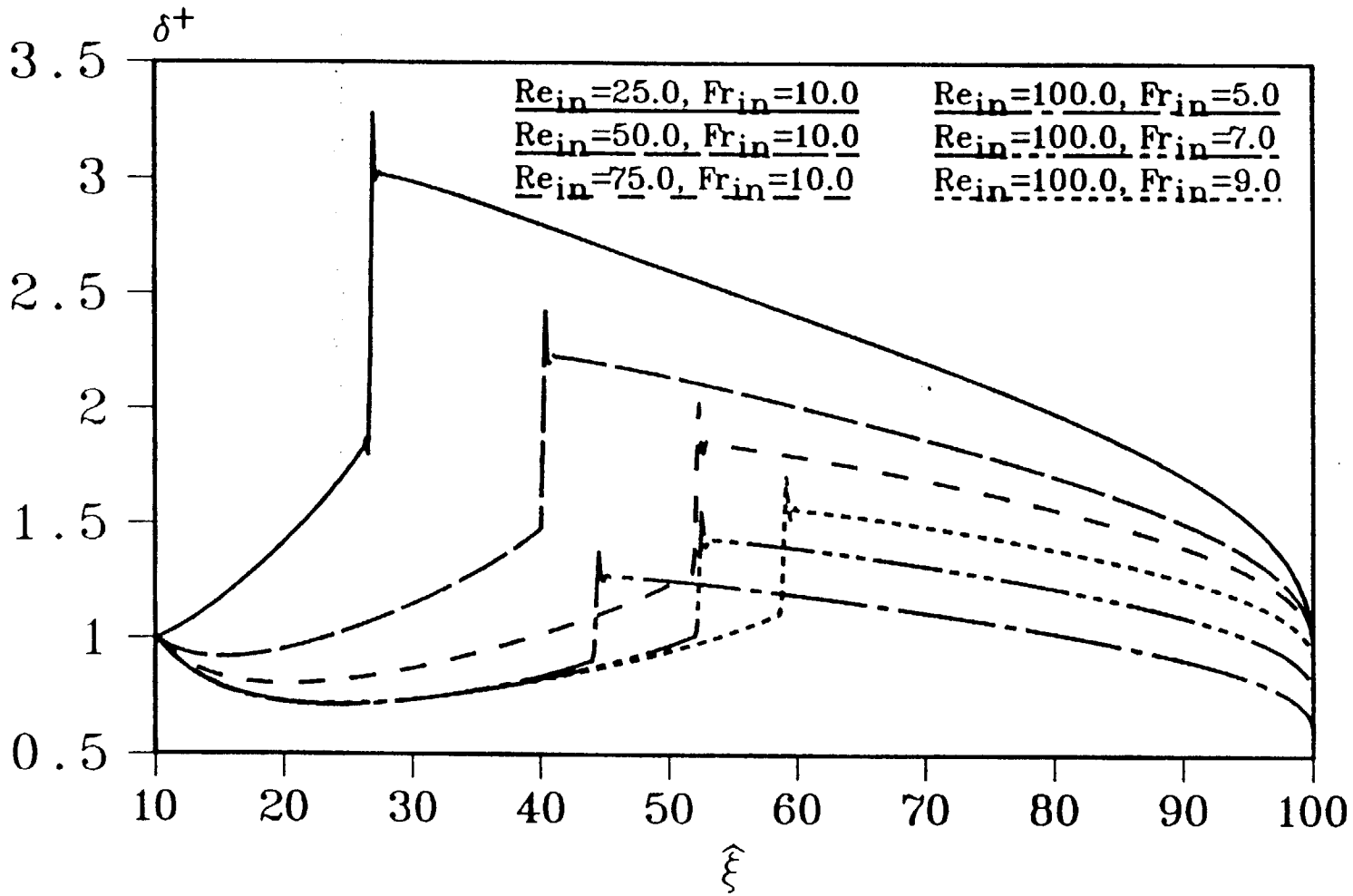

Figure 1.6. Dimensionless liquid height versus dimensionless distance for radial flow with $\hat{\xi}_{in}$=10.0, $\hat{\xi}_{out}$=100.0

have a minimum value other than the inlet height, depending upon the coefficient of friction at the plate and the inlet Froude number.

The effect of increasing the Froude number while the Reynolds number remains constant in radial flow is also shown in Fig. 1.6. The supercritical regions of the three cases overlap as in channel flow because the viscous forces on the liquid film are not changing. The hydraulic jump is moved downstream from the inlet as the Froude number is increased.

Figure 1.7 presents the effect of solid-body rotation on the dimensionless liquid film height in radial flow for one g and zero g. The Rossby number of $Ro_{in} = 10^{10}$ signifies that the inertial forces are dominant in the flow, so that a profile similar to the previous results is obtained. For the other cases presented where the Rossby number is $Ro_{in} = 10^{-1}$ and 10^{-2}, the hydraulic jump is completely washed out and the thickness of the fluid decreases at all points in the domain, which is physically realistic. The results for the low Rossby numbers also show that the dimensionless liquid film height is the same whether the gravitational body force is present or not. This is due to the fact that the centrifugal body force in this case is much greater than the gravitational body force.

Figure 1.8 presents the Nusselt number versus the dimensionless distance for plane and radial flow under one g. For these calculations, the values in equation (1.4.6) were chosen to be $\delta_{in} = 2.54 \times 10^{-4}$ m, K = 0.682 W/m-K, $\nu = 2.90 \times 10^{-7}$ m^2/s, and g = 9.81 m/s^2. The values of the thermal conductivity and the kinematic viscosity correspond to water at

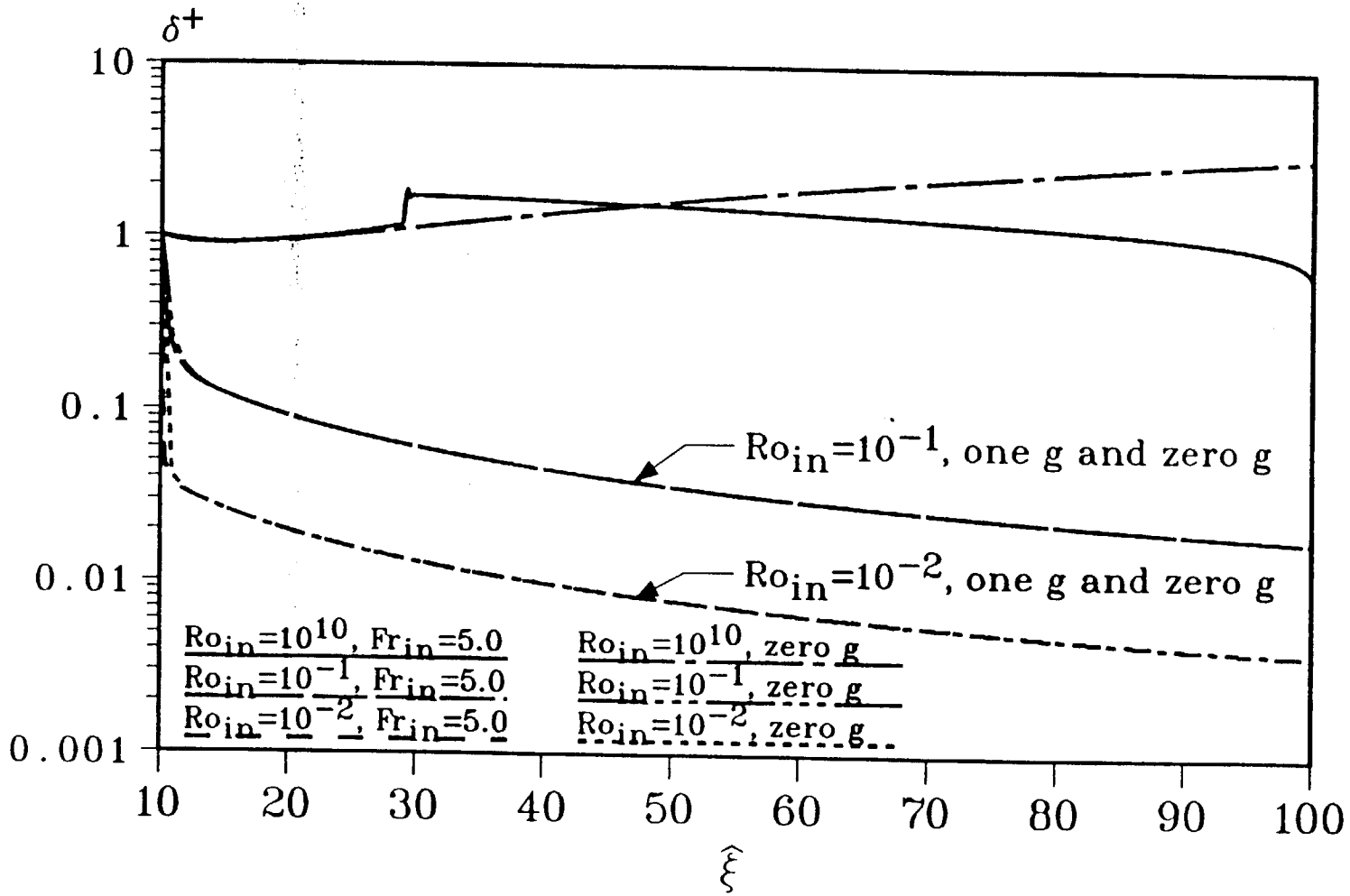

Figure 1.7. Dimensionless liquid height versus dimensionless distance for radial flow with $Re_{in}=50.0$, $\hat{\xi}_{in}=10.0$, $\hat{\xi}_{out}=100.0$ for different values of the Rossby number in one g and zero g

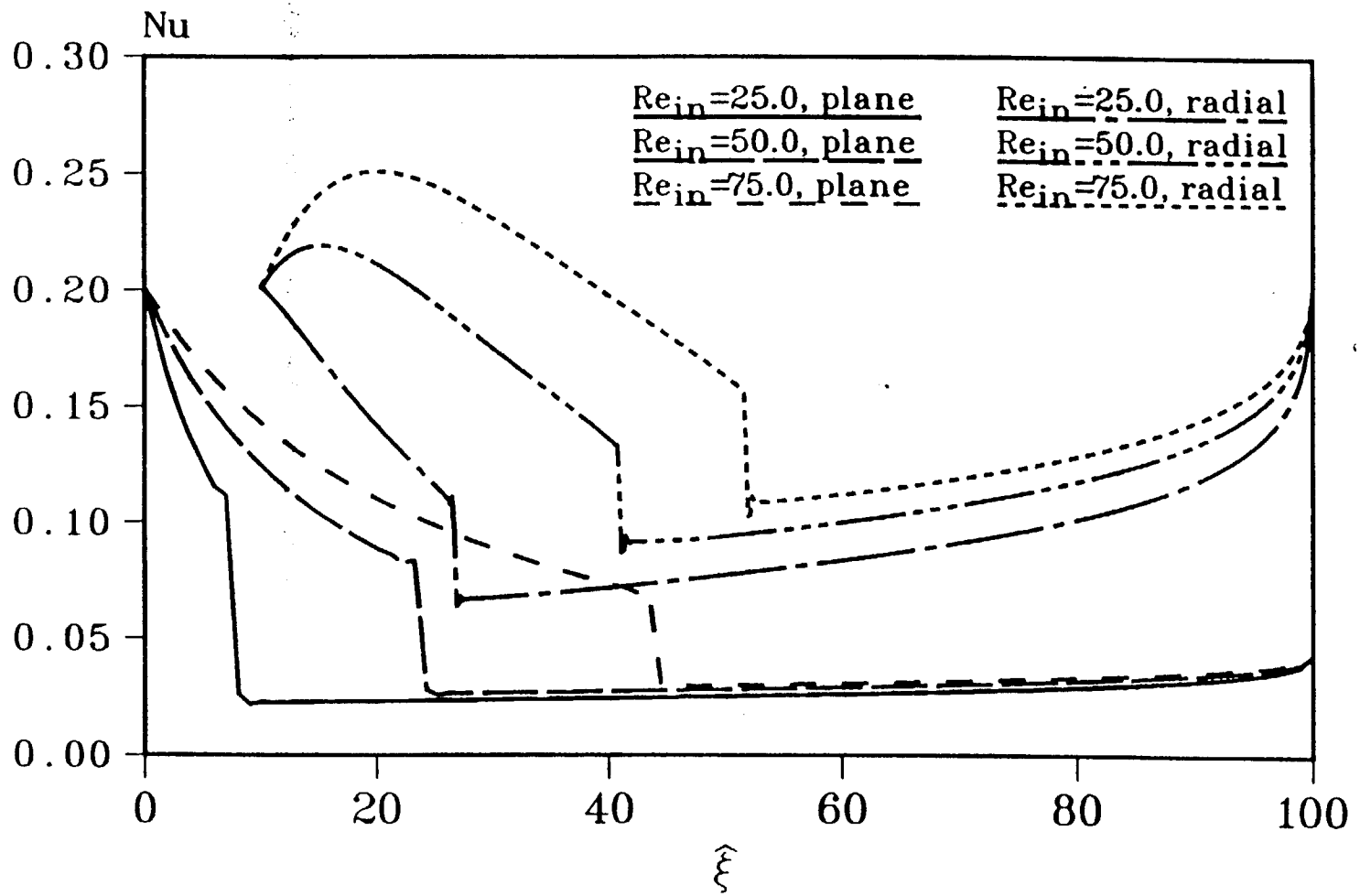

Figure 1.8. Nusselt number versus the dimensionless distance for plane and radial flow with Fr_{in}=10.0, $\hat{\xi}_{in}$=0.0 (plane), $\hat{\xi}_{in}$=10.0 (radial), $\hat{\xi}_{out}$=100.0 under one g

373 K. As would be expected, the heat transfer increases as the Reynolds number increases because the height of the film decreases at all points along the plate.

Figure 1.9 presents the Nusselt number for the case of solid-body rotation in radial flow under one g. The heat transfer to the liquid in this case is two orders of magnitude higher than that without rotation because the liquid film becomes extremely thin and the velocity of the film is very high.

It should be noted that while the heat transfer results that were presented are for thin films under one g, the heat transfer to thin films in a zero g environment can also be calculated with equation (1.4.5).

1.7 CONCLUSIONS

In studying plane and radial flows experimentally, it can be seen that the flow can experience a hydraulic jump. This is a "mixed" flow situation where the flow changes from a supercritical condition to a subcritical condition with a sudden increase of the liquid height and a decrease in the velocity of the liquid. The similarity between the hydraulic jump and the shock wave in gas dynamics suggested the use of the approach where the flow is modeled as a transient phenomenon and allowed to march in time to achieve the desired steady-state results. Therefore, the equations of motion including the transient terms were integrated across the thin liquid layer, nondimensionalized, and discretized using the MacCormack explicit method to solve for the velocity and height of the liquid film in Cartesian

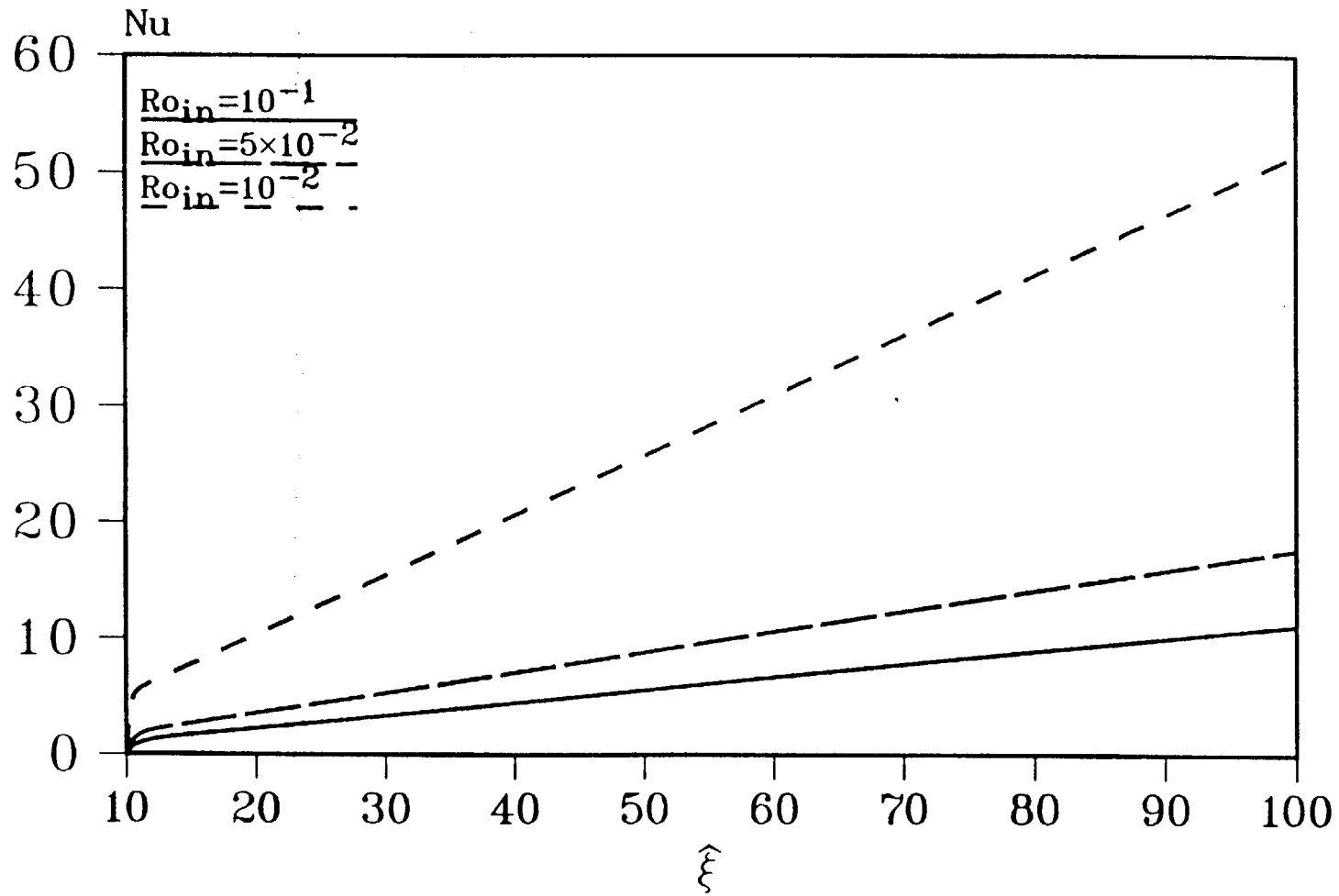

Figure 1.9. Nusselt number versus the dimensionless distance for radial flow with Fr_{in}=10.0, Re_{in}=50.0, $\hat{\xi}_{in}$=10.0, $\hat{\xi}_{out}$=100.0, under one g

and radial coordinates. Also, the steady-state heat transfer from the plate to the liquid was examined for the case of simple heating with no evaporation at the free surface. Since the numerical method of solution is explicit, large amounts of computer storage were not necessary.

For plane flow in one g, a hydraulic jump was predicted which could be forced away from the inlet by increasing the initial Froude number or Reynolds number, which agrees with what has been found in qualitative experiments. In zero g, the liquid film height increased monotonically, so that a hydraulic jump was not predicted.

For radial flow in one g, the liquid film height first decreased for high Reynolds numbers due to the increase of the flow area, and then increased to form a hydraulic jump. The hydraulic jump in radial flow could also be forced away from the inlet by increasing the initial Froude number or Reynolds number. In zero g, the hydraulic jump was not predicted in radial flow. The effect of solid-body rotation for radial flow in one g was found to thin the liquid film and "wash out" the hydraulic jump, which is physically realistic. The dimensionless film thickness under one g and zero g was the same for solid-body rotation because the centrifugal force was much greater than the gravitational body force. The heat transfer from the rotating disk was found to increase dramatically when under solid-body rotation compared to no rotation because the liquid film is very thin and moves with a high velocity.

Section II

EXPERIMENTAL MEASUREMENT OF FILM HEIGHT AND VISUALIZATION OF FLOW

2.1 SUMMARY

In this experimental study, the thickness of a thin liquid film with a free surface on a stationary and rotating disk is measured with a non-obtrusive capacitance technique. The measurements are taken when the rotational speed ranges from 0 - 300 RPM and the flow rate varies from 7.0 - 15.0 LPM. A photographic study of the thin liquid film was also performed and the results are presented herein. When the disk is stationary, a hydraulic jump is formed on the disk, which separates the supercritical and subcritical regions. As the flow rate of the fluid increases, the hydraulic jump is moved away from the center of the disk. The liquid film thickness in the supercritical region is affected by the inertial and frictional forces on the fluid and by the radial spreading of the film across the disk. The film thickness in the subcritical region is mainly determined by the surface tension of the fluid because the radius of curvature at the outer edge of the disk, which is nearly constant for flow rates up to approximately 13.0 LPM. When the disk is rotating, the film thickness depends upon the frictional, inertial, and centrifugal forces acting on the liquid. In the region near the center of the disk, the effects of friction and inertia are greater than that due to the centrifugal force, while at the outer edge of the disk the opposite is true. A flow visualization study was carried out to examine the nature of the free surface of the thin liquid film when the disk is stationary and

rotating. When the disk is stationary, surface waves were present in the supercritical and subcritical regions at all flow rates studied. The waves in the supercritical region have smaller amplitudes than those in the subcritical region. At the hydraulic jump, a "roller" with a circular cross section was found at low flow rates. As the flow rate increased, the roller flattened until it merged with the hydraulic jump. The surface tension at the edge of the disk held the thickness at this location nearly constant, except at higher flow rates where the inertial forces of the fluid became greater than the surface tension and decreased the height of the fluid at the edge. This effect was also present at low rotational speeds, where the surface tension created a standing wave at the edge of the disk. As the rotational speed increased, the film changed from the wavy-laminar region to a region in which waves ran nearly radially across the disk on top of a thin substrate of fluid. These waves appeared to be the mechanism through which most of the fluid drained from the disk.

2.2 INTRODUCTION

The heat transfer from a rotating disk to a thin film has been recognized in the past to be superior to conventional falling films because the centrifugal force tends to thin and accelerate the film, which translates into higher heat transfer coefficients. As a first step in determining the heat transfer to a thin film, it is proposed to experimentally study the hydrodynamic characteristics of a thin film with a free surface flowing over stationary and rotating disks. The present experimental investigation is directed toward the use of a thin film on a rotating disk to promote the absorption of a vapor into the liquid on the

disk. Specifically, the absorber of a space-based vapor-absorption refrigeration system will use a liquid film which is thinned by the centrifugal force on a rotating disk to enhance the absorption of the refrigerant vapor into the absorbent because a falling film cannot be produced in a microgravity environment. The vapor-absorption cycle is more appropriate for a microgravity application because the vapor compressor is replaced by a liquid pump, which is lighter, requires less maintenance, and is easier to manufacture for space-based applications.

To properly study any problem, the previous studies on the subject must be thoroughly investigated. Each of the following researchers have experimentally examined the flow of thin liquid films. A brief description of their methods and conclusions are provided.

Watson (1964) analysed a free-falling jet which impinges on a horizontal plane. The jet spreads out radially in a thin film and is surrounded by a hydraulic jump, outside of which the thickness of the liquid is much greater. Watson experimentally measured the diameter of the hydraulic jump (r_1) with dividers, the depth of the fluid outside the jump (d) with a point gage, and the flow rate (Q) with a measuring jar and stop watch. The experimental data ranged from $25.4 < r_1 < 177.8$ mm, $3.30 < d < 16.5$ mm, and $0.73 < Q < 26.8$ LPM. The jet Reynolds number $Re = Q/a\nu$ ranged from 7×10^3 to 1.2×10^5, where a is the radius of the jet. The theoretical results of the location of the hydraulic jump and the depth of the liquid outside the jump were compared to experimental results with a satisfactory agreement.

Espig and Hoyle (1965) experimentally measured the maximum thickness of a liquid film on a horizontal rotating disk. The maximum thickness is the height of the film which is measured to the crest of the waves on the film. Measurements were taken by using a needle probe which was lowered with a vernier, which completed an electrical circuit when the probe touched the film surface. The Reynolds number $Re = (4\ \dot{Q}/\pi\mu D)$ ranged from 10 to 600, where $\dot{Q}$ is the mass flow rate, μ is the dynamic viscosity, and D/2 is the distance from the center of the disk. The flow conditions were also observed visually with a stroboscope which showed rivulets, circumferential waves, and helical waves. The experimental results were in agreement with the theoretical and experimental results of previous authors.

Butuzov and Rifert (1972) experimentally measured the heat transfer of condensing steam onto one side of a rotating copper disk, the opposite side of the disk being cooled with a condenser. The results for the average heat transfer coefficient versus the disk angular speed were presented. The disk speed varied from 10 to 224 rad/sec and the heat flux ranged from 2×10^4 to 19×10^4 W/m^2. The experimental Reynolds number of the condensate was compared to the theoretical results with an agreement to within 5 - 10 percent. The theoretical results were obtained by using a previously derived equation for the thickness of a laminar liquid film on a rotating disk. This was related to the flow rate of the condensate on the disk for steam condensation.

Charwat et al. (1972) studied the effects of varying the viscosity and surface tension of a thin liquid film on a rotating glass plate. The film

thickness was determined by the infra-red absorption technique, and it was found that the thickness varied from 1 - 150 μm for flow rates up to 0.78 LPM. Concentric, spiral, and irregular waves were found on the surface of the film, and were strongly affected by varying the viscosity (1 - 2.5 cP) and surface tension (20 - 72 dynes/cm).

Matsumoto et al. (1973) compared various theoretical solutions of previous authors with a polynomial approximation for the thickness of a thin liquid film on a rotating disk. The authors also devised an experiment where constant temperature liquid was supplied to the center of a rotating disk by a feed nozzle above the disk. The liquid film height was measured along the radius by a needle attached to two micrometer screws. The kinematic viscosity of the liquid ranged from 9.61 to 58.3 cS, the rotational speed varied from 250 to 1500 RPM, and the flow rate ranged from 0.3 to 1.87 LPM. It was concluded that a polynomial of fourth degree or higher agreed very well with the experimental results.

Miyasaka (1974) compared the results of an experimental study with those of a theoretical study of the thickness of a thin viscous film on a rotating disk. The liquid film was generated with a jet of liquid falling onto the center of a horizontal rotating disk. The film height was measured by comparing the resistance of the liquid on the disk with that of a standard thickness of the liquid, which resulted in an accuracy of ± 0.02 mm. The jet Reynolds number was varied from 200 to 18,000. The theoretical values were obtained by solving the governing equations of motion with the boundary-layer approximation. The theoretical results include the values of the liquid film when viscosity is and is not present. It was concluded

that the theoretical values were in agreement with the experimental results.

Ishigai et al. (1977) experimentally measured the liquid film thickness and heat transfer from a thin film generated by an impinging liquid jet onto a perpendicular surface. The film thickness was measured with a needle and micrometer arrangement, and a voltage source applied to the surface of the plate. When the needle touched the surface of the film an electric circuit was completed, which was read by an oscilloscope. The flow rate ranged from 3.0 to 30 LPM. The experimental data of the liquid film height was compared to the analytical equation given by Watson (1964) with satisfactory results.

Labus and DeWitt (1978) experimentally examined the flow patterns of the free surface of an impinging jet of liquid on a disk perpendicular to the jet in zero gravity. This was achieved in a drop facility in which a 2.2 second period of 10^{-5} g's could be sustained. Flow visualization studies revealed that surface tension and inertia were the major forces acting on the liquid.

Craik et al. (1981) experimentally studied the circular hydraulic jump formed by an impinging jet of liquid on a horizontal plate. The liquid film thickness in the region near the hydraulic jump was measured using a light-absorption technique with a laser and a strong dye. The parameters which were varied are as follows: the flow rate, 0.27 to 1.56 LPM; the jet radius, 1.0 to 2.15 mm; the jump radius, 12.0 to 40.0 mm; and the outer depth, 1.8 to 3.5 mm. The experimental data was compared to Watson's

(1964) theory with unsatisfactory results. Flow visualization studies were performed, and an eddy just downstream of the hydraulic jump was found.

Muzhilko et al. (1983) experimentally measured the liquid film thickness on a horizontal rotating disk where the liquid is introduced onto the center of the disk by an impinging jet. The film thickness was measured by sensing electrodes embedded into the surface of the disk, whose resistance is a function of the film thickness. The mean film thickness was measured at radii of 30, 60, and 90 mm. The angular velocity ranged from 95 to 1900 RPM, and the flow rate varied from 0.04 to 1.2 LPM. The mean film thickness results were correlated by an empirical equation which predicts the data to within ±15 percent in the laminar-wavy region.

Carper et al. (1986) experimentally studied the heat transfer from one side of a rotating disk with an approximately uniform surface temperature. The liquid was supplied to the center of the disk by a nozzle. The average Nusselt number was presented for the following parameters: the rotational Reynolds number ($16{,}000 < Re_r = \omega D^2 \nu < 545{,}000$), the Prandtl number ($87 < Pr < 400$), and the impinging jet Reynolds number ($180 < Re_j = dU_j/\nu < 1300$). D is the disk diameter, ω is the angular velocity, ν is the kinematic viscosity, d is the jet nozzle diameter, and U_j is the average jet velocity. An empirical equation for the average Nusselt number is derived by a multiple linear regression analysis which represents 95 percent of the data to within ±30 percent.

Most of the previous experimental investigations were concerned with thin liquid films which were generated by an impinging jet onto the center

of the rotating or stationary disk. In the present study, the liquid film is generated on the rotating disk by a circular collar which directs the pressurized liquid onto the center of the rotating disk with a constant initial height and velocity. This collar arrangement can be extended to collars on each side of the disk, and then multiple disks can be stacked onto a rotating pipe so that a very large surface area for absorption can exist in a small volume. Also, this arrangement is amenable to numerical simulation because of the known inlet conditions.

The effect of two parameters on the thickness of the liquid film were studied: the flow rate (7.0-15.0 LPM) and the rotational speed (0-300 RPM) at the steady state. The liquid film thickness was measured with a non-obtrusive capacitance probe and digital micrometer arrangement. The characteristics of the waves on the free surface were studied with a video camera at low and high shutter speeds.

2.3 EXPERIMENTAL SETUP

The purpose of this experiment was to measure the liquid film thickness on a stationary and rotating horizontal disk where the liquid emanates from a pressurized vessel in the center of the disk. In the future, this apparatus can also be used to determine the heat transfer from the heated disk to the thin liquid film when the disk is stationary and rotating. De-ionized water was used as the working fluid because the properties are well-known and it is non-toxic.

The schematic of the experimental setup is shown in Fig. 2.1. The specifications of all of the equipment used in this experiment are listed in Appendix B following this report. The 406.4 mm dia. rotating disk [1] is mounted on a high-precision stainless steel spindle [3] which is hollow from the 101.6 mm dia. stainless steel collar [2] to the rotating union [21]. The rotating disk is made of aluminum with a surface finish of 3.8×10^{-4} mm. The working fluid flows from the circulating pump [25] through the stationary pipe to the rotating union, which couples the stationary pipe and the hollow spindle. The liquid then passes up above the rotating disk and through eight 3.17 mm dia. radial holes in the hollow rotating spindle, which are covered by the collar. The collar directs the eight liquid streams down and outwardly so that the fluid is directed onto the top side of the disk with a velocity only in the radial direction and with a uniform initial height. The collar also makes sure that the height of the liquid at the collar does not change with respect to the azimuthal direction. The gap height between the bottom face of the collar and the top of the disk (0.267 mm) is set by a stainless steel shim which separates them. After the fluid flows over the disk, it is collected by the water tank [20] to be recirculated. The flow rate of the liquid can be varied by the large and small metering valves [26 and 27], which act as the gross and fine adjustments. The volumetric flow rate was determined with the turbine flow sensor [28] and the digital flow meter [29]. The rotational speed was varied by the frequency inverter speed controller [5] attached to the electric motor [4] and is read with the rotary encoder [7] and the speedometer [8].

In order to decrease the vibrations in the system, it is mounted onto

1. Rotating disk
2. Collar
3. High-precision spindle
4. Electric motor
5. Frequency inverter
6. 208v-460v transformer
7. Rotary encoder
8. Speedometer
9. Non-contact capacitance sensor
10. Capacitance sensor readout
11. Digital micrometer
12. Digital micrometer readout
13. Precision linear slide
14. Linear slide readout
15. Etched foil heater
16. Ceramic insulation
17. Thermocouples
18. Digital thermometer
19. Slip-ring capsule
20. Lexan water tank
21. Rotating union
22. Heat exchanger
23. 230v-460v transformer
24. 0-230v variac
25. Pressure booster pump
26. Small metering valve
27. Large metering valve
28. Turbine flow sensor
29. Digital flow meter

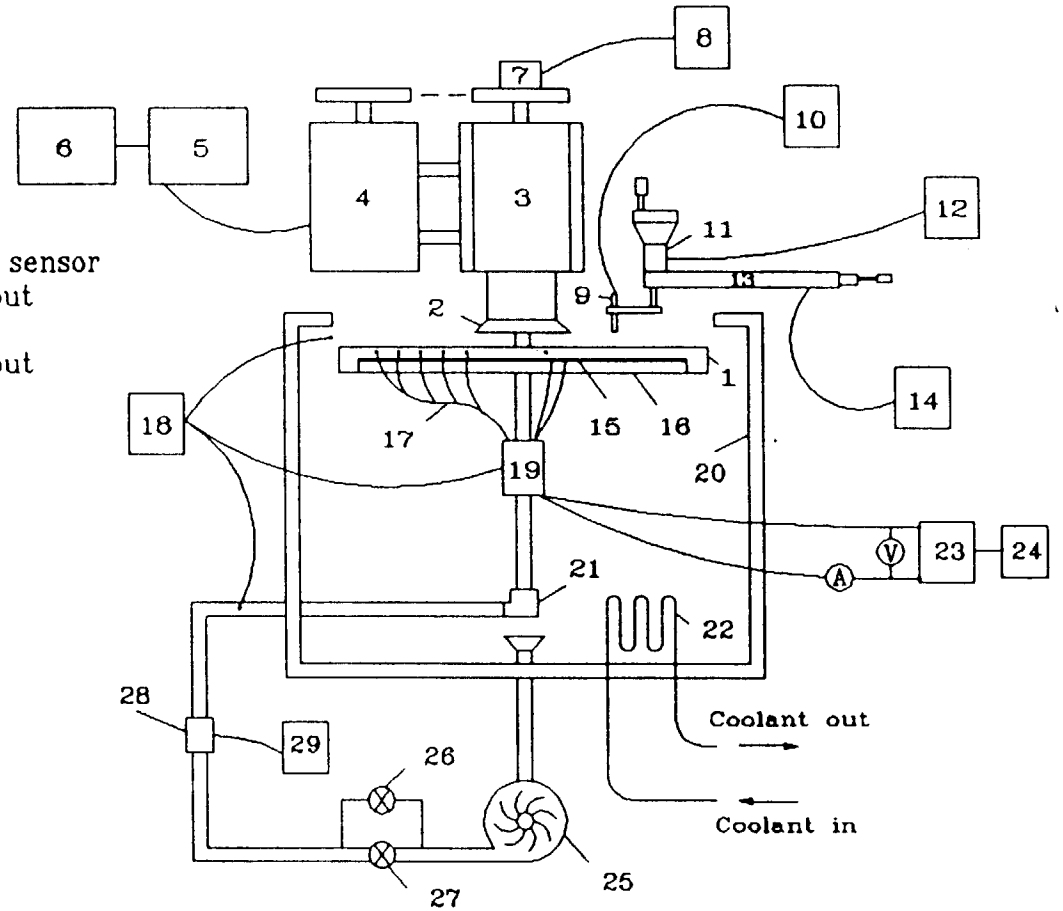

Figure 2.1. Experimental setup of rotating disk unit

a machine table. The total mass of the frame and the machine table is approximately 450 kg, which helps to damp out oscillations. The table is also fitted with four vibration mounts which are made of neoprene and are approximately 25 mm thick x 75 mm in diameter. The system is located in the corner of the building, which aids in decreasing the vibrations seen in the laboratory by being very close to the foundation.

To measure the height of the liquid film, a non-obtrusive measurement technique was devised as shown in Fig. 2.1. A non-contact capacitance sensor [9] is used to locate the surface of the disk and the surface of the liquid. The capacitance sensor directly relates the strength of the electric field to the air gap between the sensor and the target. This relation is linear within the stated range of the probe. The sensor is attached to a digital positioner [11] by which the sensor can be raised or lowered. The probe and digital positioner are both mounted onto a linear slide [13] which moves the sensor along the radius of the disk. The radial location of the capacitance probe is measured by a linear potentiometer attached to the linear slide. The procedure to measure the liquid film height is described below. The procedure is shown graphically in Fig. 2.2.

1. The capacitance probe was calibrated to the digital micrometer by bringing the probe down until it touched the disk very lightly, which could be seen with a light directed behind the probe. This is the datum 1 line shown in Fig. 2.2. The capacitance sensor was then zeroed at this point with the offset adjustment. The capacitance probe was raised slightly above the disk, where the digital micrometer was zeroed. The probe was then raised until it read the maximum value

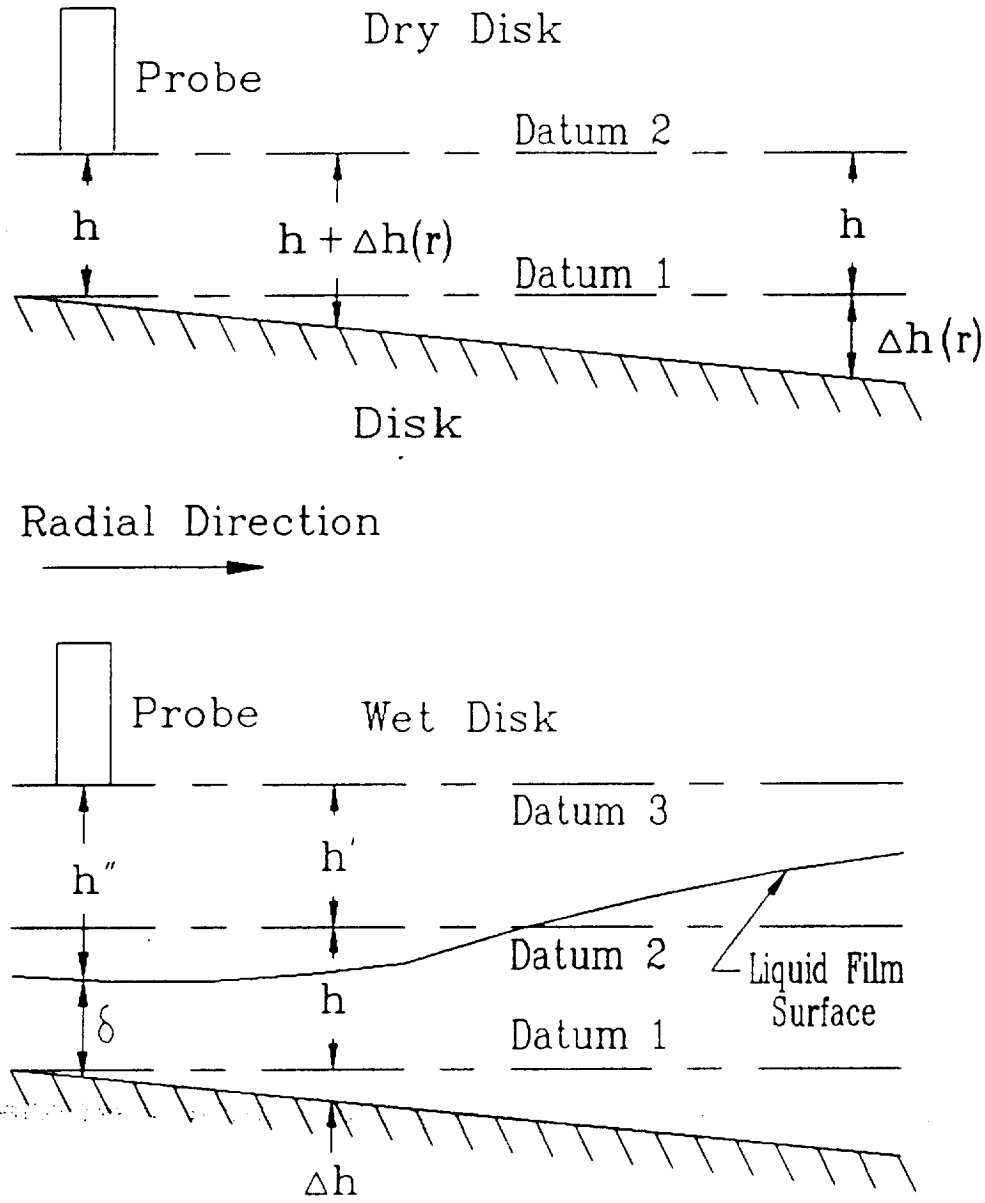

$$\delta(r) = h + \Delta h(r) + h'(r) - h''(r)$$

Figure 2.2. Liquid film height measurement

of its range. The value read on the capacitance sensor readout [10] was compared to what was shown on the digital micrometer readout [12]. Any discrepancy could be eliminated by a gain adjustment which is supplied on the capacitance sensor readout. This set the slope of the linear curve which relates the electric strength to the height of the air gap. It was found that the digital micrometer does have a small amount of backlash (< 0.008 mm), but this could eliminated by raising the probe to the desired location instead of lowering it.

2. With the disk dry, the capacitance probe was then moved to the datum 2 line with the digital micrometer, which was set to zero at this location. The height at the inner radius was set to an arbitrary value h, which is within the range of the probe.

3. The probe was moved along the radius to measure the deviation of the disk from the datum 1, which is called the tare data ($h + \Delta h$).

4. The probe was then raised to datum 3. The liquid flow was started and allowed to reach the steady state. The distance between datum 2 and datum 3 (h') was shown on the digital micrometer. The distance from datum 3 to the liquid film surface (h") was measured by the capacitance probe. The liquid film height δ along the radius of the disk can be found with the following equation:

$$\delta = h' + (h + \Delta h) - h''$$

The capacitance sensor readout [10] is equipped with a 10 VDC output

which is proportional to the air gap between the probe and the target. This voltage signal was sampled by a Fluke 2280A Datalogger at a rate of one every two seconds to average the readings and to determine the standard deviation of each reading. This procedure was necessary due to the waves present on the surface of the liquid film. Thus, the liquid film height reported here is actually the mean film height. Also, the capacitance probe has a sensing spot which has a diameter of 11.28 mm, so a given reading was assigned to the radial location underneath the center of the sensing spot. When the disk was rotating, the same procedure was followed except that the tare data ($h + \Delta h$) and the air gap measurements between the probe and the free surface (h'') were averaged in the azimuthal direction as well.

The heat transfer from the heated disk to the liquid will be studied in future experiments by using a 6 KW etched foil heater [15] between the underside of the disk [1] and the ceramic disk insulator [16]. The heater is held between the plate and the insulation by screws that are through the insulation and are threaded into the plate. The heater is supplied with a piece of backing paper that will be placed between the heater and the insulation to assure that the heater is evenly compressed against the plate. An etched foil heater was chosen for this purpose due to the improved uniformity of the heat flux compared to a conventional wire heater.

Since the disk is able to rotate, a sealed slip-ring capsule [19] is employed to pass the power from the stationary source [23 and 24] to the disk, and to pass thermocouple readings from the disk to the digital

thermometer [18]. To avoid problems with creating extra junctions on the thermocouples mounted on the rotating disk, the slip-ring capsule was manufactured with six constantan wire circuits for thermocouples. In this way, an extraneous junction will not be created because a constantan wire and a copper wire coming from two separate slip rings will be used to create the thermocouple bead. The copper and constantan wires from the stationary part of the slip rings will be directly attached to the digital thermometer. The only extraneous junction is on the brushes and the gold slip rings. Since the brushes and the gold slip rings are very small, these junctions are nearly isothermal, so the contribution due to these junctions should be negligible. Thermocouples [17] mounted in holes in the disk along one radius will monitor the temperature of the disk while other thermocouples will measure the temperature of the liquid before and after it flows over the disk. The thermocouples in the holes in the plate will be a distance of 1.58 mm from the surface of the disk in order to measure the interface temperature as closely as possible. The thermocouples will be cemented into the holes with a thermally conductive epoxy which will not be degraded by the operating fluid. The mean temperature of the fluid at different radial locations will be measured by a sheathed thermocouple which will be moved with the digital micrometer [11] and the linear slide [13]. Since the liquid is in a closed system, a heat exchanger [22] will be used to keep the temperature of the inlet water at a constant value.

2.4 ERROR ANALYSIS

The errors in the liquid film measurements are described and quantified, which involve two instruments: the digital micrometer, and the capacitance

sensor. A brief summary of the method to determine the error will now be given. A more detailed description is presented in Appendix C and a full discussion on error analysis is given by Miller (1989).

The liquid film height is given by the following equation shown in Fig. 2.2:

$$\delta = h' + (h + \Delta h) - h'' \qquad (2.4.1)$$

Following the standard error analysis procedures, the root-sum-square error of the system is given by

$$E_{rss} = \sqrt{(\Delta h')^2 + [\Delta(h + \Delta h)]^2 + (\Delta h'')^2} \qquad (2.4.2)$$

The first term in equation (2.4.2) is the stated accuracy of the digital micrometer, which was calibrated at the factory with an NBS traceable Mark-Tech Laser Gage Model 7980. The maximum deviation over the range of movement reported on the calibration certificate is 0.001 mm, which was taken as the error of the instrument.

The second term involves the accuracy of the capacitance sensor, which is given by the manufacturer to be ±0.1 percent of the range when calibrated to a known standard, which was the digital micrometer. The capacitance probe was calibrated at the beginning of each test against the digital micrometer as described in Sec. 2.3. The maximum deviation from linearity of the capacitance probe was 0.008 mm. This value was added to

the stated accuracy of the probe.

The second term in equation (2.4.2) takes on different values when the disk is stationary or rotating. When stationary, the second term is the accuracy of the capacitance sensor given by the manufacturer plus the maximum deviation from linearity, which is 0.01 mm.

When the disk is rotating, the error due to the disk not being perfectly flat and the wobble caused by the bearings must be taken into account. This error is given by the sum of the standard deviation of the air gap measurement between the probe and the dry disk taken at the outer edge of the disk (where it is maximum) and the error of the capacitance sensor. Multiple populations with an increasing number of samples were taken and the means were compared with a two-tailed z-test to give a sample number which ensures a mean at the 95 percent confidence level. The standard deviation of the dry rotating disk with 50 samples is σ = 0.02 mm, so the error in the second term in equation (2.4.2) is 0.03 mm.

The last term in equation (2.4.2) is again the error associated with the capacitance sensor. Due to the fact that the mean film thickness is being reported, further comments concerning the third term in equation (2.4.2) are necessary. At all flow rates and rotational speeds, waves were present on the free surface of the liquid film. A test was performed to compare the means of different numbers of samples in the subcritical and supercritical regions to determine a suitable number of data points for a mean which falls in the 95 percent confidence level. For subcritical flow, a normal z-test was performed, and it was found that for 125 and 250

samples, the means were equal at the 95 percent confidence level, so 250 samples were taken for each data point reported. Likewise, for supercritical flow 80 samples were taken in order to achieve the same confidence level. A similar test performed when the disk was rotating showed that the number of samples needed for the 95 percent confidence level was the same as that for the stationary supercritical region. The root-sum-square error in the liquid film height measurement is as follows:

Stationary disk - $E_{rss} = \pm 0.01$ mm

Rotating disk - $E_{rss} = \pm 0.03$ mm

The gap between the collar and the disk was measured with feeler gages and the error in this data point was found to be ±0.01 mm.

2.5 RESULTS AND DISCUSSION

2.5.1 Liquid Film Thickness Measurements

The mean thickness of a liquid film of de-ionized water as it flows across a horizontal disk has been measured experimentally. The flow rate ranged from 7.0 - 15.0 LPM and the rotational rate varied from 0 - 300 RPM. Figures 2.3 - 2.8 present the film thickness when the rotational speed is held constant and the flow rate is varied. Figures 2.9 - 2.11 show the film thickness when the flow rate is held constant and the rotational speed is changed. In all of the measurements presented in this report, a duplicate measurement was made and the two runs were within 5 percent of each other, which is within the experimental error of the film thickness measurement system.

Figure 2.3 shows the film thickness when the disk is stationary in both the supercritical and subcritical regions. As the flow rate increases, the hydraulic jump is moved toward the outer edge of the disk. The hydraulic jump is the sudden increase in the film thickness and is actually a momentum balance between the supercritical flow and the subcritical flow. The exact shape of the jump could not be determined with the present measuring instrument because if an attempt was made to measure the film thickness in the supercritical region very near the jump, the free surface of the subcritical region would touch the side of the capacitance sensor and saturate the signal. Therefore, the straight line without data points between the supercritical and subcritical regions is where the hydraulic jump resided.

The first data point at 50.8 mm is the gap height between the collar and the rotating disk (0.267 mm). The next data point at 76.2 mm is the first point which could be read by the capacitance probe. Therefore, the line connecting these two points is simply a linear interpolation and no conclusions can be drawn concerning this region. Even though the outer radius of the disk is 203.2 mm, measurements are not reported past 195.6 mm because the sensing spot of the capacitance sensor was over the edge of the disk.

In Fig. 2.3, it can be seen that the film is nearly horizontal in part of the subcritical region when the flow rate is 7.0 LPM and then drops off near the edge of the disk. This decrease in the film thickness at the edge is due to the acceleration of the flow as the liquid exits the disk. The radius of curvature at the edge was nearly constant up to approximately

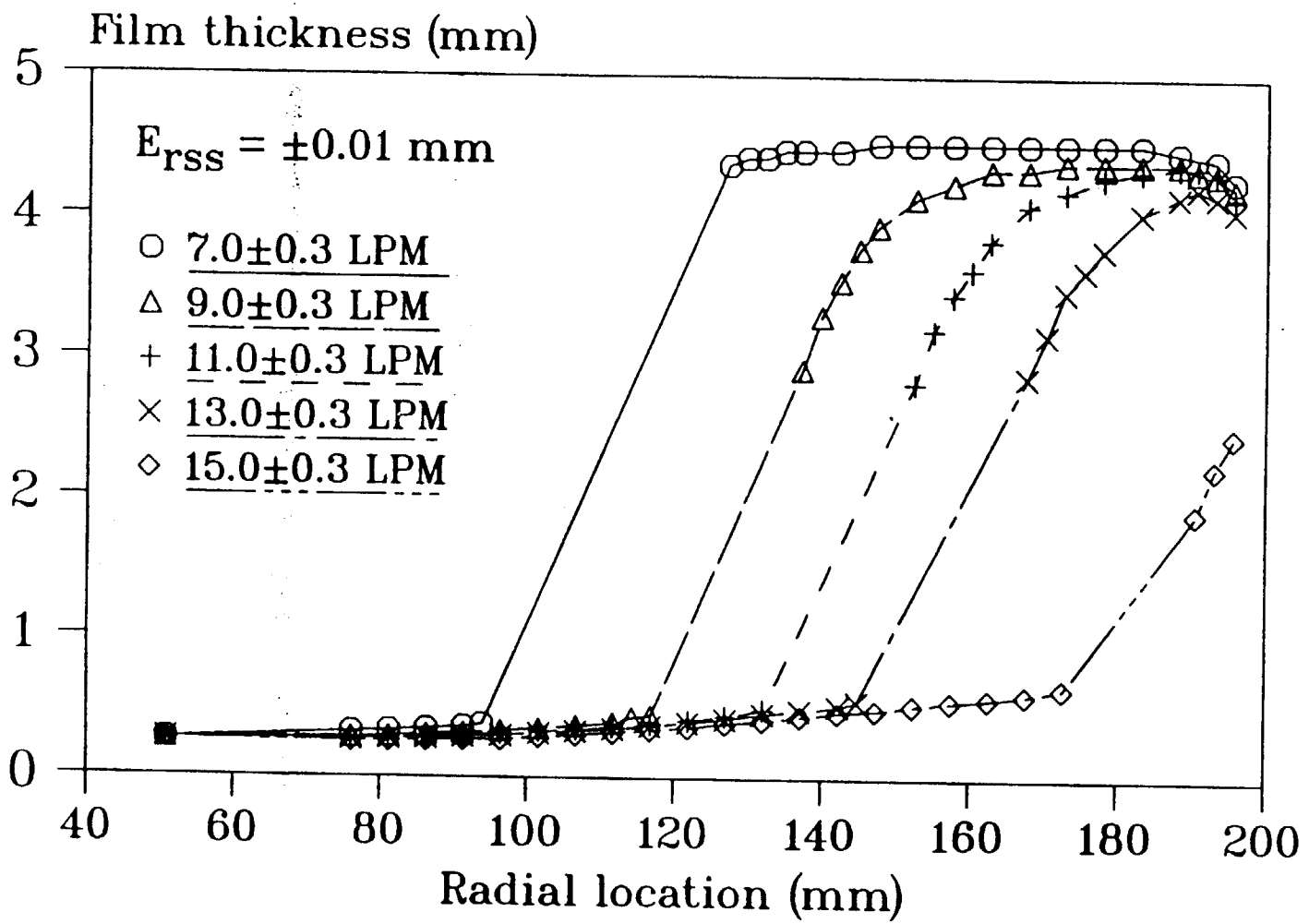

Figure 2.3. Film thickness versus radial location for different flow rates (stationary disk)

13.0 LPM and produces significant surface tension effects. This can be noticed in Fig. 2.3 by the curves showing 7.0 - 13.0 LPM, which approach the same film thickness near the edge of the disk. For 15.0 LPM, the hydraulic jump was nearly pushed off the edge of the disk, so it did not reach the same height as the curves with lower flow rates. Figure 2.3 also shows that the liquid film thickness in the subcritical region is an order greater than that in the supercritical region.

In Fig. 2.4, the film thickness in the supercritical region when the disk was stationary can be seen to increase along the radius of the disk. In the supercritical region, the major forces on the liquid film are those due to inertia and friction. Since the frictional forces tend to slow the liquid, the film thickness increases due to continuity.

Figure 2.4 also shows that the film thickness in the supercritical region may increase monotonically or may first decrease and then increase downstream. This decrease in the film thickness is due to the radial spreading of the fluid as it travels across the disk. This effect is then overtaken by that due to friction, at which point the film thickness increases. For flow rates of 11.0 LPM or less, the effect of friction is dominant over the effect of the spreading of the liquid, so the liquid increases monotonically. As the flow rate (or Reynolds number) increases, the film thickness decreases because the effect of the radial spreading of the film becomes greater than the effect of friction.

The film thickness for different flow rates when the rotational speed is 55 RPM is shown in Fig. 2.5. Up to approximately 120 mm the flow has

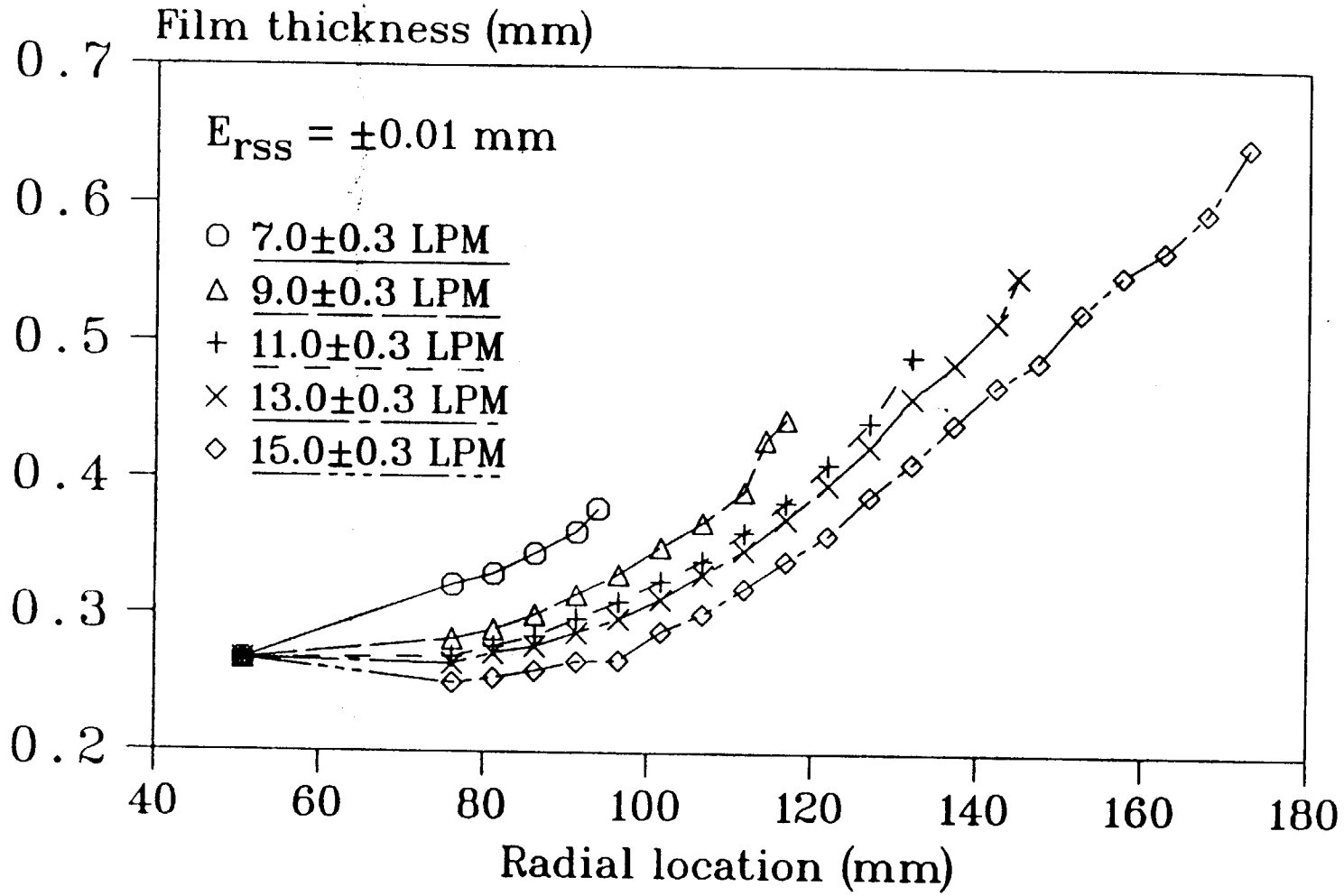

Figure 2.4. Film thickness versus radial location in the supercritical region for different flow rates (stationary disk)

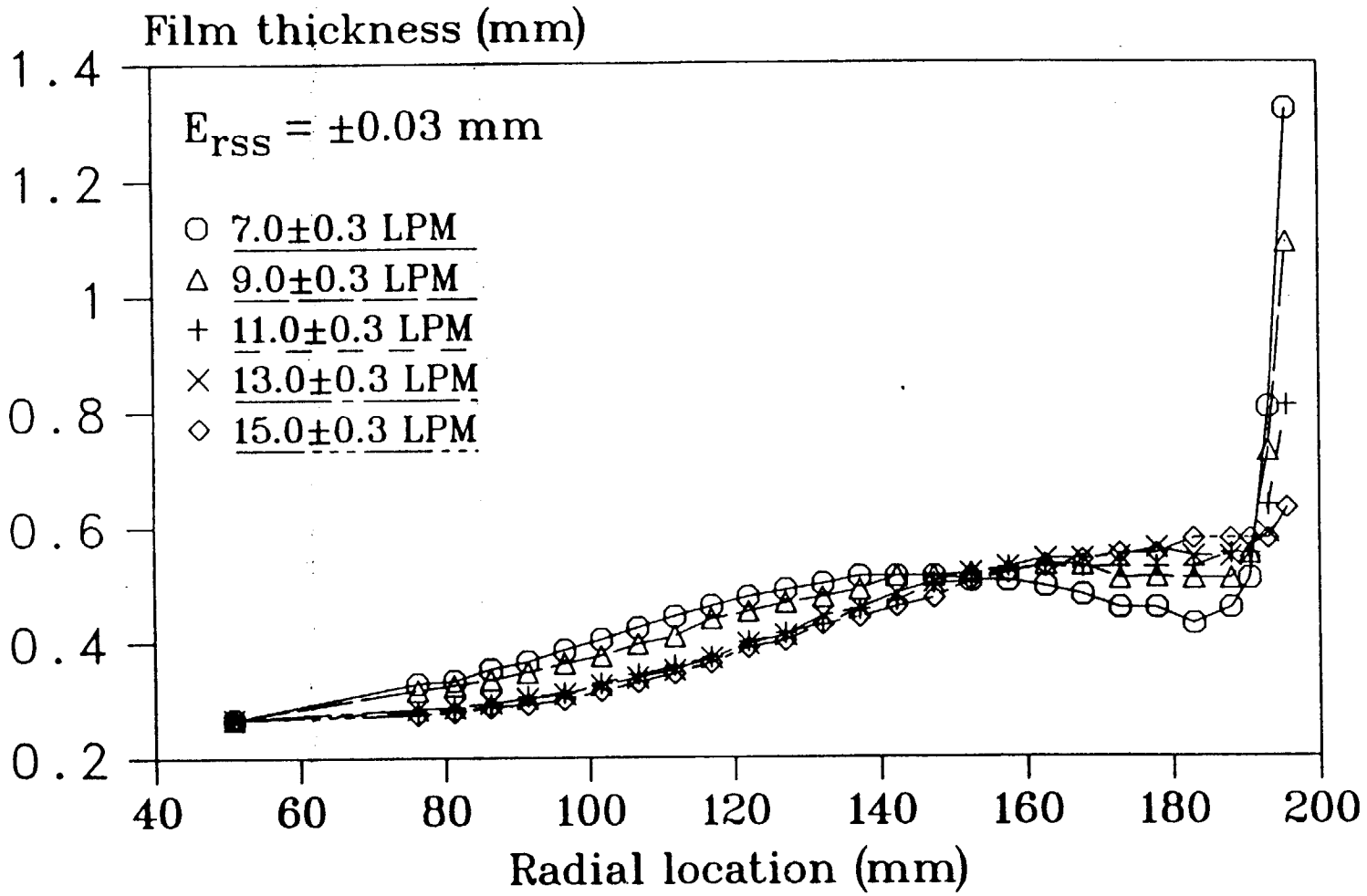

Figure 2.5. Film thickness versus radial location for different flow rates (55±2 RPM)

the same trend as the supercritical flow of the stationary disk: as the flow rate increases, the film thickness decreases due to the effect of the radial spreading of the flow overtaking the effect of friction. Past this region, however, the profile takes on a very different appearance. For 7.0 LPM, the film thickness begins to flatten out and then decrease past 120 mm. When the disk is rotating, the dominant forces on the film are as follows: frictional, inertial, and centrifugal. Near the center of the disk, the frictional and inertial forces are prevalent. Closer to the edge of the disk the centrifugal force comes into play. Therefore, near the edge of the disk one would expect that the film would accelerate because of the centrifugal force and become thinner due to continuity. It can also be seen in Fig. 2.5 that as the flow rate increases, the point where the curves begin to flatten due to centrifugal force travels downstream. This is because the effect of inertia on the flow is dominant over the effect of the centrifugal force for a longer distance. Near the edge of the disk, the film thickness increases dramatically due to the effect of surface tension at the edge. This is actually a fractional hydraulic jump which does not reach its full height before the edge of the disk. As the flow rate increases, the height of this jump decreases because the force due to the inertia of the liquid overcomes the force due to surface tension.

Figure 2.6 presents the film thickness measurements for different flow rates when the rotational speed is 100 RPM. In this graph, it can be seen that the hydraulic jump near the edge of the disk is not present because the centrifugal force is greater than the force due to surface tension. Also, the curves have the same trend as in Fig. 2.5 where the film thickness first increases because of friction and then decreases due to the

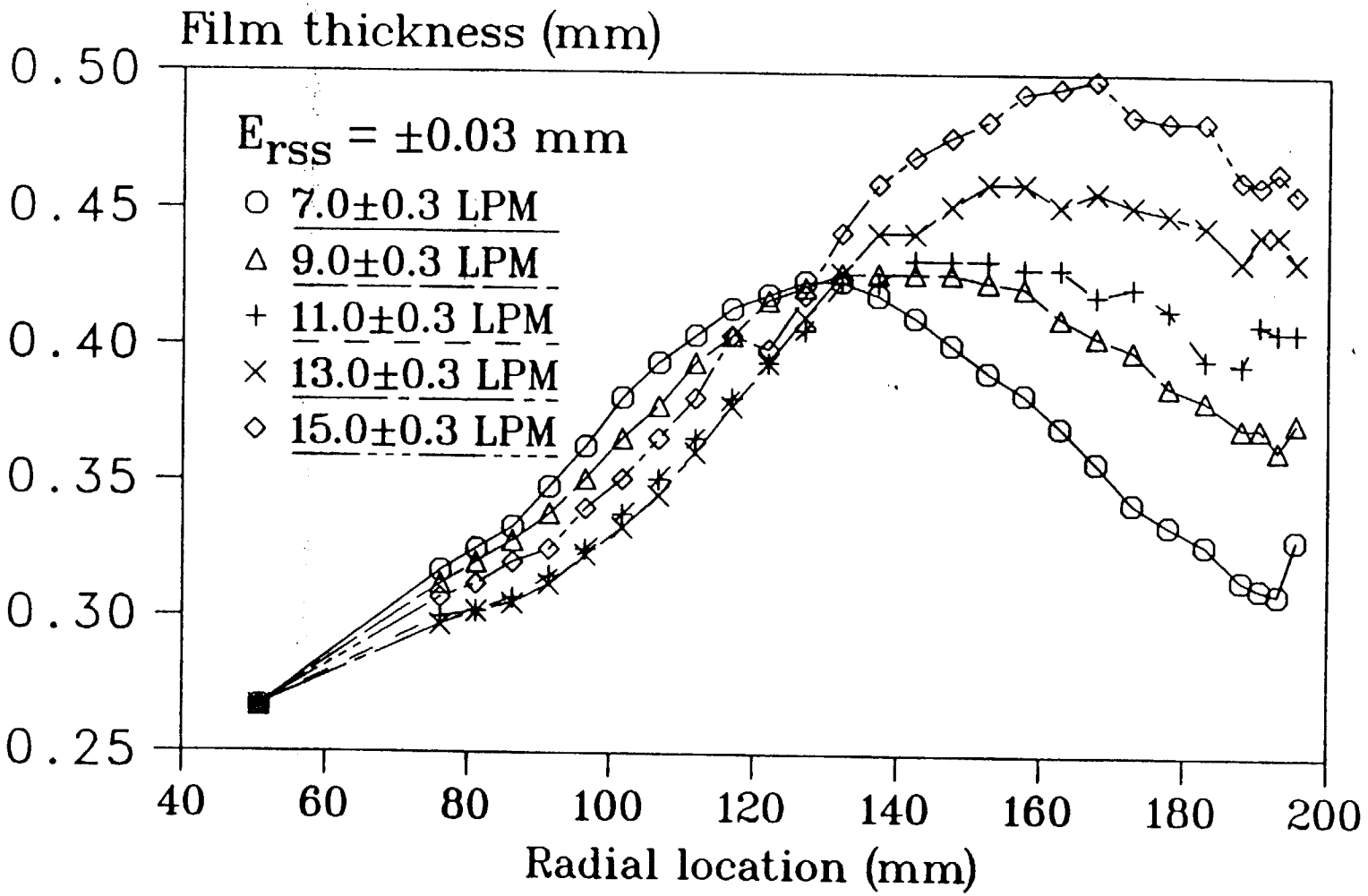

Figure 2.6. Film thickness versus radial location for different flow rates (100±2 RPM)

centrifugal force. A further examination of this figure shows that the curve of 15.0 LPM lies above those of 11.0 LPM and 13.0 LPM in the region where the film thickness is increasing. A possible reason for this is that the difference between these curves is on the order of the experimental error in the measurement system.

Figures 2.7 and 2.8 present the film thickness when the flow rate is varied from 7.0 to 15.0 LPM for rotational speeds of 200 and 300 RPM, respectively. Again, the same trend is evident where the film thickness first increases due to frictional effects and then decreases due to the effect of centrifugal force. In comparing these two figures, it can be seen that the radial location where the effect of centrifugal force begins to dominate the flow moves toward the center of the disk as the rotational speed increases. This is shown further in Figs. 2.9 - 2.11 where the flow rate is held constant (7.0, 11.0, and 15.0 LPM, respectively) and the rotational speed is varied from 55 to 300 RPM. In Fig. 2.9, as the rotational speed increases the maximum thickness occurs closer to the center of the disk. This can also be seen in Figs. 2.10 and 2.11. Also shown in Figs. 2.9 - 2.11 are the supercritical regions for the different flow rates when the disk is stationary. It can be seen that the film thickness in the supercritical region is generally close to the case when the rotational speed is 55 RPM. The exception is near the end of the supercritical region where the film thickness increases, as shown in Figs. 2.10 and 2.11. This phenomenon is due to the fact that the stationary film is not being acted upon by centrifugal forces, so the film thickness continues to increase in this region because of the effect of friction.

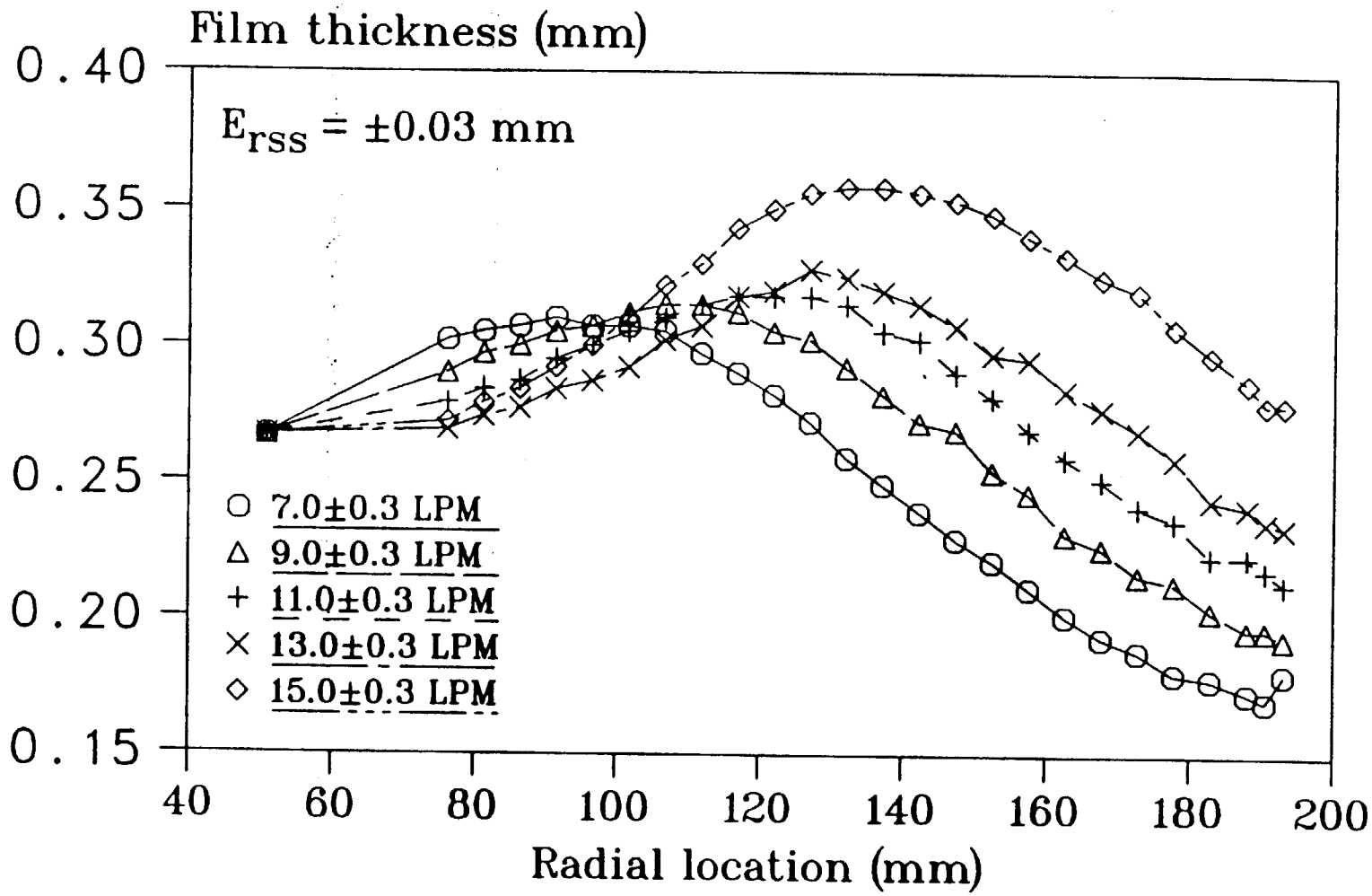

Figure 2.7. Film thickness versus radial location for different flow rates (200±2 RPM)

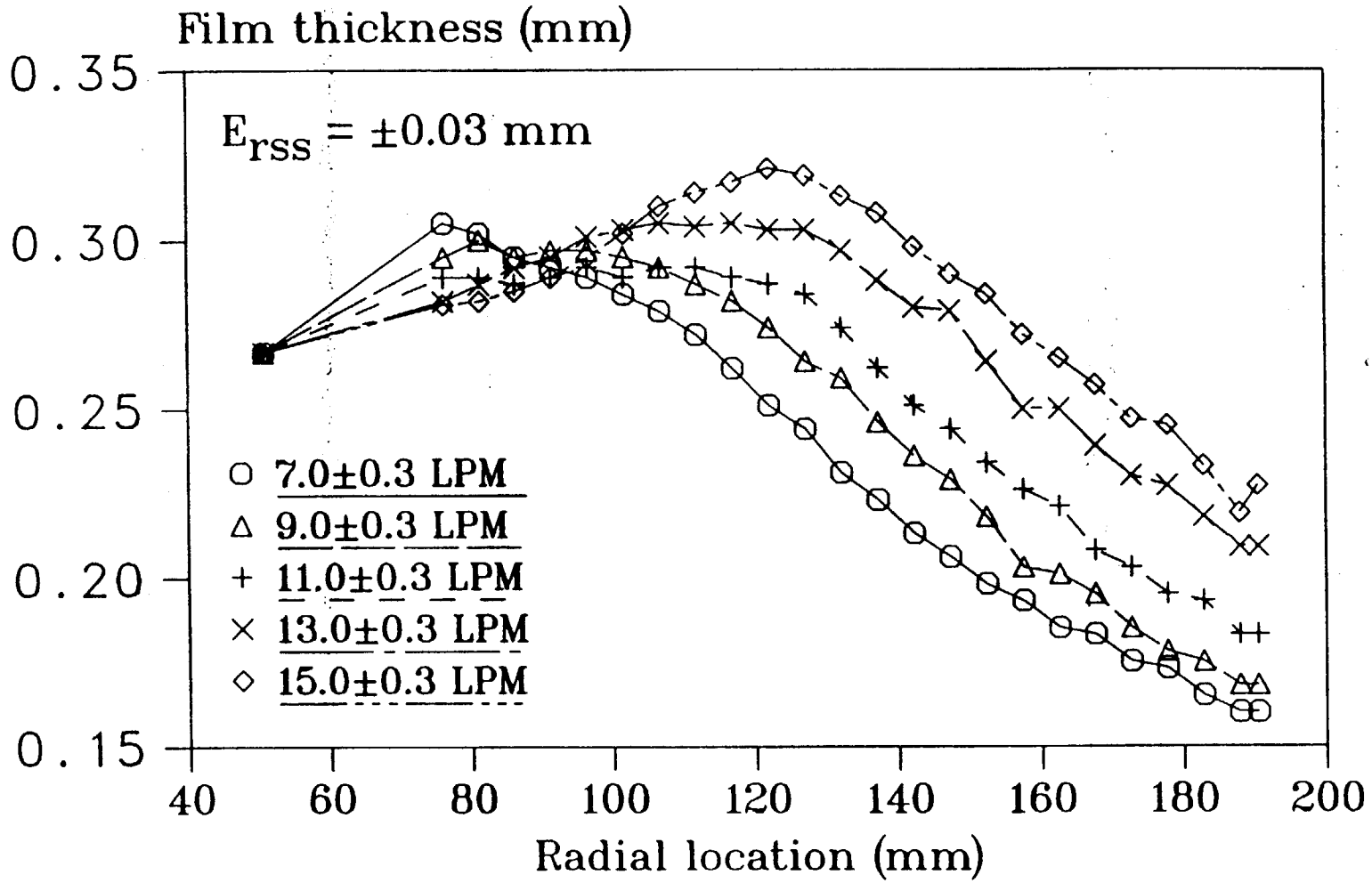

Figure 2.8. Film thickness versus radial location for different flow rates (300±2 RPM)

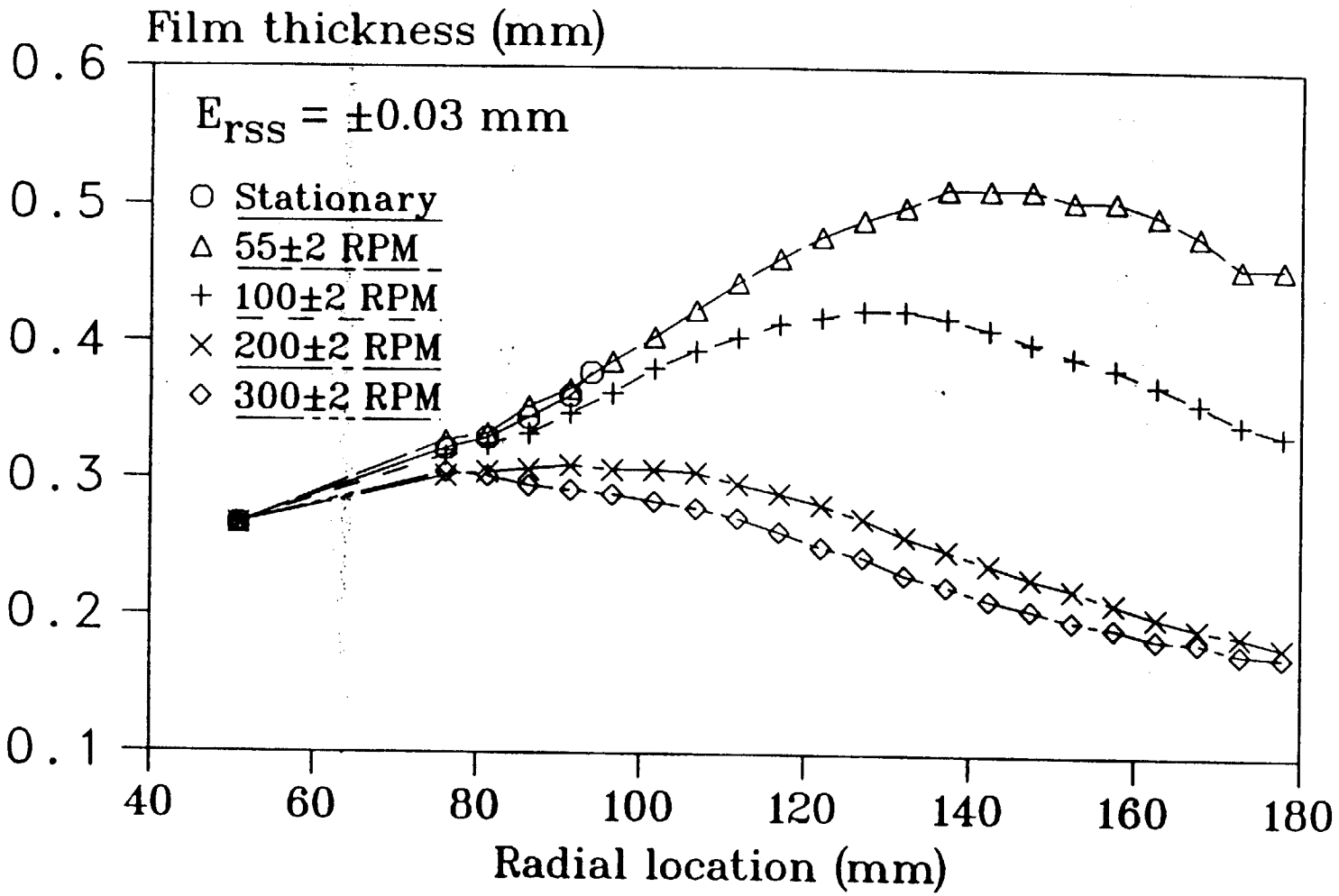

Figure 2.9. Film thickness versus radial location for different rotational speeds (7.0±0.3 LPM)

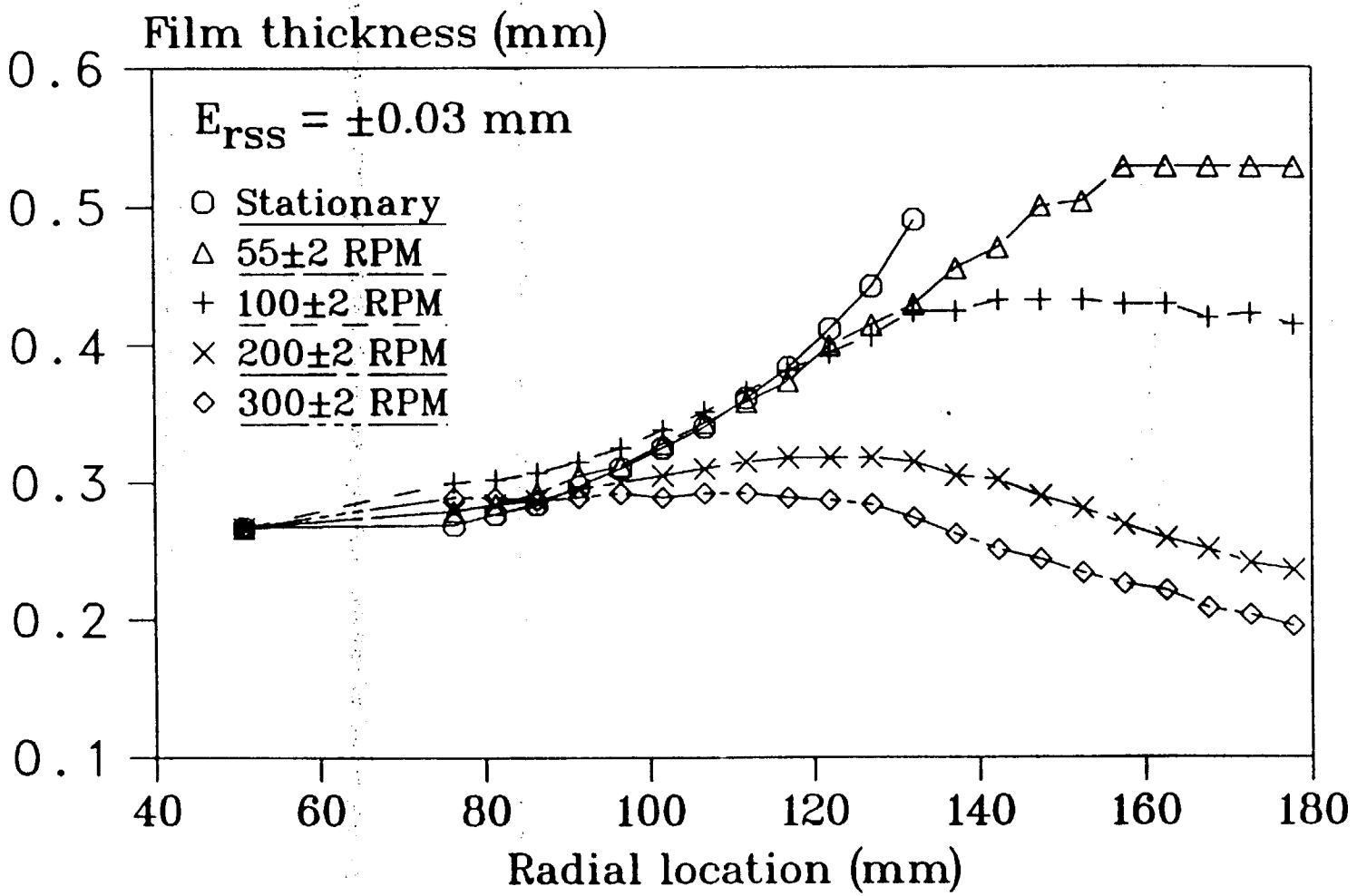

Figure 2.10. Film thickness versus radial location for different rotational speeds (11.0±0.3 LPM)

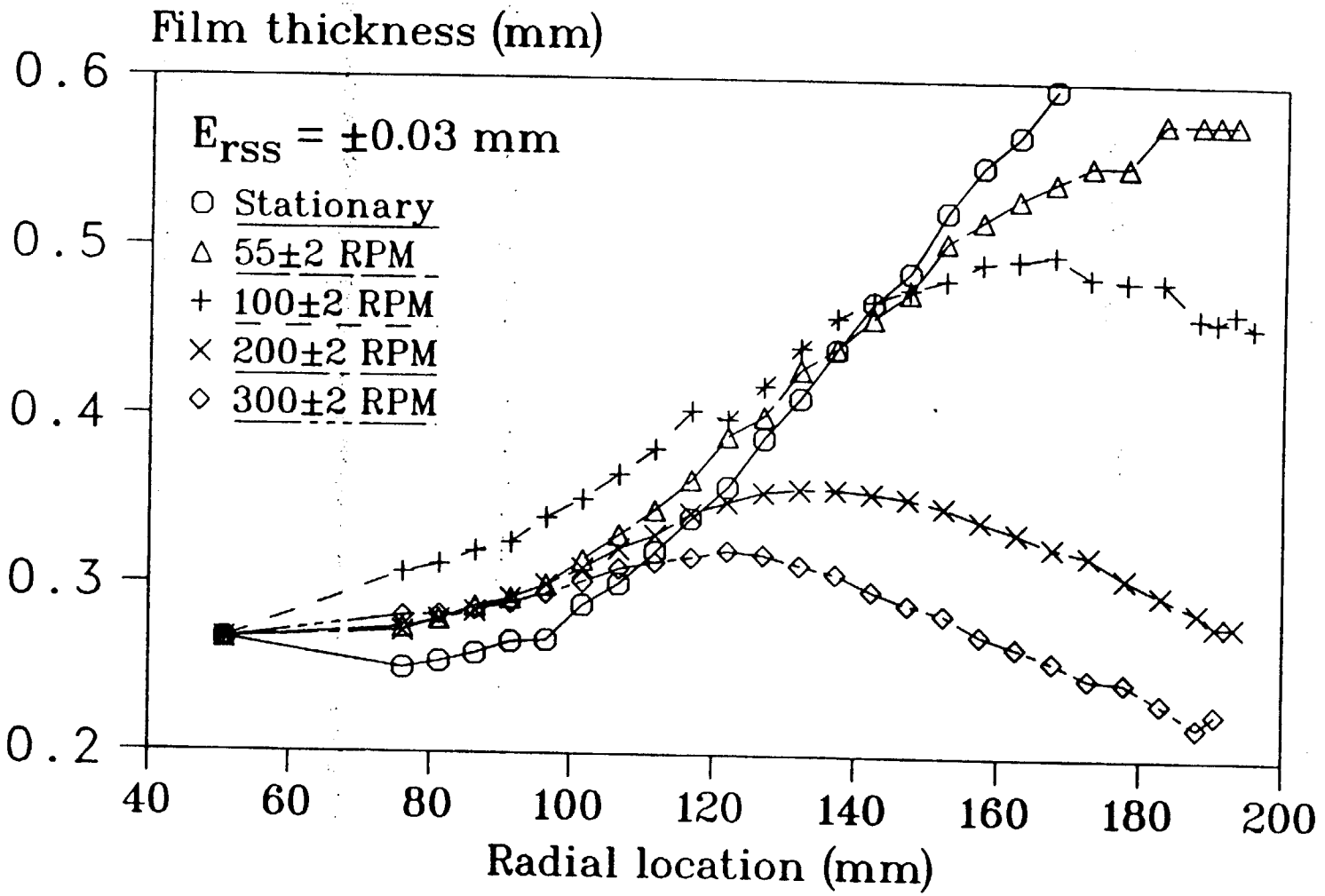

Figure 2.11. Film thickness versus radial location for different rotational speeds (15.0±0.3 LPM)

2.5.2 Flow Visualization

A photographic study was performed to determine the basic phenomena which occur when the disk was stationary and rotating. When the disk is stationary, waves can be seen both on the subcritical and supercritical regions. The waves on the subcritical region have larger amplitudes than those in the supercritical region. At low flow rates, a toroidal "roller" was found at the hydraulic jump when the disk is stationary. At higher flow rates, the roller flattened out until it could not be distinguished from the increase in the film thickness at the hydraulic jump. Also for high flow rates, the surface tension of the liquid at the free surface creates a standing wave at the edge of the stationary disk. This standing wave is also present at all flow rates when the disk is rotated at low angular speeds. At higher spin rates, waves appear on the disk which flow nearly radially across the disk on top of a thin substrate of fluid.

In Figs. (2.12 and 2.13), the disk was stationary, the flow rate was set to 7.0 LPM and the shutter speed was 1/1000 second. With this shutter speed, the waves on the free surface of the liquid film could be photographed. In all of the photographs presented, the direction of the flow is from right to left and the direction of rotation is clockwise. The waves in the supercritical region are shown in Fig. 2.12. Near the collar the amplitude of the waves is small, but close to the hydraulic jump the amplitude of the waves becomes larger. The waves in the subcritical region can be seen in Fig. 2.13. These waves have a much larger amplitude than those in the supercritical region. This was verified when the liquid film height was measured with the capacitance sensor. Even though the actual

ORIGINAL PAGE IS
OF POOR QUALITY

Figure 2.12. Stationary disk, 7.0 LPM, supercritical region highlighted

Figure 2.13. Stationary disk, 7.0 LPM, subcritical region highlighted

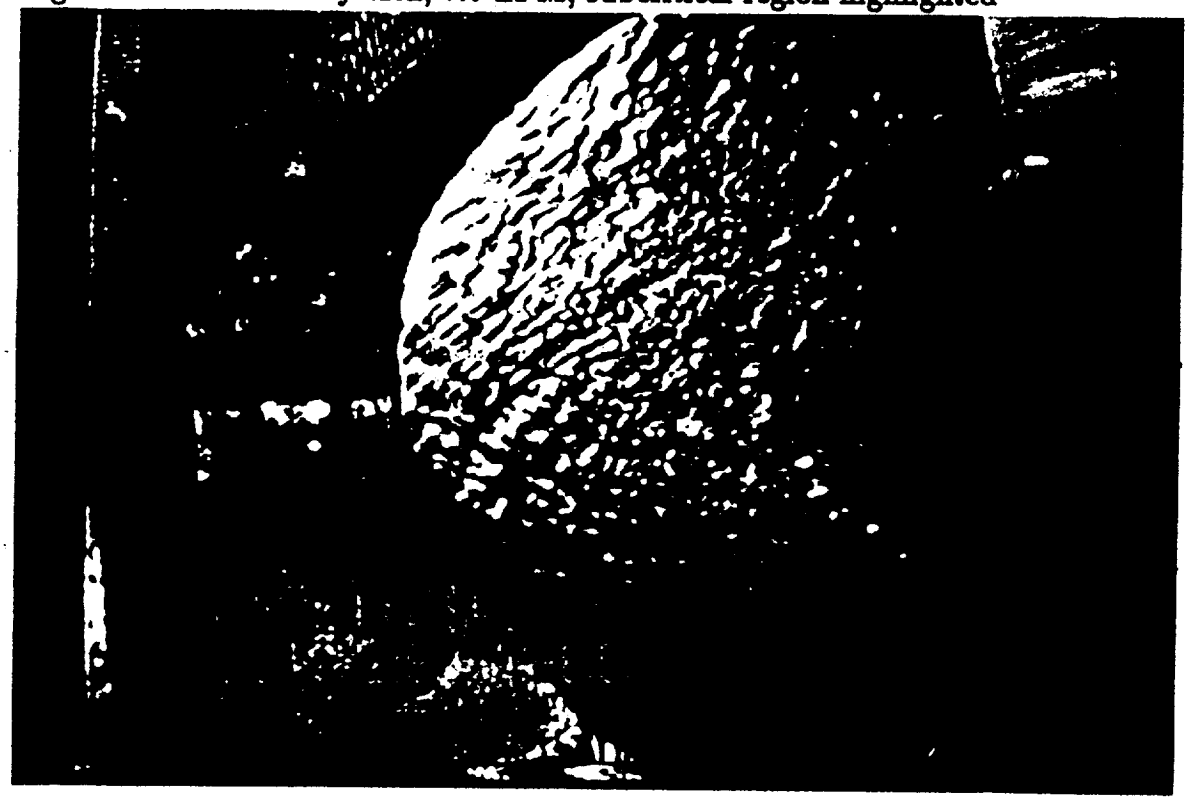

height of the waves could not be measured, the standard deviations of the signals from the mean film thickness were much larger in the subcritical region than those in the supercritical region.

Figures (2.14, 2.15 and 2.17) show the behavior of the hydraulic jump for low flow rates. These photographs were taken with a shutter speed of 1/60 second. Figure 2.14 shows the hydraulic jump at a flow rate of 3.0 LPM. The hydraulic jump occurs immediately after the liquid exits the gap between the collar and the disk. The flow rate was increased to 4.0 LPM, which is shown in Fig. 2.15. The hydraulic jump is pushed away from the collar approximately 30 mm. The shape of the jump can be seen to be a toroidal "roller". The motion of the roller is very chaotic in that its width and height oscillate in a seemingly random fashion. At this flow rate, however, the cross section of the roller is nearly circular. At higher flow rates, it was found that the shape of the roller changes significantly. A more detailed visual study was performed, and it was found that at flow rates between 3.0 - 6.0 LPM, the roller had a nearly circular cross section as shown in Fig. 2.16a. For flow rates between 7.0 - 8.0 LPM, the cross section of the roller was oval in shape as shown in Fig. 2.16b. For flow rates at and above 9.0 LPM, the shape of the roller was no longer distinguishable from the gradual increase in the film height, which is presented in Fig. 2.16c. The surface of the film at the hydraulic jump at this flow rate could clearly be seen to be falling down toward the center of the disk in the direction opposite to the main direction of the flow. Therefore, the roller had submerged such that it could not be seen photographically, but its presence was unmistakable. This change in the shape of the roller is thought to be due to the change in the balance

ORIGINAL PAGE IS
OF POOR QUALITY

Figure 2.14. Stationary disk, 3.0 LPM

Figure 2.15. Stationary disk, 4.0 LPM

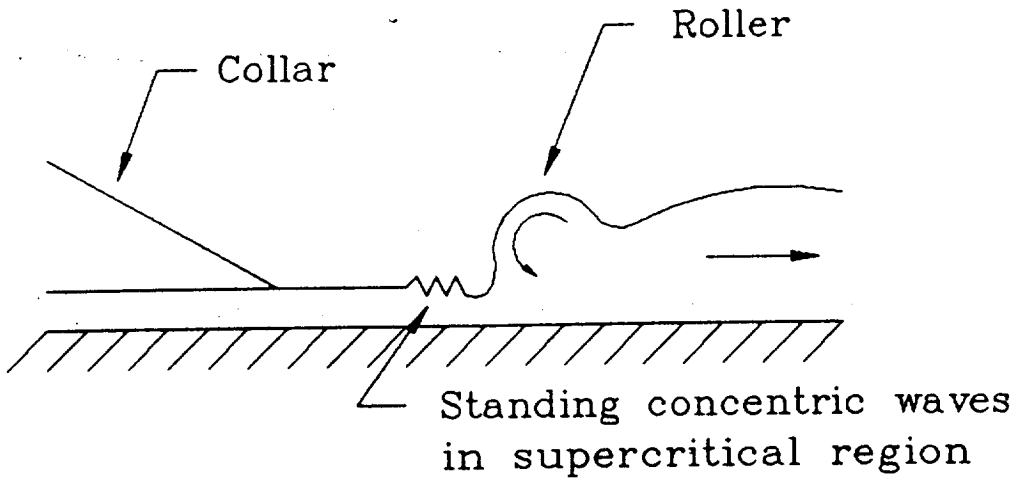

Figure 2.16a. Roller for 3.0–6.0 LPM

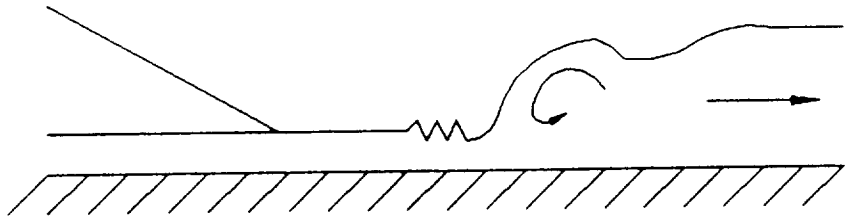

Figure 2.16b. Roller for 7.0–8.0 LPM

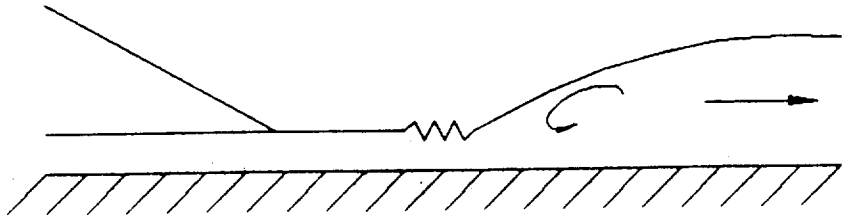

Figure 2.16c. Roller for 9.0–15.0 LPM

between the surface tension and the momentum of the fluid. At lower flow rates, the velocity of the fluid within the roller and the surface velocity of the liquid film do not have sufficient momentum to overcome the surface tension which holds the circular shape of the roller. As the flow rate and the surface velocity of the supercritical liquid film increases, the effect of momentum of the liquid overcomes that of surface tension, which results in the change in the shape of the roller.

Figure 2.17 shows the film surface when the flow rate is 5.0 LPM. A series of small concentric waves immediately upstream of the hydraulic jump can be seen, which are illustrated in Fig. 2.16. These concentric waves were present at flow rates between 4.0 - 15.0 LPM and had larger amplitudes at higher flow rates.

Figures (2.18 - 2.24) present the rotating disk for a flow rate of 7.0 LPM and rotational speeds of 55, 100, 150, 200, 250, 300, and 350 RPM, respectively. Figure 2.18 shows the disk rotating with a speed of 55 RPM. The waves on the free surface appear to be similar to the waves found in the subcritical region on the stationary disk with the same flow rate (see Fig. 2.13). Measurements of the standard deviation from the mean film thickness, however, showed that the amplitude of the waves were closer in height to those in the supercritical region. Near the edge of the disk is a standing wave created by the surface tension of the fluid. In this case, the rotational speed is slow enough that the fluid follows the edge of the disk downward instead of flying off the disk horizontally. Therefore, the radius of curvature of the free surface around the edge of the disk acts to increase the film height immediately upstream from the edge of the disk.

ORIGINAL PAGE IS
OF POOR QUALITY

Figure 2.17. Stationary disk, 5.0 LPM

Figure 2.18. Rotating disk, 7.0 LPM, 55 RPM

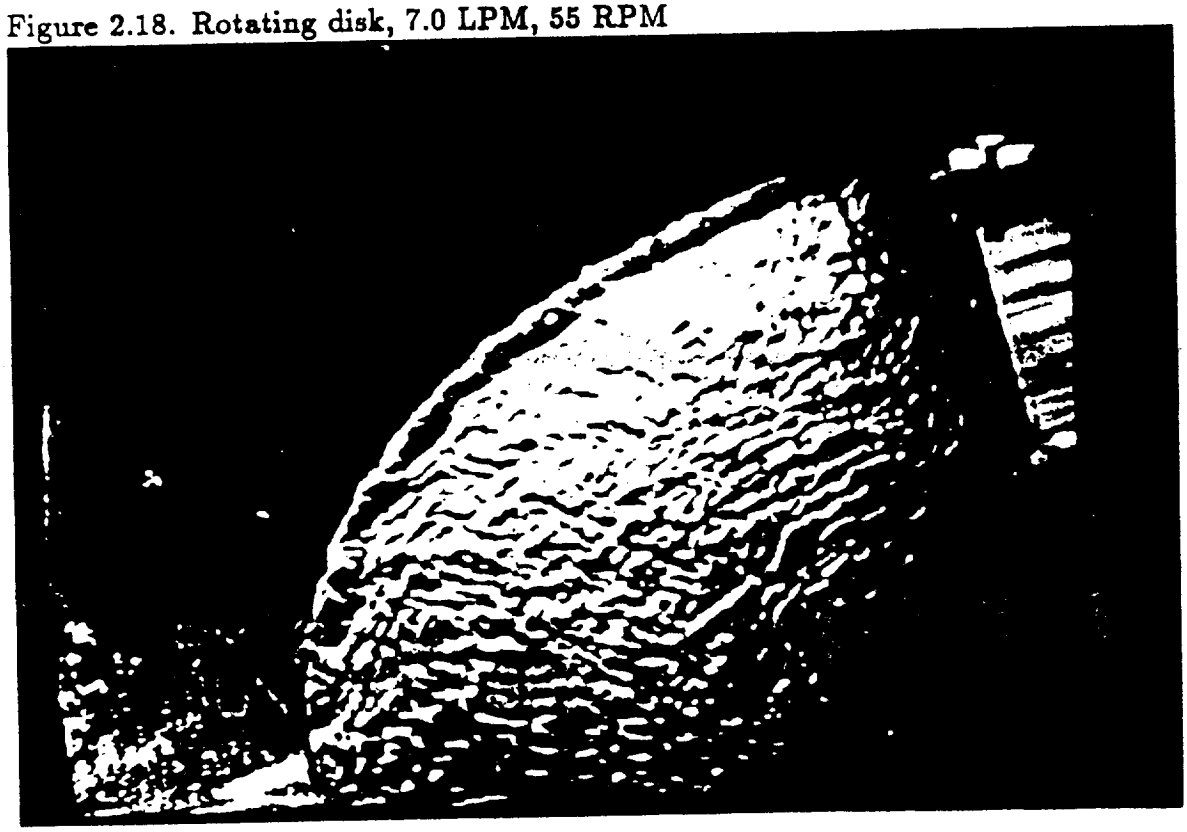

ORIGINAL PAGE IS
OF POOR QUALITY

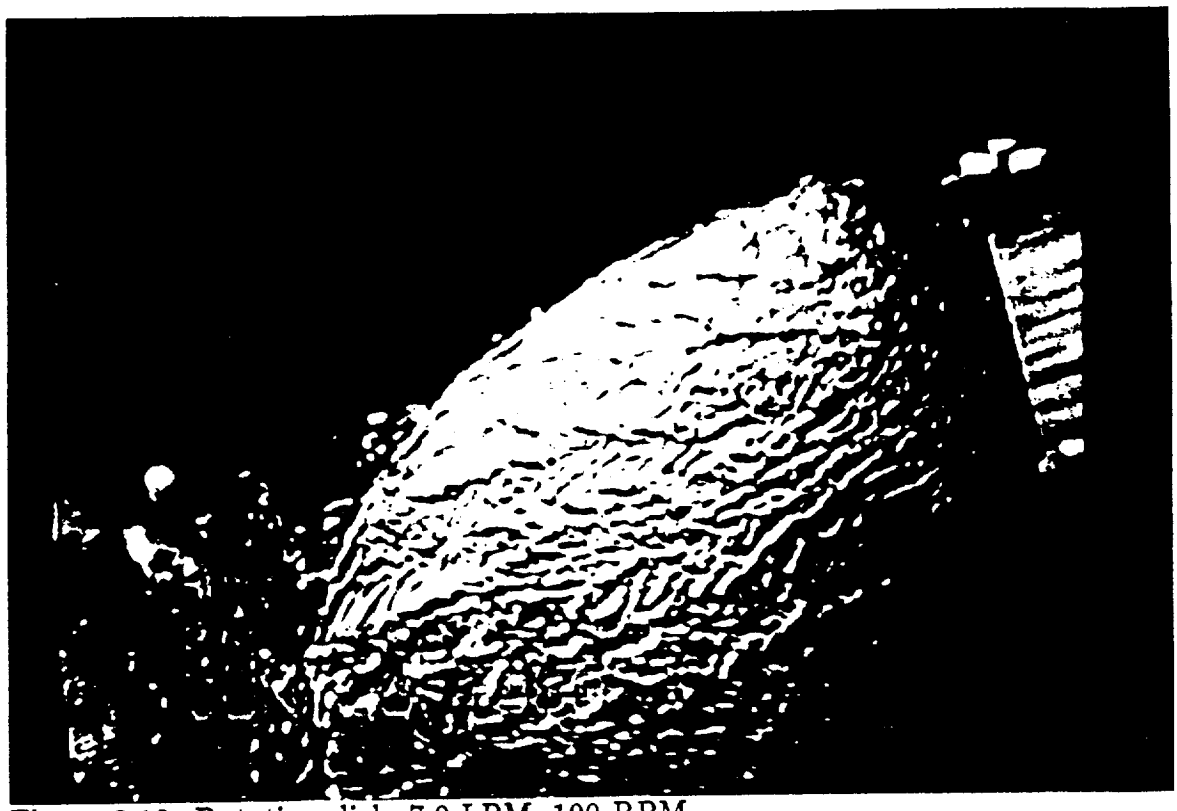

Figure 2.19. Rotating disk, 7.0 LPM, 100 RPM

Figure 2.20. Rotating disk, 7.0 LPM, 150 RPM

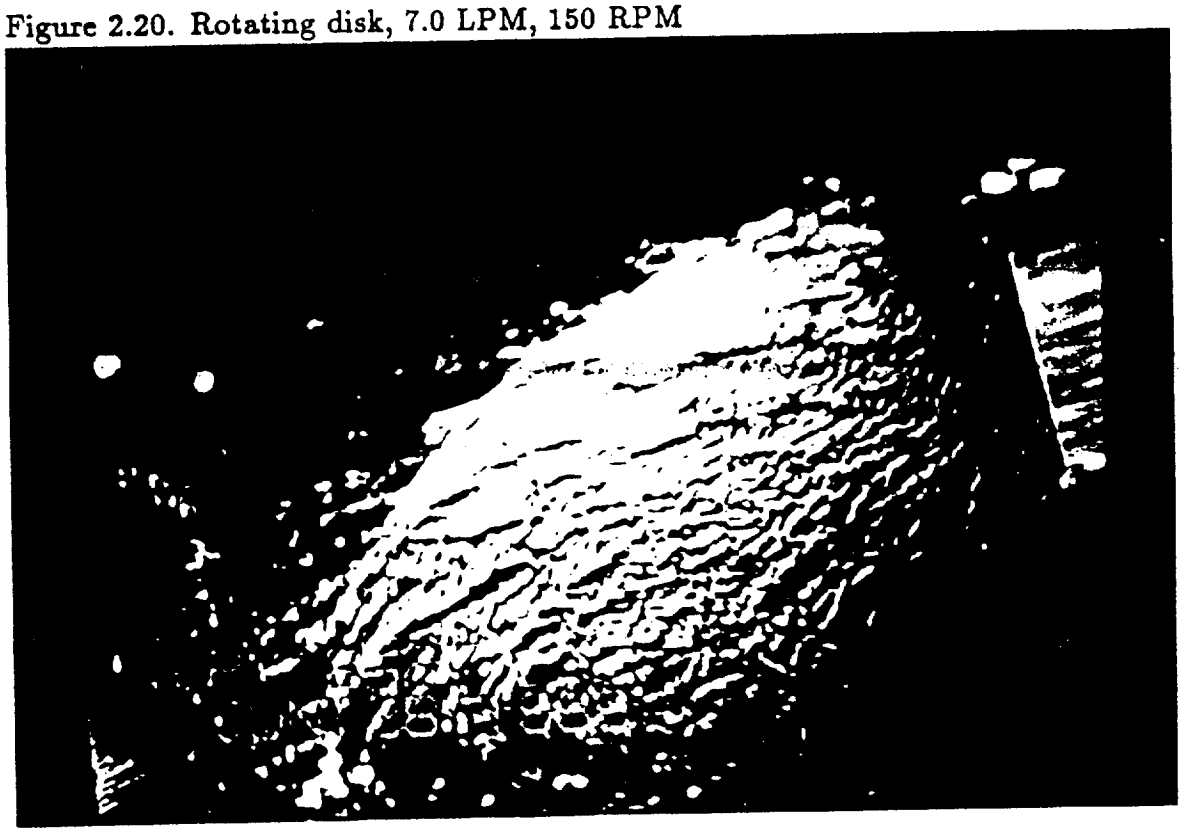

ORIGINAL PAGE IS
OF POOR QUALITY

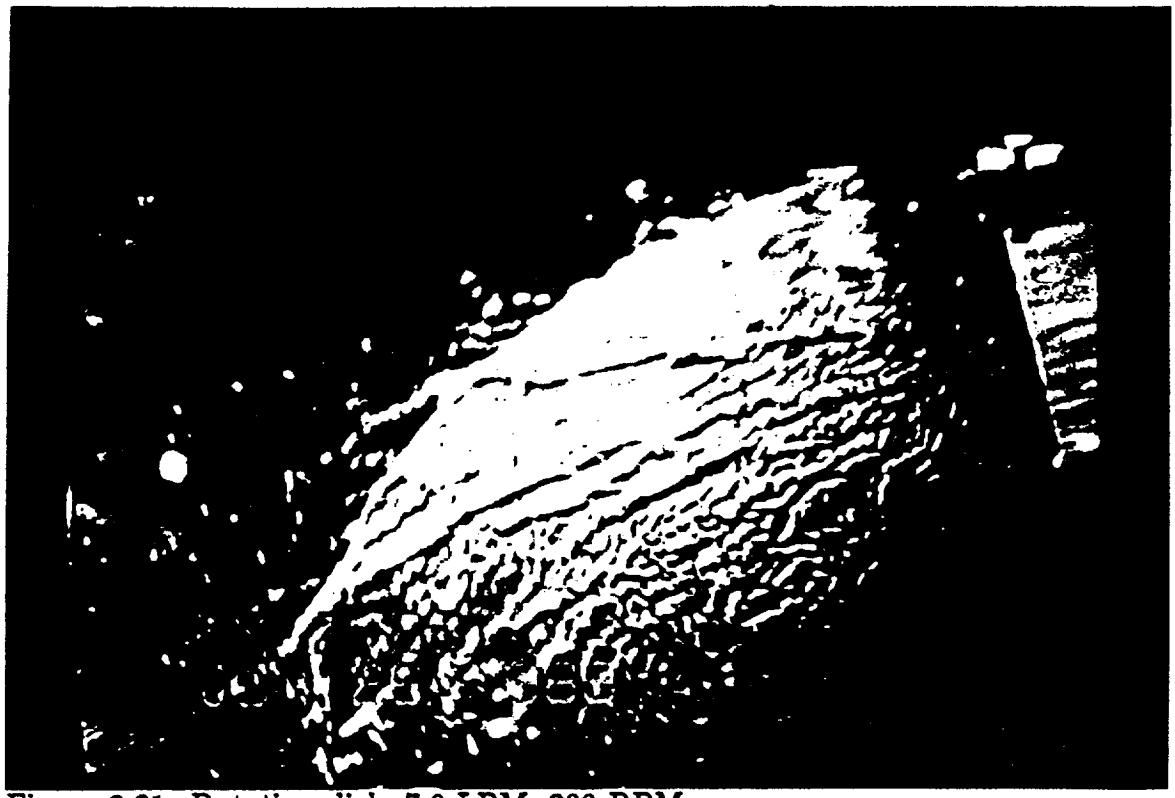

Figure 2.21. Rotating disk, 7.0 LPM, 200 RPM

Figure 2.22. Rotating disk, 7.0 LPM, 250 RPM

ORIGINAL PAGE IS
OF POOR QUALITY

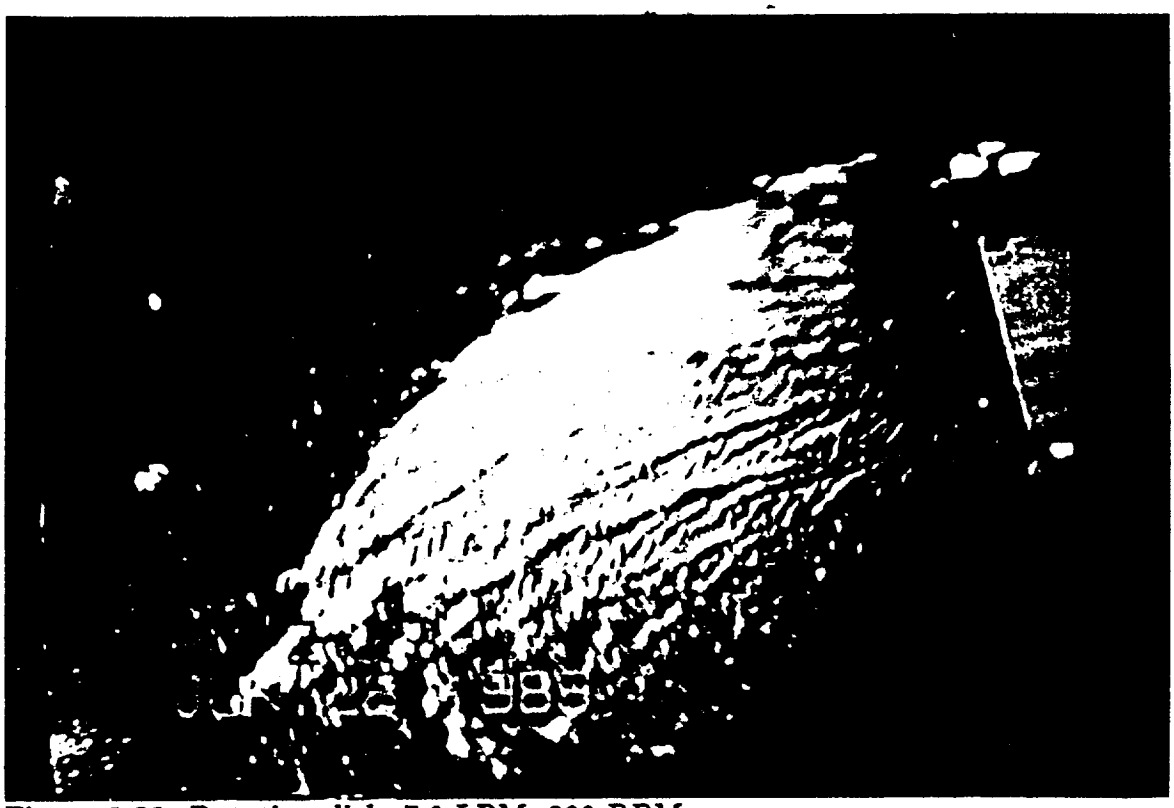

Figure 2.23. Rotating disk, 7.0 LPM, 300 RPM

Figure 2.24. Rotating disk, 7.0 LPM, 350 RPM

Two flow regimes were found to exist on the rotating disk: wavy-laminar and radial wave flow. The transition from the wavy-laminar flow to the radial-wave flow has been visually examined for 7.0 and 13.0 LPM and is presented in Figs. (2.18 - 2.31). The wavy-laminar flow is seen at lower rotatinal speeds and the radial-wave flow occurs at high rotational speeds. The wavy-laminar flow is shown in Fig. 2.18 for 7.0 LPM and 55 RPM. In this regime, no recurring wave patterns are distinguishable except the end effects at the outer edge of the disk. The radial-wave regime is shown in Fig. 2.30 for 13.0 LPM and 300 RPM. Several well-defined radial waves can be seen which appear to flow across the disk on top of a thin substrate and carry the bulk of the fluid off of the disk. In Fig. 2.30, a radial wave is exiting the disk on the left-hand side in the center. Immediately below this wave, very little fluid is leaving the disk where the thin substrate is present. The transition between these two regimes will now be discussed.

When the rotational rate was slowly changed from 55 RPM to 100 RPM for 7.0 LPM, the waves on the free surface began to form a pattern which could be easily distinguished, as shown in Fig. 2.19. Parts of the free surface broke free from the wavy-laminar regime to form V-shaped waves that ran at a diagonal angle between the radial and circumferential directions opposite to the rotation of the disk. At the lower rotational speeds, these waves were present only at the outer edge of the disk. The film thickness at the base of the 'V' was greatest, and that at the top of the V was least. It is felt that the effect of the centrifugal force eventually overcame that of the surface tension, so that the liquid film began to run in rivulets toward the edge of the disk. As the rotational speed increased, the width

of the V-shaped waves decreased and the length increased until the waves traversed the radius of th disk as shown in Fig. 2.21. It can be seen in Fig. 2.22 that the spacing between the radial waves increases with the radius because of the increase in the flow area. For rotational speeds at and above 200 RPM, the radial waves could be seen in almost every still photograph, so the transition region for 7.0 LPM is 100-200 RPM.

Figures (2.25 - 2.31) present the surface waves for 13.0 LPM at rotational speeds of 55, 100, 150, 200, 250, 300, and 350 RPM. Upon examining these figures, the transition region was determined to be approximately 150 - 200 RPM, which is higher than that of 7.0 LPM. It is thought that at the higher flow rate, the transition is delayed because the effect of centrifugal force must overcome the increased effect of the radial momentum of the fluid.

Figures (2.18 and 2.25) compare two flow rates (i.e., 7.0 and 13.0 LPM, respectively) at the same rotational speed (i.e., 55 RPM). In Fig. 2.18, the width of the standing wave at the edge is much larger than that of Fig. 2.25, which has a higher flow rate. This shows that at higher flow rates, the momentum of the flow overcomes the effect of surface tension.

2.6 CONCLUSIONS

The characteristics of a thin liquid film with a free surface on a stationary and rotating disk have been examined experimentally. The film thickness was measured for different flow rates and rotational speeds with a non-contact capacitance technique. Also, the nature of the waves on the

ORIGINAL PAGE IS
OF POOR QUALITY

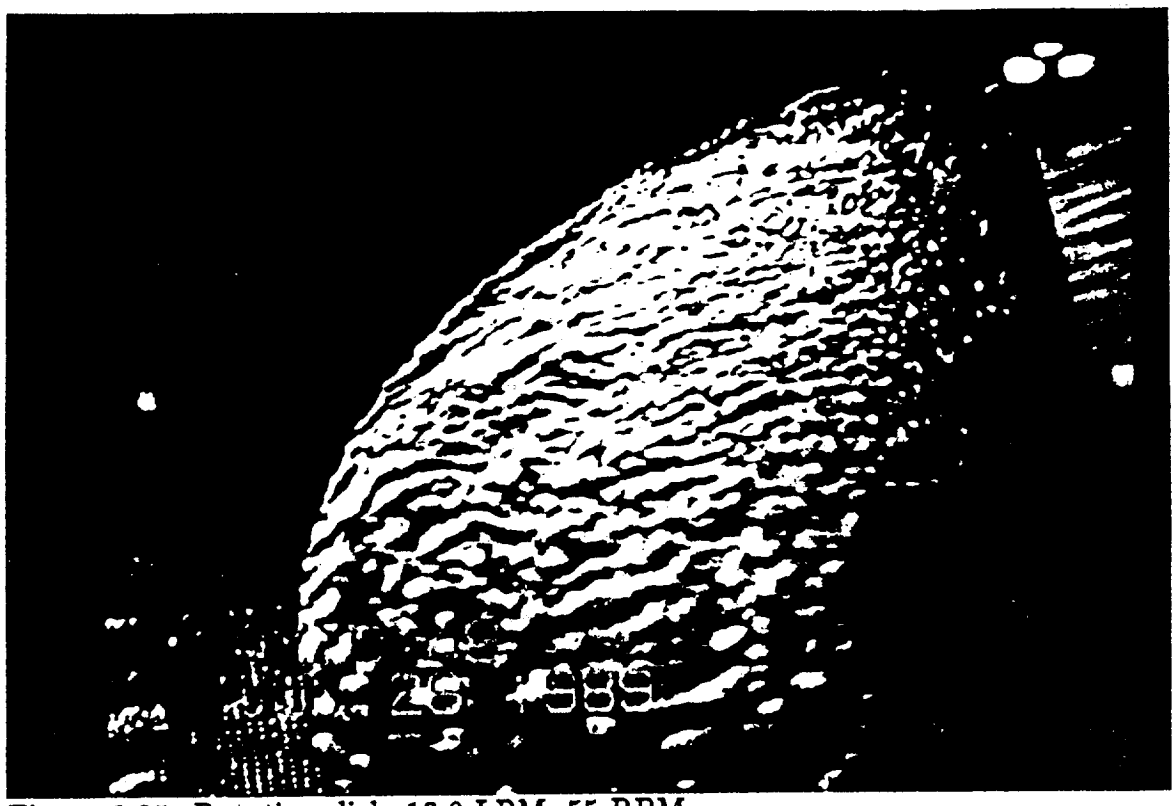

Figure 2.25. Rotating disk, 13.0 LPM, 55 RPM

Figure 2.26. Rotating disk, 13.0 LPM, 100 RPM

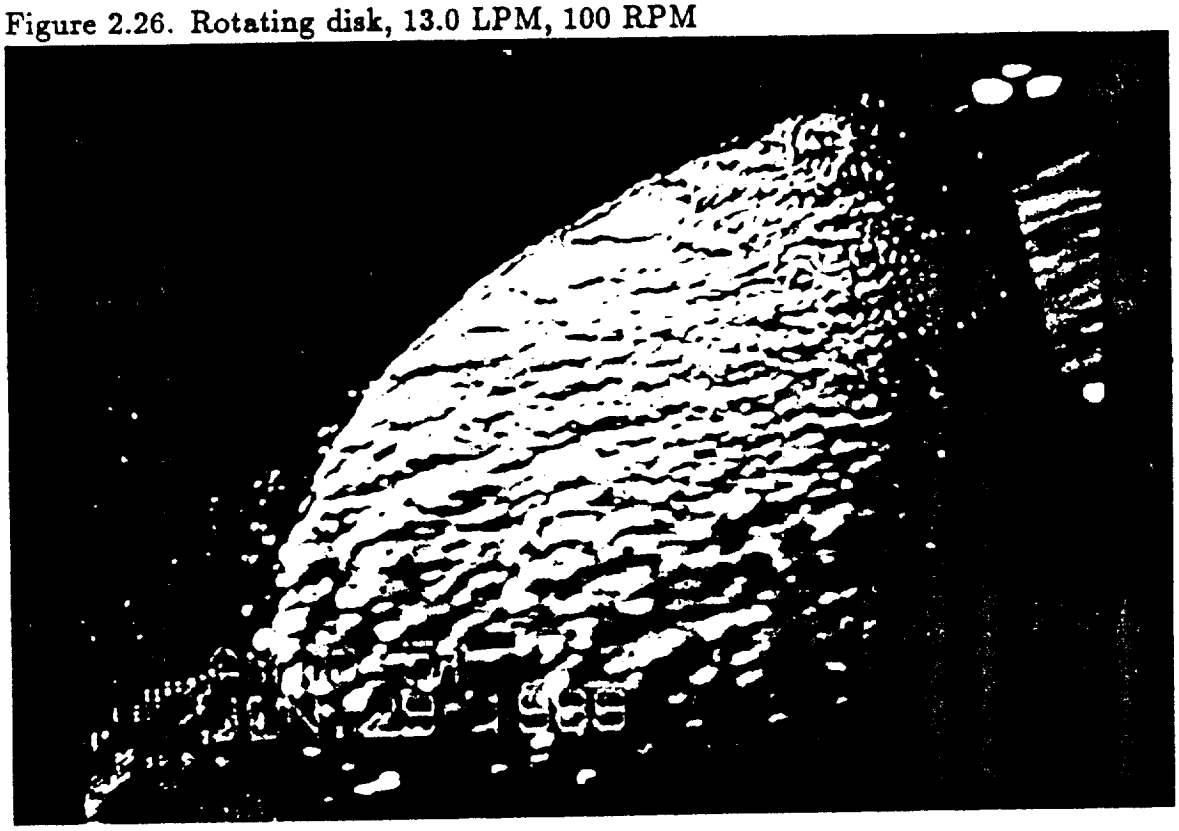

ORIGINAL PAGE IS
OF POOR QUALITY

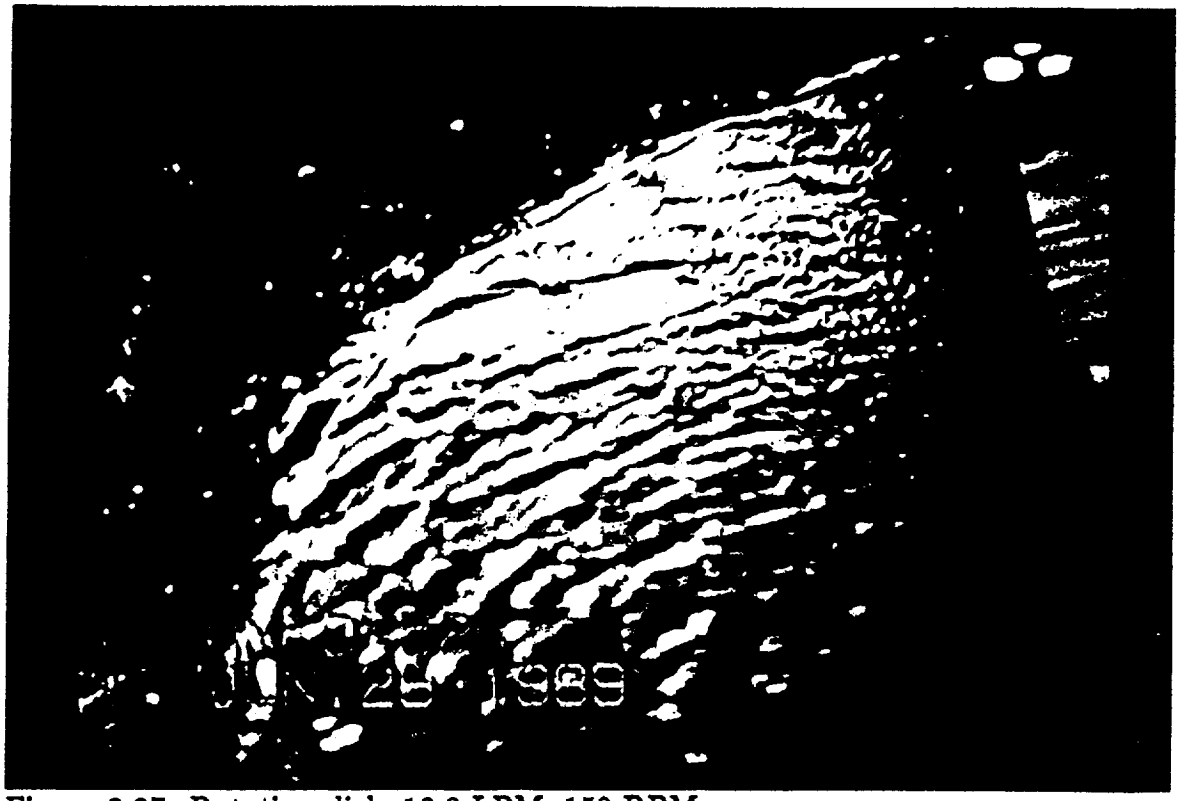

Figure 2.27. Rotating disk, 13.0 LPM, 150 RPM

Figure 2.28. Rotating disk, 13.0 LPM, 200 RPM

ORIGINAL PAGE IS
OF POOR QUALITY

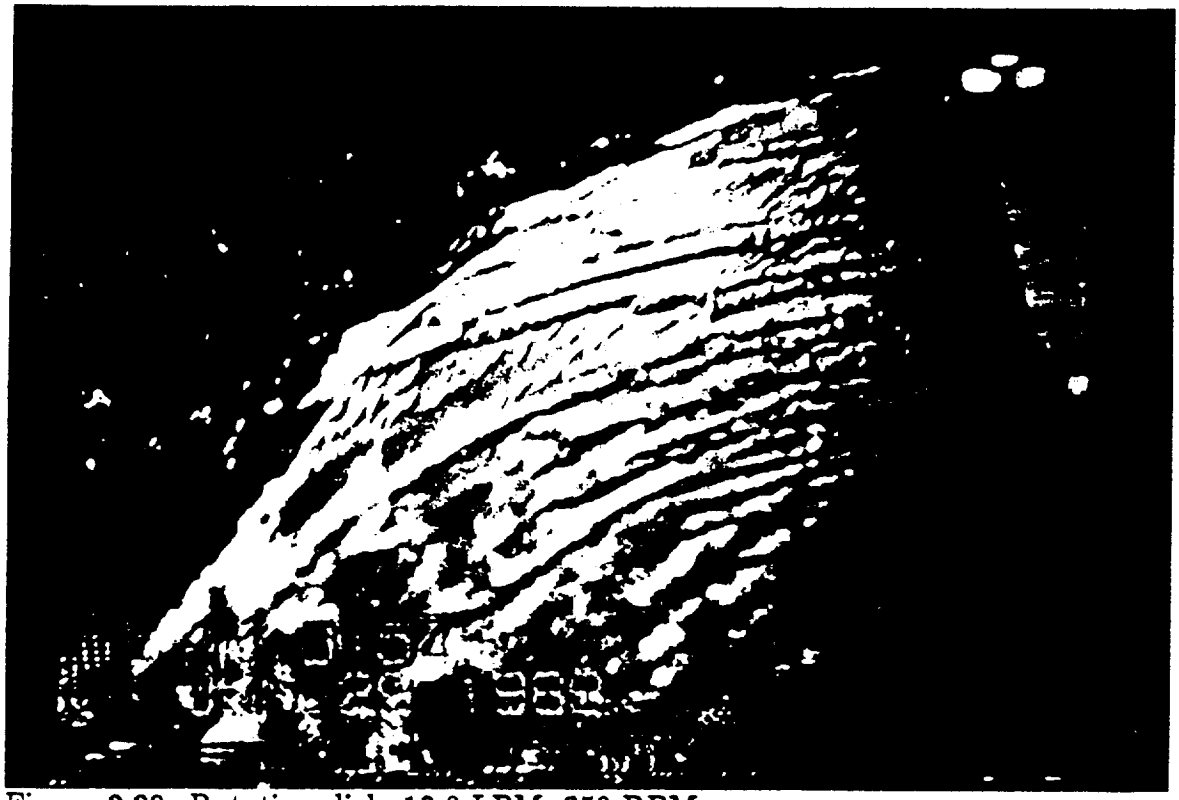

Figure 2.29. Rotating disk, 13.0 LPM, 250 RPM

Figure 2.30. Rotating disk, 13.0 LPM, 300 RPM

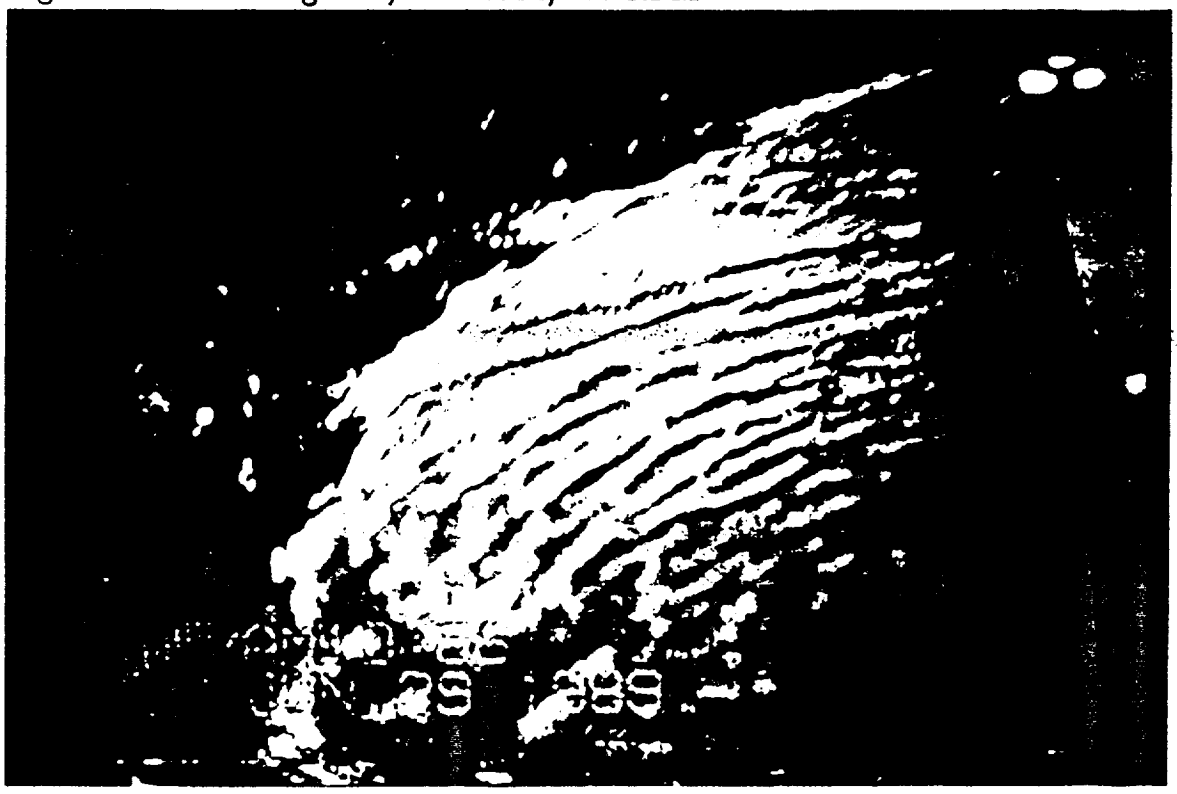

ORIGINAL PAGE IS
OF POOR QUALITY

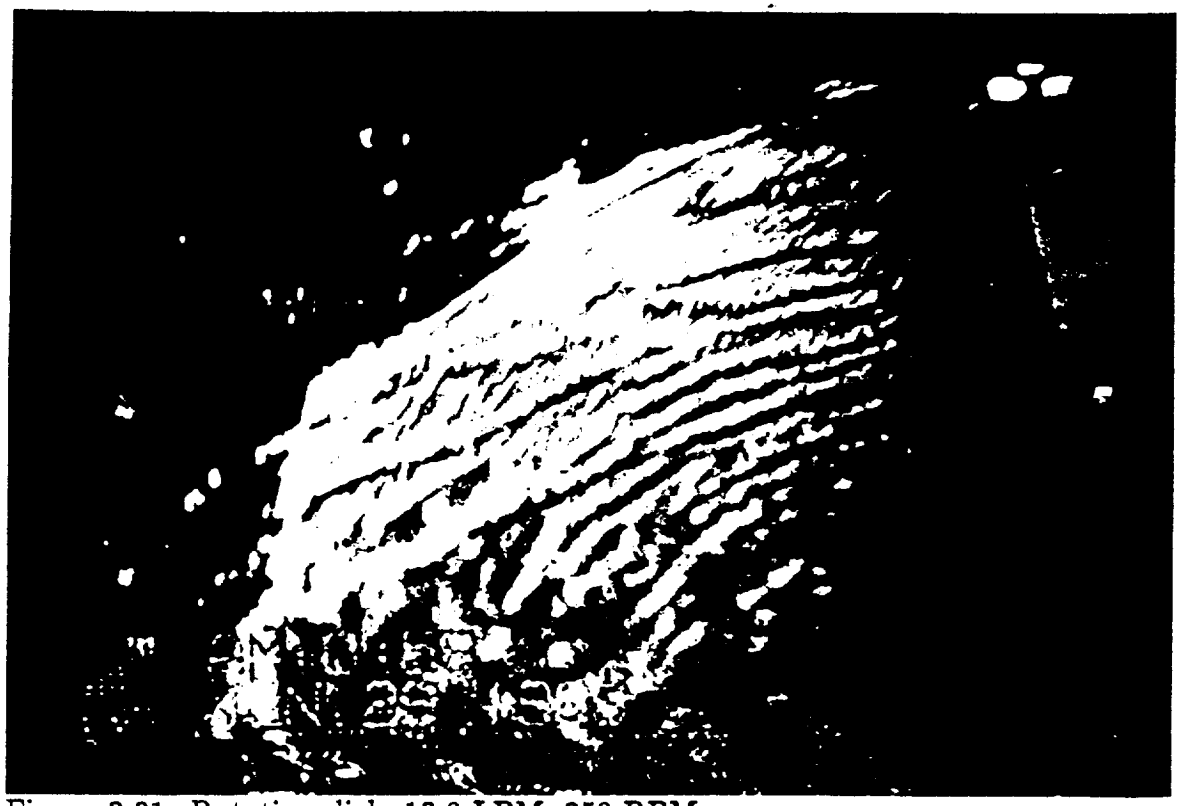

Figure 2.31. Rotating disk, 13.0 LPM, 350 RPM

free surface was determined photographically. When the horizontal disk was stationary, the thin film experienced a hydraulic jump, in which the velocity decreases and the thickness increases at a certain radial distance. In the region upstream of the jump, the film thickness was governed by the inertial and frictional forces on the fluid, as well as the radial spreading of the fluid. Downstream from the jump, the film thickness was mainly determined by the radius of curvature of the liquid at the outer edge of the disk. The liquid film thickness on the rotating disk was affected by the inertial and frictional forces on the fluid near the center of the disk, and by the centrifugal force near the outer edge of the disk. The flow visualization study revealed the presence of a "roller" at the hydraulic jump on the stationary disk, whose shape changed with the flow rate. Also, the transition between wavy-laminar flow to radial-wave flow was observed on the rotating disk as the rotational speed was increased. The range of transition shifted to higher rotational speeds as the flow rate increased.

Section III

TWO-DIMENSIONAL COMPUTATION OF THE FREE SURFACE FLOW OF A THIN LIQUID FILM USING "PRESSURE OPTIMIZATION METHOD"

3.1 SUMMARY

The results of numerical computations are presented for the free surface flow of a thin liquid film in the presence or absence of a gravitational body force. Three different flow systems were studied: (a) a falling film down a vertical wall, (b) plane and radial film flows under zero gravity and (c) plane and radial film flows along a horizontal plate in the presence of gravity. In the case of film flow along a horizontal plate where gravity acts across the thickness of the film, the Froude number, which characterizes the flow regime (i.e., supercritical or subcritical), is found to be the most dominant parameter. The transformation of the flow from supercritical to subcritical is associated with a hydraulic jump. The distributions of the film height, film velocity and friction coefficient are presented.

3.2 INTRODUCTION

The flow of a thin liquid film is encountered in many engineering devices. A thin film is quite commonly found during evaporation or condensation on a solid surface in a compact heat exchanger or cooling tower, spin coating in metal industries, and impingement cooling of a solid wall with a liquid jet. Besides practical applications, the fluid mechanics of thin film flows is important from a theoretical point of view since both viscosity and free-surface effects are significant in these flows. Moreover, the understanding of such flows under reduced or zero gravity is essential for the proper design of heat exchangers and heat pumps for space applications, which was the primary motivation for the present study.

The falling of a thin liquid film along a plane vertical wall has been studied by many investigators since the turn of this century. For steady fully-developed laminar flow, a theoretical solution can be derived from a simple balance between the gravitational body force and the shear force at the solid wall (Bird et al. (1960)). The film height remains constant and the velocity profile across the film becomes parabolic in the fully developed region. The results of developing flow when a film is introduced at its equilibrium height is presented in the review aritcle by Faghri and Payvar (1979). This review also included the experimental studies on laminar flow with constant thickness. A film falling under the influence of gravity ceases to be laminar and constant in thickness when the flow rate is high. Waves tend to appear on the surface and the flow becomes turbulent as the flow rate is increased. A number of theoretical as well as experimental studies have been performed to understand the wavy-laminar

and turbulent flows (see, for example, Seban and Faghri (1976, 1978) and Hirshburg and Florschuetz (1982)).

A somewhat less studied problem is the spread of a liquid film over a plate. Watson (1964) presented results of analytical and experimental studies of the radial spread of a liquid jet impinging on a horizontal plane for laminar and turbulent flows. By using the boundary layer approximations for the governing equations, analytical solutions using a similarity transformation along with the Pohlhausen integral method were derived. The analysis covered the regions where the boundary layer thickness is less than the film height and where the film is totally engulfed by the boundary layer. The effects of the gravitational pressure gradient was discussed. The possibility of a hydraulic jump in such a flow was also anticipated. However, the analysis was applicable only to the supercritical flow before the jump. An equation was also presented to predict the jump height for any given location of the jump. The agreement between the experimental data and the analysis was satisfactory.

Another interesting problem of thin film research is the spreading of the film under the action of centrifugal force as seen in a rotating system. An approximate analytical solution for laminar flow on a rotating disk was developed by Rauscher et al. (1973). An asymptotic expansion technique was used where the radial spread of the fluid was perturbed to determine the effects of convection, Coriolis acceleration, radial diffusion, surface curvature and surface tension. These higher order effects were discussed on a physical basis.

In all of the previous studies concerning thin liquid films, the investigators have tried to develop analytical models or have taken experimental data. Some of these models are quite approximate in nature and do not bring out the finer details of the flow field. Moreover, in all of the previous numerical studies (Faghri and Payvar (1979)) concerning the laminar falling film, a constant thickness was used in the calculation domain and no degree of freedom was permitted for the variation of free surface along the flow. A general numerical finite-difference solution of a thin film flow accounting for the variation of free surface height is not available at the present time. These flows are difficult to solve by the finite-difference method since the geometry of the free surface is not known ahead of time, and the surface profile cannot be fitted in a regular Cartesian or cylindrical coordinate system. Moreover, none of the studies mentioned above has considered the flow under reduced or zero gravity, which is expected to be different from the flow under normal gravity. A proper understanding of such flows is essential in the design of space cooling systems.

The present study is undertaken to develop a general numerical solution procedure for free surface thin film flows which can be applicable to both plane and radial systems, and to both normal and zero gravity environments. The results highlight the effects of gravity for different configurations of the flow.

3.3 PROBLEM FORMULATION

The equations governing the conservation of mass and momentum in a thin film of fluid which is Newtonian with constant properties are given by

$$\nabla \cdot \vec{V} = 0 \qquad (3.1)$$

$$\rho \frac{D\vec{V}}{Dt} = - \nabla p + \mu \nabla^2 \vec{V} + \rho \vec{g} \qquad (3.2)$$

These governing equations have to be supplemented with appropriate boundary conditions. At the solid wall, the no-slip condition exists, therefore, $\vec{V} = 0$. On the free surface, the shear stress vanishes which implies $\partial \vec{V}/\partial n = 0$, where n is the coordinate normal to the free surface. Moreover, in the absence of any significant surface tension, the static pressure on the free surface must equal the ambient pressure. By setting p equal to the difference between the actual and ambient pressures, then p = 0 on the free surface since pressure is a scalar quantity. Boundary conditions must also be assigned in the direction of the flow at two locations: the inlet and exit to the control volume or computational domain. The appropriate conditions were determined by analyzing the characteristic behavior of the flow, which is presented in a later section. These depend on whether the flow is supercritical, subcritical, or mixed. For a supercritical flow, which includes most of the cases considered here, $h = h_{in}$ and $\vec{V} = \vec{V}_{in}$ at the inlet and $\partial \vec{V}/\partial n = 0$ at the exit, where n is the coordinate normal to the exit plane. For subcritical flow, $h = h_{out}$ at the exit was prescribed instead of the inlet height. Moreover, the pressure was prescribed at the exit boundary. The boundary-fitted coordinate system used here is shown in Fig. 3.1 and the boundary conditions in component form are listed in Table 3.1 for plane and radial flows. The coordinate system is dicussed in detail in a later section of the paper.

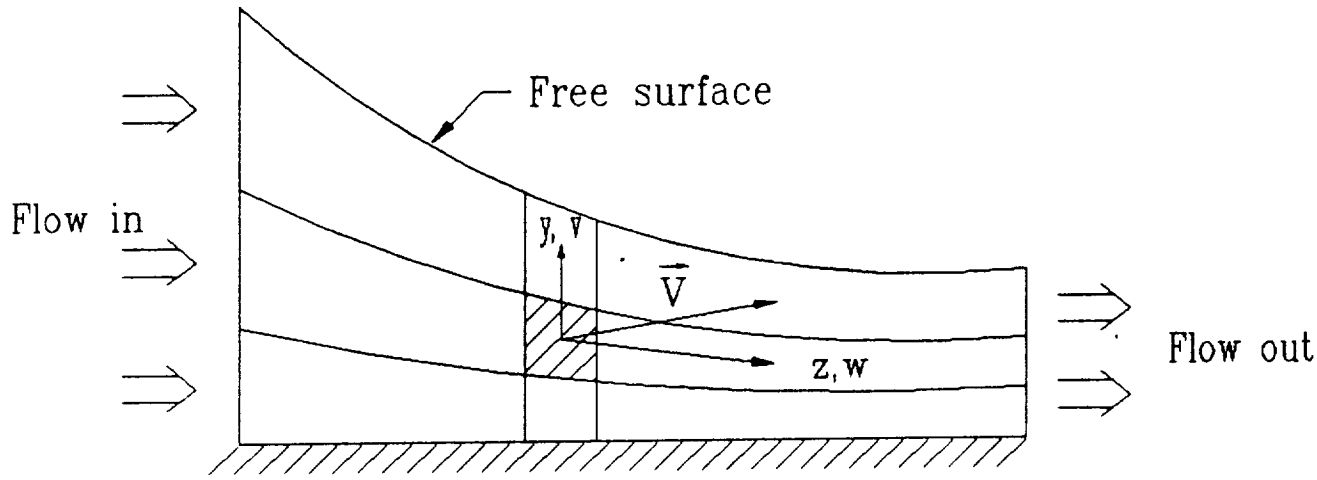

Fig. 3.1. The coordinate system on a grid cell

Table 3.1: Boundary Conditions for Plane Flow and Radial Flow

at $y = 0$:	$v = w = 0$
at $y = \delta$:	$\underline{\tau} \cdot \vec{n} = 0, \quad \underline{\tau} \cdot \vec{t} = 0$
at $z = 0$ or r_{in}:	$v = 0$, $\begin{cases} w = W_{in}, \text{ for uniform entrance} \\ w = 1.5\, W_{in} \left[2\left(\frac{y}{\delta}\right) - \left(\frac{y}{\delta}\right)^2 \right], \text{ for parabolic entrance} \end{cases}$
at $z = L$ or r_{out}:	$\begin{cases} p = 0, \text{ for cases 1 and 2} \\ p = \rho g\, (\delta - y), \text{ for case 3} \end{cases}$

The flow configurations considered in the present investigation are shown in Fig. 3.2. They can be broadly classified into three groups according to the presence and orientation of the gravitational body force:

(1) Falling film along a vertical wall

(2) Film flow under zero gravity

(3) Film flow along a horizontal plate in the presence of gravity.

The three possible orientations with respect to gravity will be denoted by 1, 2, and 3. Moreover, P and R will denote plane and radial flows and A, B and C will denote different combination of flow parameters. The parameters used for this study are listed in Table 3.2.

The first case is a classical problem where the major driving mechanism is the gravitational body force. This problem was used to check the accuracy of the present numerical methodology. The effects of introducing the film at a height other than the equilibrium height for a given flow rate will also be investigated for this case.

For film flow under zero gravity, two problems will be considered:

(2P) Plane film flow under zero gravity

(2R) Radial film flow under zero gravity

In the absence of any gravitational body force, the orientation of the plate becomes immaterial. The flow remains the same whether the plate is vertical, horizontal, or inclined. In this case the flow is driven by inertia and viscous forces. In the radially spreading flow, the area available for the film increases downstream and acts as an added mechanism for the reduction of the film velocity.

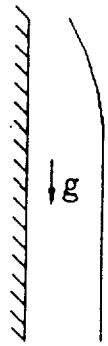

1P. Vertical falling film

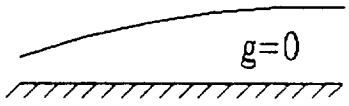

2P. Plane flow at zero gravity

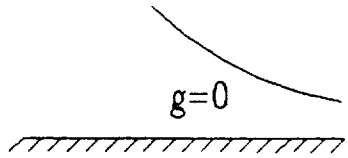

2R. Radial flow at zero gravity

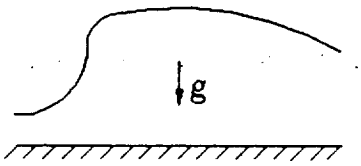

3P. Horizontal plane flow

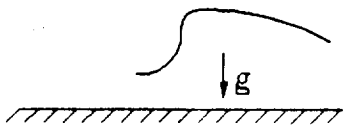

3R. Horizontal radial flow

Fig. 3.2. Flow systems in the present investigation

Table 3.2: Flow Conditions and Free Surface Specifications

Case 1PA: $\delta_{in} = \delta_{fd}$, $(= 0.000595\ m)$
$Re = 12.5$, $g/g_s = 1$, $L = 0.03\ m$
Free surface: $\Delta = 1$

Case 1PB: $\delta_{in} = 1.2\delta_{fd}$, $\delta_{fd} = 0.000595\ m)$
$Re = 12.5$, $g/g_s = 1$, $L = 0.03m$
Free surface: $\begin{cases} \Delta = (1 + A\xi)^{an}, & \text{for } \xi < \xi_1 \\ \Delta = 1, & \text{for } \xi \geq \xi_1 \end{cases}$

Case 1PC: $\delta_{in} = 0.8\delta_{fd}$, $(\delta_{fd} = 0.000595\ m)$
$Re = 12.5$, $g/g_s = 1$, $L = 0.03\ m$
Free surface: $\begin{cases} \Delta = (1 + A\xi)^{an}. & \text{for } \xi < \xi_1 \\ \Delta = 1, & \text{for } \xi \geq \xi_1 \end{cases}$

Case 2P: $\delta_{in} = 0.000595\ m$
$Re = 12.5$, $g/g_s = 0$, $L = 0.03m$
Free surface: $\Delta = (1 + A\xi)^{an}$

Case 2RA: $\delta_{in} = 0.005\ m$, $r_{in} = 0.0508\ m$, $r_{out} = 0.1953\ m$
$Re_{in} = 404$, $g/g_s = 0$
Free surface: $\Delta = (1 + A\xi)^{an}$

Case 2RB $\delta_{in} = 0.000508\ m$, $r_{in} = 0.0508\ m$, $r_{out} = 0.1\ m$
$Re_{in} = 8.5$, $g/g_s = 0$
Free surface: $\Delta = (1+ A\xi)^{an}$

Continued on next page

Case 3P:

$Re = 88.75, \quad g/g_s = 1, \quad L = 0.1445$ m

$$Fr_{in} = \begin{cases} 5.661, \text{ for case 3PA} \\ 8.582, \text{ for case 3PB} \end{cases}$$

$Fr_{out} = 1.0$

Free surface:

$\Delta = (1 + A\xi)^{an}$, supercritical

$\Delta = C\,[2 - (D + B\xi)^{bn}]$, subcritical $(\xi \neq 1)$

Case 3R:

$Re_{in} = 50.5, \; g/g_s = 1, \; r_{in} = 0.0508$ m, $r_{out} = 0.1953$ m

$$Fr_{in} = \begin{cases} 7.442, \text{ for case 3RA} \\ 10.96, \text{ for case 3RB} \end{cases}$$

$Fr_{out} = 1.0$

Free surface:

$\Delta = (1 + A\xi)^{an}$, supercritical

$\Delta = C\,[2 - (D + B\xi)^{bn}]$, subcritical $(\xi \neq 1)$

In the third group, we will again consider two problems according to the flow geometry under consideration:

(3P) Plane film flow along a horizontal plate in the presence of gravity

(3R) Radial film flow along a horizontal plate in the presence of gravity

In the case of horizontal thin film flow where the gravitational body force acts across the thickness of the film, different flow regimes (i.e., supercritical, subcritical, or both) may be present according to the local film velocity and height. The transition of the flow from supercritical to subcritical can take place through a hydraulic jump. Since a sudden transition of the flow takes place across a jump, special analytical and computational tools are required to calculate the flow around this singular point.

3.4 NUMERICAL SOLUTION PROCEDURE

The complete governing transport equations (3.1 and 3.2) along with the appropriate boundary conditions (Table 3.1) were solved numerically using a finite-difference scheme. Since the free surface geometry cannot be handled very well with a regular rectangular or cylindrical coordinate system, a boundary-fitted curvilinear coordinate system had to be used. In this system, the free surface of the film was used as one of the boundaries of the control volume.

A curvilinear system can be either orthogonal or non-orthogonal depending on whether the faces of the control cells are orthogonal to each other or not. The orthogonal system has the advantage of simplicity compared to the non-orthogonal system. In either system, the vectorial

form of the governing equations [i.e., eqns. (3.1) and (3.2)] can be written in terms of components and can be discretized to determine the finite-difference equations. In most of the computations presented, the coordinate system was non-orthogonal.

Within the range of the general non-orthogonal coordinate system there exist several options in formulating the equations. These options arise from the freedom available in the choice of velocity components and their direction with reference to the coordinates. Thus, velocity and force vectors can be resolved either into their Cartesian, covariant or contravariant components. Moreover, the problem can be solved in a physical domain or transformed into a domain where the grid cells are rectangular and other physical quantities are non-dimensional or reduced in dimension. Although all these options are obviously equivalent to each other from the physical point of view, they are substantially different as far as numerical treatment is concerned, each presenting its own problems. In the present study, the problem was solved in the physical domain where covariant velocity components were used. These are components parallel to the cell faces.

The grid system used can be considered as a distorted version of the usual orthogonal Cartesian grid system in which grid lines and control cells are stretched, bent and twisted in an arbitrary manner, subject to the cells retaining their topologically Cartesian character. This means that grid cells always had four sides and four corners in the two-dimensional domain considered here.

As shown in Fig. 3.1, the local coordinates are defined along lines joining adjacent cell centers. The z-axis was taken in the streamline direction and y-axis in the direction across the film. The resolutes of the velocity vectors in the y and z directions are v and w, respectively, and can be defined as

$$v = \vec{V} \cdot \vec{j}$$

$$w = \vec{V} \cdot \vec{k}$$

Here $\vec{j}$ and $\vec{k}$ are unit vectors in the direction of the coordinate axes. In general, the resolutes are not the same as the velocity components in these directions, but can be related to them by geometrical factors.

The finite-difference equations were derived by the application of the principle of conservation of mass and momentum to the grid cells. The transport processes for each cell are convection and diffusion. Moreover, there may be a momentum or mass source within the cell. The mass flux across a cell boundary was computed exactly from the scalar product of the velocity vector and the vector representing the area of the cell face. Note that this can be written out in terms of velocity resolutes and geometrical factors including angles between cell faces. In the calculation of convection across a cell face, special attention was given to the change of the orientation of the coordinate axes from cell to cell and the curvature of a cell face. These resulted in extra terms in the calculation of convection. However, the representation of convection was exact and did not involve any approximation due to the non-orthogonality of

the grids.

The calculation of diffusion is somewhat more complicated than convection. The diffusion flux was calculated assuming the coordinate system to be locally orthogonal. This obviously neglects cell curvature and non-orthogonal orientation and may incorporate a substantial amount of error where the process is primarily diffusive. However, in the thin film calculation this approximation should not introduce severe inaccuracies, particularly when the film enters the control volume with a reasonably high velocity.

The relative importance of convection and diffusion at each cell was determined from the magnitude of the local Peclet number. A hybrid difference scheme demonstrated by Patankar (1980) was used. The calculation of the momentum source due to the pressure gradient and that due to the gravitational body force could be accomplished without any approximation for non-orthogonality.

The grid generation was achieved in two steps. First, the grid cells were formed by algebraic interpolation between the boundary points. This provided an approximately equal volume for each control cell. The boundaries for the interior cells were then smoothed to make the cell faces more orthogonal to each other. This was achieved by solving the Laplace equation for grid geometry. This latter operation resulted in a better representation of diffusion in the flow field and more accurate computations. The details of the formulation in a body-fitted coordinate system and the generation of grid cells are described in the work by

Spalding et al. (1986).

The number of grids in the z-y plane was determined from a series of computations with different grid sizes. For radial flow, it was found that the free surface profile along with other computed quantities do not change any further if the computational mesh is refined beyond 50 x 25 grids in the z-y direction. Computations with 50 x 25 and those with 55 x 27 grids yielded identical results. For plane flow 40 x 20 grids in the z-y plane was found to be adequate, which precisely predicted the friction coefficient and velocity profile in a fully developed falling film flow. Therefore, all computations were carried out using 40 x 20 grids for plane flow and 50 x 25 grids for radial flow.

The flow field was solved by using the SIMPLEST algorithm as discussed by Spalding (1980). One special feature of this algorithm is that in the discretized form of the momentum equation, the convection terms are lumped together with the source term. This results in a faster convergence for some flow conditions. The algorithm works in an iterative manner where the continuity equation is transformed and used as a pressure correction equation. The computation starts by guessing a pressure field. This is used to determine velocity components from their corresponding momentum equations. The modified continuity equation is then used to determine the amount of pressure correction. The guessed pressure, the amount of pressure correction and the solution corresponding to the momentum equations are then assembled together to give the flow rate and pressure field for that step. The new pressure serves as a guess for the next step. The solution proceeds until the normalized residual for each equation was

approximately 10^{-6}. The above finite-difference formulation and solution procedure is incorporated in the computer program PHOENICS that was used in the present study.

In the free surface flow discussed here, both the zero-shear condition and the $p = 0$ condition at the free surface need to be satisfied. These two conditions cannot be simultaneously given at a boundary with the existing program. On the other hand, the free surface geometry, which is unknown in the problem has to be given before solving the flow field by a finite-difference method. To avoid this difficulty, an iteration scheme has been adapted as described below.

(1) Guess a free surface height distribution. One may use the one-dimensional solution for a good start.

(2) Solve the flow field completely for that distribution using the zero-shear condition on the free surface boundary.

(c) Find the pressure distribution on the free surface and calculate its deviation from an ideal zero-pressure free surface. The measure used here is the normalized RMS (root-mean-square) error referenced to the initial total head. It is defined as

$$\text{Normalized RMS Error} = \frac{\sqrt{\frac{1}{n}\sum_{k=1}^{n}(p_k)^2}}{\left(\rho g h_{in} + \frac{\rho W_{in}^2}{2}\right)}$$

where p_k is the free surface pressure at the kth node, and n is the number of nodes adjacent to the free surface.

(d) Calculate and reduce the RMS error on the free surface by successive alteration of the surface height distribution.

(e) The results with the minimum error give the required final solution.

The optimization technique used here is known as the exhaustive search method. In this method, a general form of the equation representing the free surface is assumed. The equation contains a number of arbitrary parameters depending on the desired degrees of freedom. To start the process, the parameters are given values either from experience (i.e., the one-dimensional solution) or just guessed. Only one parameter is then changed while the other are held constant and the trend of the RMS error is observed. That parameter is changed continuously in successive steps until a minimum RMS error is obtained. The parameter is then kept at its optimum value while the other parameters are changed one by one following the same procedure. Once the first round of optimization is complete, the first parameter is changed again in either direction to see whether the error increases or decreases. The process is continued with the other parameters until an absolute minimum for a combination of parameters is obtained. The accuracy of this process depends somewhat on the assumption of the form of free surface. In the results presented here, hyperbolas with two or more degrees of freedom (Table 3.2) were used to represent the computational domain.

The numerical algorithm had to be modified slightly when a jump was present in the flow field. This happened in the case of horizontal film flow in the presence of gravity. Under some flow conditions, both

supercritical and subcritical flows are present, separated by a hydraulic jump. When a jump was present, the two regimes of flow (i.e., supercritical and subcritical) had to be computed separately and the conditions were matched at the jump interface. It involved the following operations.

(a) Compute the supercritical film height by imposing the inlet film height and velocity and by optimizing the free surface profile to give the minimum RMS error in the pressure.

(b) Calculate the jump height from the supercritical film height using the equation

$$\frac{\delta_2}{\delta_1} = \frac{1}{2}\left[\sqrt{1 + 9.6\ Fr_1^2} - 1\right] \qquad (3.3)$$

where subscript '1' denotes the supercritical condition before the jump and '2' denotes the condition following the jump. This relationship can be derived from the momentum balance at the jump while the velocity profile before and after the jump are assumed to be parabolic in nature.

(c) Compute the subcritical film height by imposing the flow rate and exit film height corresponding to Fr = 1 and optimizing the free surface profile to give the minimum RMS error for the pressure.

(d) The supercritical and subcritical flows are calculated for the same flow rate, but for supercritical flow the inlet Froude number is fixed, whereas for subcritical flow the exit Froude number is fixed.

(e) The intersection of the jump height and the subcritical film height

determines the location of the jump. The film height before the jump is given by the supercritical height whereas after the jump the film height is given by the subcritical height.

In order to increase the computational accuracy for both subcritical and supercritical flows, the flow involving a hydraulic jump was always assumed to have a parabolic velocity profile at the inlet. Moreover, the flow was well-established by evolving the flow with a few extra nodes at the upstream side of the computational domain.

3.5 RESULTS AND DISCUSSION

3.5.1 Falling Film

The flow of a plane film along a vertical wall under the influence of gravity is a classical fluid mechanics problem where an analytical solution is available for fully-developed laminar flow. In the fully-developed region, the film height remains constant and the velocity profile has a parabolic appearance. Numerical computations using the present methodology were performed for a film which has already reached the fully-developed condition. A parabolic velocity profile with the same shape as given by the analytical solution was used for the incoming fluid. The Reynolds number for the film was Re = 12.5. It was found that for the entire domain, the velocity profile across the film remains about the same and the friction coefficient was equal to that of the analytical solution. In the present investigation, the friction coefficient is defined in terms of local average velocity of the fluid across the film in contrast to the inlet velocity. This definition is applicable for both plane and radial flows. For plane flow with constant thickness, V is constant because of

continuity.

The distribution of pressure on the free surface was also computed and the normalized RMS error was determined to be 0.011. This non-zero value for the error may be attributed to the inaccuracy associated with the representation of the flow field by finite-difference equations. This error can be further reduced by more grid points and more degrees of freedom in the free surface equation.

The developing flow of a falling film when introduced at a height equal to, above, or below the equilibrium height was also investigated. The flow conditions are summarized in Table 3.2 (cases 1P) and the results are shown in Table 3.3 and Figs. 3.3 and 3.4. When the film enters the control volume at the equilibrium height, the height remains the same and the development of the velocity profile from uniform to parabolic occurs as the flow moves downstream. When the film enters with a height other than the equilibrium height, a gradual adjustment of the height takes place until the flow reaches the equilibrium height. The adjustment of the free surface and the development of the velocity profile occur simultaneously in this flow. To model the free surface, a height distribution of the form given in Table 3.2 (cases 1PB and 1PC) was assumed. The first part of this distribution ($\xi<\xi_1$) provides the variation of the free surface height in the developing flow region and the second part ($\xi\geq\xi_1$) gives the height after the adjustment is completed. The downstream location where the free surface adjustment is complete is ξ_1.

For the computation with $\delta_{in} = \delta_{fd}$, the normalized RMS error on the

Table 3.3: Summary of Computed Optimum Profiles and Normalized RMS Error in Pressure

Problem	Optimum Profile	Normalized RMS Error in Pressure
Case 1PA (Parabolic Inlet)	uniform	0.011
Case 1PA (Uniform Inlet)	uniform	0.073
Case 1PB	A = 7.5 an = 0.2 ξ_1 = 0.2	0.024
Case 1PC	A = 3000 an = 0.0445 ξ_1 = 0.05	0.026
Case 2P	A = 10 an = 0.93	0.054
Case 2RA	A = 1.43 an = -0.64	0.039
Case 2RB	A = 27.3 an = 0.72	0.091
Case 3PA	A = 1.47 an = 1.52 C = 8.42 D = 1.04 B = 0.29 bn = 1.5	0.014
Case 3PB	A = 1.47 an = 1.83 C = 11.11 D = 1.04 B = 0.29 bn = 1.5	0.025

Continued on next page

Case 3RA	A = 2.05 an = 2.2 C = 8.51 D = 1.04 B = 0.37 bn = 1.4	0.033
Case 3RB	A = 2.05 an = 2.7 C = 11.01 D = 1.04 B = 0.37 bn = 1.4	0.036

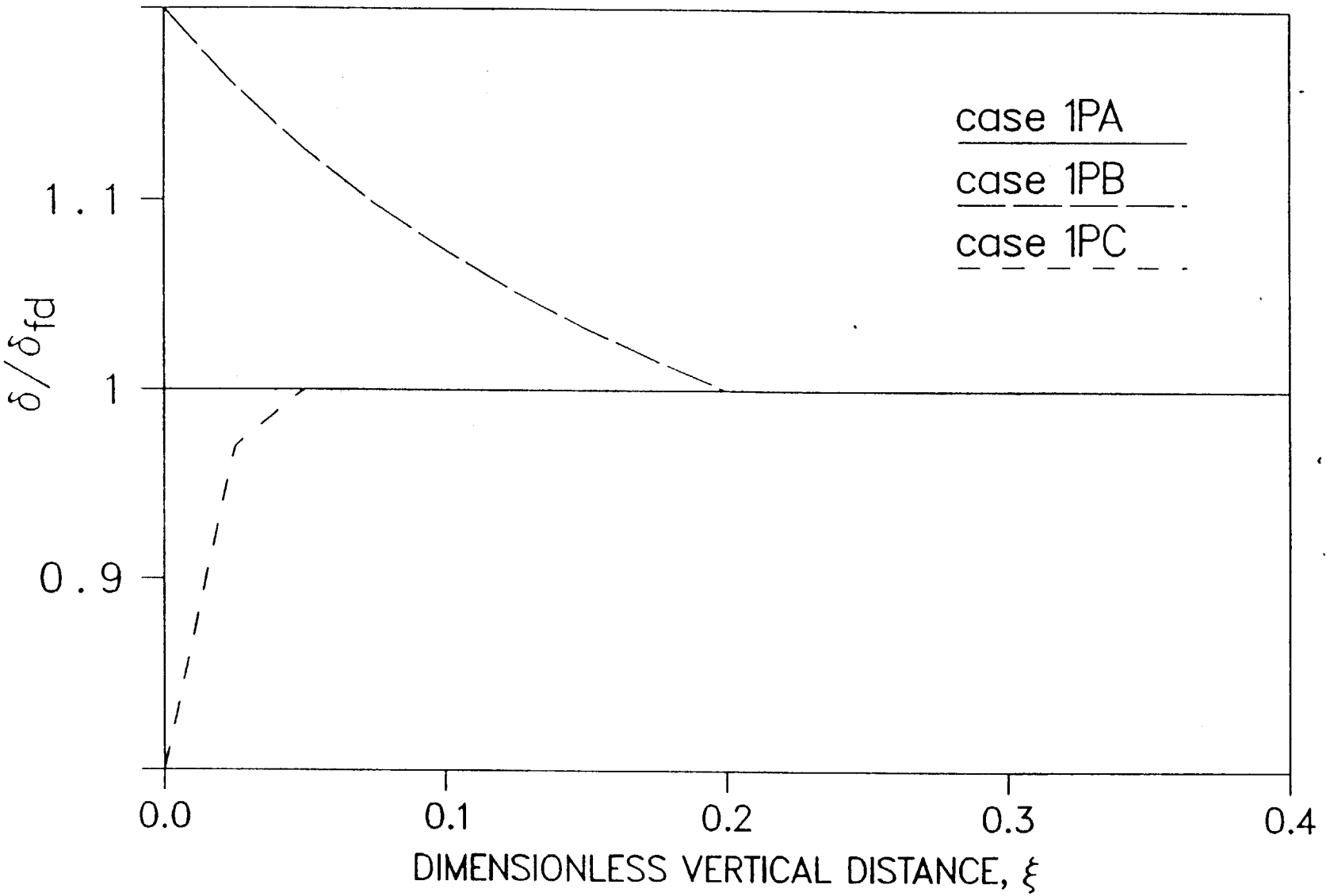

Fig. 3.3 Film height in a developing falling film flow

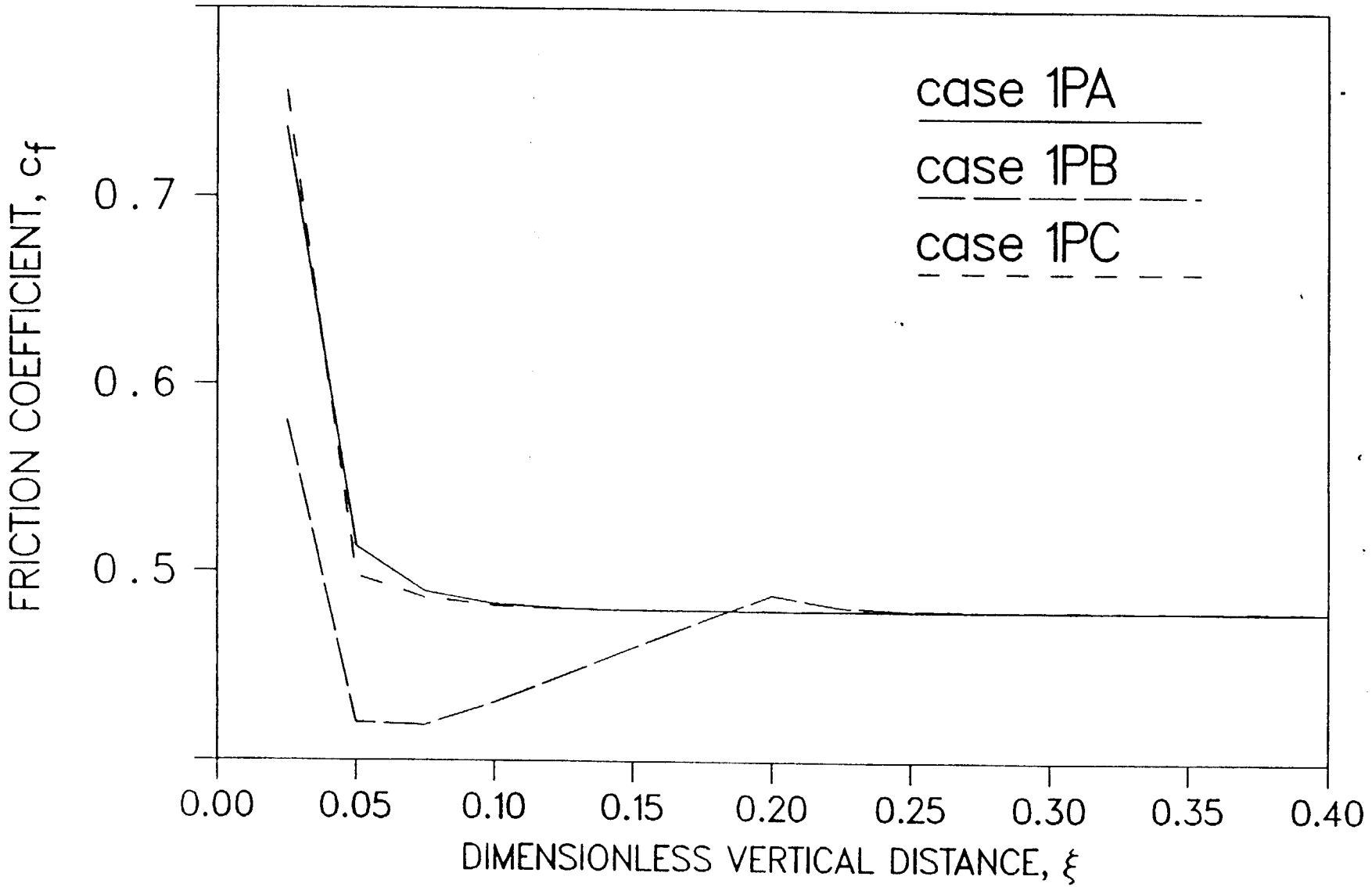

Fig. 3.4 Friction coefficient in a developing falling film flow

free surface condition is 0.073. The uniform entrance condition provides a higher RMS error than the parabolic entrance since a developing flow regionis present where the pressure has to conform with the flow development. An error of this order may be acceptable for a free surface computation since no variation of height is expected to take place when a film is introduced at the equilibrium height. In the present investigation, the normalized RMS error corresponding to the optimum free surface profile did not exceed a limit of 0.1. The distance required for flow development was found to be about five times the film thickness in this case. A flow is defined to be fully-developed when the friction coefficient is within 2 percent of the final equilibrium value. This definition is similar to that given by Kays and Crawford (1980) for developing flow in closed conduits.

As seen in Fig. 3.3, the adjustment of the film height takes places for a length of approximately 0.2 L, which in terms of equilibrium height came out to be $10\delta_{fd}$ when a film is introduced at a height 20 percent more than the equilibrium height. In this situation, the velocity profile also becomes fully-developed at the same location. A film introduced at a height 20 percent lower than the equilibrium is found to require a shorter distance for the adjustment of the free surface and the velocity profile.

The variation of the friction coefficient along the length of the film is shown in Fig. 3.4. The distributions for $\delta_{in} = \delta_{fd}$ and $\delta_{in} = 0.8\delta_{fd}$ are very close to each other, but for $\delta_{in} = 1.2\delta_{fd}$ the variation is significantly different. In the last case, the friction coefficient first decreases to a value lower than that for the equilibrium condition and then

rises up to the equilibrium value. This is due to two counter-acting phenomena that affect the film in the developing flow region in this case. The wall friction propagates outward as the boundary layer develops beginning from the entrance point which tends to reduce the velocity of the fluid. The thickness of the film, however, decreases and tends to increase the fluid velocity due to the area available for the flow. Since the first effect starts from the wall, it is more dominant in the earlier part of the flow development and then the second effect takes over in the region downstream. It can also be mentioned that when the film is introduced below the equilibrium height, the increase in the film height and the propagation of the shear stress tend to reduce the film velocity, so the behavior is not analogous to the case when the film is introduced above the equilibrium height. In all situations, a plane falling film eventually attains a fully-developed flow. This was confirmed by comparison of the velocity profile in a location near the exit. The variation of the velocity and the friction coefficient were found to be identical in all situations.

3.5.2 Film Flow Under Zero Gravity

In the absence of gravity, the orientation of the plate becomes immaterial and an identical flow condition is achieved if the plate is horizontal, vertical, or inclined. A situation is considered herein where the film is introduced at a height equal to the equilibrium fully-developed flow in a falling film system as discussed in the previous section. In the absence of gravity, the flow is acted on only by viscous and inertial forces and the film height is expected to increase downstream. To model the free surface, a profile of the form given in Table 3.2 (case 2P) is

assumed. The flow conditions are also listed in the same table. The results are shown in Table 3.3 and Figs. (3.5-3.7).

Figure 3.5 shows the variation of the dimensionless film height with distance, which increases monotonically. The figure also shows the analytical solution derived in a previous section. The analytical solution requires the specification of a friction coefficient. In the present investigation, the friction coefficient was taken from the numerical solution instead of assuming it to be constant throughout the region. The comparison between the analytical and numerical solutions appears to be good in most regions of the flow.

The variation of the w-component of the velocity at three different locations is shown in Fig. 3.6. In contrast to the falling film, the velocity changes as the flow moves downstream and does not attain a fully-developed situation. The profile, however, becomes approximately parabolic in nature downstream from the entrance. A test of the velocity profile with a true parabola showed that the maximum deviation is less than 10 percent. The shear stress exerted by the solid wall and the corresponding friction coefficient are plotted in Fig. 3.7. It can be noticed that the shear stress decreases continuously as the flow moves downstream, whereas the friction coefficient has a minimum at an intermediate location and then increases. The largest variations of the shear stress occur close to the entrance due to the development of the velocity from a uniform to a parabolic profile. After the velocity profile is fully developed in shape, the slight reduction in the shear stress is due to the deceleration of the flow, which is small compared to the

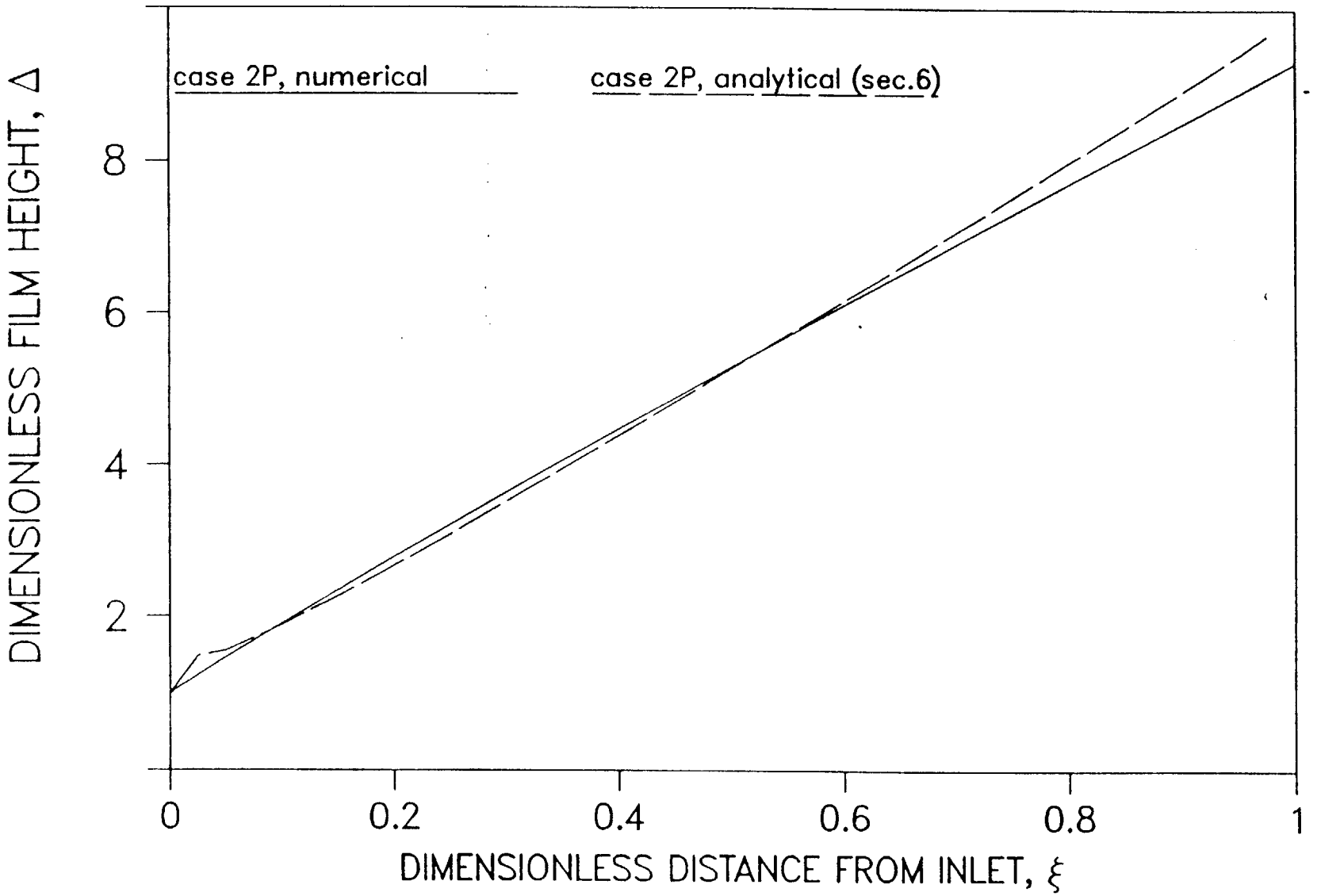

Fig. 3.5 Film height for plane flow under zero gravity

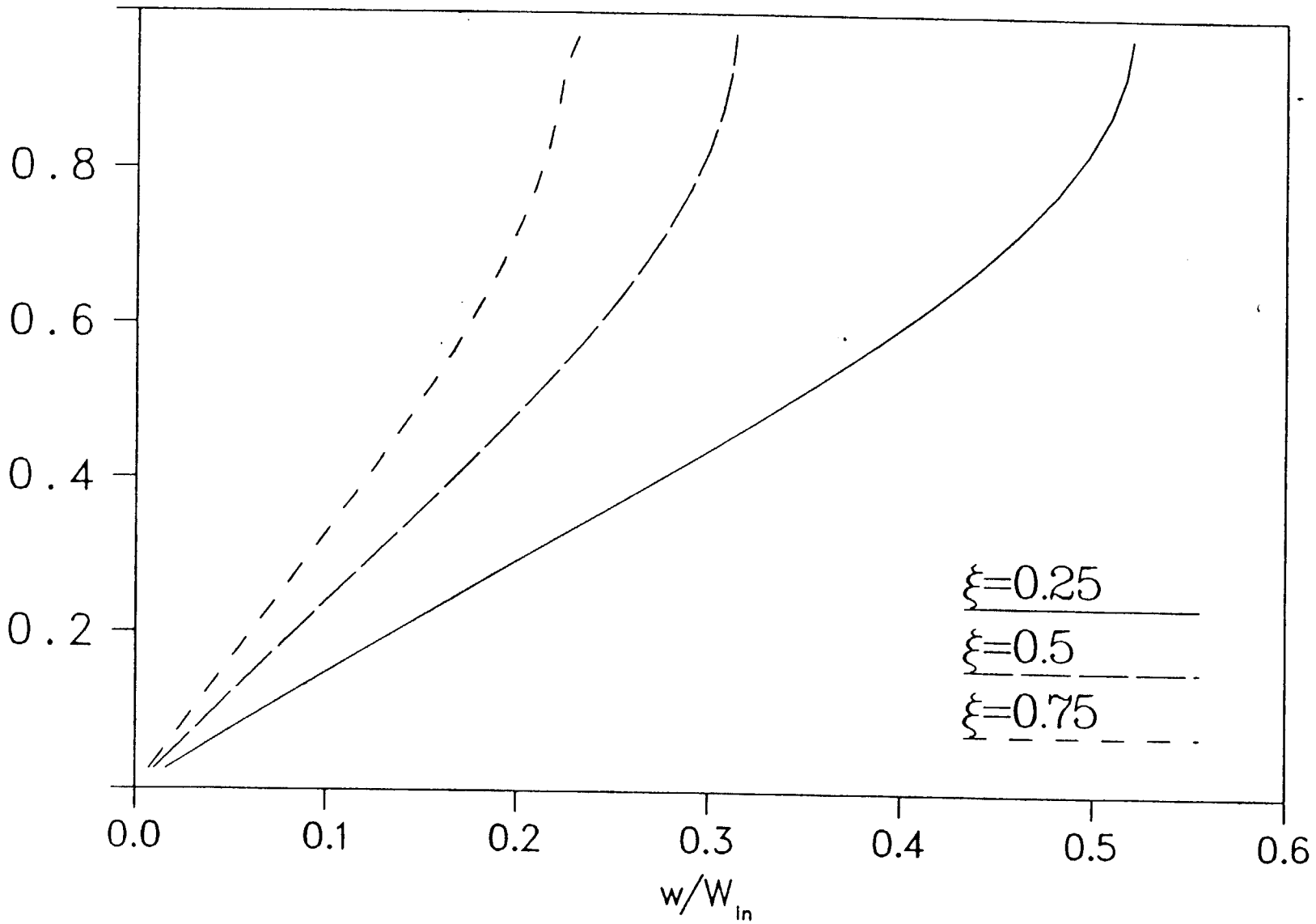

Fig. 3.6 Velocity profile for plane flow under zero gravity (case 2P)

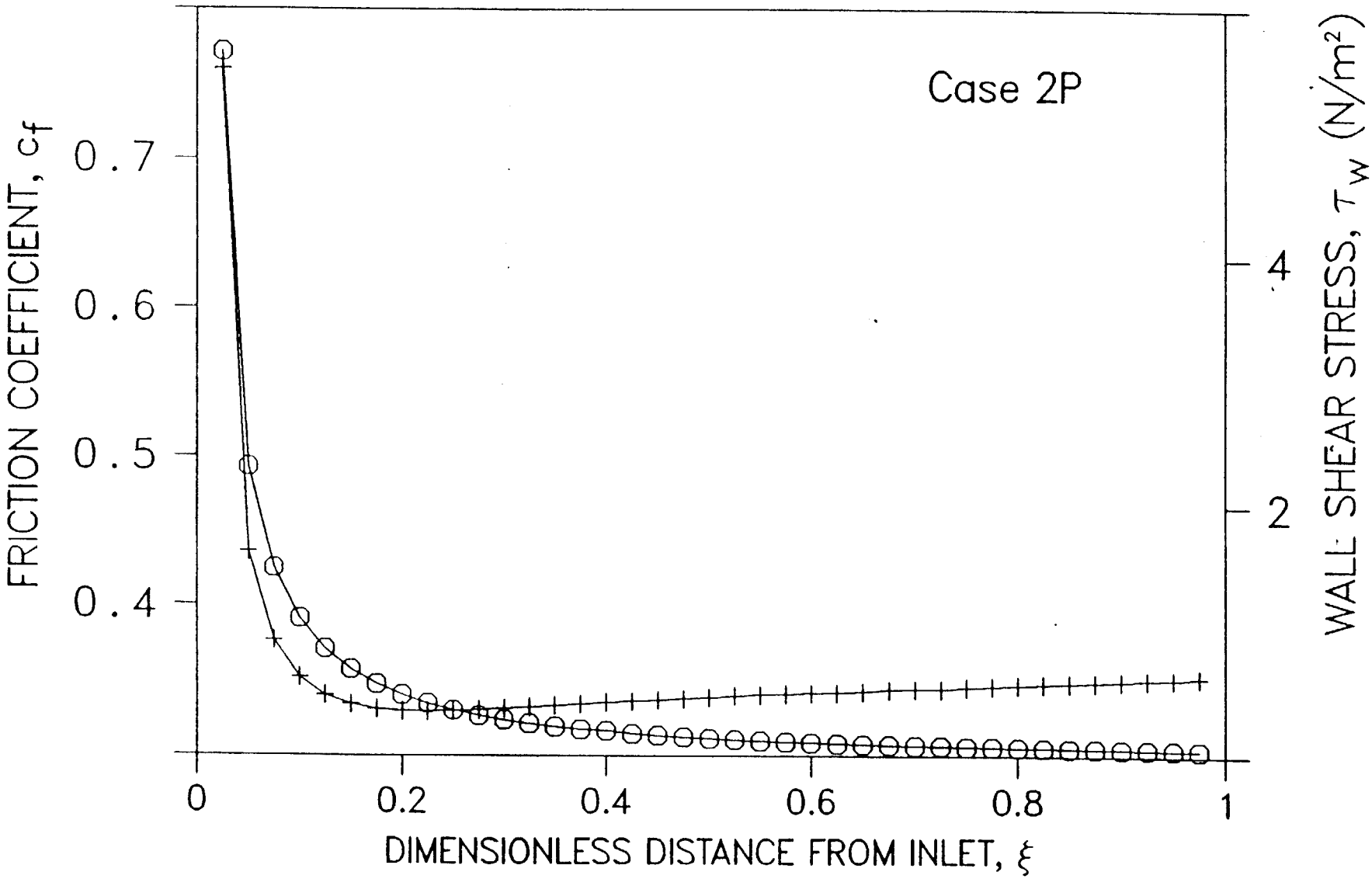

Fig. 3.7 Wall shear stress (o) and Friction coefficient (+) for plane flow under zero gravity

reduction of the average velocity in regions away from the entrance. This results in an increase in the friction coefficient.

The system where a fluid is introduced at the center of a circular horizontal plate and spreads uniformly in all radial directions was also studied. Two different inlet Reynolds numbers were chosen. The flow parameters corresponding to these cases are shown in Table 3.2 (cases 2RA and 2RB). The surface profile and corresponding normalized RMS error for the surface pressure are listed in Table 3.3.

Figure 3.8 shows the variation of the film height with radial distance. Case 2RA corresponds to a higher Reynolds number than that of Case 2RB. It appears that the inlet Reynolds number is a very strong parameter in determining the behavior of the film as it spreads radially under zero gravity. At a high Reynolds number, the film decreases in height monotonically because the inertial forces are greater than the frictional resistance exerted by the solid wall. When the Reynolds number is small, the film enters the control volume with a smaller amount of inertia and is easily overpowered by the frictional resistance. The strong resistance to the flow causes a rather rapid increase in the film height as it flows downstream. The figure also shows the film height distribution predicted by the one-dimensional analysis for case 2RA. The analytical prediction for this case is found to be comparable with the two-dimensional numerical solution.

The variation of the velocity across the film thickness is shown in Fig. 3.9 for two different locations. In both cases, the profile is almost

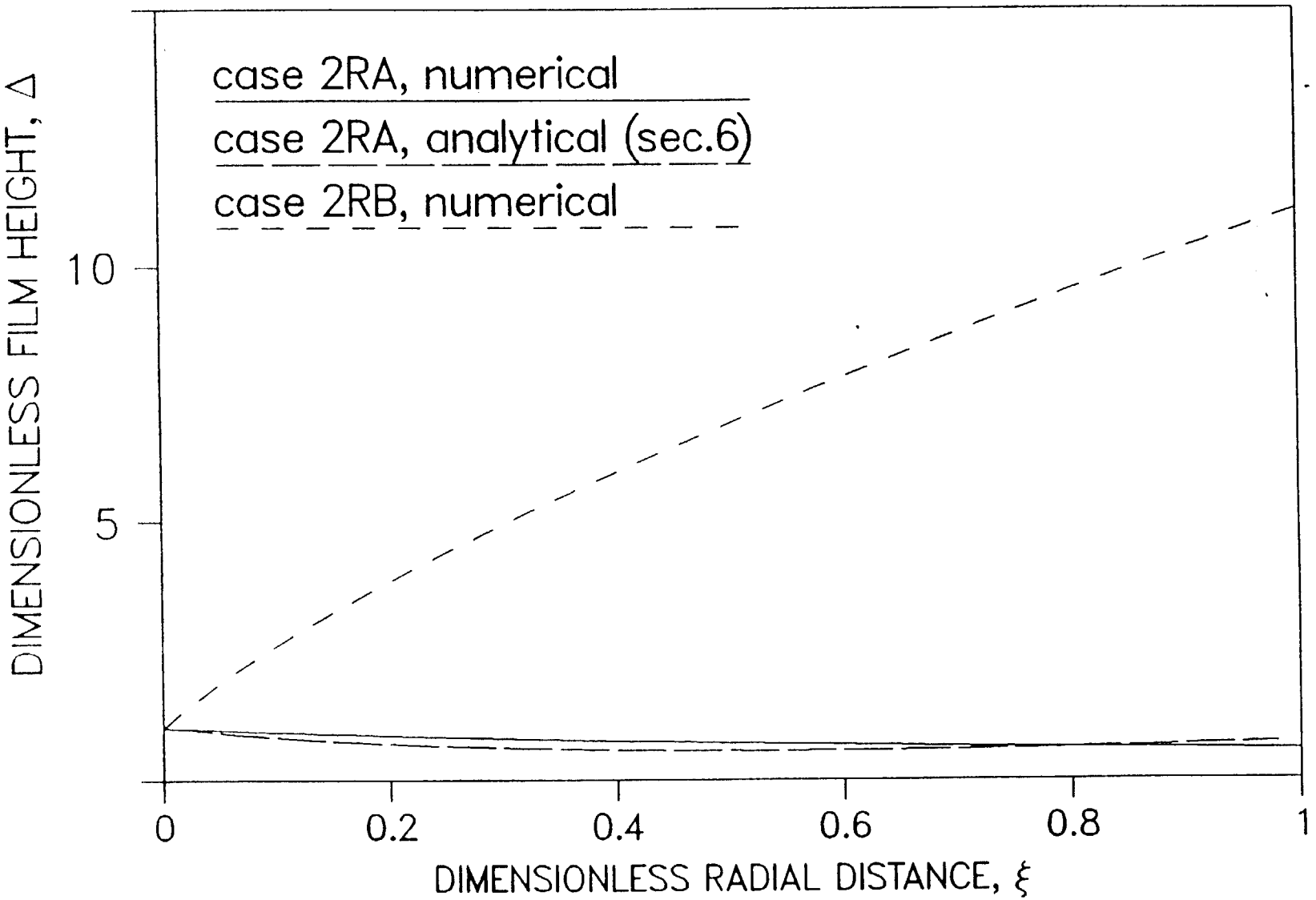

Fig. 3.8 Film height for radial flow under zero gravity

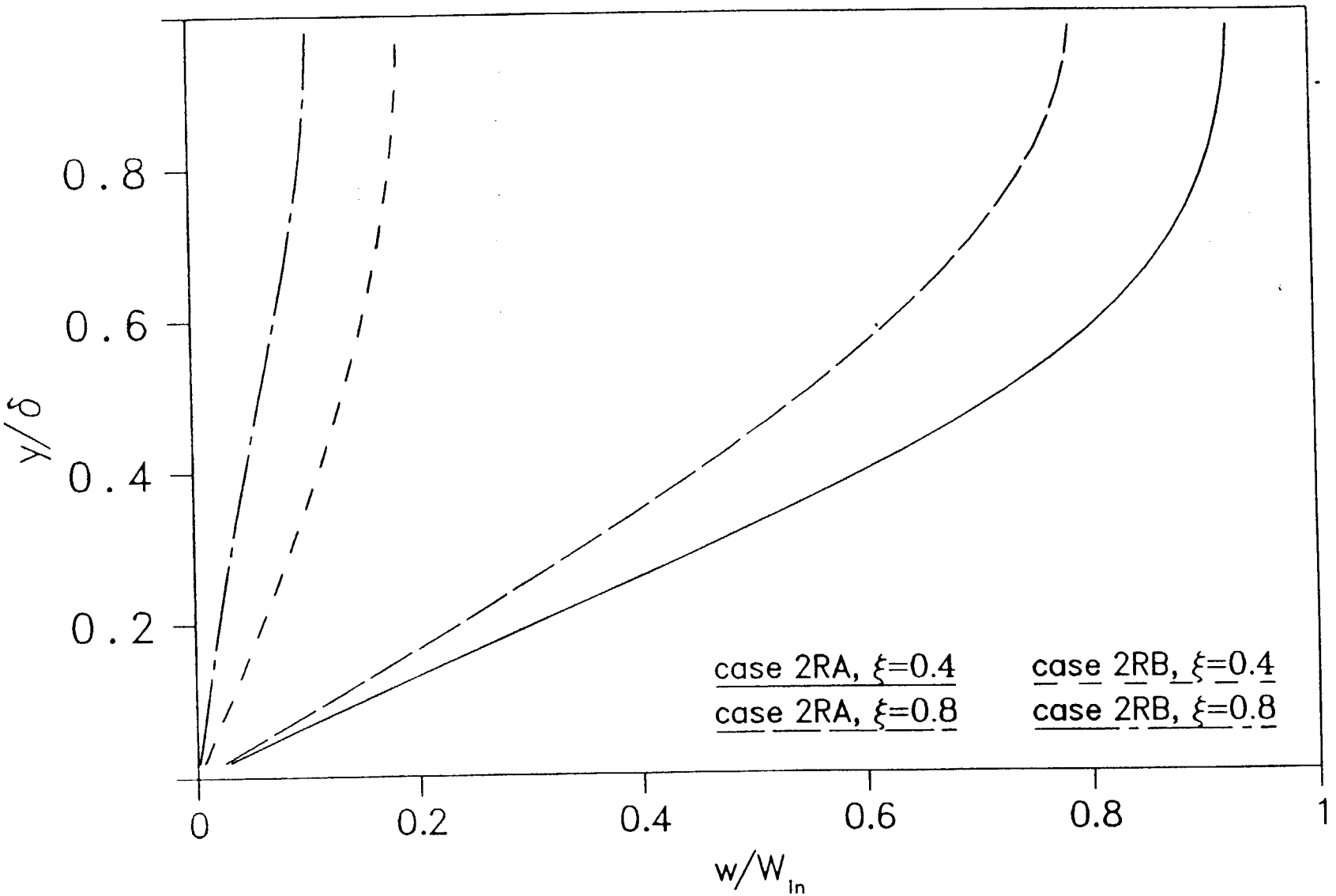

Fig. 3.9 Velocity profile for radial flow under zero gravity

parabolic (deviation within 2 percent) but its magnitude decreases downstream due to the increase in area available for the flow. The friction coefficients for these two cases are plotted in Fig. 3.10. In case 2RA, the friction coefficient is smaller in magnitude than that of case 2RB because the friction coefficient is a function of the wall shear stress and the local velocity. Case 2RA, which corresponds to a higher fluid velocity, is expected to encounter more resistance from the wall. This is precisely the situation as seen in the computed values of the wall shear stress. However, the magnitude of the velocity is a stronger parameter in the friction coefficient and causes the coefficient to be lower in case 2RA. In the figure it can be also noticed that in case 2RB, which corresponds to a smaller flow rate, the friction coefficient starts increasing soon after the entrance, attains a maximum value at an intermediate location and then decreases further downstream. In contrast to case 2RA the velocity profile at the inlet was assumed to be parabolic in nature. Therefore, a rapid decrease of friction coefficient near the entrance, which is characteristic of a developing flow, is not found here. The decrease of the friction coefficient downstream indicates that the shear stress also decreases very rapidly in that region. This suggests the possibility of a zero-shear condition further downstream.

3.5.3 Horizontal Film Flow in the Presence of Gravity

The flow of a plane film and a radially spreading film were also investigated for a horizontal orientation of the plate where the gravity acts across the thickness of the film instead of in the direction of the main flow. The flow conditions used here are listed in Table 3.2 (cases 3) and the corresponding free surface geometry is described in Table 3.3.

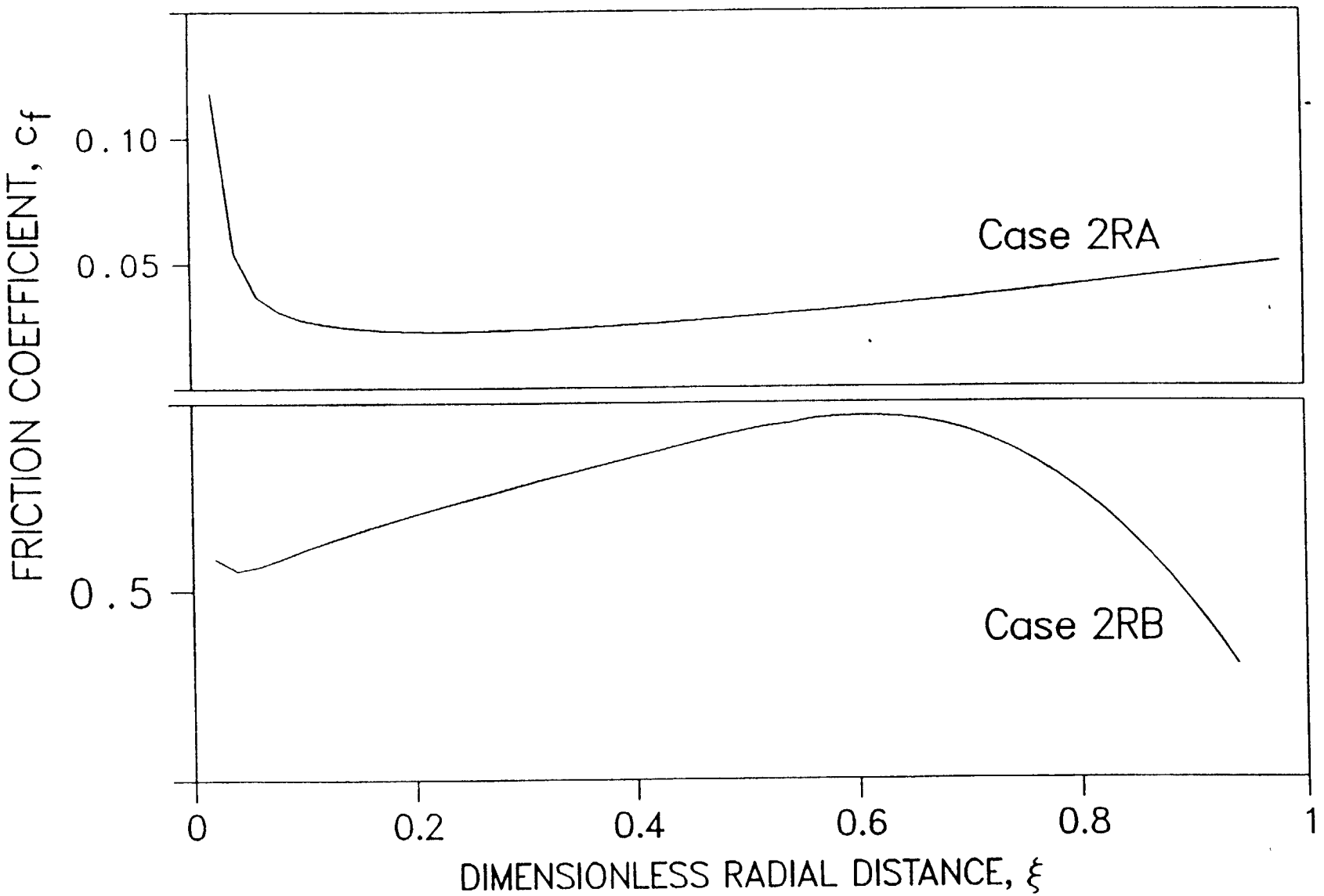

Fig. 3.10 Friction coefficient for radial flow under zero gravity

Figures 3.11 and 3.12 present the computational results.

In the case of horizontal flow, two different flow regimes are encountered. The flow is subcritical or supercritical depending on the Froude number. Both subcritical and supercritical flows move toward a critical condition. When the flow enters the control volume as subcritical, it remains subcritical in the entire domain since a transition from subcritical to supercritical is not possible. However, if the flow enters the control volume as supercritical, it may remain supercritical or transform into a subcritical flow depending on the amount of inertial, gravitational, and viscous forces it encounters during the flow. Moreover, if a transition is present it must happen as a jump where the height before and after the jump can be related by the jump condition (eqn. 3.3). In the present investigation, the supercritical and subcritical branches of the flow were computed separately and the location of the jump was determined via the jump condition. In the computation of supercritical flow, the inlet height and Froude number were appropriately prescribed, whereas for subcritical flow the outlet condition was prescribed.

In Fig. 3.11, it can be noticed that the jump moves downstream with an increase in the inlet Froude number. When the inlet Froude number is high, the flow can maintain its supercritical status for a longer distance. Figure 3.12 shows the subcritical and supercritical solutions and the corresponding jump height distribution for the two plane flow cases considered here. When the inlet Froude number is increased, the inlet height decreases if the flow rate is held constant. This causes the supercritical height of the film to decrease and the jump height to

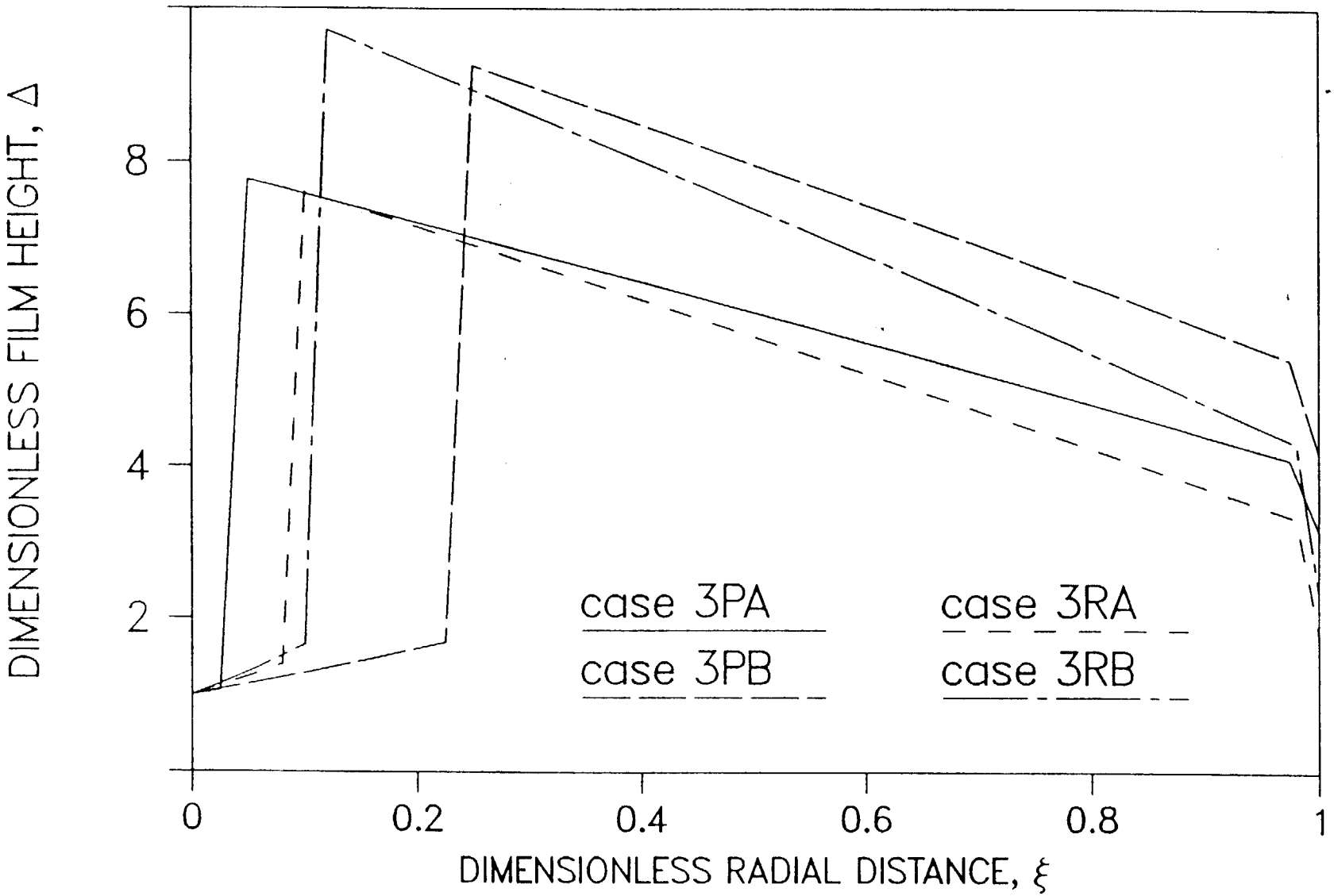

Fig. 3.11 Film height for plane and radial horizontal flow

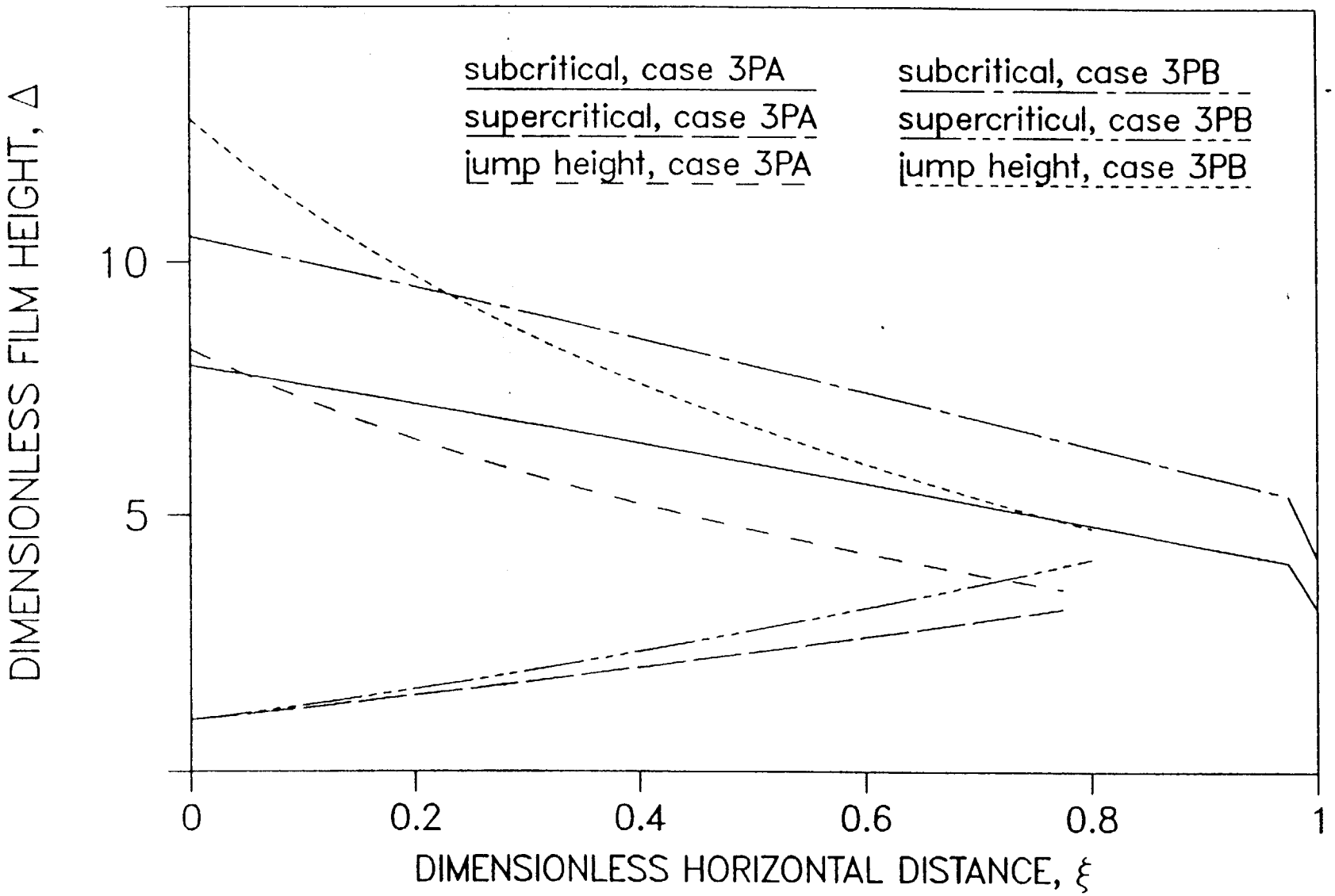

Fig. 3.12 Supercritical and subcritical film height for plane horizontal flow

increase. When the Froude number is gradually increased at the inlet, a condition is reached when the jump height curve goes above the subcritical curve and no intersection of the two curves is found in the computational domain. At that situation, no jump is possible in the region under consideration and the flow remains supercritical over the entire plate. Similarly, when the Froude number is gradually decreased at the inlet, the jump height curve goes below the subcritical curve. In this situation, no supercritical flow can be sustained and the jump occurs at the entrance.

Comparing the results of plane flow and radial flow, it can be seen that the propagation of the jump location downstream with an increase in the Froude number is greater for plane flow than radial flow. In the case of radial flow, the area increases downstream and causes the flow to slow down. This results in more rapid reduction of the Froude number of the flow. Therefore, in a radial system a jump is likely to be present for a larger range of inlet Froude numbers.

3.6 CONCLUSIONS

A numerical solution procedure for the computation of plane or radial free surface thin film flows in a normal or zero gravity environment has been developed. An analytical solution was also derived for a one-dimensional approximation of the flow. A reasonable agreement between the numerical and analytical solutions was obtained for most flow configurations considered here. Three different flow systems were studied: (a) plane falling film, (b) plane and radial flow under zero gravity and (c) plane and radial flow on a horizontal plate in the presence of gravity.

A plane falling film, whether introduced at its equilibrium height or at a height above or below the equilibrium, eventually attains the fully-developed condition. In the fully developed region, the numerical velocity profile, which is parabolic, matched exactly with the analytical solution. An estimate on the error bound of the free surface pressure was developed from the calculation of the developing flow of the falling film and it was concluded that a normalized RMS error of less than 0.1 may be acceptable. The length of the developing region was found to be small. Both the free surface height and velocity profile appeared to arrive at the equilibrium condition within 10 times the equilibrium film thickness. The length was found to be relatively larger when the film begins with a height above the equilibrium height.

For a plane flow under zero gravity, it was found that the film thickness monotonically increases as the flow moves downstream. The velocity profile is parabolic except for regions very close to the entrance. The shear stress at the wall decreases as the flow moves downstream. The friction coefficient was computed in terms of the local average velocity and was found to increase after coming to a minimum at an intermediate location on the plate.

For radial flow under zero gravity, it was found that at a higher Reynolds number the film decreases monotonically in thickness as it spreads downstream. At a smaller Reynolds number, there is a relatively rapid rise in height and the flow develops a parabolic velocity profile as it moves downstream.

For both plane flow and radial flow on a horizontal plate in the presence of gravity, two different flow regimes (i.e., supercritical and subcritical) are found to be present. The transition of the flow from supercritical to subcritical is accompanied by a hydraulic jump. The location of the jump moves downstream with an increase in the inlet Froude number.

Section IV

COMPUTATION OF HEAT TRANSFER IN TWO-DIMENSIONAL THIN FILM FLOW

4.1 SUMMARY

The numerically computed flow field and heat transfer coefficient are presented for the flow of a thin liquid film in the presence or absence of a gravitational body force. The flow systems studied here include (1) a film falling down a vertical wall, (2) plane and radial film flow at zero gravity and (3) plane and radial film flow along a horizontal plate in the presence of gravity. The heating conditions include isothermal and uniformly heated surfaces. The transport conditions considered at the free surface are an adiabatic condition when there is no heat loss from the free surface and an evaporative free surface maintained at its saturation temperature. The height of the free surface, flow field and heat transfer coefficient were found to be strongly affected by the magnitude and direction of the gravitational body force. They were also found to depend on the Reynolds number and Froude number of the incoming fluid. The flow conditions changed continuously downstream except for the falling film, where a fully-developed condition was established at some downstream distance. In the case of horizontal flow in the presence of gravity, a hydraulic jump was found to be present under some flow conditions.

4.2 INTRODUCTION

The heating and evaporation of a thin liquid film are found in many engineering processes. The desalination of sea water, the distillation of petroleum products and evaporation in a cooling tower are examples. The use of evaporative cooling is also becoming common in computer and space technology because of the high heat rejection requirement per unit surface area. An understanding of the flow and heat transfer in a thin film for different magnitudes and orientations of the gravitational body force is also essential for an appropriate design of the absorber unit of a heat pump absorption system in earth and space, which was the motivation for the present study.

The flow and heat transfer in a falling thin liquid film along a plane vertical wall has been studied by many investigators since the turn of this century. For steady fully-developed laminar flow, a theoretical solution can be derived from a simple balance of momentum and energy (Bird et al. (1960) and Edwards et al. (1979)). The film height remains constant and the velocity profile across the film becomes parabolic in the fully developed region. The friction and heat transfer coefficients become constant in this region.

The analysis of developing flow when a film is introduced at its equilibrium height is also available in the literature. Faghri and Payvar (1979) presented numerical results for laminar flow of a thin liquid film down a vertical wall. Both uniformly heated and isothermal surface conditions were considered. The effects of evaporation and gas absorption on the free surface were also considered in addition to the simple case of

heating, where the free surface can be considered to be adiabatic. Their results compared reasonably well with the available experimental data.

A film falling under the influence of gravity ceases to be laminar and constant in thickness when the flow rate is high (Re > 50). Waves tend to appear on the surface and the flow becomes turbulent as the flow rate is increased. A number of theoretical as well as experimental studies have been performed to understand the flow in wavy-laminar and turbulent regions. Seban and Faghri (1978) reviewed the experimental data and correlations to find the amount of heat transfer augmentation due to surface waves by comparing with results for constant film thickness. Even though the nature of the waves could not be identified in general, the heat transfer enhancement due to waves appeared to be significant. The study covered the cases of heating, evaporation and gas absorption and identified the nature of the augmentation peculiar to each of these cases. In a later study, Faghri and Seban (1981) presented a theoretical analysis of wavy flow assuming a sinusoidal form of the wave. A numerical treatment of turbulent flow was presented by Seban and Faghri (1976) for three different turbulence models. The numerical and asymptotic solutions were compared with their own data as well as previous experiments by Chun and Seban (1971). In all these numerical heat transfer studies related to falling films, the height of the free surface was assumed to be constant at its equilibrium value except for the wavy flow where a sinusoidal form of the wave was assumed.

The radial spreading of a liquid film over a horizontal plate is also an interesting free surface problem. Watson (1964) presented results of

analytical and experimental studies of the radial spread of a liquid jet impinging on a horizontal plane for laminar and turbulent flows. By using the boundary layer approximations for the governing equations, analytical solutions were derived using a similarity transformation along with the Pohlhausen integral method. The analysis covered the regions where the boundary layer thickness is less than the film height and where the film is totally engulfed by the boundary layer. The effects of the gravitational pressure gradient was discussed. The possibility of a hydraulic jump in such a flow was also anticipated. However, the analysis was applicable only to supercritical flow before the jump. An equation was presented to predict the jump height for any given location of the jump. The agreement between the experimental data and the analysis was satisfactory. In this study, the fluid, plate, and the surroundings were maintained at the same temperature and no heat transfer was present.

Another area of thin film research is the spreading of a film under the action of a centrifugal force as seen in a rotating system. Sparrow and Gregg (1959) developed an analytical solution for condensation of saturated vapor on a rotating surface. The complete Navier-Stokes and energy equations were simplified to a set of ordinary differential equations by using a similarity transformation and then integrated numerically. Their results gave the condensate layer thickness and the heat transfer coefficient along with temperature and velocity profiles. Later, Butuzov and Rifert (1972) performed experiments to verify the solution of Sparrow and Gregg (1959). In a more recent study, Butuzov and Rifert (1973) presented experimental as well as theoretical results for the reverse problem of film evaporation from a rotating disk.

In all of the previous studies concerning thin liquid films, the investigators have tried to develop analytical models or have taken experimental data. Some of these models are quite approximate in nature and do not bring out the finer details of the flow field. A numerical finite-difference solution was attempted only for a falling film flow where thickness is uniform and known ahead of time. In general, a free surface flow is difficult to solve by the finite-difference method since the surface geometry changes along the path of the flow, is unknown ahead of time and cannot be fitted in a regular Cartesian or cylindrical coordinate system. Moreover, none of the studies mentioned above considered the flow under a reduced or zero gravity, which is expected to be different from the flow under normal gravity. A proper understanding of such flows is essential in the design of space-based cooling systems.

In a very recent study, Rahman et al. (1989a) (described in section III of this report) have developed a finite-difference solution method applicable for fluid mechanics of thin film flows under zero and normal gravity. A body-fitted coordinate system was used where the free surface was approximated by a curve and iterated for the best possible solution. The present study is a continuation of that work where an analysis of the heat transfer to a thin film is given. In addition to numerical heat transfer results, the present study includes an approximate theoretical analysis using the Pohlhausen integral method. The results illustrate the effects of gravity on the transport for both plane and radial flows.

4.3 MATHEMATICAL MODEL

The flow configurations considered in the present investigation are

shown in Fig. 4.1. They can be broadly classified into three groups according to the presence and orientation of the gravitational body force:

(1) Falling film along a vertical wall

(2) Film flow under zero gravity

(3) Film flow along a horizontal plate in the presence of gravity.

The three possible orientations with respect to gravity are denoted by 1, 2, and 3. Moreover, P and R denote plane and radial flows.

The first case is a classical problem where the major driving mechanism is the gravitational body force. This problem is used to check the accuracy of the present numerical scheme. The effects of introducing the film at a height other than the equilibrium height for a given flow rate will be investigated for this case.

For film flow under zero gravity, two problems will be considered:

(2P) Plane film flow under zero gravity

(2R) Radial film flow under zero gravity

In the absence of any gravitational body force, the orientation of the plate becomes immaterial. The flow remains the same whether the plate is vertical, horizontal or inclined. In this case the flow is driven by inertia and viscous forces. In the radially spreading flow, the area available for the film increases downstream and acts as an added mechanism for the reduction of the film velocity.

In the third group, two problems will again be considered according to the flow geometry under consideration:

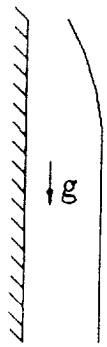

1P. Vertical falling film

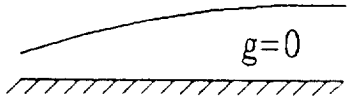

2P. Plane flow at zero gravity

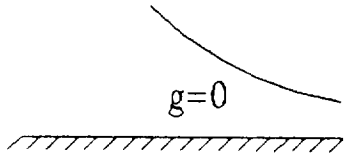

2R. Radial flow at zero gravity

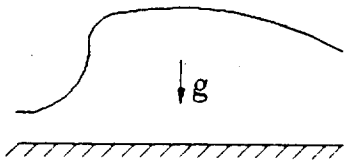

3P. Horizontal plane flow

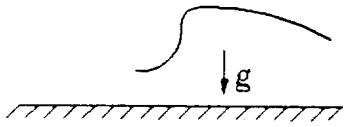

3R. Horizontal radial flow

Fig. 4.1. Flow systems in the present investigation

(3P) Plane film flow along a horizontal plate in the presence of gravity

(3R) Radial film flow along a horizontal plate in the presence of gravity

In the case of horizontal thin film flow where the gravitational body force acts across the thickness of the film, different flow regimes (i.e., supercritical, subcritical or both) may be present according to the local film velocity and height. The transition of the flow from supercritical to subcritical takes place through a hydraulic jump. Since a sudden transition of the flow takes place across a jump, special analytical and computational tools are required to calculate the flow around this singular point.

Two different heating conditions are considered. They are an isothermally heated plate (denoted by symbol T) and a uniform heat flux on the plate (denoted by H). The thermal condition on the free surface may be different depending on whether or not there is any evaporation on that surface. In the case of simple heating with no evaporation, the free surface may be assumed to be adiabatic in nature. In the case of evaporation, the free surface temperature will be the same as the equilibrium temperature corresponding to the ambient vapor pressure. In the present study, the evaporation is assumed to be small so that the loss of fluid at the free surface is negligible compared to the mainstream flow.

The equations governing the conservation of mass, momentum and energy in a thin film may be written as

$$\nabla \cdot \vec{V} = 0 \tag{4.1}$$

$$\rho \frac{D\vec{V}}{Dt} = - \nabla p + \mu \nabla^2 \vec{V} + \rho \vec{g} \tag{4.2}$$

$$\frac{DT}{Dt} = \alpha \nabla^2 T \tag{4.3}$$

The fluid is assumed to be Newtonian with constant properties over the range of temperatures encountered in the problem.

The body-fitted coordinate system is shown in Fig. 4.2. The local coordinate axes are directed along the lines joining the centers of adjacent grid cells. The z-axis is directed in the streamline direction and the y-axis across the thickness of the film. The velocity resolutes in the z- and y- directions are w and v, respectively. The boundary conditions are given by:

at $y = 0$:

$$v = w = 0$$

$$\begin{cases} T = T_w, & \text{for isothermal wall} \\ -K \frac{\partial T}{\partial y} = q_w, & \text{for constant flux wall} \end{cases} \tag{4.4}$$

at $y = \delta$:

$$\tau = 0, \quad v = 0, \quad p = 0$$

$$\begin{cases} q = 0, & \text{for heating} \\ T = T_{sat}, & \text{for evaporation} \end{cases} \tag{4.5}$$

at $z = 0$ or r_{in}:

$$\begin{cases} w = W_{in}, & \text{for uniform entrance} \\ w = 1.5\, W_{in} \left[2\left(\frac{y}{\delta}\right) - \left(\frac{y}{\delta}\right)^2 \right], & \text{for parabolic entrance} \end{cases} \tag{4.6}$$

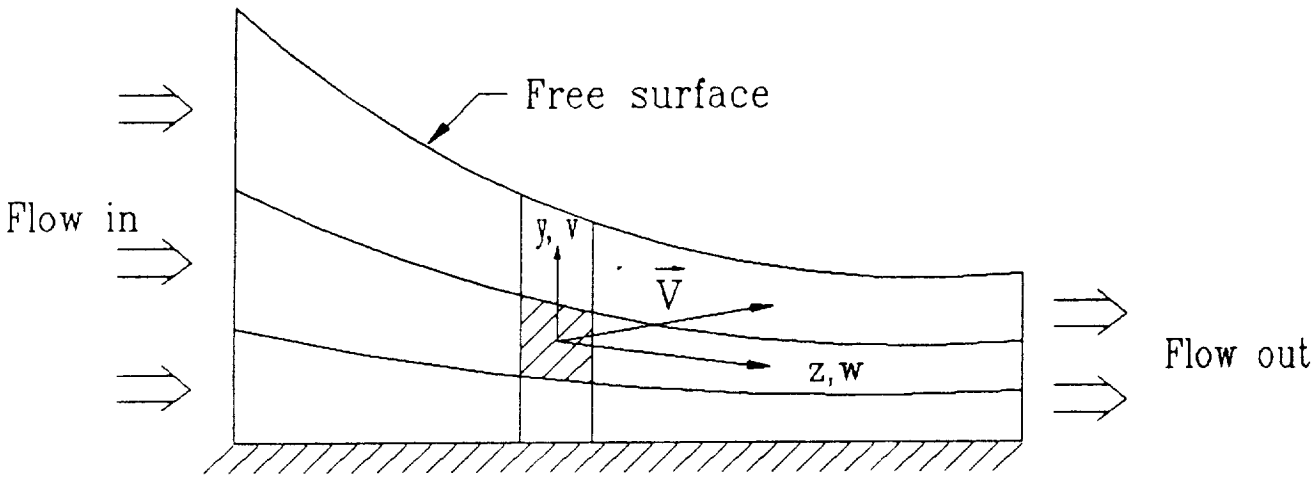

Fig. 4.2. The coordinate system on a grid cell

at $z = L$ or r_{out}: $\frac{\partial w}{\partial z} = 0$

$$\begin{cases} p = 0, \text{ for cases 1 and 2} \\ p = \rho g\,(\delta - y), \text{ for case 3} \end{cases} \qquad (4.7)$$

The difference between the static pressure in the flow and the ambient pressure is denoted by p. On the free surface this quantity has to be zero when the surface tension is negligible.

4.4 NUMERICAL SOLUTION PROCEDURE

The governing conservation equations (4.1 - 4.3) along with the appropriate boundary conditions (4.4 - 4.7) were solved numerically using a finite-difference scheme. Since the free surface geometry cannot be handled very well with a regular rectangular or cylindrical coordinate system, a boundary-fitted curvilinear coordinate system had to be used. In this system, the free surface of the film was used as one of the boundaries of the control volume.

As shown in Fig. 4.2, the local coordinates are defined along lines joining adjacent cell centers. The z-axis was taken in the streamline direction and y-axis in the direction across the film. The resolutes of the velocity vectors in the y- and z-directions are v and w, respectively. In general, the coordinate system was non-orthogonal in nature, i.e., the faces of a grid cell are not orthogonal to each other. The velocity and force vectors were resolved into covariant components and the problem was solved in its physical domain.

The finite-difference equations were derived by the application of the

principle of the conservation of mass, momentum, and energy to the grid cells. The transport processes for each cell are convection and diffusion. The mass flux across a cell boundary was computed exactly from the scalar product of the velocity vector and the vector representing the area of the cell face. Note that this can be written out in terms of velocity resolutes and geometrical factors including angles between cell faces. In the calculation of convection across a cell face, special attention was given to the change of the orientation of the coordinate axes from cell to cell and the curvature of a cell face. This resulted in extra terms in the calculation of convection. However, the representation of convection was exact and did not involve any approximation due to the non-orthogonality of the grids.

The calculation of diffusion was somewhat more complicated than convection. The diffusion flux was calculated assuming the coordinate system to be locally orthogonal. This neglected the effects of cell curvature and non-orthogonal orientation. However, the effects were small in the thin film calculation since the flow is convection dominated, particularly when the film entered the control volume with a reasonably high velocity.

The relative importance of convection and diffusion at each cell was determined from the magnitude of the local Peclet number. A hybrid difference scheme demonstrated by Patankar (1980) was used. The calculation of the momentum source due to the pressure gradient and that due to the gravitational body force could be accomplished without any approximation for non-orthogonality.

The grid generation was achieved in two steps. First, the grid cells were formed by algebraic interpolation between the boundary points. This provided an approximately equal volume for each control cell. The boundaries for the interior cells were then smoothed to make the cell faces more orthogonal to each other. This operation resulted in a better representation of diffusion in the flow field and more accurate computations. A more elaborate discussion of the numerical formulation is presented in Rahman et al. (1989a) (or section III of this report) and the methodology used here is similar to the work by Galea and Markatos (1987) where a body-fitted coordinate system was used to predict fire development in an aircraft.

The number of grids in the z-y plane was determined from a series of computations with different grid sizes. For radial flow, it was found that the free surface height along with other computed quantities do not change any further if the computational mesh is refined beyond 50 x 25 grids in z-y direction. For plane flow 40 x 20 grids in the z-y plane was found to be adequate, which precisely predicted the friction and heat transfer coefficients and the velocity profile in a falling film system. Therefore, all of the computations were carried out using 40 x 20 grids for plane flow and 50 x 25 grids for radial flow.

The flow field was solved by using the SIMPLEST algorithm as discussed by Spalding (1980). One special feature of this algorithm is that in the discretized form of the momentum equation, the convection terms are lumped together with the source term. This results in a faster convergence for some flow conditions. The algorithm works in an iterative manner where the

continuity equation is transformed and used as a pressure correction equation. The computation starts by guessing a pressure field. This is used to determine the velocity components from their corresponding momentum equations. The modified continuity equation is then used to determine the amount of pressure correction. The guessed pressure, the amount of pressure correction and the solution corresponding to the momentum equations are then assembled together to give the flow rate and pressure field for that step. The new pressure serves as a guess for the next step. In each step, once the velocity components are known, the temperature field is determined by solving the energy equation (4.3). Since temperature is a scalar quantity and its equation is linear, the computation of temperature is less involved than the velocity components. The solution proceeds until the normalized residual for each equation was approximately 10^{-6}. In the free surface flow discussed here, both the zero-shear condition and the p = 0 condition at the free surface need to be satisfied. These two conditions cannot be simultaneously given at a boundary with the existing program. On the other hand, the free surface geometry, which is unknown in the problem has to be given before solving the flow field by a finite-difference method. To avoid this difficulty, an iteration scheme has been adapted as described below.

(a) Guess a free surface height distribution.

(b) Solve the flow and temperature fields completely for that height using the zero-shear condition on the free surface boundary.

(c) Find the pressure distribution on the free surface and calculate its deviation from an ideal zero-pressure free surface. The measure used here is the normalized RMS (root-mean-square) error referenced to the initial total head, which is defined as

$$\text{Normalized RMS Error} = \frac{\sqrt{\frac{1}{n}\sum_{k=1}^{n}(p_k)^2}}{\left(\rho\, g\, \delta_{in} + \frac{\rho V_{in}^2}{2}\right)}$$

where p_k is the free surface pressure at the kth node and n is the number of nodes adjacent to the free surface.

(d) Calculate and reduce the RMS error on the free surface by successive alteration of the surface height distribution.

(e) The results with the minimum error give the required final solution.

The optimization technique used here is known as the exhaustive search method. In this method, a general form of the equation representing the free surface is assumed. The equation containes a number of arbitrary parameters depending on the desired degrees of freedom. To start the process, the parameters are given values either from experience (i.e., analytical solution) or just guessed. Only one parameter is changed keeping others constant and the trend of RMS error is observed. That parameter is changed continuously in successive steps until a minimum in RMS error is obtained. The parameter is then kept at its optimum value and the other parameters are changed one by one following the same procedure. Once the first round of optimization is complete, the first parameter is changed again in either direction to see whether the error increases or decreases. The process is continued with the other parameters until an absolute minimum for a combination of parameters is obtained. The accuracy of this process depends somewhat on the assumption of the form of free surface. In the results presented here, hyperbolas with two or more

degrees of freedom were used to represent the computational domain.

The algorithm had to be modified slightly when a jump was present in the flow field, as in the case of horizontal film flow in the presence of gravity. Under some flow conditions, both supercritical and subcritical flows are present, separated by a hydraulic jump. When a jump was present, the two regimes of the flow (i.e., supercritical and subcritical) had to be computed separately and the conditions were matched at the jump interface. It involved the following operations.

(a) Compute the supercritical film height by imposing the inlet film height and velocity and optimizing the free surface height distribution to give the minimum RMS error in the pressure.

(b) Calculate the jump height from the supercritical film height using the equation

$$\frac{\delta_2}{\delta_1} = \frac{1}{2}\left[\sqrt{1 + 9.6\ Fr_1^2} - 1\right] \qquad (4.8)$$

where subscript '1' denotes the supercritical condition before the jump and '2' denotes the condition following the jump. This relationship can be derived from the momentum balance at the jump.

(c) Compute the subcritical film height by imposing the flow rate and exit film height and optimizing the free surface profile to give the minimum RMS error in the pressure.

(d) The supercritical and subcritical flows are calculated for the same flow rate, but for supercritical flow the inlet Froude number is

fixed, whereas for subcritical flow the exit Froude number is fixed.

(e) The intersection of the jump height and the subcritical film height determines the location of the jump. The film height before the jump is given by the supercritical height whereas after the jump the film height is given by the subcritical height.

(f) The heat transfer coefficient for the supercritical part of the flow is determined from the supercritical temperature field, where the inlet temperature to the control volume corresponds to the actual inlet temperature.

(g) The inlet temperature for the subcritical flow is determined from the exit bulk temperature corresponding to the supercritical solution. By imposing this condition, the energy balance at the jump is automatically attained. The heat transfer coefficient in the subcritical flow is then determined from the subcritical temperature field.

In order to increase the computational accuracy for the subcritical and supercritical flows, the flow involving a hydraulic jump was assumed to have a parabolic velocity profile at the inlet.

4.5 RESULTS AND DISCUSSION

4.5.1 Falling Film

The flow and transport in a falling film is a widely studied problem in classical thermo-fluid mechanics. In fully-developed laminar flow, an analytical solution can be derived for the velocity and temperature fields. A numerical computation using the present methodology was performed for a film which has already reached the fully-developed condition at the

entrance. A parabolic velocity profile with the same shape as given by the analytical solution was used for the incoming fluid. The Reynolds number for the film was Re = 12.5. It was found that for the entire domain, the velocity profile across the film remains about the same and the friction coefficient was equal to that of the analytical solution. This shows that the physical characteristics of a fully-developed flow is retained in the numerical solution. The distribution of pressure on the free surface was also computed and the normalized RMS error was determined to be 0.011. This non-zero value of the error may be attributed to the inaccuracy associated with the representation of the flow field by finite-difference equations. This error can be further reduced by more grid points and more degrees of freedom in the free surface equation.

The developing flow of a falling film when introduced at a height equal to, above, or below the equilibrium height was also investigated. The flow conditions are summarized in Table 4.1 and the results are shown in Figs. (4.3 - 4.5). When the film enters the control volume at the equilibrium height, the height remains the same and the development of the velocity profile from uniform to parabolic occurs as the flow moves downstream. When the film enters with a height other than the equilibrium height, a gradual adjustment of height takes place until the flow reaches the equilibrium height. The adjustment of the free surface and the development of the velocity and temperature profiles occur simultaneously in this flow.

For the computation where $\delta_{in} = \delta_{fd}$, the normalized RMS error on the free surface pressure was found to be 0.073. The uniform entrance

Table 4.1: Flow Parameters and Free Surface Geometry

General data: $T_{in} = T_{sat} = 10^{o}C$

$T_{w} = 30^{o}C$, for isothermal wall

$q_{w} = 1000 W/m^{2}$, for constant flux wall

Case 1PA: $\delta_{in} = \delta_{fd}$ (= 0.000595 m)

Re = 50, Pr = 7, L = 0.03 m

Free surface: $\Delta = \Delta_{fd}$

Case 1PB: $\delta_{in} = 1.2\ \delta_{fd}$

Re = 50, Pr = 7, L = 0.03 m

Free surface: $\begin{cases} \Delta = (1 + 7.5\ \xi)^{-0.2}, & \text{for } \xi < 0.2 \\ \Delta = \Delta_{fd}, & \text{for } \xi \geq 0.2 \end{cases}$

Case 1PC: $\delta_{in} = 0.8\ \delta_{fd}$

Re = 50, Pr = 7, L = 0.03 m

Free surface: $\begin{cases} \Delta = (1 + 3000\ \xi)^{0.0445}, & \text{for } \xi < 0.05 \\ \Delta = \Delta_{fd}, & \text{for } \xi \geq 0.05 \end{cases}$

Case 2P: $\delta_{in} = 0.000595$ m

Re = 50, Pr = 7, L = 0.03 m

Free surface: $\Delta = (1 + 10\ \xi)^{0.93}$

(Continued on next page)

Case 2R: $\delta_{in} = 0.005$ m,

$Re = 1616$, $Pr = 7$, $r_{in} = 0.0508$ m, $r_{out} = 0.1953$ m

Free surface: $\Delta = (1 + 1.43\ \xi)^{-0.64}$

Case 3PA: $Fr_{in} = 5.7$, $Fr_{out} = 1.0$

$Re = 355$, $Pr = 7$, $L = 0.1445$ m

Free surface:

$$\begin{cases} \Delta = (1 + 1.47\ \xi)^{1.52}, \text{ supercritical} \\ \Delta = 8.42\ [2 - (1.04 + 0.29\ \xi)^{1.5}], \text{ subcritical } (\xi < 1) \end{cases}$$

Case 3PB: $Fr_{in} = 8.6$, $Fr_{out} = 1.0$

$Re = 355$, $Pr = 7$, $L = 0.1445$ m

Free surface:

$$\begin{cases} \Delta = (1 + 1.47\ \xi)^{1.83}, \text{ supercritical} \\ \Delta = 11.11\ [2 - (1.04 + 0.29\ \xi)^{1.5}], \text{ subcritical } (\xi < 1) \end{cases}$$

Case 3RA: $Fr_{in} = 7.4$, $Fr_{out} = 1.0$

$Re_{in} = 202$, $Pr = 7$, $r_{in} = 0.0639$ m, $r_{out} = 0.1953$ m

Free surface:

$$\begin{cases} \Delta = (1 + 2.05\ \xi)^{2.2}, \text{ supercritical} \\ \Delta = 8.51\ [2 - (1.04 + 0.37\ \xi)^{1.4}], \text{ subcritical } (\xi < 1) \end{cases}$$

Case 3RB: $Fr_{in} = 11.0$, $Fr_{out} = 1.0$

$Re_{in} = 202$, $Pr = 7$, $r_{in} = 0.0639$ m, $r_{out} = 0.1953$ m

Free surface:

$$\begin{cases} \Delta = (1 + 2.05\ \xi)^{2.7}, \text{ supercritical} \\ \Delta = 11.01\ [2 - (1.04 + 0.37\ \xi)^{1.4}], \text{ subcritical } (\xi < 1) \end{cases}$$

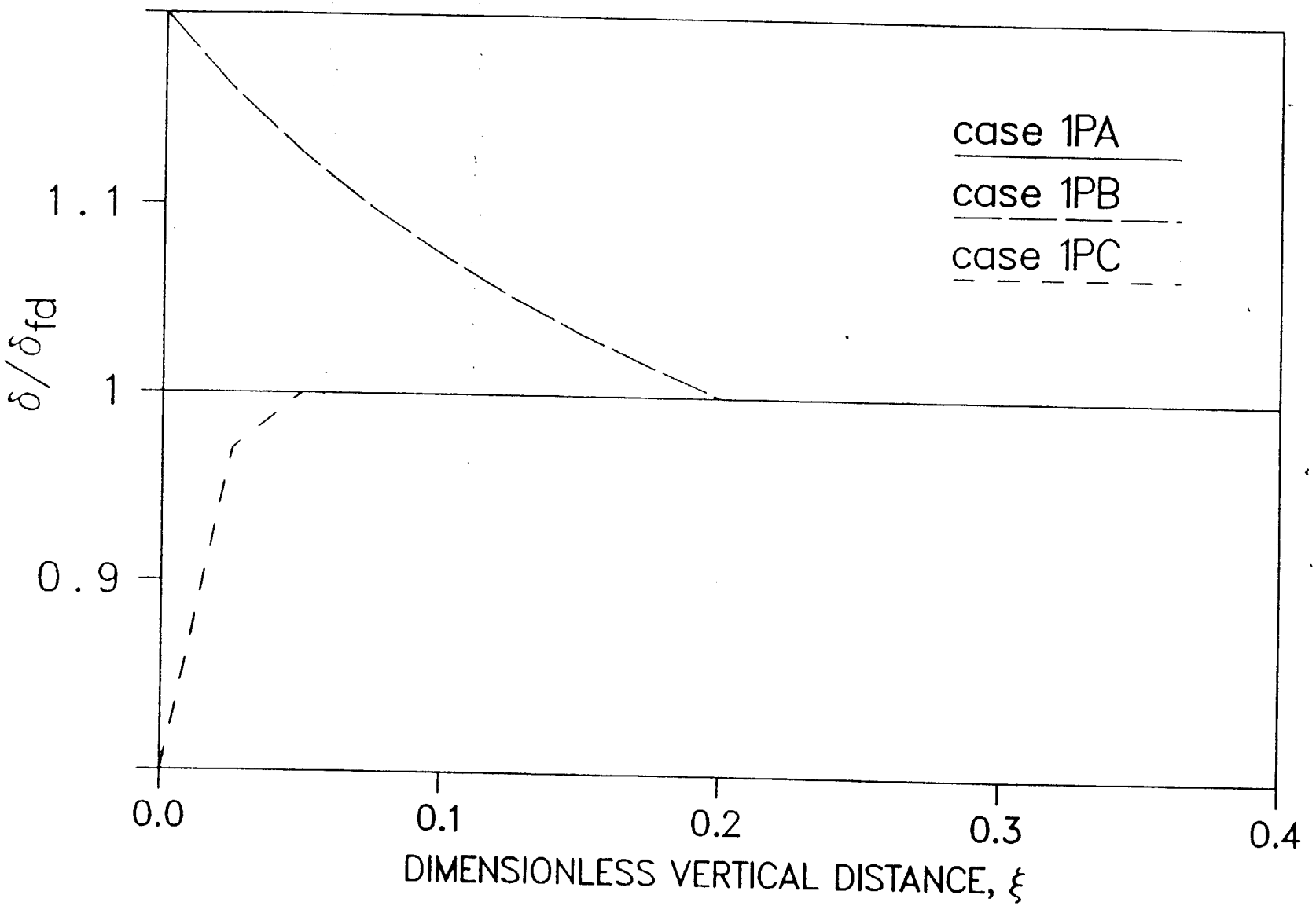

Fig. 4.3 Film height in a developing falling film flow

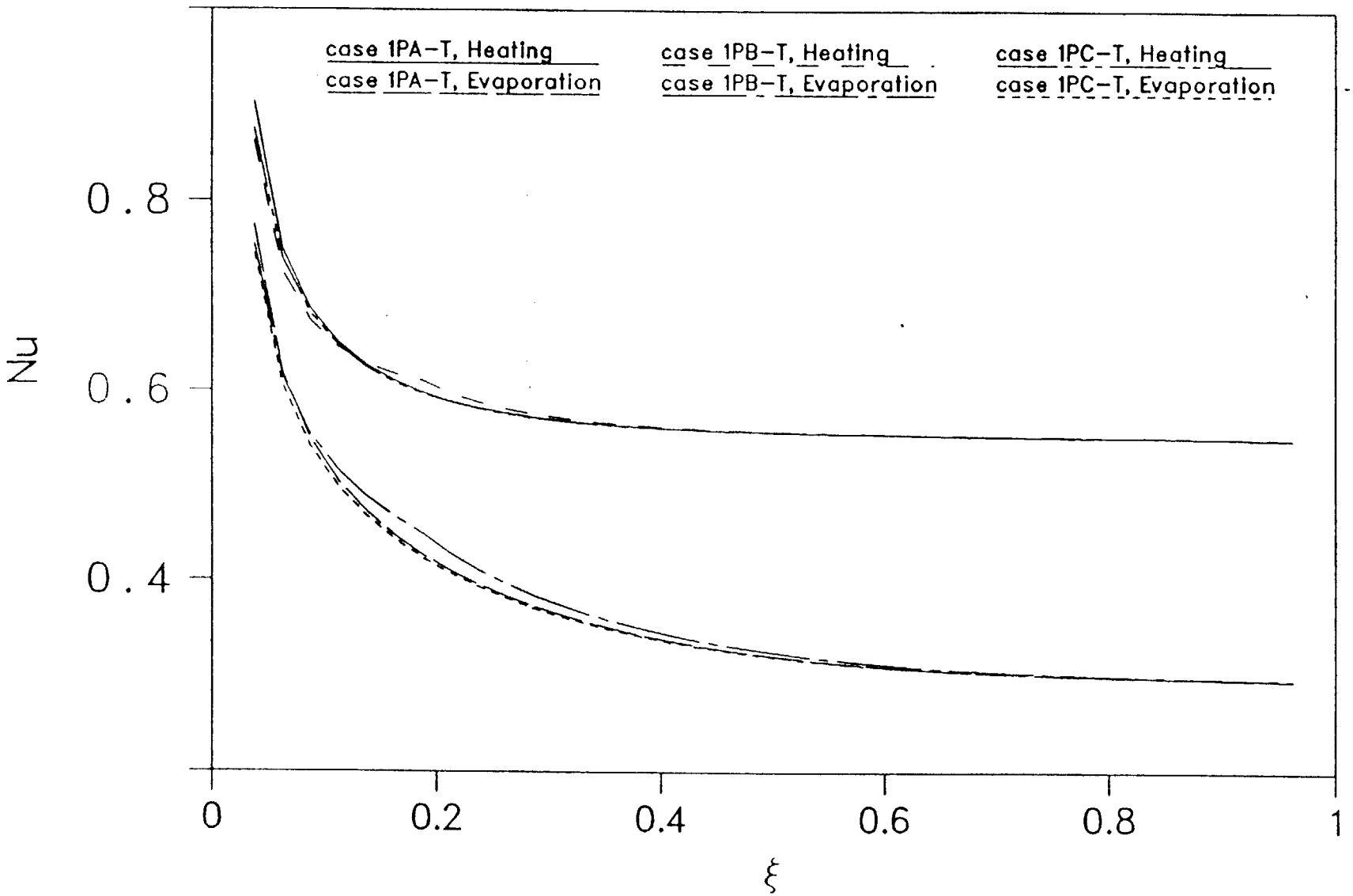

Fig. 4.4 Nusselt number in falling film flow adjacent to an isothermal surface

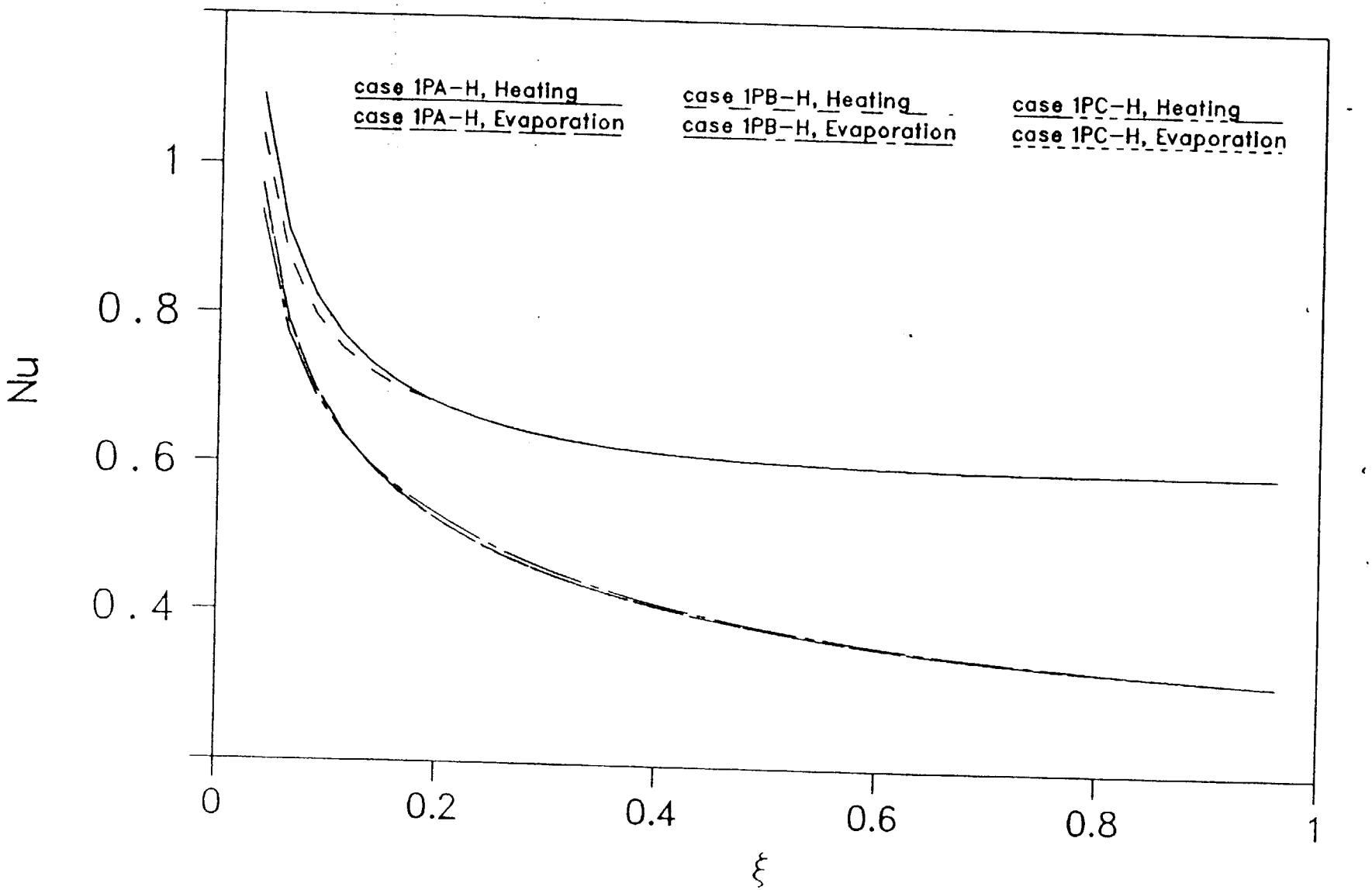

Fig. 4.5 Nusselt number in falling film flow adjacent to a uniformly heated surface

condition has a higher RMS error than the parabolic entrance since a developing flow region is present where the pressure has to conform with the flow development. An error of this order may be acceptable for a free surface computation since no variation of height is expected to take place when a film is introduced at the equilibrium height. In addition to obtaining the height distribution with the minimum error, the normalized RMS error corresponding to the optimum free surface profile does not exceed a limit of 0.1. The distance required for flow development was found to be about five times the film thickness in this case. A flow is defined to be fully-developed when the wall shear stress is within 2 percent of the final equilibrium value. This definition is similar to that given by Kays and Crawford (1980) for developing flow in closed conduits.

The distance required for the development of the temperature profile was found to be somewhat larger than the flow field. For an isothermally heated wall, the heat transfer coefficient reached within 2 percent of its final equilibrium value at about $20\delta_{fd}$ for heating and $40\delta_{fd}$ when evaporation was present on the free surface. In the case of evaporation, the fluid was assumed to enter the control volume at its saturation temperature. A flow with a uniformly heated wall required a somewhat longer entry length, which were $25\delta_{fd}$ and $45\delta_{fd}$ for heating and evaporation, respectively. It can be noticed that pure heating has a smaller entrance length than that of evaporation. In both cases, the heat transfer coefficient is very high near the entrance and reduces downstream. Since heating has a higher heat transfer coefficient, it requires a smaller length for development than the length required for evaporation. It is also worth mentioning that the definition of the heat transfer coefficient

is different in the two cases as given by

$$h = \begin{cases} q_w\ (T_w - T_b), \text{ for heating} \\ q_w\ (T_w - T_{sat}), \text{ for evaporation} \end{cases} \qquad (4.9)$$

Figure 4.3 shows the variation of the film height along the plate. The adjustment of the film height takes places for a length of approximately $10\delta_{fd}$ when the film is introduced at a height of 20 percent more than the equilibrium height. In this situation the velocity profile also becomes fully-developed at the same location. A film introduced at a height of 20 percent lower than the equilibrium is found to take a shorter distance for the adjustment of the free surface and the velocity profile.

The variation of the Nusselt number along the length of the film are shown in Figs. 4.4 and 4.5 for isothermal and uniformly heated surface conditions, respectively. The Nusselt number here has been defined as

$$Nu = \frac{h}{K} \left(\frac{\nu^2}{g} \right)^{1/3} \qquad (4.10)$$

This definition is more widely used in falling film literature where $(\nu^2/g)^{1/3}$ has been used as a length scale. Another way of defining the Nusselt number is in terms of the film thickness as given by

$$Nu^* = \frac{h\delta}{K} \qquad (4.11)$$

This is more universal and applicable for zero gravity flows which will be discussed in a subsequent section.

In all cases, the Nusselt number is very high near the entrance. This is because the thermal boundary layer starts developing from the entrance point on the plate. It decreases downstream and eventually attains an asymptotic value when the flow is fully developed. The distribution for $\delta_{in} = \delta_{fd}$ and $\delta_{in} = 0.8\ \delta_{fd}$ coincide with each other and differ by a small amount from the distribution for $\delta_{in} = 1.2\delta_{fd}$. A smaller heat transfer coefficient near the entrance when $\delta_{in} = 1.2\delta_{fd}$ is due to the fact that local film thickness there is larger and offers a greater resistance to heat transfer. Moreover, the average fluid velocity there is smaller for this case. It also appears that the heat transfer coefficient becomes uniform downstream whether the film is introduced at a larger or smaller height than the equilibrium. This is analogous to the previous observation that the film height also attains the equilibrium value after some distance from the inlet. The Nusselt number in terms of film thickness, Nu^*, was also computed. It was found that in the case of evaporation, the Nusselt number asymptotically approaches unity, the value predicted by the analysis of fully developed flow.

4.5.2 Film Flow Under Zero Gravity

In a gravity-free environment, the orientation of the plate becomes immaterial and an identical flow condition is achieved whether the plate is horizontal, vertical, or inclined. A plane flow is first considered where the film is introduced at a height equal to the equilibrium fully-developed flow in a falling film system as discussed in the previous section. The free surface is modeled by assuming a height distribution of the form given in Table 4.1. The constants appearing in this equation are optimum values determined by the minimization of the error of the free surface pressure.

The results are shown in Figs. (4.6-4.8).

Figure 4.6 shows the variation of the film height along the plate, which increases monotonically. In the absence of gravity, the flow is acted on only by viscous and inertial forces. The effect of inertia is maximum at the entrance and decreases downstream. The resistance from the wall acts to slow down the fluid, which results in an increment in the height in order to preserve the continuity of the flow. The variation of the Nusselt number for different boundary conditions for this case are shown in Figs. 4.7 and 4.8. The shape of the curves appear to be similar for pure heating and evaporation, but differ somewhat between the isothermally heated and the uniform heat flux surface conditions.

The Nusselt number considered here is Nu^*, which depends on two parameters, namely, the film height and the heat transfer coefficient. As expected in any developing flow, the heat transfer coefficient is maximum at the entrance and decreases downstream. The film height, however, has an opposite trend. The net result is the variation presented in Figs. 4.7 and 4.8. The sudden drop of the Nusselt number near the entrance is due to the rapid change of the heat transfer coefficient as the thermal boundary layer develops from the leading edge at the entrance section. Except for this region, the Nusselt number has a small variation if the plate is isothermal. Moreover, when there is evaporation over an isothermal surface, Nu^* is about unity. This shows that heat transfer process becomes primarily diffusive after a short distance from entrance. When the plate is uniformly heated, the Nu^* gradually increases downstream after the sudden drop close to the entrance. In this case, the reduction of the heat

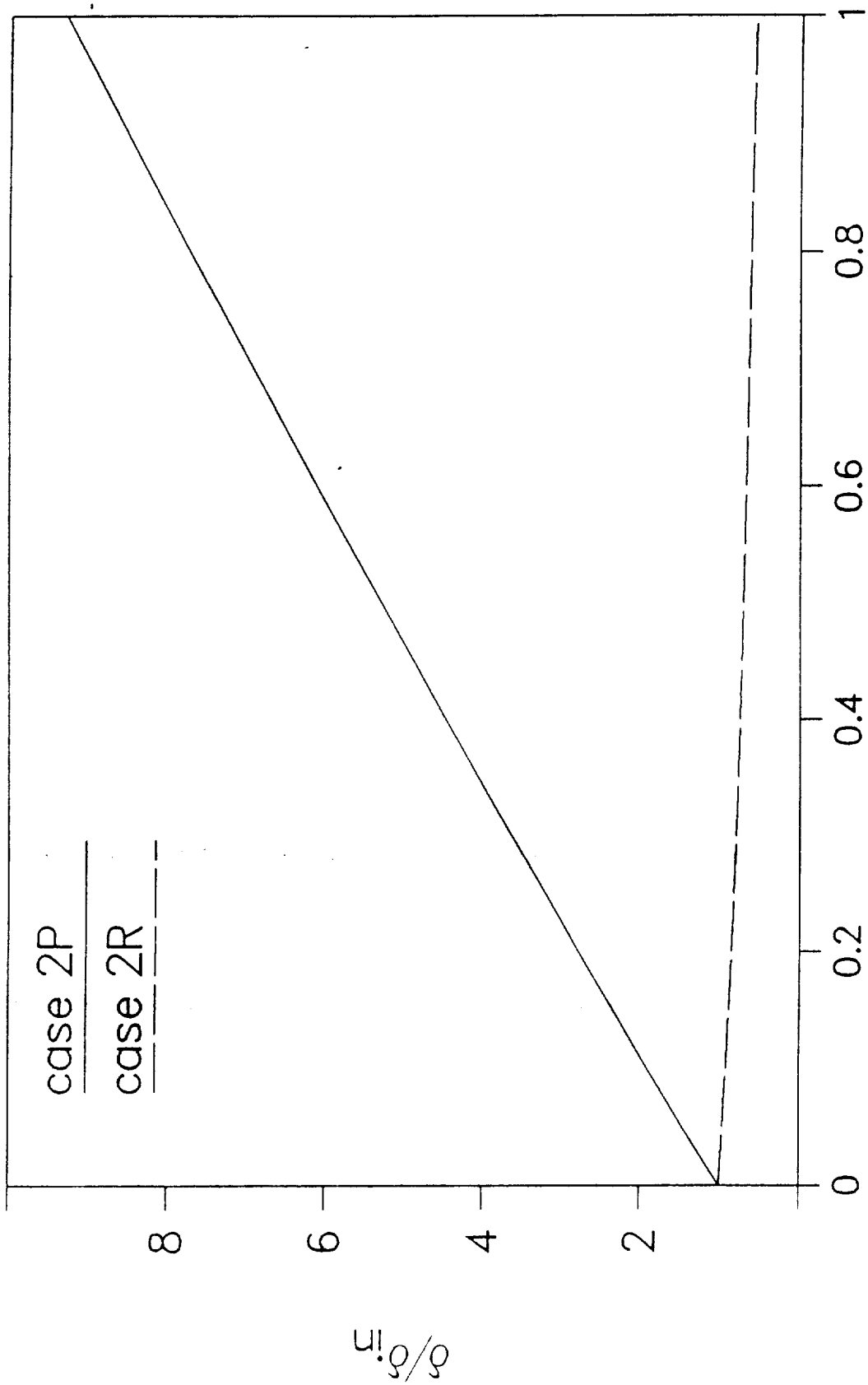

Fig. 4.6 Film height for plane flow and radial flow under zero gravity

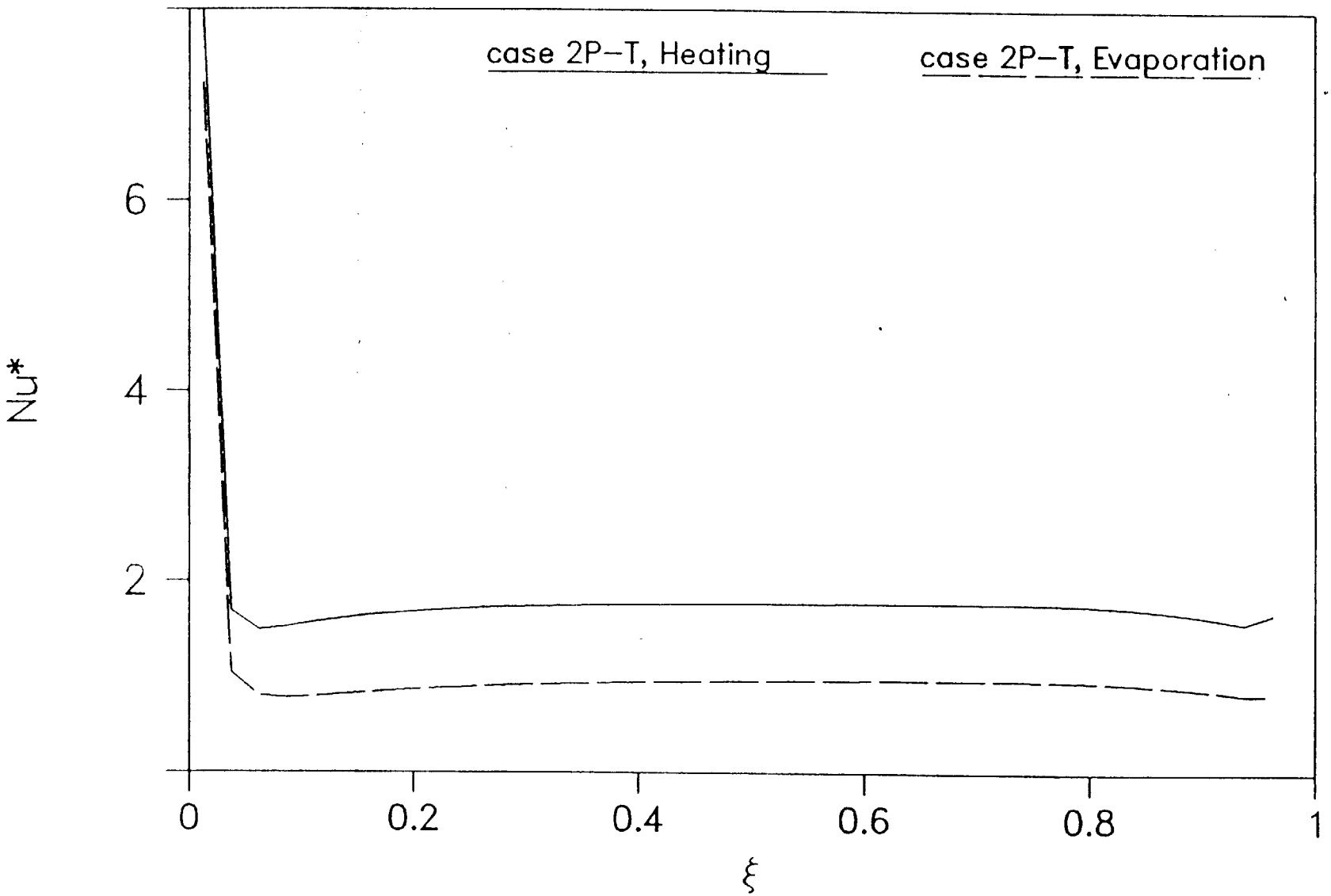

Fig. 4.7 Nusselt number for plane film flow along an isothermal surface under zero gravity

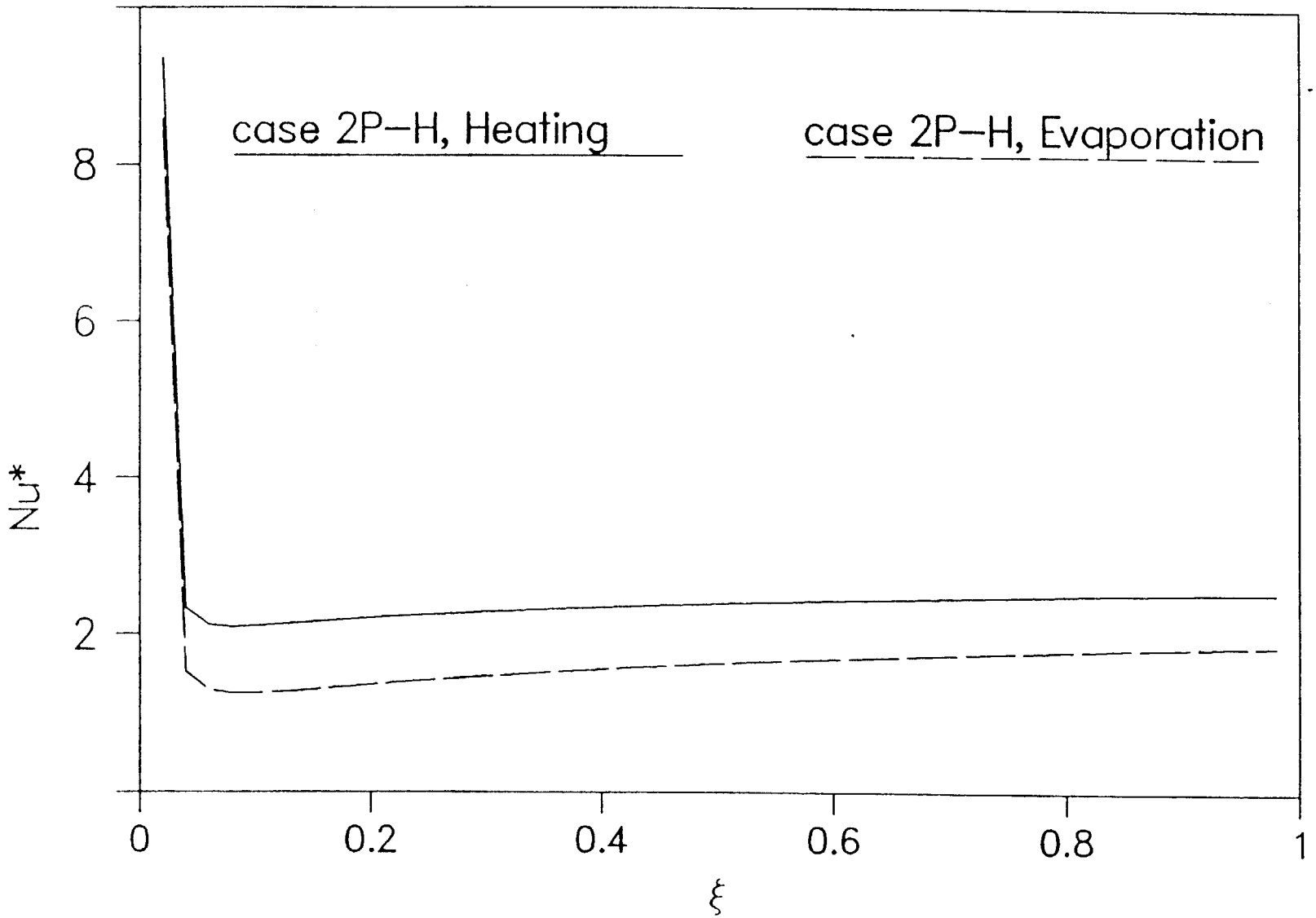

Fig. 4.8 Nusselt number for plane film flow along a constant flux surface under zero gravity

transfer coefficient with distance is relatively smaller and easily overpowered by the increment in the film height. Analogous to the falling film system, the Nusselt number for heating is always found to be larger than that for evaporation.

The situation where a fluid is introduced at the center of a circular plate and spreads uniformly in all radial directions is now considered. In a radially spreading flow, the area available for the fluid increases downstream and acts as an added mechanism to control the film height and the associated transport phenomena. Since spreading tends to reduce the film thickness and friction tends to increase it, the height of the film may increase or decrease downstream depending on the flow rate and inlet height. The behavior of the flow may be characterized by the inlet Reynolds number. The optimum film height distribution for $Re_{in} = 404$ is given in Table 4.1 and is graphically shown in Fig. 4.6. For this particular flow condition, the film height decreases monotonically downstream.

The Nusselt number variations for radial flow considered here are shown in Figs. 4.9 and 4.10. Analogous to the plane flow case, there is a sudden drop of Nu^* close to the entrance. For a uniformly heated surface, the Nusselt number keeps decreasing downstream for the heating and evaporation situations. In most developing flows, the heat transfer coefficient is maximum at the entrance and decreases with the growth of thermal boundary layer. In this case, the film height also decreases downstream, so this trend in the Nusselt number is expected. For an isothermal surface, however, the Nusselt number drops to a minimum at an

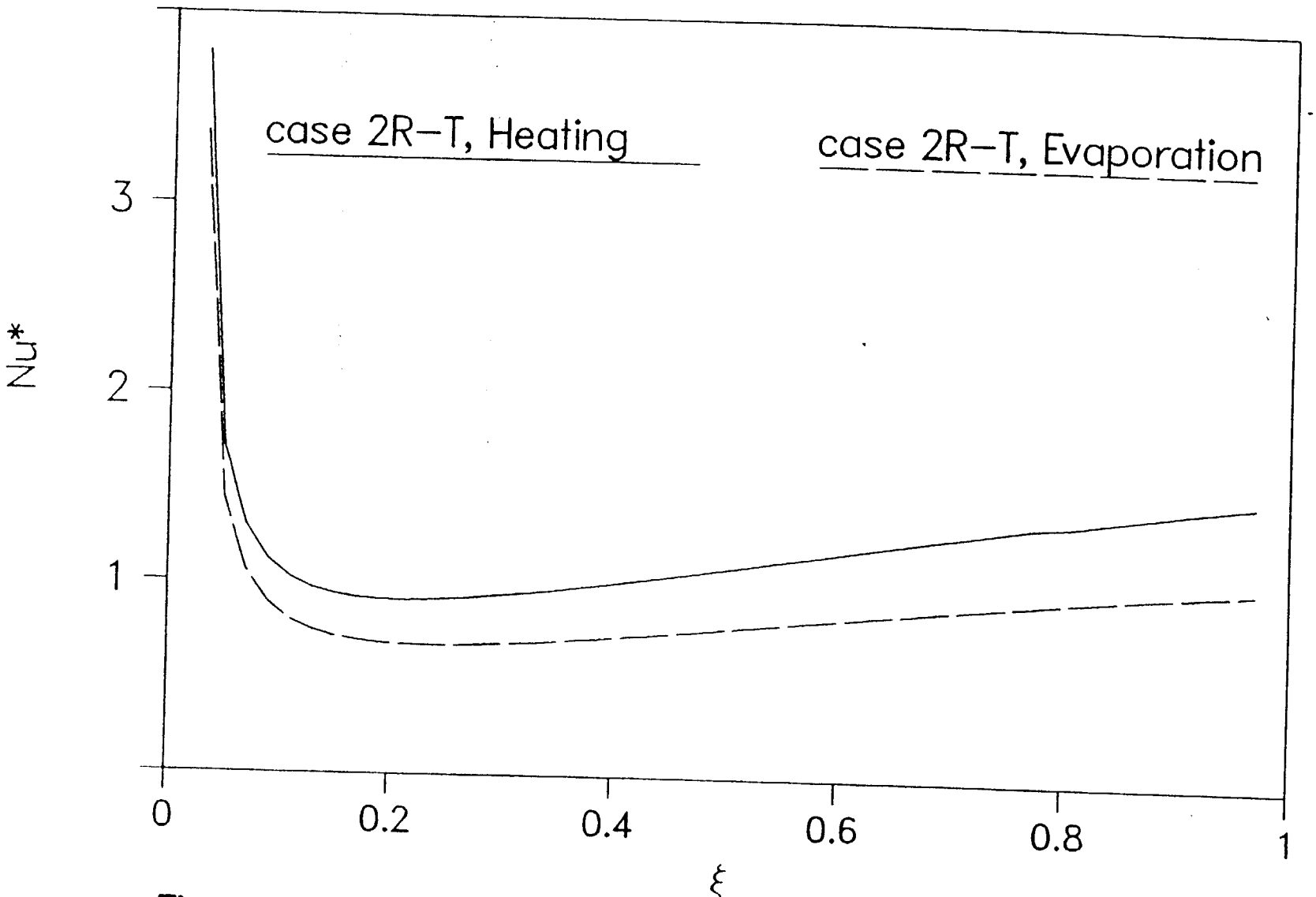

Fig. 4.9 Nusselt number for radial flow along an isothermal surface under zero gravity

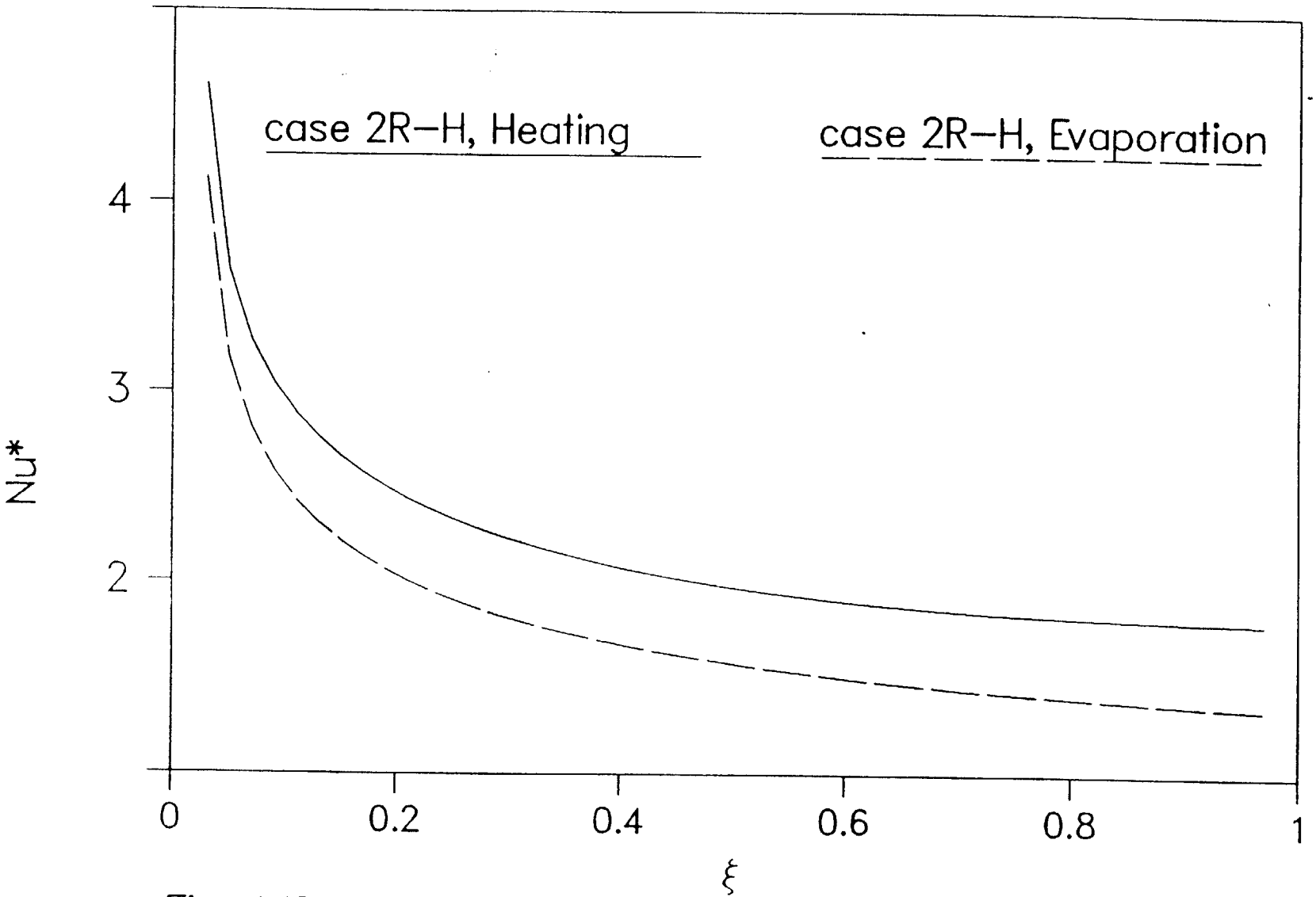

Fig. 4.10 Nusselt number for radial flow along a uniformly heated surface under zero gravity

intermediate location on the plate and then gradually increases as the flow moves further downstream. This trend also indicates that, for an isothermal surface, the heat transfer coefficient has to have a minimum at an intermediate location on the plate. In the results of the heat transfer coefficient, it was found that a minimum is indeed present for both isothermal and uniformly heated surfaces. This phenomenon can be explained by the fact that in a radially spreading flow with the rapid reduction of the film thickness, the thermal boundary layer engulfs the entire film downstream from entrance for a moderate Prandtl number fluid considered here. Therefore, with a further reduction of film thickness, the thermal boundary layer thickness also decreases and results in a reduction of the resistance to heat transfer from the wall to the fluid.

It is also worth mentioning that for both plane and radial flows at zero gravity, the flow field never came to an equilibrium fully-developed condition. The velocity profile across the film thickness, however, appears to be parabolic at most locations of the flow.

4.5.3 Horizontal Film Flow in the Presence of Gravity

The flow of a plane film and a radially spreading film were also investigated for a horizontal orientation of the plate where the gravity acts across the thickness of the film instead of in the direction of the main flow. The flow conditions used here and the corresponding free surface height distribution are listed in Table 4.1. Figures (4.11-4.16) present the computational results.

Two different flow regimes are encountered in the case of horizontal

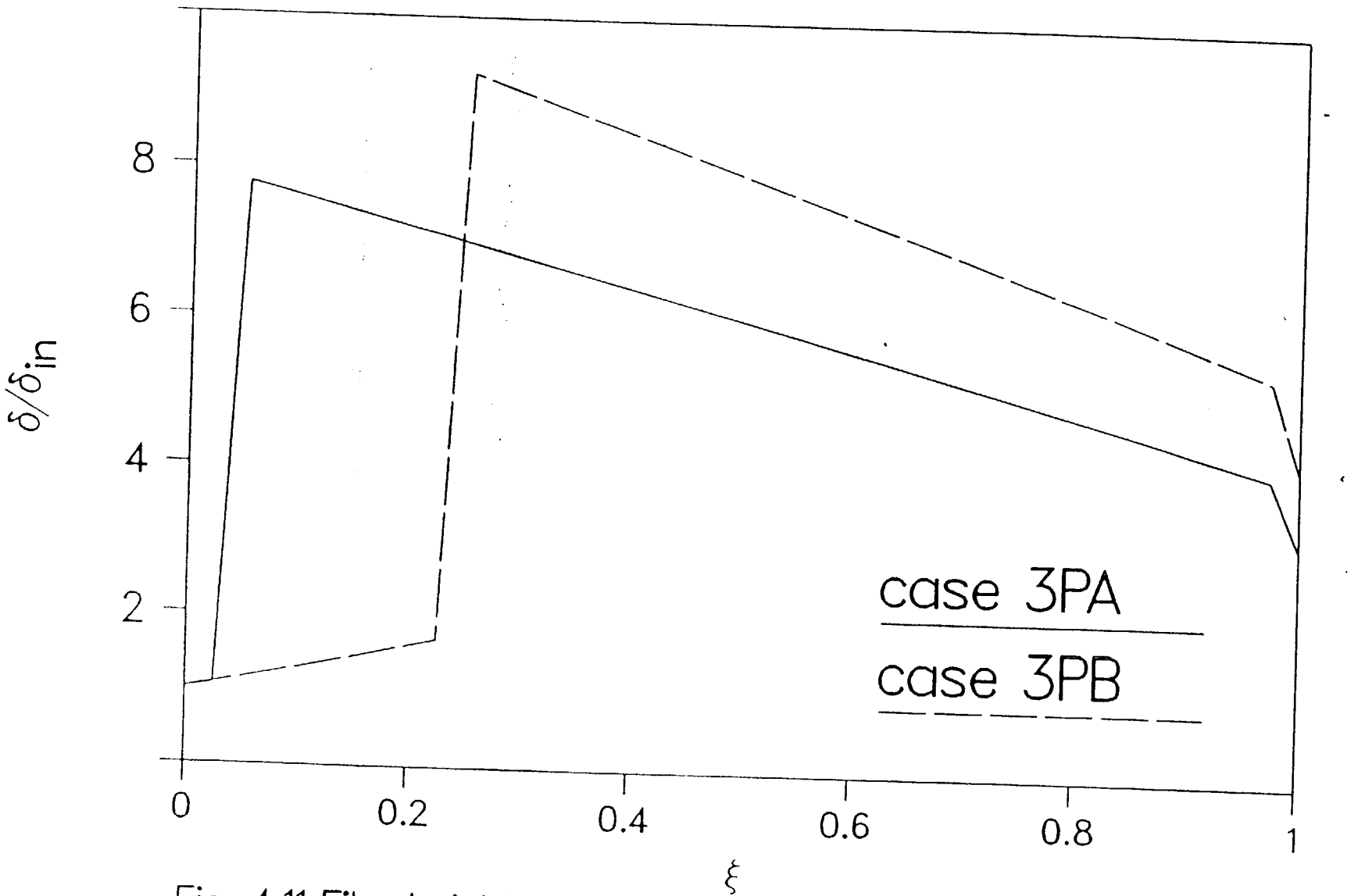

Fig. 4.11 Film height for plane horizontal flow in the presence of gravity

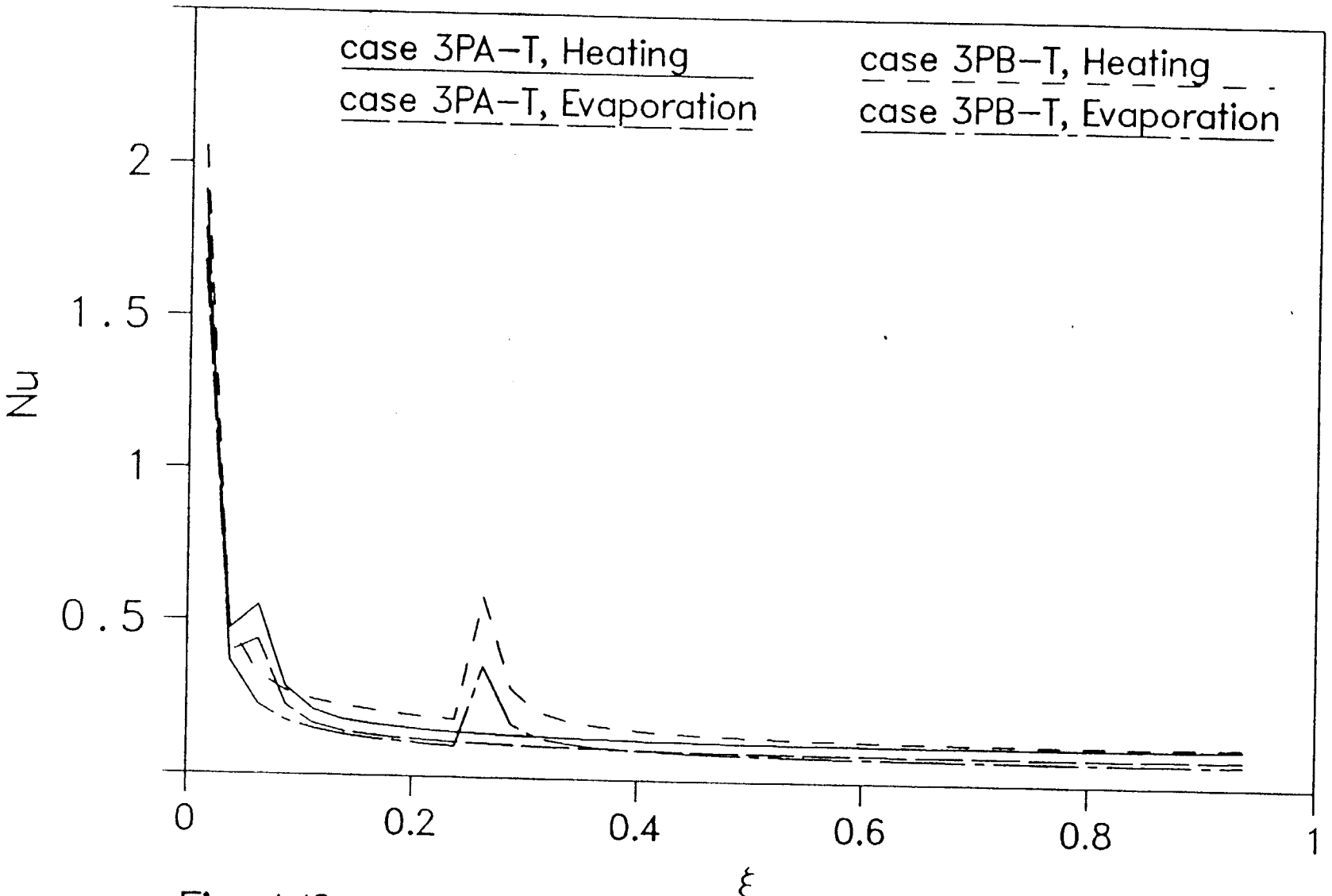

Fig. 4.12 Nusselt number in plane horizontal flow on an isothermal surface

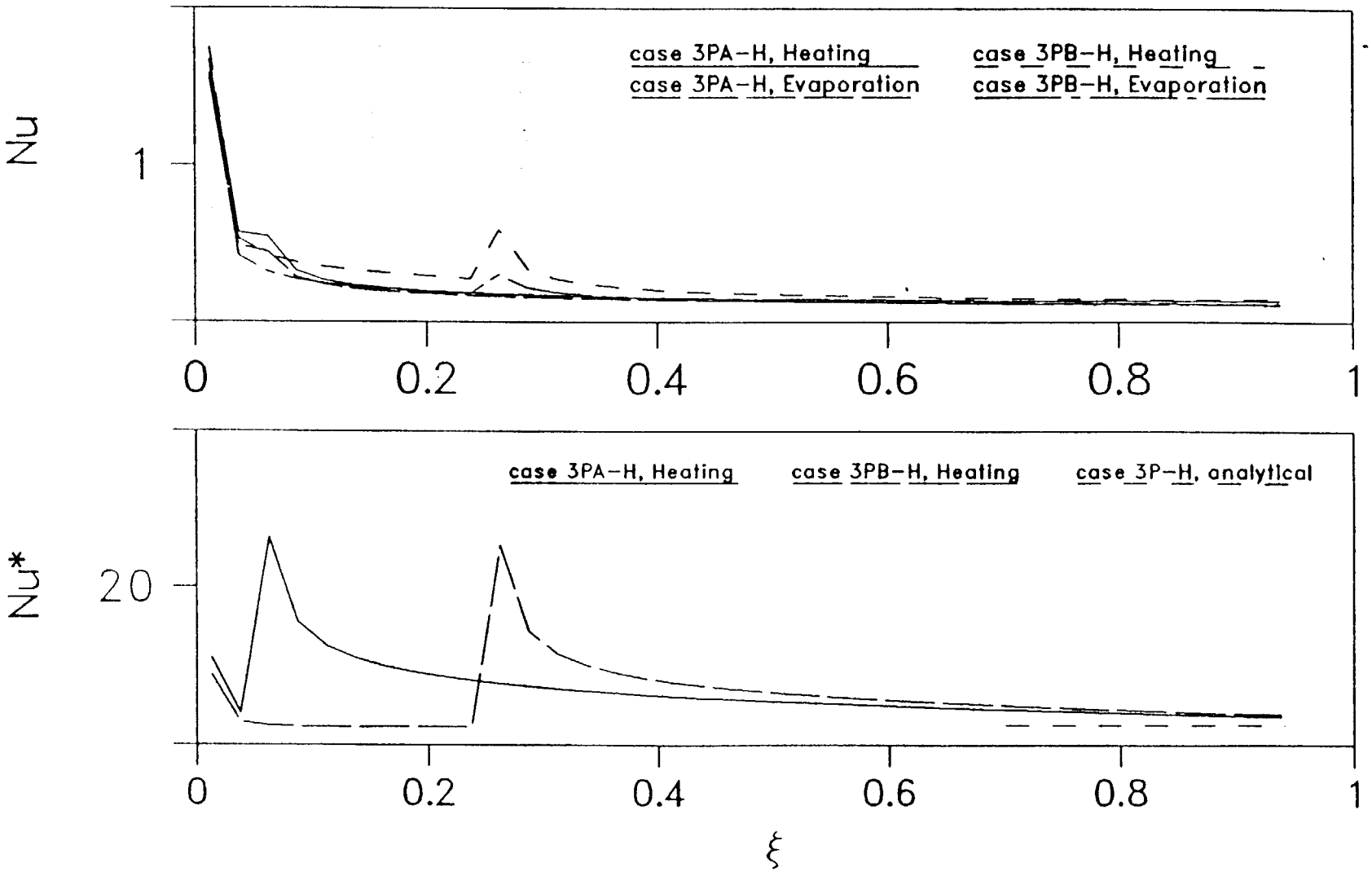

Fig. 4.13 Nusselt number in plane horizontal flow on a uniformly heated surface

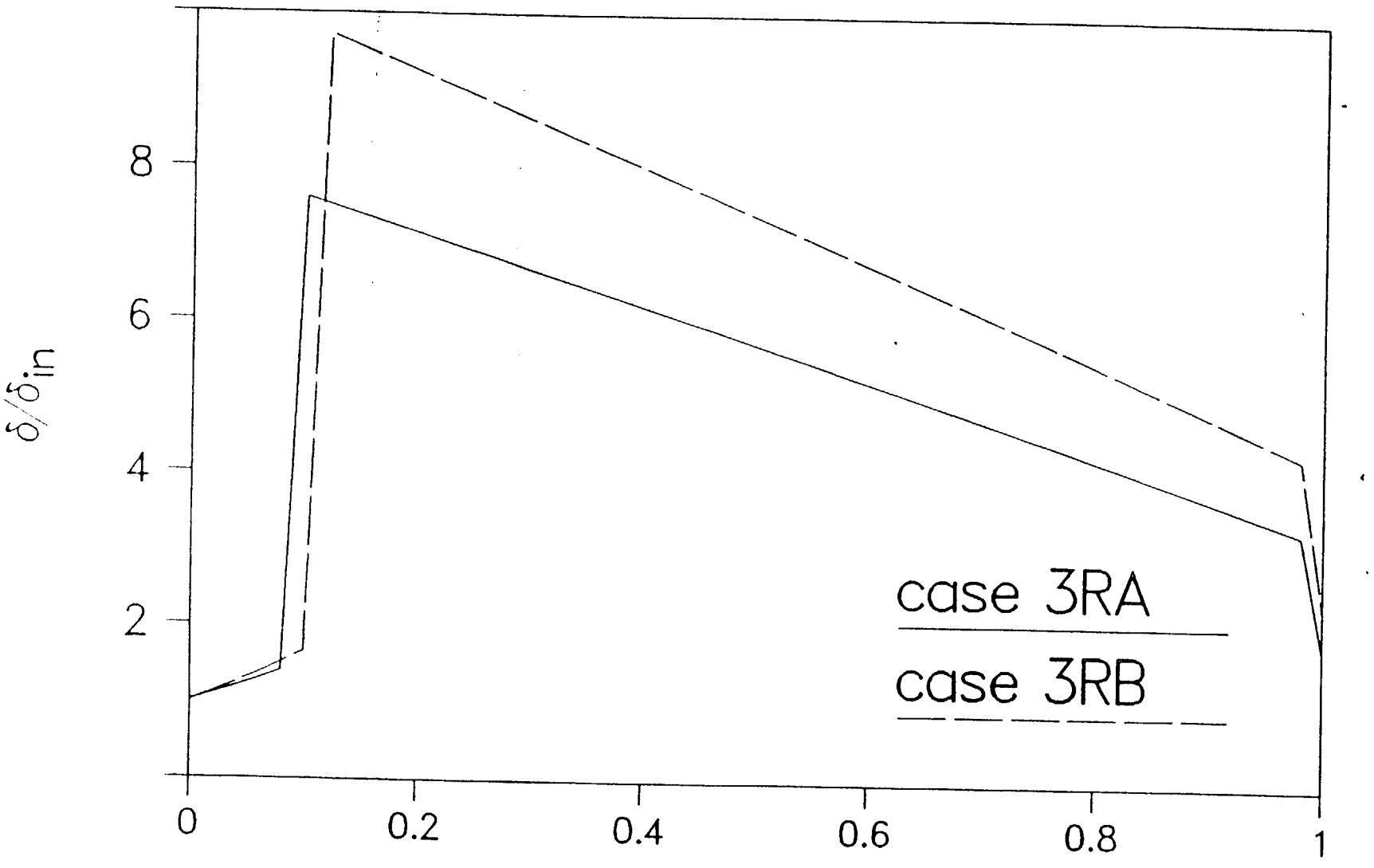

Fig. 4.14 Film height for horizontal radial flow in the presence of gravity

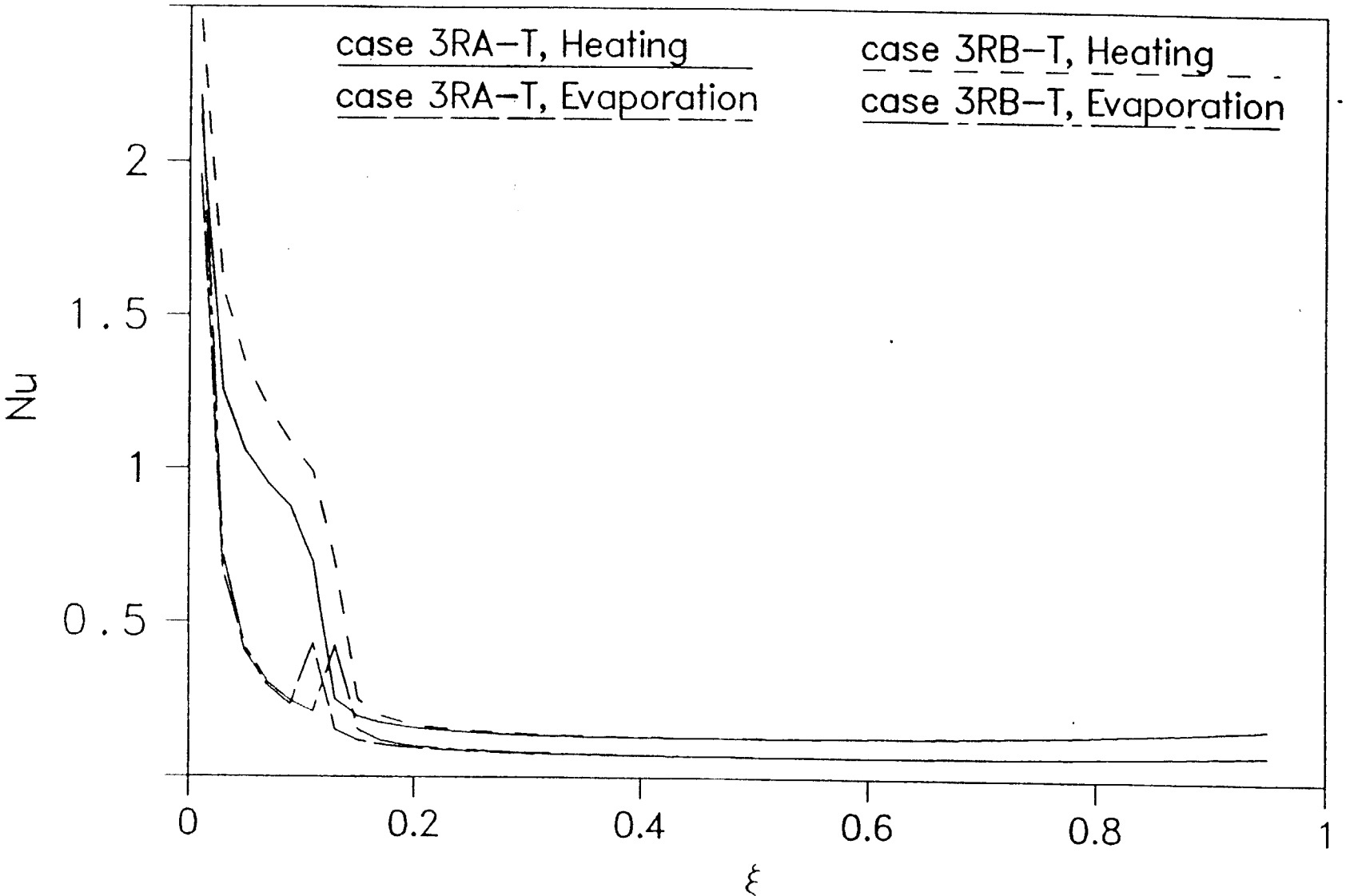

Fig. 4.15 Nusselt number in radial horizontal flow on an isothermal surface

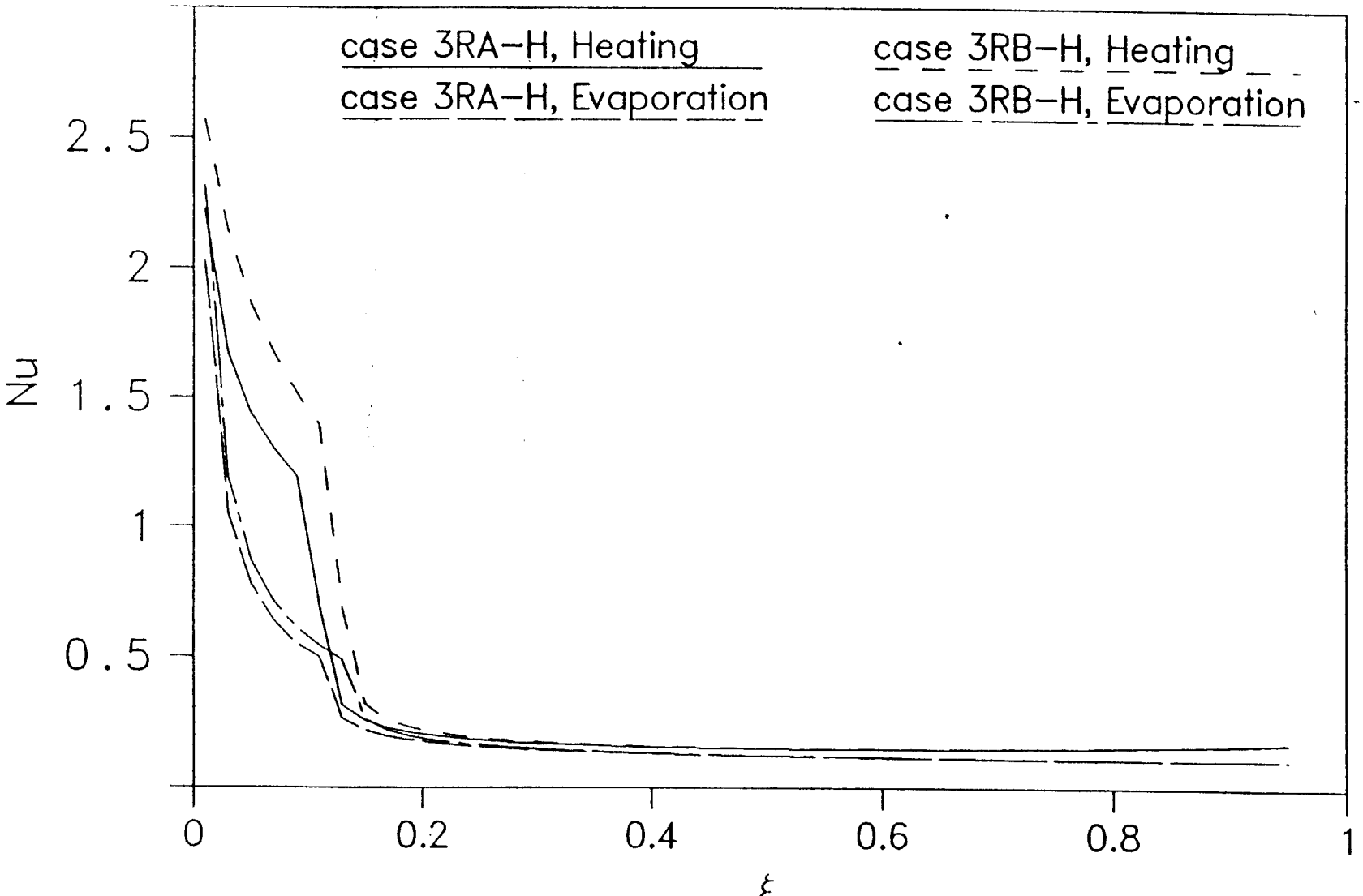

Fig. 4.16 Nusselt number in radial horizontal flow on a uniformly heated surface

flow. The flow is either subcritical or supercritical depending on the Froude number. The subcritical and supercritical flows move towards a critical condition. When the flow enters the control volume as subcritical, it remains subcritical in the entire domain since a transition from subcritical to supercritical is not possible. However, if the flow enters the control volume as supercritical, it may remain supercritical or transform into a subcritical flow depending on the amount of inertial, gravitational, and viscous forces it encounters during the flow. Moreover, if a transition is present it must happen as a jump where the height before and after the jump can be related by the jump condition [equation (4.8)]. In the present investigation, the supercritical and subcritical stems of the flow were computed separately and the location of the jump was determined via the jump condition. In the computation of supercritical flow, the inlet height and Froude number were appropriately satisfied, whereas for subcritical flow, the outlet condition was satisfied.

In Figs. 4.11 and 4.14, it can be noticed that the jump moves downstream with an increase in the inlet Froude number. When the inlet Froude number is high, the flow can maintain its supercritical status for a longer distance. It can also be seen that the propagation of the jump location downstream with an increase in the Froude number is greater for the plane flow than the radial flow. In the case of radial flow, the area increases downstream and causes the flow to slow down. This results in more rapid reduction of the Froude number of the flow. Therefore, in a radial system a jump is likely to be present for a larger range of inlet Froude numbers.

The distribution of the heat transfer coefficient for different thermal boundary conditions are plotted in Figs. 4.12 and 4.13 for plane flow and in Figs. 4.15 and 4.16 for radial flow. It appears that the Nusselt number decreases rapidly close to the entrance as the thermal boundary layer develops. Also, the Nusselt number increases at the location of the jump. A sudden transition of the flow happens at the jump and the thermal boundary layer starts growing again after the jump. In the present study, the heat transfer in the supercritical and subcritical flows were computed separately by matching the temperature and heat flux at the jump location. Therefore, the heat transfer coefficient at the jump location may not be correct. However, the trend that the heat transfer coefficient increases at the jump is consistent with the physical behavior of the flow. Except for the jump and leading edge of the boundary layer, the Nu decreases slowly with the horizontal distance in the supercritical part of the flow and remains approximately constant in the subcritical stem of the flow. In Figs. 4.11 and 4.14, it is noticed that for both plane and radial flows, in supercritical regime the film height increases with distance, whereas in the subcritical regime it decreases with distance. When the height of the free surface increases and the fluid velocity decreases, the heat transfer from the plate to the fluid is expected to decrease downstream. In subcritical flow, however, the fluid velocity itself is smaller and a balance is established between the thickness of the thermal layer and the velocity of the fluid near the wall. Figure 4.13 also shows a plot of Nu^* for the case of heating on a horizontal uniform flux surface. It can be noticed that the increment of Nu^* at the jump is much larger than that corresponding to Nu. Since the film height and heat transfer coefficient both increase at the jump, this rise in Nu^* is quite

expected. The figure also shows that the numerical value of Nu^* approaches the value predicted by theoretical solution.

4.6 CONCLUSIONS

Numerically computed results for heat transfer in a thin liquid film are presented. The flow situations considered are: (a) plane falling film, (b) plane and radial flow under zero gravity and (c) plane and radial flow on a horizontal plate in the presence of gravity. In all cases, two thermal boundary conditions at the wall, namely, isothermal and constant heat flux, and two free surface thermal boundary conditions, namely, adiabatic and evaporative are considered. A curvilinear body-fitted coordinate system is used to handle the irregular flow geometry.

It was found that in a falling film system, an equilibrium fully-developed region is present where the gravitational body force is balanced by the viscous shear force at the wall. The film, whether introduced at the equilibrium height or at a height above or below the equilibrium, eventually attains this fully-developed condition. In the fully developed region, the numerical velocity profile matched exactly with the analytical solution irrespective of the entrance condition of the film. The heat transfer coefficient also attained its fully-developed value and matched well with the analytical solution for all of the entrance conditions.

The length required for the development of the flow was found to be small. Both the free surface height and the velocity profile appeared to arrive at the equilibrium condition within 10 times the equilibrium film

thickness. The development length was found to be relatively larger for heat transfer. A length of 20-25 times the film thickness was required for the development of the equilibrium heat transfer conditions when the film was just heated and no evaporation was present on the free surface. In the presence of evaporation, the development length was even longer, being about 40-45 times the film thickness. There was a small difference in the heat transfer coefficient and the development length for different entry conditions considered here.

For a plane flow under zero gravity, it was found that the film thickness monotonically increases as the flow moves downstream. For an isothermally heated wall, the heat transfer coefficient gradually decreased downstream. The Nu^* in this situation was approximately constant except for regions very close to the entrance. For a uniformly heated wall, the Nu^* reached a minimum at an intermediate location close to the entrance and then increased slowly downstream.

In the case of radial flow under zero gravity, it was found that for the flow rate considered here the film thickness decreases monotonically as it spreads downstream. In this situation, the Nusselt number was also found to decrease monotonically when the plate is uniformly heated. For an isothermal wall, however, the Nusselt number reached a minimum and then slowly increased downstream. This behavior of the heat transfer is related to the thinning of the film and growth of thermal boundary layer in a diffusion-dominated heat transfer process.

For both plane flow and radial flow on a horizontal plate in the

presence of gravity, two different flow regimes (i.e., supercritical and subcritical) are found to be present. The transition of the flow from supercritical to subcritical is accompanied by a hydraulic jump. The location of the jump moves downstream with an increase in the inlet Froude number. The heat transfer coefficient is discontinuous at the jump. In the supercritical region, it decreases gradually downstream, whereas in the subcritical region, it remains approximately uniform at most locations on the plate.

Section V

DEVELOPMENT OF A NEW COMPUTATIONAL METHODOLOGY FOR THE FREE SURFACE FLOWS USING A PERMEABLE WALL

5.1 SUMMARY

A new computational procedure for determining the structure of the free surface flow of a thin liquid film is presented. The iterative method assumes the free surface to be a porous wall where transpiration through the wall is allowed while maintaining it at a constant pressure condition with no shear stress. The Eulerian computation uses a body-fitting coordinate system and an iteration procedure where successive improvements of the free surface geometry is attained from the velocity components on the free surface. In the final iteration, the transpiration becomes negligibly small and thereby the free surface forms a streamline. This new algorithm has the advantage over existing computational methods in that a complete two-dimensional solution of the flow field and heat transfer coefficient can be obtained and can be applied to complex flow problems like a hydraulic jump. The computed results include plane and radial flows involving a hydraulic jump and those flows at zero gravity where no jump can be present. The details of the flow structure, the friction coefficient and the heat transfer coefficient are presented.

5.2 INTRODUCTION

Free surface flows are encountered in a wide variety of physical phenomena. The flow in a river or water channel, the flow of a thin film during evaporation or condensation, and the impingement and spreading of a liquid jet on a solid wall are a few examples. All of these phenomena share a common feature in that the domain of interest has an unknown boundary, the structure of which depends on the flow and the ambient conditions. The complexity of the subject is associated with the knowledge of the free surface location in conjunction with the satisfaction of the appropriate boundary conditions and governing equations. These flows are also heavily influenced by the magnitude and direction of the gravitational body force. The motivation of this study is to develop a comprehensive computational tool for free surface flows both on earth and in space.

Like any external flow adjacent to a solid surface, the viscous effects in a free surface flow are also confined to a boundary layer adjacent to the solid boundary. Therefore, inviscid flow models can be used for flows involving a depth much larger than the boundary layer thickness. The open channel flows in a river fall into this category. An extensive review of numerical methods for potential flow involving a free surface is presented by Yeung (1982). His review covered both linear and non-linear flow problems and three major categories of methods: finite-difference, finite element, and boundary integral equations. The possibility of using a boundary-fitted coordinate system for the representation of free surfaces was also discussed. He concluded that hybrid methods based on matching an interior numerical solution with an exterior analytical representation is the most rational procedure.

The potential flow solution becomes inadequate when viscous effects are important for the flow under consideration, and the solution of the complete Navier-Stokes equation becomes necessary. The numerical techniques presently in use for this class of problems can be divided into three categories, namely, (a) surface-tracking methods, (b) volume-tracking methods and (c) moving-grid methods.

In surface-tracking methods, the interface is specified by an ordered set of imaginary points; between these points its position is approximated by an interpolant, which is usually a piecewise polynomial. This time-dependent interface divides the flow domain into connected regions in which different fluids exist. One of the variants of the surface-tracking method is the height-function method used by Hirt et al. (1975). The free surface was represented by its distance from a fixed surface. This distance (height) changed with time and was governed by an equation expressing the fact that the interface must move with the local flow field. A more commonly used technique to track a surface is to track a string of imaginary particles spread along the density interface. Awn (1979) applied this method for solving flame propagation. Jun (1986) developed an improved version of the interface-tracking method where the location of the interface was solved by a scalar equation. He applied his technique to compute the sloshing motion of a liquid in a tilted tank, as well as the drainage of a pipe under normal and zero gravity conditions.

In a volume-tracking method, the interface is specified by the common boundary of the two regions adjacent to each other. The region is identified by its possession of fluid markers of a particular kind. The

reconstruction of the actual surface shape requires the knowledge of fluid markers in the area under consideration. One of the earliest volume-tracking methods is the Marker and Cell (MAC) method of Harlow and Welch (1965). Marker particles are scattered initially to identify each fluid region in the calculation domain. These particles are transported in a Lagrangian manner along with the fluids. Amsden and Harlow (1970) developed a simplified MAC method called SMAC, which had some mathematical advantages over its predecessor. More recently, Hirt and Nichols (1981) designed a different variation of the volume-tracking method called the fractional volume of fluid (VOF) method, which requires less storage than the MAC method.

In moving-grid methods, the original grid system can be adjusted to approximate the interface. The governing equations are then solved on the new distorted grid by treating the grid points on the density interface as a moving boundary. In this manner, undesirable numerical mixing between the different fluid regions is reduced or avoided. One way to formulate a moving grid algorithm is to use a rectangular Cartesian or cylindrical coordinate system and at each iteration move the interface to the nearest cell wall so that a grid cell always contains one particular fluid. A more improved method, as used by Jun (1985), is to partially block a grid cell to form the interface within a rectangular Cartesian or cylindrical grid cell.

The numerical methods described above have mostly used a Lagrangian approach for solution and dealt primarily with transient problems. Moreover, none of these studies have considered low Reynolds number flow

like a thin film flow where viscous effects are predominant. In a very recent study, Rahman et al. (1989a) (described in section III of this report) developed a new moving-grid method, where a boundary-fitted coordinate system was used and the free surface was taken as one of the boundaries of the computational domain. The primary emphasis of that study was to understand low Reynolds number flows as encountered in a thin film, both in normal and zero gravity environments. Both plane flow over a surface and radially spreading flow were considered. Their results showed that the gravitational body force has a strong influence on the structure of the free surface. A hydraulic jump was found to be present when a gravitational body force acted across the thickness of the film. In that situation, two distinct flow regimes were found to be present, which are supercritical flow upstream from the jump and subcritical flow downstream from the jump. In that study, the free surface was represented by an analytical equation with two or more arbitrary constants. The constants were optimized with an exhaustive search method where the final solution most closely matched the atmospheric (or ambient) pressure distribution on the free surface.

Even though the study by Rahman et al. (1989a) handled most low Reynolds number flows fairly well, difficulties were encountered in handling flows involving a hydraulic jump, where two regions of the flow (supercritical and subcritical) could not be computed as a single-domain problem. The computations were done separately for the two regions and the solutions were matched at the location of the jump. This procedure, even though the location of the jump was correctly predicted, could not account for the details of the flow field and heat transfer behavior in the vicinity of the jump. An effort to remove this drawback led to the

invention of the present algorithm, which can solve the problems involving a hydraulic jump as a single domain problem. It is essential to have this feature in the calculation of thin film flow over a rotating surface, which is one of the motivations for the initiation of the present efforts. It is also found that the present algorithm is more universally applicable to any free surface problem in the presence or absence of a gravitational body force. Unlike any other method presented above, the present procedure assumes the free surface to be a permeable wall through which fluid may leave or enter the control volume depending on the ambient and local static pressures. The location of the surface is improved by successive iterations until penetration through the free surface become negligible.

5.3 GOVERNING EQUATIONS

The present numerical methodology will be tested against a number of steady free surface problems both in normal and zero gravity environments. The problems considered here are schematically shown in Fig. 5.1. They are:

(a) The two-dimensional flow of a plane thin film over a plate, as introduced from a pressurized fluid reservoir in a gravity-free environment.

(b) The radially spreading flow of a thin film over a plate as initiated by an impinging fluid jet or pressurized reservoir at the center of the plate in a gravity-free environment.

(c) The plane flow over a horizontal plate in the presence of gravity where a hydraulic jump is present.

(d) The radially spreading flow over a horizontal plate in the presence of gravity where a hydraulic jump is present in the computation domain.

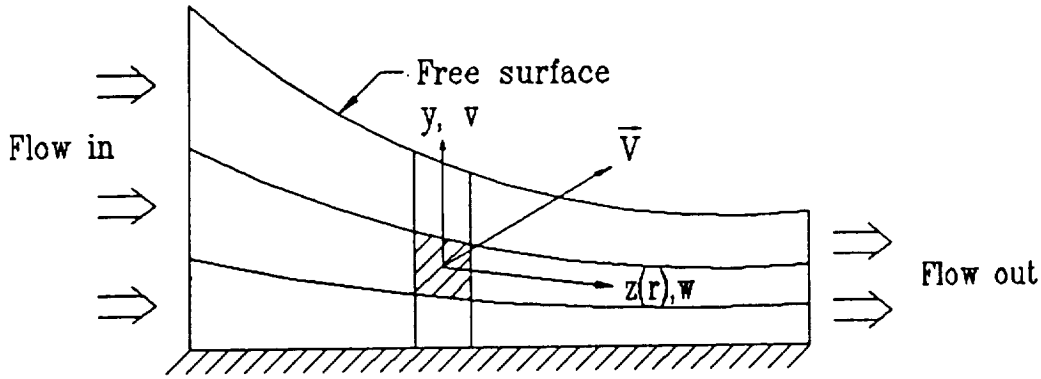

The coordinate system on a grid cell

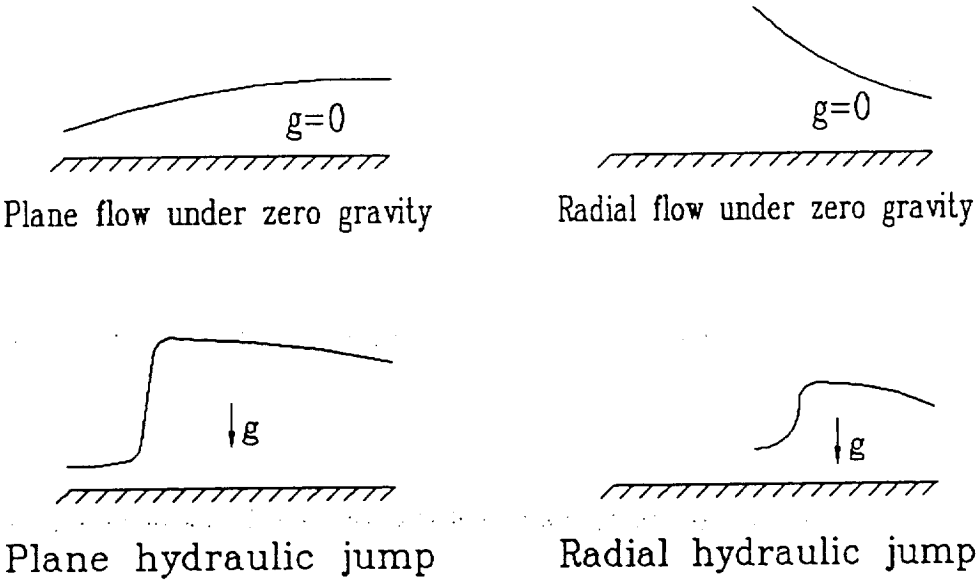

Plane flow under zero gravity

Radial flow under zero gravity

Plane hydraulic jump

Radial hydraulic jump

Fig. 5.1. The coordinate and flow systems in the present investigation

In all of these problems, the heat transfer behavior in the liquid layer will be studied by assuming the solid wall temperature to be higher than the temperature at which liquid enters the control volume. The wall also remains at an isothermal condition for the entire length of the flow. In the case of simple heating with no evaporation, the free surface may be considered to be adiabatic in nature. In the case of evaporation, the free surface remains at an isothermal condition with a temperature equal to the saturation temperature corresponding to the ambient vapor pressure. For the problems considered here, the evaporation is assumed to be small so that the loss of fluid at the free surface is negligible compared to the mainstream flow.

The equations governing the conservation of mass, momentum and energy in a liquid layer involving a Newtonian, constant-property fluid can be written as

$$\nabla \cdot \vec{V} = 0 \tag{5.1}$$

$$\frac{D\vec{V}}{Dt} = -\frac{1}{\rho}\nabla p + \nu\nabla^2 \vec{V} + \vec{g} \tag{5.2}$$

$$\frac{DT}{Dt} = \alpha\nabla^2 T \tag{5.3}$$

Figure 5.1 also shows the coordinate system used here. The local coordinates are directed along the lines joining the centers of the adjacent grid cells. The z-axis is directed along the direction of the mainstream flow and y-axis is directed across the thickness of the film.

The velocity resolutes in the y- and z-directions are v and w, respectively. The boundary conditions for the problems considered here are given by

$$\text{at } y = 0: \qquad v = w = 0, \quad T = T_w \tag{5.4}$$

$$\text{at } y = \delta: \qquad \underline{\tau}.\vec{n} = 0, \quad \underline{\tau}.\vec{t} = 0$$

$$\begin{cases} q = 0, & \text{for heating} \\ T = T_{sat}, & \text{for evaporation} \end{cases} \tag{5.5}$$

$$\text{at } z = 0 \text{ or } r_{in}: \quad w = W_{in}, \text{ for uniform entrance} \tag{5.6}$$

$$\begin{cases} w = 1.5\, W_{in} \left[2 \left(\frac{y}{\delta}\right) - \left(\frac{y}{\delta}\right)^2\right], & \text{for parabolic entrance} \\ v = 0 \end{cases}$$

$$\text{at } z = L \text{ or } r_{out}: \quad \frac{\partial w}{\partial z} = 0, \quad p = \rho g\, (\delta - y) \tag{5.7}$$

$$Fr = 1, \text{ for flows involving a jump}$$

The normal stress condition on the free surface leads to equations balancing the pressure and other stresses including surface tension. Scaling these equations, one can show that, for thin film flow where Re^* and We are large, the pressure on both sides of the free surface must be the same. The quantity p is defined to be the difference between the static pressure in the flow and the ambient pressure. In the absence of any significant surface tension and tangential stress from the ambient fluid, this quantity becomes zero on the free surface. At the outlet end, the pressure gradient is hydrostatic in nature. The local parabolic approximation in numerical computation eliminate any rigorous specification

of v and w at that point.

5.4 NUMERICAL SOLUTION PROCEDURE

A finite-difference numerical scheme was used for the solution of the governing equations (5.1-5.3) along with the appropriate boundary conditions (5.4-5.7) for the different problems considered here. To properly handle the irregular free surface geometry, a curvilinear body-fitted coordinate system was used, where the free surface was taken as a coordinate surface.

The computational domain was divided into a non-uniform mesh where more grid cells were placed at locations where steeper variations of the flow and heat transfer are expected to take place, like the vicinity of a hydraulic jump. The cells were formed by an algebraic interpolation between boundary points. In general, the cell faces were non-orthogonal in nature.

The local coordinates were defined along lines joining the adjacent grid cells as shown in Fig. 5.1. The z-axis is in the streamline direction and the y-axis is across the thickness of the fluid layer. The velocity vectors were resolved into co-variant components and the problem was solved in its physical domain.

The finite-difference equations were derived by the application of the principles of the conservation of mass, momentum and energy to the grid cells. The derivations used ideas similar to those presented by Rahman et al. (1989a) or section III of this report. The hybrid difference scheme,

as demonstrated by Patankar (1980) was also incorporated in the formulation. This basically determined the total contribution (convection and diffusion) to a cell from its neighbors as a function of the cell Peclet number.

The flow field was solved by using the SIMPLEST algorithm as presented by Spalding (1980). One special feature of this algorithm is that in the discretized form of the momentum equation, the convection terms are lumped together with the source term. This results in a faster convergence than its predecessors SIMPLE or SIMPLER as described in Patankar (1980). The SIMPLEST method also works in a iterative manner where the continuity equation is transformed and used as a pressure correction equation. The computation starts by guessing a pressure field. This is used to determine the velocity components from their corresponding momentum equations. The modified continuity equation is then used to determine the amount of pressure correction. The guessed pressure, the amount of pressure correction and the solution corresponding to the momentum equations are then assembled together to give the flow rate and pressure field for that iteration step. The new pressure serves as a guess for the next step. The discretized equations for the velocity components were solved slab-by-slab marching in the z-direction, whereas the pressure and temperature were solved by the whole-field method. The convergence of the solution was monitored by examining the normalized residuals for each equation and by spot-checking values of the pressure, velocity components, and temperature at critical locations in the flow. The computation proceeded until the magnitude for all of the residuals became negligibly small and the spot-checked values attained an invariant condition. The computed results

were also tested for grid independence by systematically varying the number of grids in both the y- and z-directions. A value of 25 grids was found to be adequate in the y-direction, whereas 50 to 150 grids were used in the z-direction for the problems considered here.

In any computational scheme for a free surface flow, the major difficulties encountered are in handling the free surface itself. First, the geometry of the free surface needs to be specified before solving the flow using a finite-difference scheme. On the other hand, the geometry itself is dependent on the flow conditions. Moreover, a number of boundary conditions needs to be satisfied: (a) the free surface is a streamline (the velocity vector on the surface must be tangent to the surface itself at all locations) (b) a zero-shear condition must exist on the surface and (c) in the absence of any significant surface tension, the static pressure of the fluid next to the free surface must be equal to the ambient pressure. All of these conditions are satisfied simultaneously for only the correct location of the free surface, and therefore some of the conditions are violated when an assumed free surface profile is used to initialize the solution process. Thus, one has a choice of which boundary condition he wants to satisfy exactly. In the present algorithm, the boundary conditions (b) and (c) are satisfied exactly, whereas an iteration process is introduced to arrive at condition (a).

It is assumed that the free surface is a permeable wall through which fluid particles may leave or enter depending on the pressure on the two sides of the surface. The ambient pressure is prescribed. An outflow takes place when the static pressure of the fluid inside the control volume

is higher than the ambient pressure, whereas an inflow occurs when the ambient pressure is higher. Since inflow or outflow is permitted, the velocity vector at the surface is no longer aligned with it, so an iterative scheme can be devised to adjust the surface so that a streamline condition on the free surface can be approached. Another criterion to follow is to minimize the loss or gain of fluid through the surface. The scheme works as follows:

(1) Prescribe a free surface height distribution.

(2) Solve the flow field completely for that height using $p = 0$ as the boundary condition on the free surface.

(3) Find the amount of penetration of the fluid through the surface at all locations along the flow.

(4) Calculate the deviation from the zero-penetration condition. The measure used here is the normalized root-mean-square of the penetration.

$$\text{Normalized penetration} = \frac{\sqrt{\frac{1}{n}\sum_{k=1}^{n}(Q_{loss})_k^2}}{Q_{in}}$$

(5) Calculate the new free surface height by adding a correction to the old height. As shown below, the correction is determined from the Cartesian components of the velocity vector on or near the free surface by satisfying the condition that the free surface is a streamline. The method is analogous to the moving height function approach used by Hirt et al. (1975).

(6) Continue iterating until the normalized penetration attains a minimum value.

(7) Once the location of the free surface is determined, solve for both the flow and temperature fields for that surface profile.

The correction in the film height is determined from the penetration rate at the free surface. The velocity component across the film that is associated with the penetration can be estimated to be

$$v_{loss} = v_c - \frac{d\delta}{dz} w_c \tag{5.8}$$

where v_c and w_c are the Cartesian components of the velocity vector at the cell next to the free surface. We need to drive v_{loss} to zero to arrive at the streamline condition on the free surface. Therefore, a new height can be determined as

$$\delta_k^{i+1} = \delta_k^i + (v_{loss}) \frac{\Delta z}{|w_c|} \tag{5.9}$$

A central difference is used to calculate the slope of the free surface from the height in the previous iteration. This resulted in the equation

$$\delta_k^{i+1} = \delta_k^i + \left[(v_c)_k^i - \frac{1}{2\Delta z} (\delta_{k+1}^i - \delta_{k-1}^i) (w_c)_k^i\right] \frac{\Delta z}{|(w_c)_k^i|} \tag{5.10}$$

An alternative formulation for the film height correction was also derived by using the MacCormack predictor-corrector method, as presented by Anderson et al. (1984), which resulted in the formulation:

$$\delta_k^{i+1} = \delta_k^i + \left[\frac{3}{8}\left(\frac{v_c}{w_c}\right)_k^i + \frac{1}{8}\left(\frac{v_c}{w_c}\right)_{k-1}^i\right]\Delta z - \frac{1}{8}\delta_{k+1}^i + \frac{3}{4}\delta_k^i + \frac{3}{8}\delta_{k-1}^i,$$

for $w_c > 0$ (5.11a)

$$\delta_k^{i+1} = \delta_k^i - \left[\frac{5}{8}\left(\frac{v_c}{w_c}\right)_k^i - \frac{1}{8}\left(\frac{v_c}{w_c}\right)_{k-1}^i\right]\Delta z + \frac{3}{8}\delta_{k+1}^i + \frac{3}{4}\delta_k^i - \frac{1}{8}\delta_{k-1}^i,$$

for $w_c < 0$ (5.11b)

The correction scheme needed to be modified slightly at the downstream boundary since only the values on one side of the cell were available. The upstream boundary did not pose any problem since the film height there remained constant. Computations with either equations (5.10) or (5.11) were found to be equally good, and lead to the same final solution.

The procedure required a reasonably good guess of the initial free surface height for uniform convergence within a reasonable number of iterations. Since penetration is allowed on the free surface, a surface profile far from the actual free surface produces outflow on the order of the mainstream flow and leads to divergence. Therefore, an initial guess is limited to a surface which yields penetration smaller in magnitude than the mainstream flow. In the calculations presented here, the start-up solution was calculated using a 'pressure-optimization method' as presented by Rahman et al. (1989a) or section III of this report. Since that method is robust and was available to us, it was used here to obtain faster convergence. However, one may start from an approximate analytical solution given in section VI or the one-dimensional numerical solution presented in section I. However, as expected the convergence time depends on the initial condition. Hence, a crude starting solution may take a

relatively longer period for convergence. The recommended procedure is to use the present method in combination with the 'pressure-optimization method' presented by Rahman et al. (1989a). The former doing the fine tuning on the global variations predicted by the latter.

The correction scheme for the free surface height may require under-relaxation to make the algorithm stable and uniformly convergent. Also, some smoothing may be required to get around fluctuations that are of the same order of the grid size. When the fluctuations were large, a polynomial fit of the new height was used. As used by Hirt et al. (1975), the smoothing of the free surface from one iteration to the next is required to preserve a better continuity of the free surface profile.

In order to dampen out the effects of flow development, a parabolic velocity profile is assumed to be present at the inlet during the iteration procedure. Since penetration through the surface is primarily a function of the pressure and velocity components, and the energy equation is not coupled to the continuity or momentum equations, the flow field is solved first as an isothermal problem during the iterations and the energy equation is solved only when the free surface location is established. This minimizes the computational effort to some extent.

5.5 DISCUSSION OF RESULTS

5.5.1 Film Flows in the Absence of Gravity

We now consider the flow of a thin film in a gravity-free environment. In the absence of any other body or surface force, the flow is acted on only by inertial and viscous forces. Therefore, the orientation of the

solid wall, whether vertical, horizontal or inclined, does not play any role in the behavior of the flow. Both plane and radial flows are considered here. The results are presented in Figs. 5.2-5.6.

The predicted variation of the film height for plane film flow under zero gravity is presented in Fig. 5.2. The Reynolds number for the flow is Re = 50, which is in the laminar flow regime. The properties used are for water at $20^{o}C$ under normal atmospheric conditions. The film height increases monotonically with distance. As the fluid moves downstream, it decelerates due to friction and consequently the height of the film increases to preserve the continuity of the flow. The figure also shows the film height predicted in previous investigations. The previous results for two-dimensional flow using the pressure optimization method is quite close to the present numerical solution. This is expected since both studies preserved the two-dimensional behavior of the flow field, and did not make any approximations to simplify the problem. One constraint on the free surface geometry in the studies of Rahman et al. (1989a) is that the free surface conforms to an algebraic equation with two or three degrees of freedom. This constraint is removed in the present study, where the free surface can conform to the local flow conditions in a more exact fashion. The degree of freedom attained here is the same as the number of grids in the main flow direction. Even though an algebraic equation is easier to use, the discrete representation of the free surface as done here leads to more accurate results. Figure 5.3 shows the distribution of the penetration rate through the free surface. Comparing the amount of flow through the free surface, it was found that the present free surface has about 30% less penetration than the surface predicted by the method in Rahman et al.

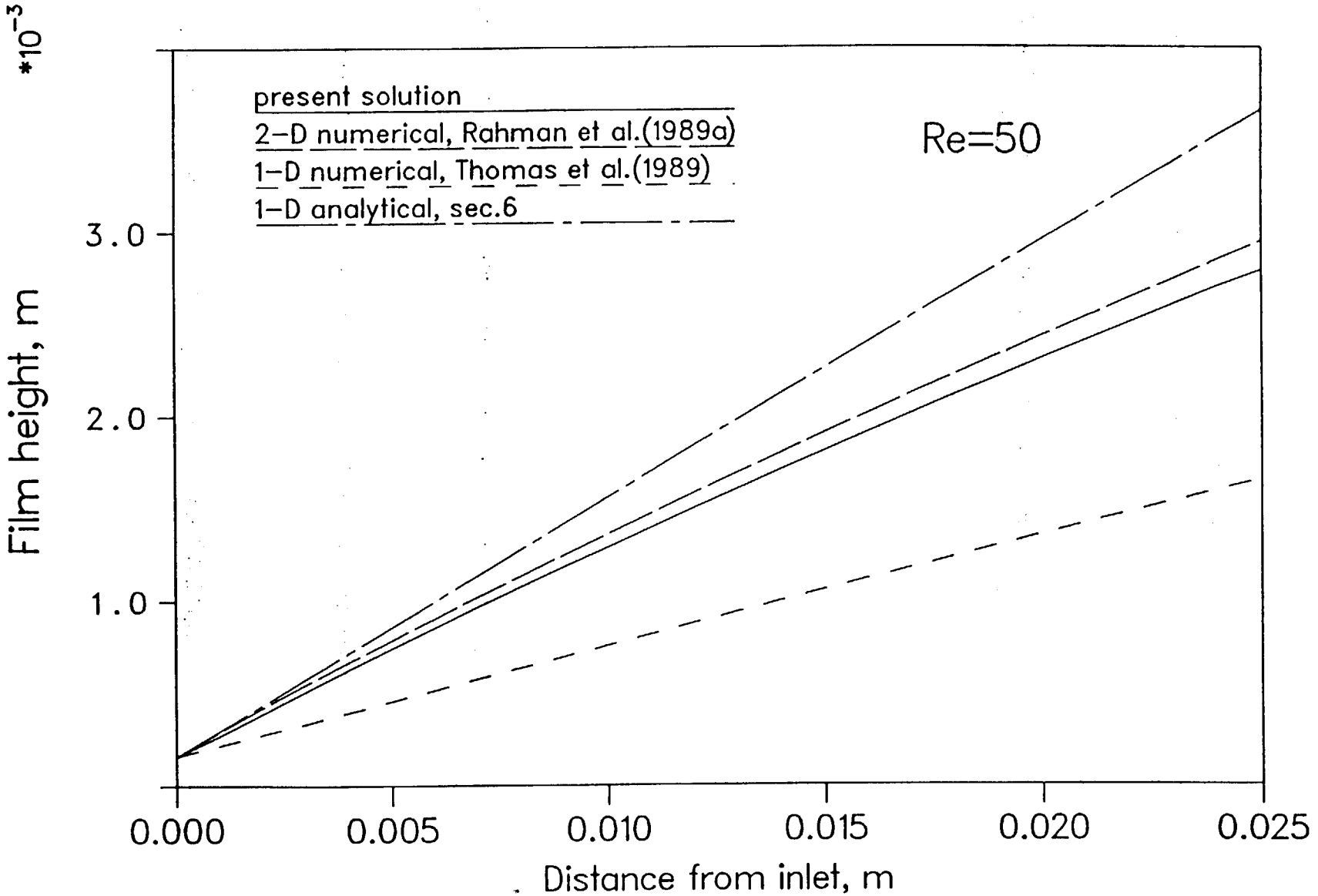

Fig. 5.2 The film height variation for plane flow under zero gravity

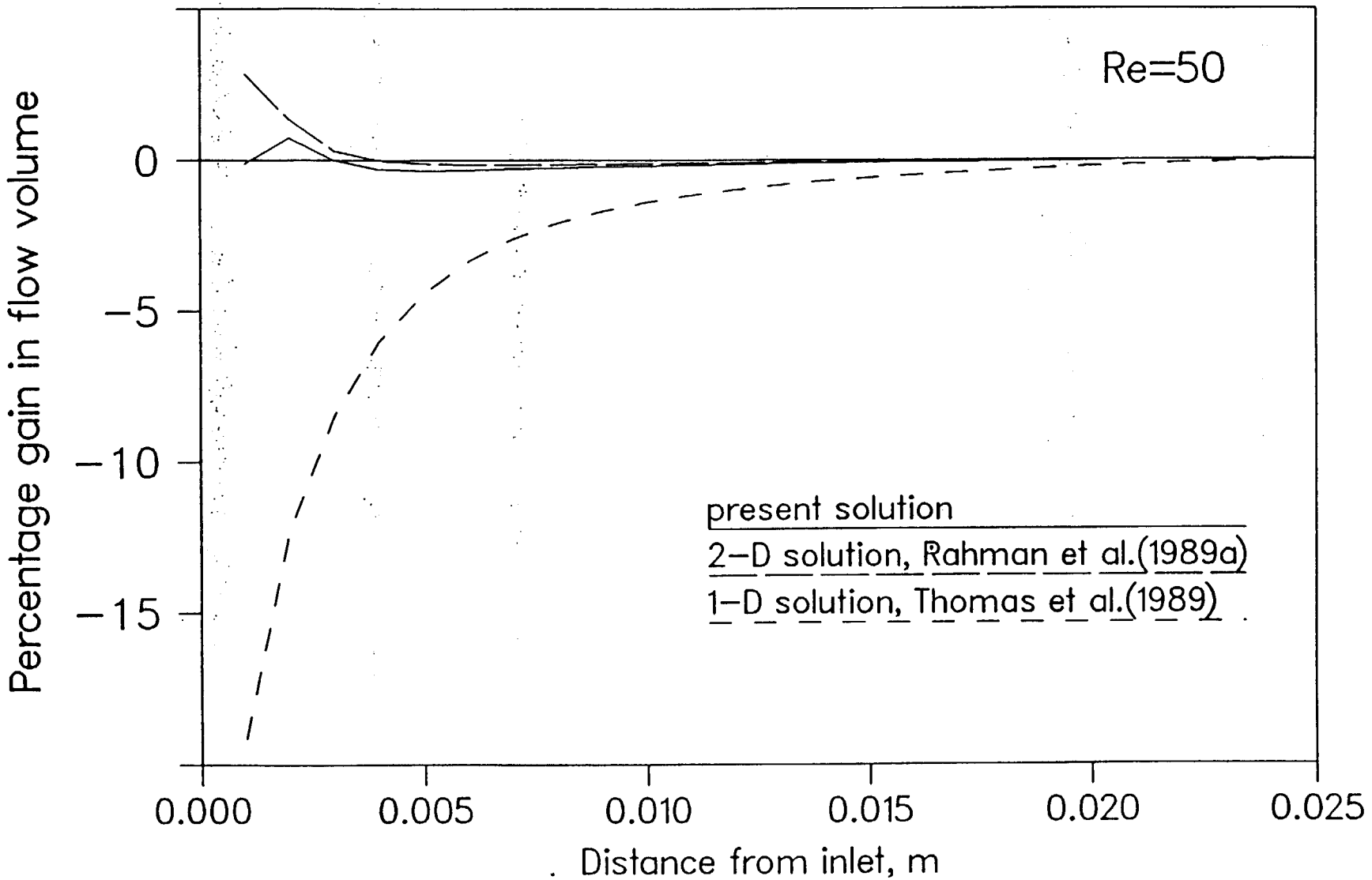

Fig. 5.3 Penetration through the free surface for plane flow under zero gravity

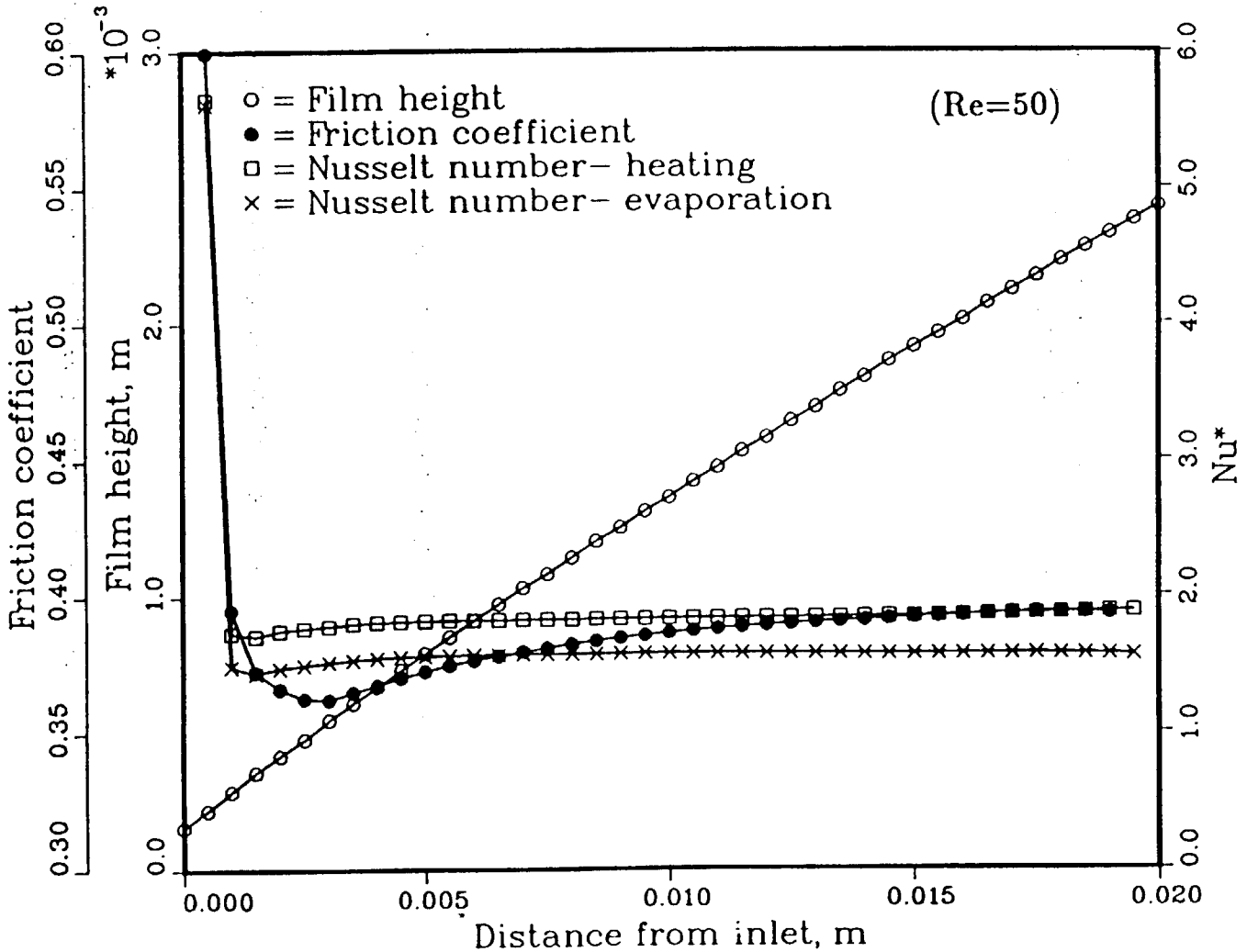

Fig. 5.4 Computed results for plane film flow under zero gravity

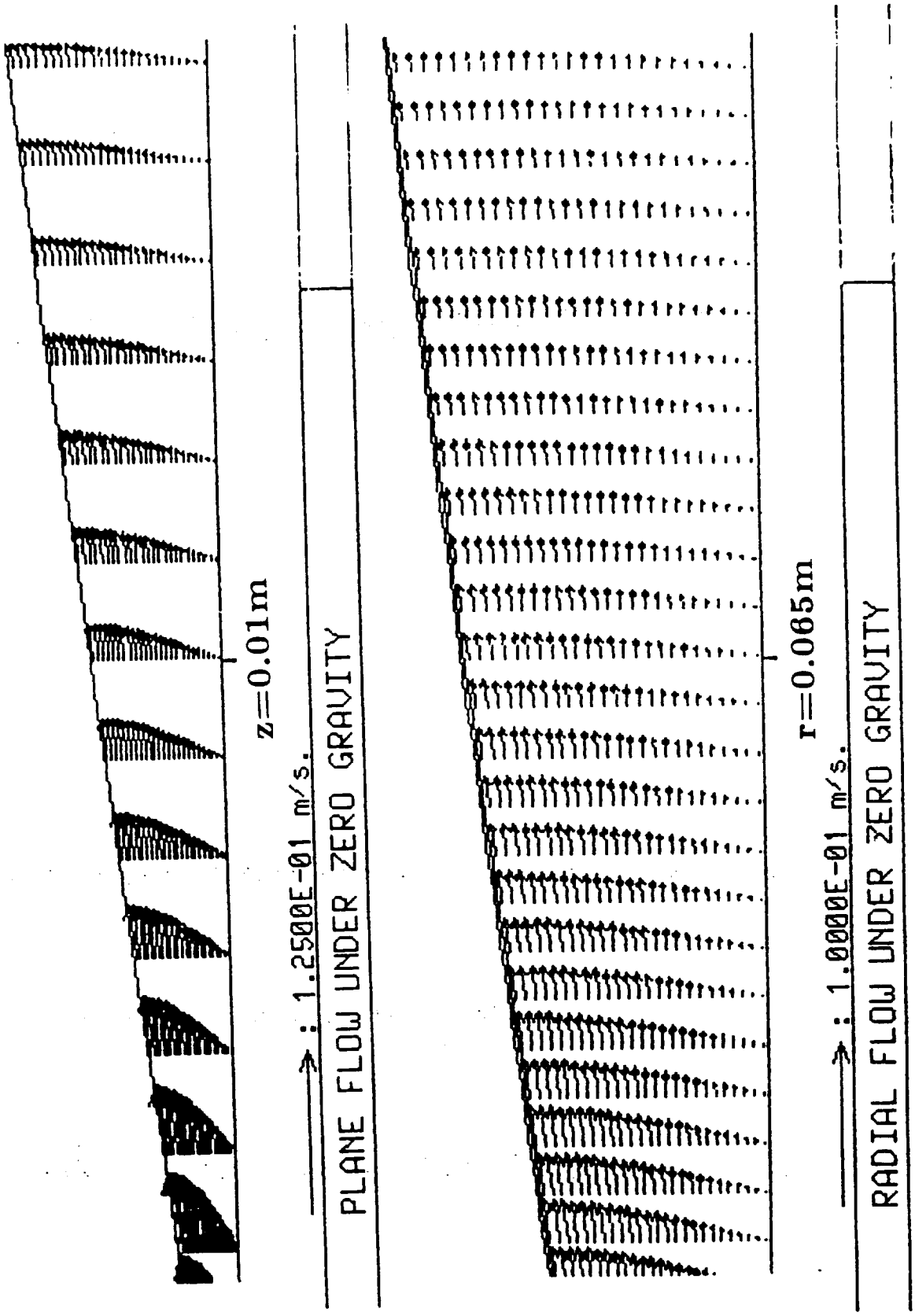

Fig. 5.5 Velocity vectors for plane and radial flows under zero gravity

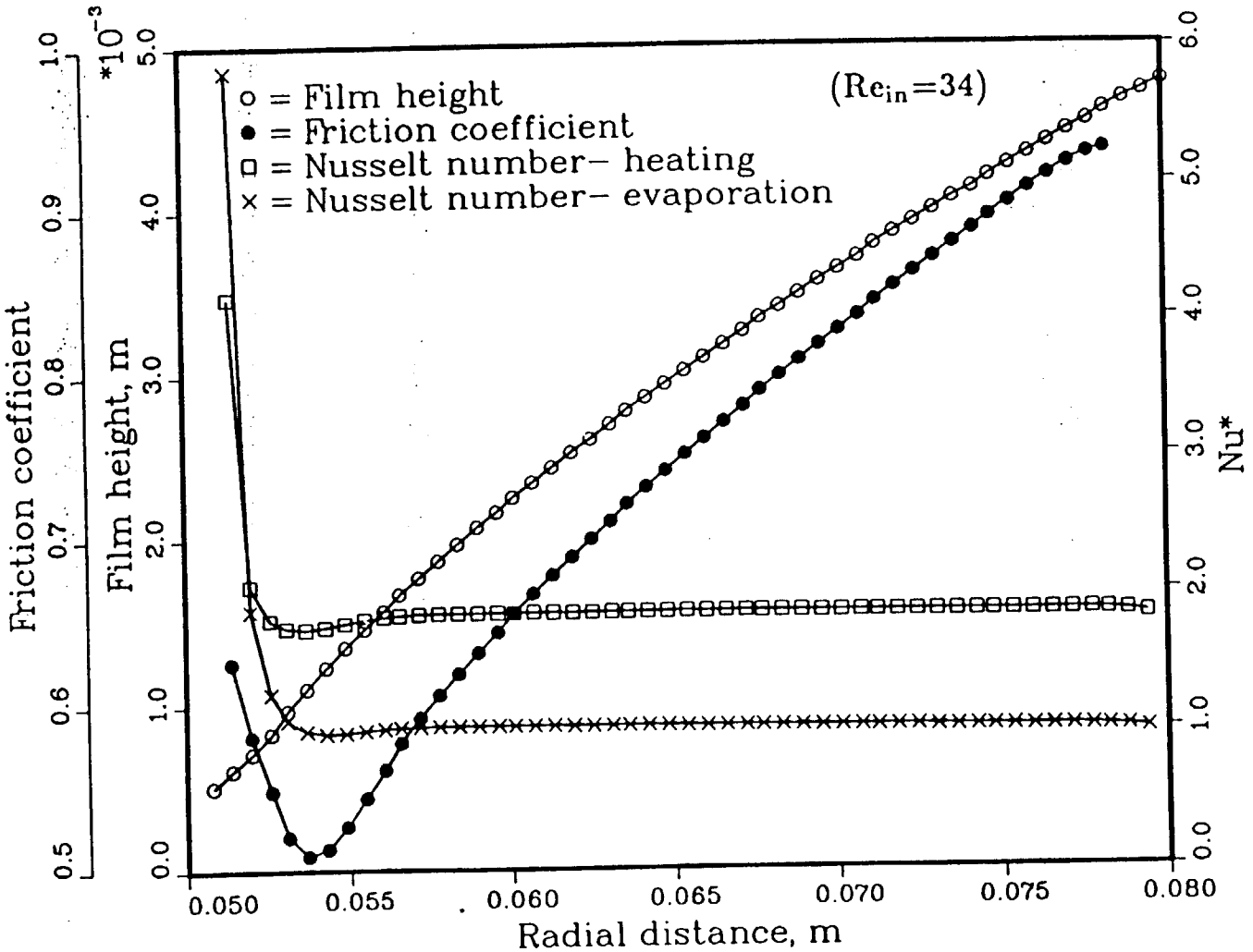

Fig. 5.6 Computed results for radial film flow under zero gravity

(1989a) for the same flow conditions. The average penetration rate through the surface was found to be only 0.6% of the entrance flow. This suggests that the present methodology is practically applicable, and leads to results that are more accurate than the previous two-dimensional method.

Figure 5.2 also compares the film height with that predicted by Thomas et al. (1989) where the variations of the velocity across the thickness of the film were integrated out using a parabolic velocity profile and the height was explicitly solved by using the MacCormack predictor-corrector method. The one-dimensional solution seems to predict a smaller film height than either the present or previous two-dimensional numerical solution. In addition to neglecting any variation of the velocity across the thickness of the film, the one-dimensional solution assumes a friction factor based on the boundary layer thickness. These approximations lead to results that are somewhat different than the two-dimensional solution presented here. Looking at Fig. 5.3, it can be noticed that the surface predicted by the method proposed by Thomas et al. (1989) results in penetrations that are much higher than the solution presented here. Comparing the present solution with the analytical results presented in section VI, the present film height is found to be lower than that predicted by the analytical solution. The analytical solution assumes a uniform velocity profile across the film thickness, which is apparently not the case in reality. The friction factor used for the final solution, however, was the average friction factor obtained from the present numerical solution. The above observations suggest that the free surface flow of a thin film is two-dimensional in nature and the one-dimensional results (analytical or numerical) can be used only as an approximation.

The variation of the friction coefficient and the Nusselt number for plane flow under zero gravity are presented in Fig. 5.4. The friction coefficient decreases rapidly close to the entrance and gradually increases thereafter all the way to the exit. The steep drop near the entrance is associated with the development of the velocity profile from a uniform entrance condition to a parabolic configuration downstream. By running the problem with a parabolic entrance flow, it was found that the rapid drop near the entrance mostly disappeared, but the friction coefficient after a short distance from the entrance coincides with the plot presented here. One may also notice that the friction coefficient is calculated in terms of the average local velocity, which decreases gradually downstream. Observing the numerically calculated values of the wall shear stress, it was found that the shear stress decreases monotonically beginning from the entrance. Near the entrance, the drop in shear stress is also very rapid. It levels off as the flow moves downstream. Therefore, the rise in the friction coefficient is due to the rapid deceleration of fluid velocity downstream.

The Nusselt number for plane flow under zero gravity also shows a rapid drop close to the entrance due to the development of the thermal boundary layer. After a short distance, however, the Nusselt number becomes nearly constant for the cases of heating and evaporation. As also seen by previous investigators, the Nusselt number for heating is larger than the Nusselt number for evaporation. A plot of the velocity vectors for plane flow under zero gravity is shown in Fig. 5.5. It is observed that the velocity profile is parabolic in nature and the magnitude of the velocity decreases downstream.

The results of radial flow under zero gravity is shown in Figs. 5.5 and 5.6 for Re_{in} = 34. It can be seen that for the flow conditions considered here the film height increases monotonically from the entrance. However, as demonstrated by Rahman et al. (1989a), the film height may increase or decrease in radial flow in contrast to plane flow where the film height always increases. The film height is basically a function of the inlet Reynolds number. The friction coefficient, in the case of radial flow, is found to decrease first, attain a minimum, and increase thereafter all the way to the exit. As discussed for the case of plane flow, the decrease of the friction coefficient near the entrance is associated with the development of the velocity profile from a uniform entrance condition. The rise of the friction coefficient after the minimum in this case is found to be much more rapid than that in plane flow. This is because the flow velocity decreases more rapidly due to the spreading of the fluid as it moves downstream. The Nusselt number for radial flow has basically the same kind of behavior as in plane flow. The values of the Nusselt number are different however, particularly in the case of evaporation where there is a loss of heat from the free surface. The vector plot in Fig. 5.5 shows that in radial flow the velocity decreases more rapidly downstream, while maintaining a parabolic structure across the film. It can be also noticed from Fig. 5.5 that the flow in a zero gravity environment is well-structured and no instability or separation is found to be present in the flow field.

5.5.2 Film Flows Involving a Hydraulic Jump

A hydraulic jump is found to be present under some flow conditions where a film flows along a horizontal or inclined surface under the

presence of a gravitational body force. Two different flow regimes are found to be present in this kind of flow: a supercritical flow before the jump, and a subcritical flow after the jump. Depending on the Reynolds number, the Froude number, and the length of the flow domain, the flow may be only supercritical, only subcritical or mixed in the computational domain. A mixed flow is the focus of our attention here, since a hydraulic jump can occur only in that kind of flow. Both plane and radial hydraulic jumps are considered in this section. The results for plane flow are demonstrated in Figs. 5.7 and 5.8.

Figure 5.7 shows a plane hydraulic jump at Re = 355 and Fr_{in} = 9.0. The Froude number at the outlet is assumed to be 1.0 to simulate a critical outflow condition. A critical outflow is present when a film moves off of the plate and experiences a free fall under the action of gravity. If the plate is extended beyond the computational domain, the outflow is simply subcritical and an appropriate Froude number needs to be specified.

As seen in the figure, the film height increases slowly before the jump, experiences a rapid rise at the jump front and thereafter decreases gradually all the way to the exit. A wave-like structure is found to be present at the commencement of the subcritical regime. This shape was previously photographed by Francis and Minton (1984) for a hydraulic jump in a water channel, but could not be captured in previous numerical investigations. Looking at the velocity vector plot in Fig. 5.8, it can be noticed that the fluid separates from the plate due to the sudden rise of the free surface at the jump location. Most of the mainstream flow tries to orient itself along the free surface since a zero-shear condition exists on

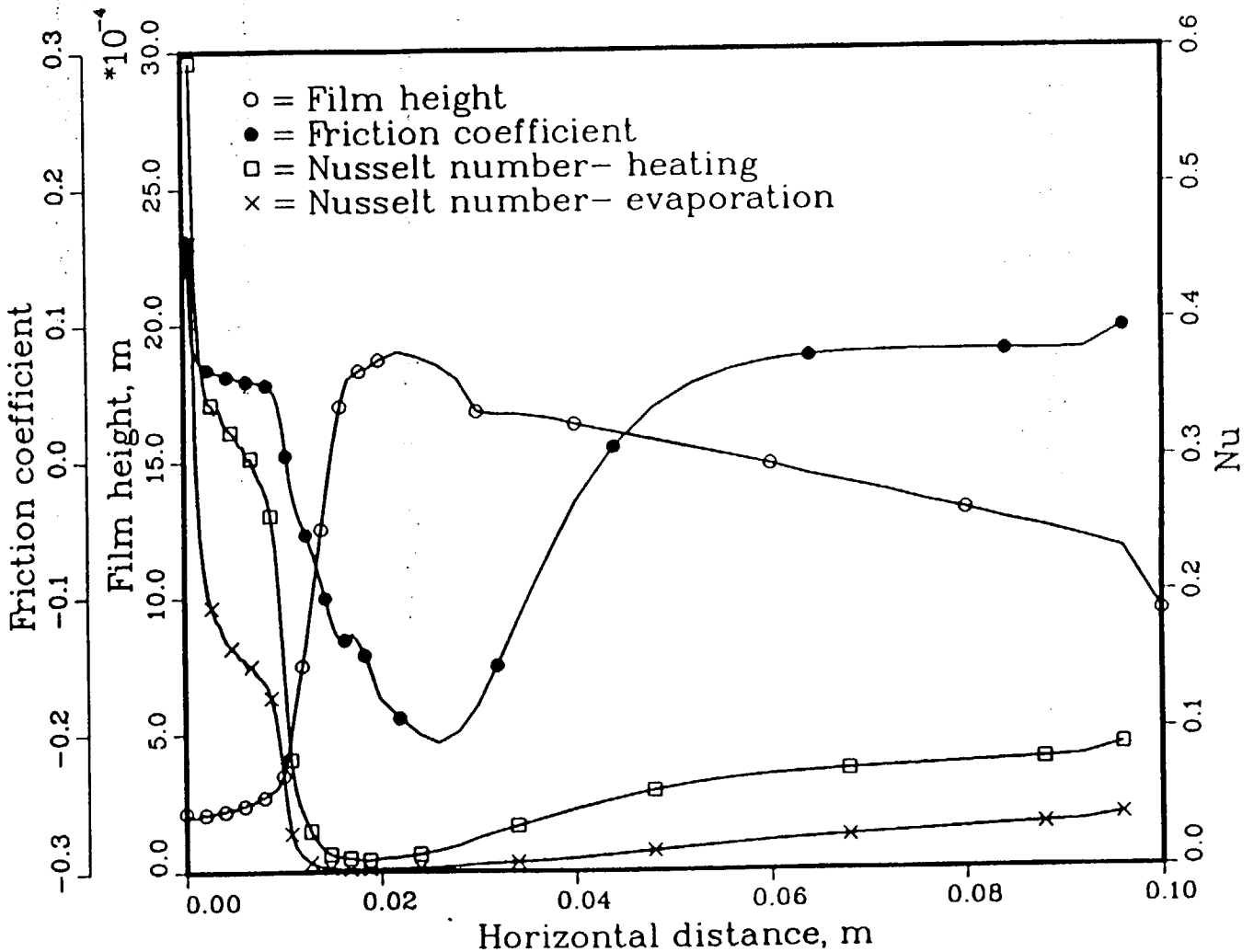

Fig. 5.7 Computed results for plane hydraulic jump ($Re=355, Fr_{in}=9$)

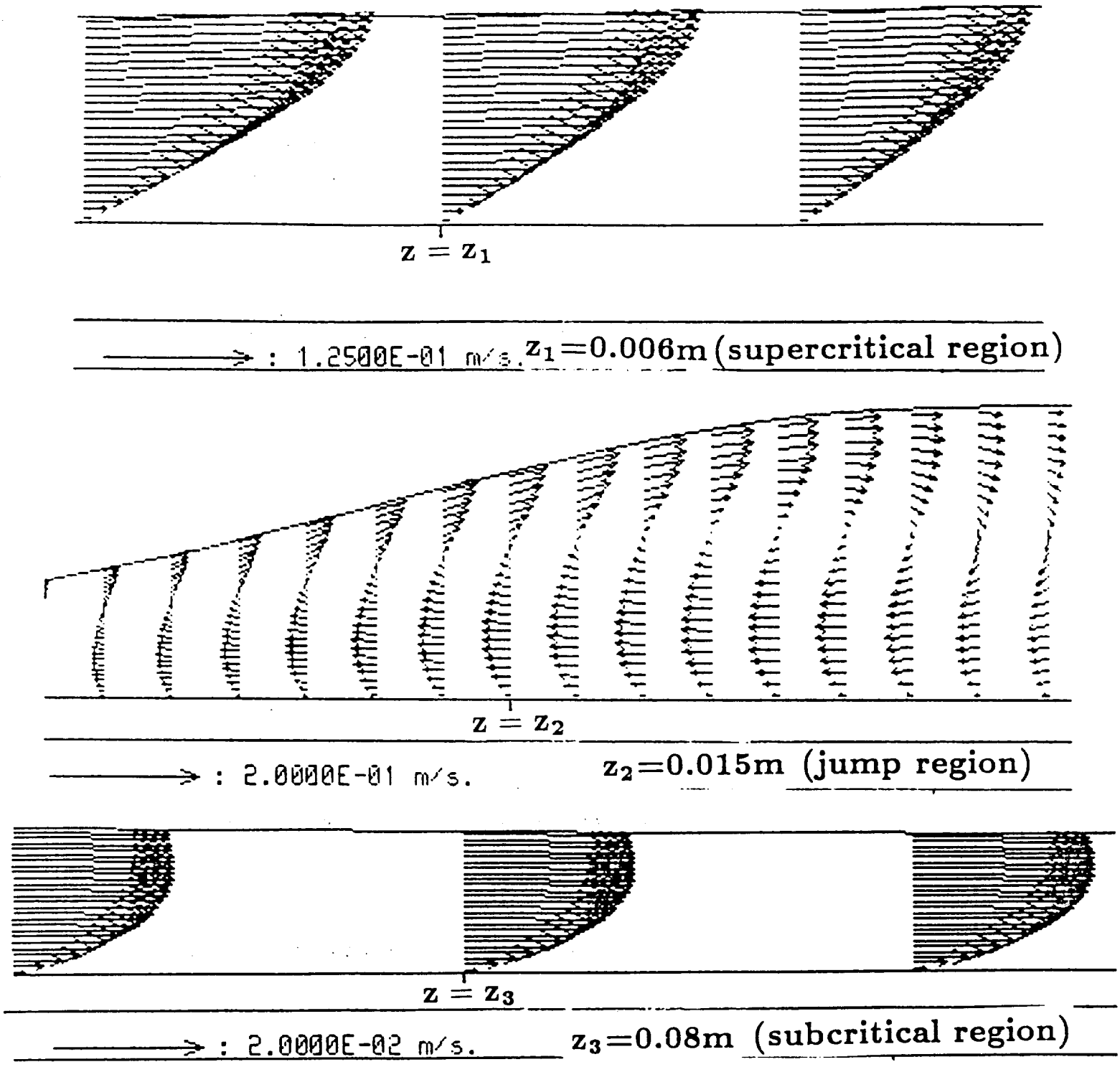

Fig. 5.8 Velocity vectors in plane hydraulic jump ($Re=355, Fr_{in}=9$)

that surface. This results in a recirculating flow near the solid wall. After a distance following the jump, the flow reattaches again to the surface and eventually develops into a parabolic profile. The flow is also seen to be parabolic in the supercritical regime before the jump. The separation of the flow from the solid wall also results in a negative shear stress near the jump location as seen in the plot of the friction coefficient in Fig. 5.6. The friction coefficient decreases rapidly near the entrance due to the development of the flow from a uniform entrance condition to a parabolic structure. The separation and reattachment points can be identified from this plot as the locations where the friction coefficient is equal to zero. After the flow reattaches, the friction coefficient increases slowly due to the reduction of the flow velocity due to friction as the fluid moves downstream.

The plots of the Nusselt number are shown in Fig. 5.7 for the cases of simple heating and evaporation. In both cases, the solid wall was assumed to be at a uniform temperature higher than the ambient. In both cases, the Nusselt number decreases rapidly, comes to a minimum and then increases further downstream.

A hydraulic jump during the radial spread of fluid along a horizontal plate is demonstrated in Figs. 5.9 and 5.10, where Re_{in} = 50 and Fr_{in} = 11.0. As in the case of a hydraulic jump in plane flow, a critical outflow condition is assumed. As seen in Fig. 5.9, the supercritical flow is sustained for a short distance, where the film height increases faster than the plane flow. At the jump, there is a rapid rise in fluid level, which is followed by a gradual decrease in the subcritical region. The velocity

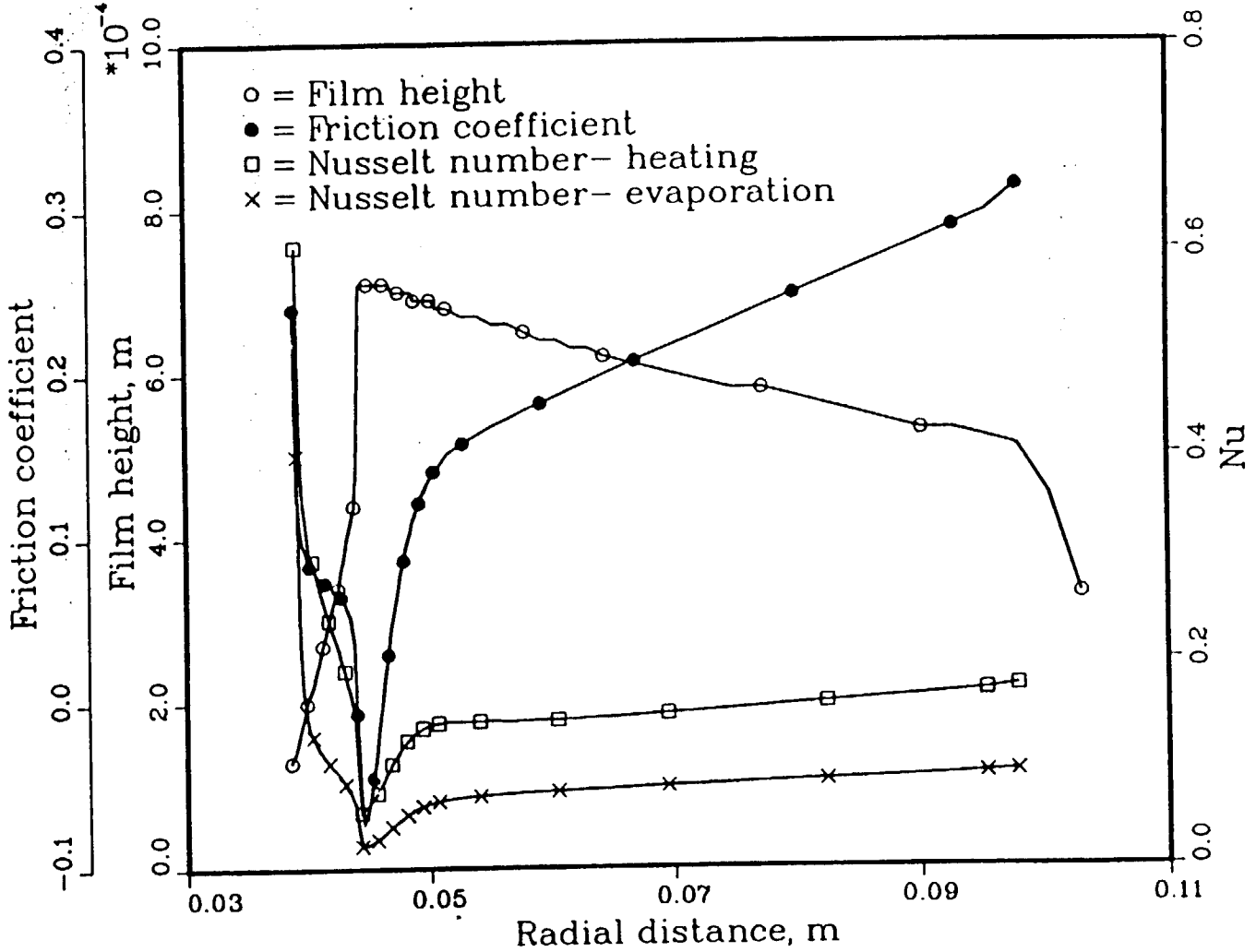

Fig. 5.9 Computed results for radial hydraulic jump (Re_{in}=355,Fr_{in}=11)

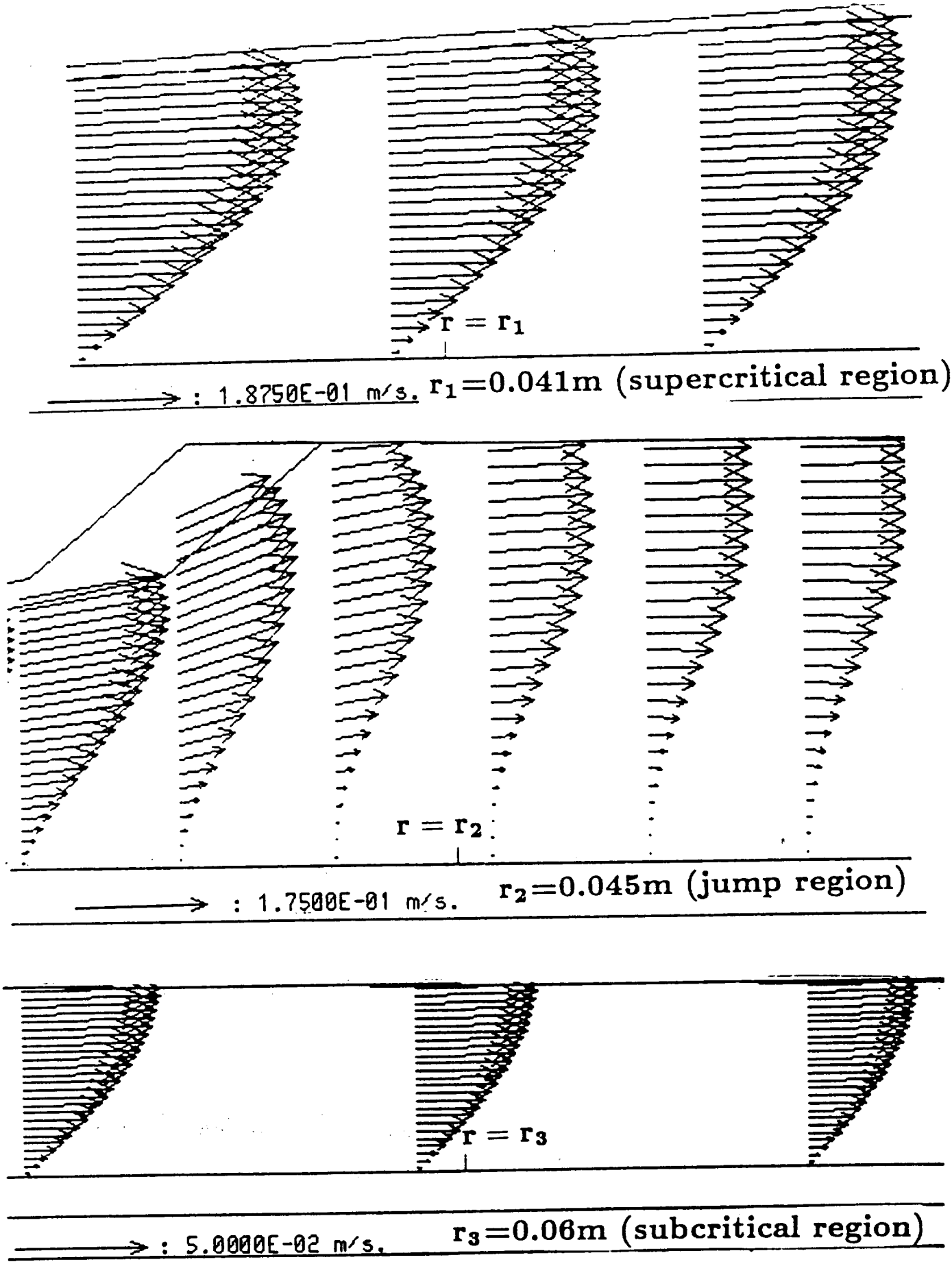

Fig. 5.10 Velocity vectors in radial hydraulic jump (Re_{in}=355,Fr_{in}=11)

of the fluid decreases downstream, due to the combined actions of radial spreading and friction from the solid wall. There is a short separation region as seen in both vector plots in Fig. 5.10 and the plot of friction coefficient in Fig. 5.9. The profile is approximately parabolic in both the supercritical flow before the jump and the subcritical flow following the reattachment. The rapid drop of the Nusselt number and the friction coefficient are associated with the rapid flow development near the entrance. As seen in plane flow, the Nusselt number reaches a minimum in the separated flow region. The Nusselt number rises slightly after the flow reattaches to the surface.

5.6 CONCLUSIONS

The results of a new methodology for the computation of the free surface flow of a thin liquid film is presented. The problems considered are plane and radial flows involving a hydraulic jump and plane and radial flows in a zero-gravity environment when no jump can be present. The new method computes the whole flow field as a single domain problem irrespective of any regime change in the computational domain. This allows the determination of the details of the flow field and the friction and heat transfer behavior around a jump location. It was also found that the new method yields results that are more accurate than any other existing method for all of the problems considered here.

In both plane and radial flows where a hydraulic jump is present, it was found that a distinct supercritical regime is present before the jump and a subcritical regime exists downstream of it. The very rapid rise in the fluid level at the jump location results in the separation of the flow

from the solid wall and the development of a backward circulation. The flow, however, reattachs to the surface after some downstream distance in the subcritical region. The back flow was found to be stronger in plane flow and at higher Reynolds numbers. The location of the separation and reattachment can be determined from the plot of the friction coefficient, which is negative in the recirculation region. The Nusselt number was found to have a minimum in the jump region.

In the case of plane and radial flows in a zero gravity environment, it was found that the variation of the film thickness is monotonic and no separation of the flow is present. The friction coefficient decreases rapidly close to the entrance, attains a minimum and thereafter increases gradually downstream. The Nusselt number remains almost constant except for the entrance region, and is higher for heating than for evaporation.

Section VI

ANALYSIS OF THE FLUID FLOW AND HEAT TRANSFER IN A THIN LIQUID FILM IN THE PRESENCE AND ABSENCE OF GRAVITY

6.1 SUMMARY

The hydrodynamic and thermal behavior of a thin liquid film flowing over a solid horizontal surface is analyzed for both plane and radially spreading flows. The situations where the gravitational force is completely absent and where it is significant are analyzed separately and their practical relevance to a micro-gravity environment is discussed. In the presence of gravity, in addition to Reynolds number, the Froude number of the film is found to be an important parameter that determines the supercritical and subcritical flow regimes and any associated hydraulic jump. A closed-form solution is possible under some flow situations, whereas others require numerical integration of ordinary differential equations. The approximate analytical results are found to compare well with the available two-dimensional numerical solutions.

6.2. INTRODUCTION

A thin film may be generated either by impingement of a jet on a solid wall or by discharge of fluid through a slot from a pressurized container. It may also occur during a melting or condensation process. Such situations may occur in the Space Shuttle for inflow to a propellant tank and in the absorber unit of a heat pump absorption system. The understanding of such flows in a micro-gravity environment is essential for the optimal design of fluid flow and heat exchange processes in a space vehicle.

The inviscid flow of a liquid jet impinging on a solid wall is a classical hydrodynamics problem which is available in textbooks (Batchelor (1967)). It is concerned with irrotational, incompressible and inviscid flow, in which the effects of gravity and surface tension are neglected. One of the major attractions of this type of approach is that it can be handled using complex potential theory and therefore can be treated analytically.

In nature, however, viscous effects become important, particularly when the thickness of the liquid layer becomes small. Also, gravity cannot be neglected entirely in most situations. Watson (1964) analyzed the fluid mechanics of thin films produced by the impingement of a liquid jet on a flat horizontal surface under the action of gravity. By using the boundary layer approximations of the governing transport equations, analytical solutions using a similarity transformation along with the Pohlhausen integral method were derived. The analysis covered the regions where the boundary layer thickness is less than the film

height and where the film is totally engulfed by the boundary layer. The possibility of a hydraulic jump in such a flow was also anticipated. However, the analysis was applicable only to the supercritical flow before the jump. The height of the jump was predicted for any given location of the jump. The heat transfer counterpart of the impinging jet problem was considered by Chaudhury (1964). The energy equation was solved in closed form including the effects of viscous dissipation by approximating the temperature profile with a fourth-order polynomial. Nusselt numbers for different values of the Prandtl number were presented.

The impingement of a liquid jet in a gravity-free environment was presented by Labus and DeWitt (1978). They included the effects of surface tension, but entirely neglected the viscous forces. From a scaling analysis, it was shown that for a large jet Reynolds number, the flow can be approximated to be inviscid. Numerical solutions of the governing transport equations were obtained and compared with experimental measurements. Three distinct flow patterns of the jet were obtained which were classified in accordance with relative importance of inertia and surface tension.

In the studies mentioned above, the investigators considered either inviscid flow or viscous supercritical flow up to the location of the jump. The fluid flow in the vicinity of the jump or in the subcritical region following the jump is also important from an engineering point of view. Moreover, all of the studies mentioned above are concerned with a thin film formed by impingement of a liquid jet. The driving

mechanism of these flows are flow rate and jet diameter which are characterized by jet Reynolds number. So, the findings in these studies cannot be applied readily to a situation where the film is formed by discharge from a pressurized container. This situation was considered in recent studies by Rahman et al. (1989a, 1989c, 1989d). A systematic numerical study of two-dimensional fluid flow and heat transfer in a thin liquid film in both plane and radially spreading flows was performed. The studies covered both zero and normal gravity environments. In the absence of gravity, no jump was found and the flow remained supercritical in the entire domain. In the presence of gravity, a jump was found under some flow conditions. In all of these studies, the flow field was computed numerically using a boundary-fitted coordinate system where the irregular free surface of the film was taken as one of the boundaries of the computation domain. The inertial, viscous and pressure forces were identified to be dominant and the surface tension was found to be negligible in most regions. The computational methodology presented by Rahman et al. (1989a and 1989d) (described in sections III and IV of this report) is termed the 'pressure optimization method' where the shape of the free surface was represented by an algebraic equation with two or more arbitrary constants. The constants were optimized using an exhaustive search which minimized the difference between the computed free surface and ambient pressures. The method was found to be robust and was extremely satisfactory for zero-gravity flows. However, when a jump was present in the computation domain, the pressure optimization method was unable to compute the jump as a single-domain problem. The subcritical and supercritical flows were computed separately and were matched at the

jump interface preserving the conservation of mass, momentum and energy.

The two-dimensional numerical method presented by Rahman et al. (1989c) (described in section V of this report) is termed 'porous wall method'. In this method, the free surface was assumed to be a permeable wall where fluid particles could cross this boundary depending on the difference in fluid and ambient pressures. The shape of the surface was improved by successive iterations until the free surface conformed to a streamline where no penetration occurred. This method proved to be successful in handling the regions before and after the jump as a single-domain problem. The details of the flow structure in the vicinity of the jump were presented along with values of the skin friction and heat transfer coefficients.

Even though the complete numerical solution for the flow field and heat transfer coefficient are available to us, the need for a simple systematic, analytic method to describe the flow is inevitable. The numerical results are limited to the flow parameters used for the computation, and cannot be extended in general. Moreover, an analytical expression is easier to use and implement in addition to the understanding of the limiting behavior of the flow. The present work is intended to analyze both zero-gravity flows and the flows where gravity is significant. The application of these results in a micro-gravity situation will be examined. Unlike previous analytical studies, it will cover both supercritical and subcritical regions and the jump connecting the two domains. In addition to analyzing the flow field, the heat transfer will be studied.

6.3. EQUATIONS OF MOTION

The schematic of the problem under consideration is shown in Fig. 6.1. A thin liquid film is flowing adjacent to solid heated wall. Two classes of flows are considered here.

(a) Plane flow: where the film moves in a two-dimensional fashion along a plane horizontal wall.

(b) Axisymmetric radial flow: where the liquid is introduced at the center of a circular horizontal plate and spreads out radially.

The z(r) axis is directed along the longitudinal (radial) direction, and y-axis is directed normal to the plate. The velocity components in these two directions are w and v, respectively. The height of the free surface from the solid wall is denoted by δ which varies with the longitudinal (radial) location of the plate.

The equations governing the conservation of mass, momentum and energy for an incompressible constant property flow are given by

$$\nabla \cdot \vec{V} = 0 \tag{6.1}$$

$$\frac{D\vec{V}}{Dt} = -\frac{1}{\rho}\nabla p + \nu\nabla^2 \vec{V} + \vec{g} \tag{6.2}$$

$$\frac{DT}{Dt} = a\,\nabla^2 T \tag{6.3}$$

Here we have also assumed that heat generation due to viscous dissipation and pressure work are negligible, and there is no generation

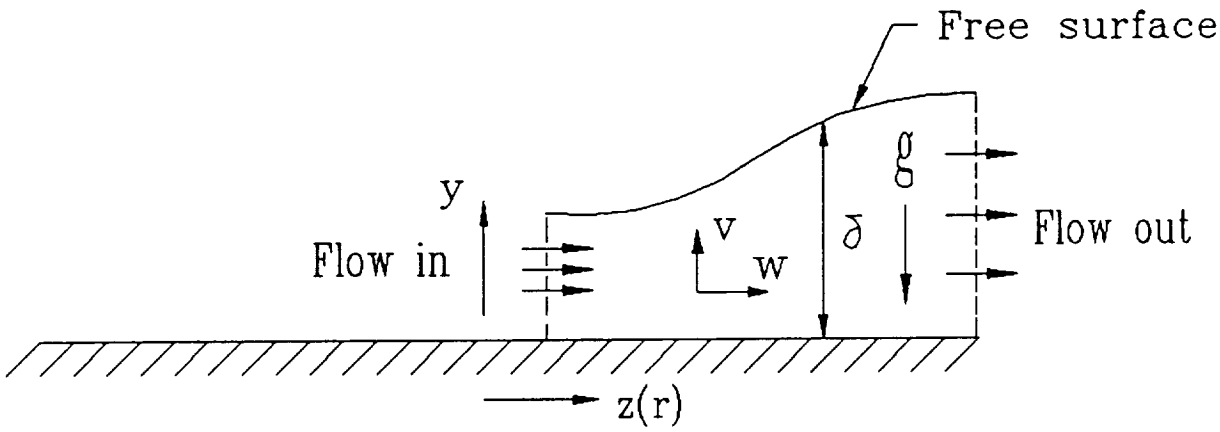

Fig. 6.1. Schematic of the physical problem

of heat or mass. The velocity vector $\vec{V}$ can be resolved into components as

$$\vec{V} = w\vec{k} + v\vec{j}$$

The vectorial representation used in equations (6.1-6.3) is easier to handle since it can be readily transformed to Cartesian or cylindrical components as needed. The boundary conditions in component form are given by

at $y = 0$: $v = w = 0$

$$\begin{cases} T = T_w, & \text{for isothermal wall} \\ -k\dfrac{\partial T}{\partial y} = q_w, & \text{for constant flux wall} \end{cases} \tag{6.4}$$

at $y = \delta$: $\dfrac{d\delta}{dz} = \dfrac{v}{w}$, $p = p_e$, $\tau_e = 0$

$$\begin{cases} T = T_{sat}, & \text{for evaporation} \\ q_e = 0, & \text{for adiabatic condition} \end{cases} \tag{6.5}$$

at $z = 0$ or $r = r_{in}$: $w = W_{in}$, $T = T_{in}$ (6.6)

at $z = L$ or $r = r_{out}$: $\dfrac{\partial p}{\partial y} = -\rho g$, $\dfrac{\partial T}{\partial z} = 0$ (6.7)

$$\begin{cases} \dfrac{\partial w}{\partial z} = 0, & \text{for zero gravity} \\ Fr = Fr_{out}, & \text{for non-zero gravity} \end{cases}$$

On the free surface, both streamline and stress-free conditions have to be satisfied. The balance of normal stresses, in general,

relate fluid pressure to the ambient pressure via surface tension and other stresses. From a scaling analysis, it can be shown that (see Rahman et al. (1989c)), for a reasonably large Weber number and flow rate that is typical for these flows, these stress terms are found to be an order of magnitude lower than the pressure. So, the surface tension can be assumed to be negligible in most regions of the flow leading to the $p = p_e$ condition on the free surface.

Both plane and radial flows described above will be solved for zero and normal gravity situations. In the following two sections, we will analyze the flow using uniform and parabolic velocity distributions, respectively. The former is more common in fluid flow literature concerning a hydraulic jump or shock wave and will be carried out in details. The latter section will improve on the analysis by using a parabolic velocity distribution across the film, which is more appropriate for laminar thin film flow.

6.4 ANALYSIS OF FLOW USING ONE-DIMENSIONAL UNIFORM VELOCITY

We first consider the situation where the velocity variation across the thickness of the film is neglected, and the film is assumed to propagate downstream with its uniform average velocity. Let W be the average velocity of the film in the longitudinal (radial) direction of the plate and Q be the volumetric flow rate. In the case of plane flow, Q is the volume flow rate per unit width. The continuity equation (6.1) can be written as

$$Q = (2\pi r)^{\lambda} \delta W \tag{6.8}$$

where $\lambda = \begin{cases} 0, \text{ for plane system} \\ 1, \text{ for radial system} \end{cases}$

Integrating eqn. (6.2) across the thickness of the film, expressing the resistance from the solid wall in terms of friction coefficient and substituting eqn. (6.8) results in

$$\frac{d}{dr}\left(\frac{W^2}{2} + g\delta\right) = -\frac{c_f}{2}\frac{W^2}{\delta} \tag{6.9}$$

This momentum equation must be solved along with eqn. (6.8) to determine the flow field, and will be carried out in the following subsections.

6.4.1 Flow Under Zero Gravity

For a steady flow under zero gravity, the governing equations (6.8 and 6.9) reduce to

$$Q = (2\pi r)^{\lambda}\, \delta W = \text{constant} \tag{6.10}$$

$$W\frac{dW}{dr} = -\frac{c_f}{2}\frac{W^2}{\delta} \tag{6.11}$$

Eliminating δ from eqns. (6.10 and 6.11) gives

$$W^{-2}\, dW = -\frac{c_f}{2Q}(2\pi r)^{\lambda}\, dr$$

Integrating this equation assuming a constant c_f and substituting the conditions at one location of the flow (i.e., at $r = r_{in}$, $W = W_{in}$

and $\delta = \delta_{in}$) yields the solution in the form

$$\frac{W}{W_{in}} = \frac{1 - \frac{c_f}{2}\frac{r}{(\lambda + 1)\delta}}{1 - \frac{c_f}{2}\frac{r_{in}}{(\lambda + 1)\delta_{in}}} = \frac{\delta_{in}}{\delta}\left(\frac{r_{in}}{r}\right)^{\lambda} \qquad (6.12)$$

Solving for δ results in the following relation

$$\frac{\delta}{\delta_{in}} = A\frac{r}{r_{in}} + (1 - A)\left(\frac{r_{in}}{r}\right)^{\lambda} \qquad (6.13)$$

where $A = \frac{c_f}{2}\frac{r_{in}}{(\lambda + 1)\delta_{in}}$ (6.14)

From equation (6.13) we may express the distribution of film height for plane and radial flows.

For plane flow ($\lambda = 0$), the equation simplifies to

$$\frac{\delta}{\delta_{in}} = 1 + \frac{c_f}{2}\frac{z}{\delta_{in}} \qquad (6.15)$$

This indicates that for a constant friction coefficient the film height increases linearly with distance. This increase in film height is because of the decrease in flow velocity due to the resistance from the wall. We may also notice that for inviscid flow when no resistance is exerted by the solid wall, the film height remains the same at all downstream locations beginning from the entrance.

In real flow situations, however, the friction coefficient varies along the plate. Usually, near the entrance the friction coefficient is greater due to the rapid changes in the velocity profile as the boundary layer develops beginning from the entrance plane. A good estimate of the friction coefficient can be made using the Blasius solution (see Kays and Crawford (1980)) for forced convective boundary layer adjacent to a plate. This results in

$$c_f = \frac{0.664}{\sqrt{\frac{Wz}{\nu}}}, \quad \text{for plane flow} \tag{6.16a}$$

$$\text{and } c_f = \frac{0.664}{\sqrt{\frac{W\,(r-r_{in})}{\nu}}}, \quad \text{for radial flow} \tag{6.16b}$$

However, unlike any other external flow, in a thin film the boundary layer thickness is frequently of the order of the film height. So, after some distance downstream, the viscous effects propagate all the way to the free surface. Then c_f can be better estimated from the equation presented in a later section of this paper (equation 6.46). The location where one should switch over from one formulation to the other may be estimated from the solution of the boundary layer thickness for forced convection. The thickness of the momentum boundary layer is given by

$$\delta_B = 5.0 \sqrt{\frac{\nu z}{V}} \quad \text{, for plane flow}$$

and

$$\delta_B = 5.0 \sqrt{\frac{\nu (r - r_{in})}{V}} \quad \text{, for radial flow}$$

As shown by Thomas et al. (1989), the two friction factor estimates yield the same value at $\delta = 1.81\ \delta_B$. So, for continuity, one may use equation (6.16) for $\delta/\delta_B > 1.81$ and equation (6.46) for $\delta/\delta_B < 1.81$.

The one-dimensional analytical solution with the friction coefficient described above has been compared with the numerical solution of Rahman et al. (1989a) in Fig. 6.2 for Re = 12.5, L = 0.03 m and δ_{in} = 0.000595 m for plane flow. Similar to the analytical solution, a uniform inlet velocity has been assumed for the numerical solution. The predicted film height distribution is found to be somewhat higher than the two-dimensional numerical solution. A test run with the friction coefficient reported in Rahman et al. (1989a) yielded a solution almost coincident with the numerical film height. So, the discrepancy is primarily due to approximations inherent with the estimation of the friction coefficient. The Blasius solution is perfectly valid for boundary layer flow where the free stream extends through a large distance and no free surface is present. However, the comparison is reasonable considering the approximations inherent in the simple analytical formulation.

A plot of equation (6.13) for radial flow under zero gravity is presented in Fig. 6.3 for different values of A. For A = 0.0, which

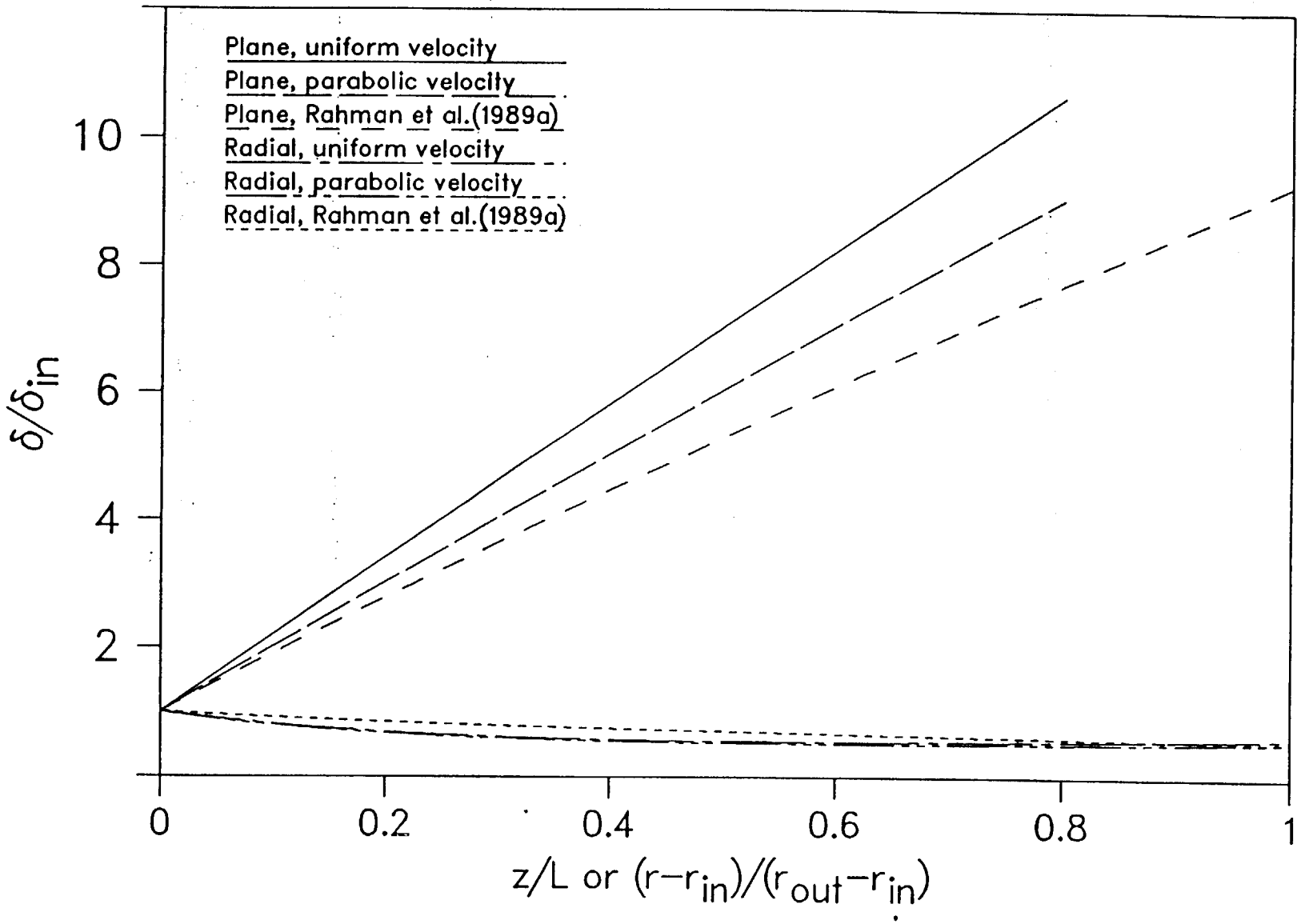

Fig. 6.2 Film height for plane and radial flows under zero gravity

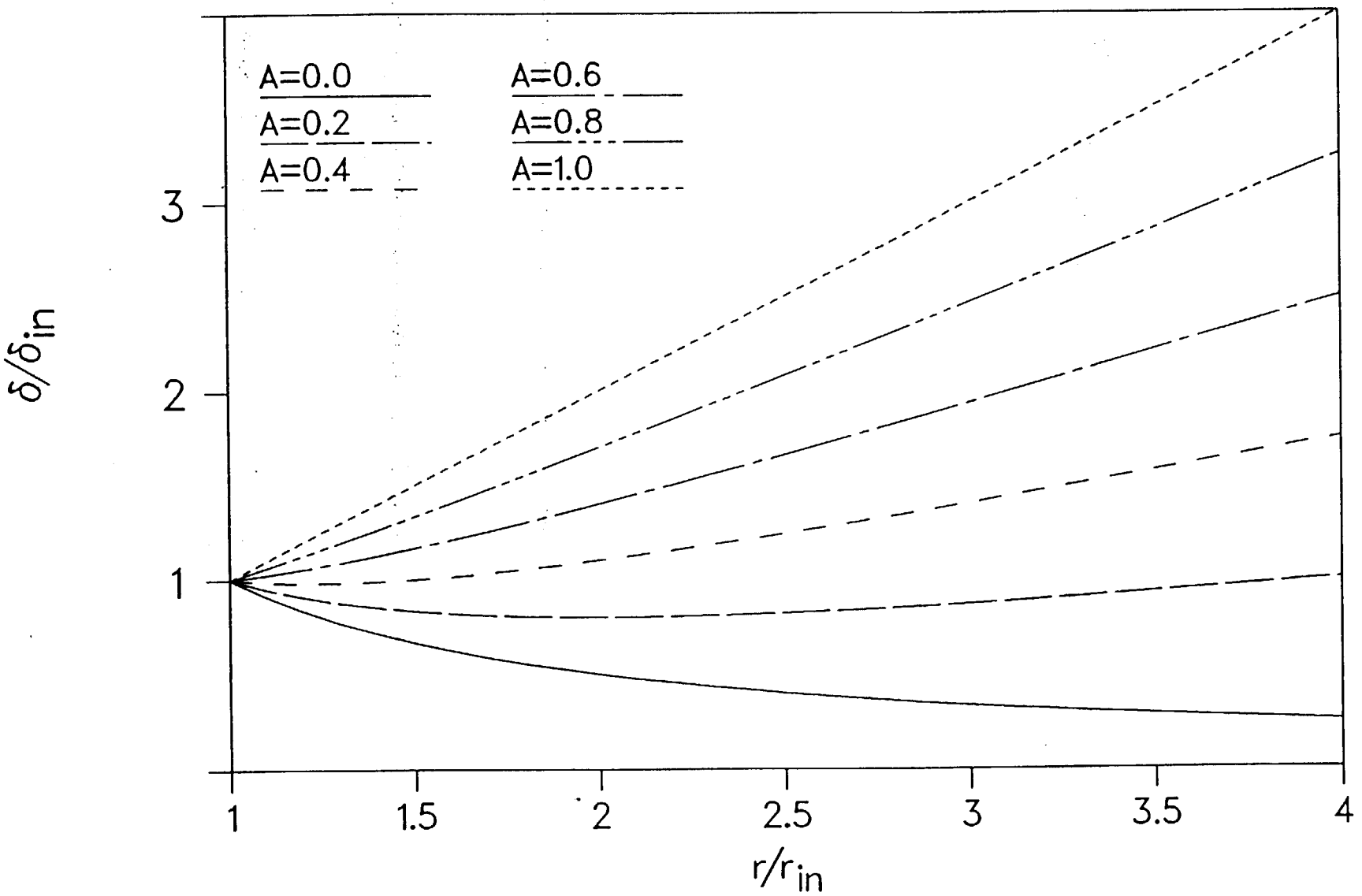

Fig. 6.3 Analytical film height for radial flow under zero gravity

corresponds to inviscid flow, the film height monotonically decreases with radial distance. This is quite expected since, in the absence of any friction, the velocity of fluid particles will remain constant. Therefore, the film height has to decrease with radius as more and more area becomes available to the flow. In this plot we also notice that when friction is present ($A > 0$), the film height may increase or decrease depending on the value of A and the radial location. Also, for a given radial location the value of the film height is more for a larger value of A, since A quantifies the frictional resistance compared to the inertial forces. For $A = 0.2$ and 0.4, the film height decreases first, attains a minimum and then increases further downstream. The location for minimum δ can be determined by differentiating equation (6.13) which gives

$$\left(\frac{r}{r_{in}}\right)_{\text{for min } \delta} = \left(\frac{1 - A}{A}\right)^{1/2} \tag{6.17}$$

$$\left(\frac{\delta}{\delta_{in}}\right)_{min} = 2\sqrt{A}\sqrt{1 - A} \tag{6.18}$$

From eqn. (6.17) we find that a minimum exists if $A < 1/2$. Otherwise, the film height increases continuously from the entrance as seen in plots corresponding to $A > 0.5$. At $A = 1.0$, the film height increases linearly with radius.

The analytical solution for a particular case of $Re_{in} = 404$, $\delta_{in} = 0.005$ m, $r_{in} = 0.05$ m and $r_{out} = 0.2$ m is shown in Fig. 6.2 where it is compared to the two-dimensional numerical solution given by Rahman et

al. (1989a). Here, we have also used the friction coefficient estimated by equations (6.16) and (6.46). The results are very close except for the fact that the analytical solution shows a minimum in the flow domain. The minimum is indeed present as verified from the value of A. The numerical solution could not accommodate this behavior since a continuous hyperbolic curve was assumed to represent the free surface.

6.4.2 Flow in the presence of gravity

When the gravitational body force is significant compared to other existing forces, its effect should be included in the analysis. Unlike a regular forced or natural convection flow in outer space, the effect of gravity, even small, may be significant in a thin film flow since two potential flow regimes, namely supercritical and subcritical may be encountered. These regimes are characterized by the Froude number. The transition of the flow from supercritical to subcritical is analogous to the transition from supersonic to subsonic flow in gas dynamics, where the Mach number determines which regime is present. The analysis presented below uses the methodology commonly followed in the analysis of high speed flow with friction (i.e., Fanno flow). The application of these ideas to a thin film flow is entirely new and it enabled us to combine both flow regimes (supercritical and subcritical) in a single analysis which was not possible by previous investigators. Most previous analytical studies assumed the film height to remain constant in the subcritical region. Expressing eqns. (6.8) and (6.9) in terms of the Froude number results in

$$q = (2\pi r)^{\lambda} \sqrt{g}\, Fr\, \delta^{3/2} \tag{6.19}$$

$$\frac{d}{dr}\left[\delta\left(1 + \frac{Fr^2}{2}\right)\right] = -\frac{c_f}{2} Fr^2 \qquad (6.20)$$

These equations will be solved for plane and radial flows in the following subsections.

(a) Plane Flow

For plane flow $\lambda = 0$. Then eqns. (6.19) and (6.20) can be combined by eliminating the film height and non-dimensionalized assuming c_f to be locally uniform to give the equation

$$(1 - Fr^2)\frac{dFr}{dR1} = \frac{9}{2} Fr^{11/3} \qquad (6.21)$$

where

$$R1 = \frac{z}{\frac{6}{c_f}(\nu^2/g)^{1/3} Re^{2/3}} \qquad (6.22)$$

Integration of equation (6.21) gives

$$\frac{1}{12} Fr^{-8/3} - \frac{1}{3} Fr^{-2/3} = - R1 + c$$

To evaluate the integration constant, the Froude number must be specified at one location in the flow. Upon examining equation (6.21) we notice that the equation is singular at Fr = 1, so a critical flow situation is present at that location. This is analogous to a Mach number of unity in a compressible flow. Let this critical location be denoted by $R1^*$. Then the solution can be written as

$$R1 - R1^{*} = -\frac{1}{4} + \frac{1}{3} Fr^{-2/3} - \frac{1}{12} Fr^{-8/3} \qquad (6.23)$$

Equation (6.23) is a double-valued function as shown (in circles) in Fig. 6.4. The two branches of the function represent subcritical or supercritical flows where the Froude number is less than or greater than unity, respectively.

Since two solutions exist at any location, the possibility of a sudden jump from supercritical to subcritical flow exists. The opposite is not true since that would violate the second law of thermodynamics. The height of the film before and after the jump can be related by the conservation of mass and momentum across the jump. This is given by

$$\frac{\delta_2}{\delta_1} = \frac{1}{2} \left[\sqrt{1 + 8\, Fr_1^{\,2}} - 1 \right] \qquad (6.24)$$

where subscript 1 indicates conditions before the jump and subscript 2 indicates conditions after the jump.

In Fig. 6.4, it can be observed that both subcritical and supercritical flows move towards the critical condition. In the supercritical regime, the Froude number decreases downstream, whereas in the subcritical regime it increases with distance. Since the Froude number is inversely related to the film height, the film height is expected to increase downstream in the supercritical region and decrease downstream in the subcritical region. A flow starting with Fr<1 will follow the subcritical curve all the way to the exit. However, a flow

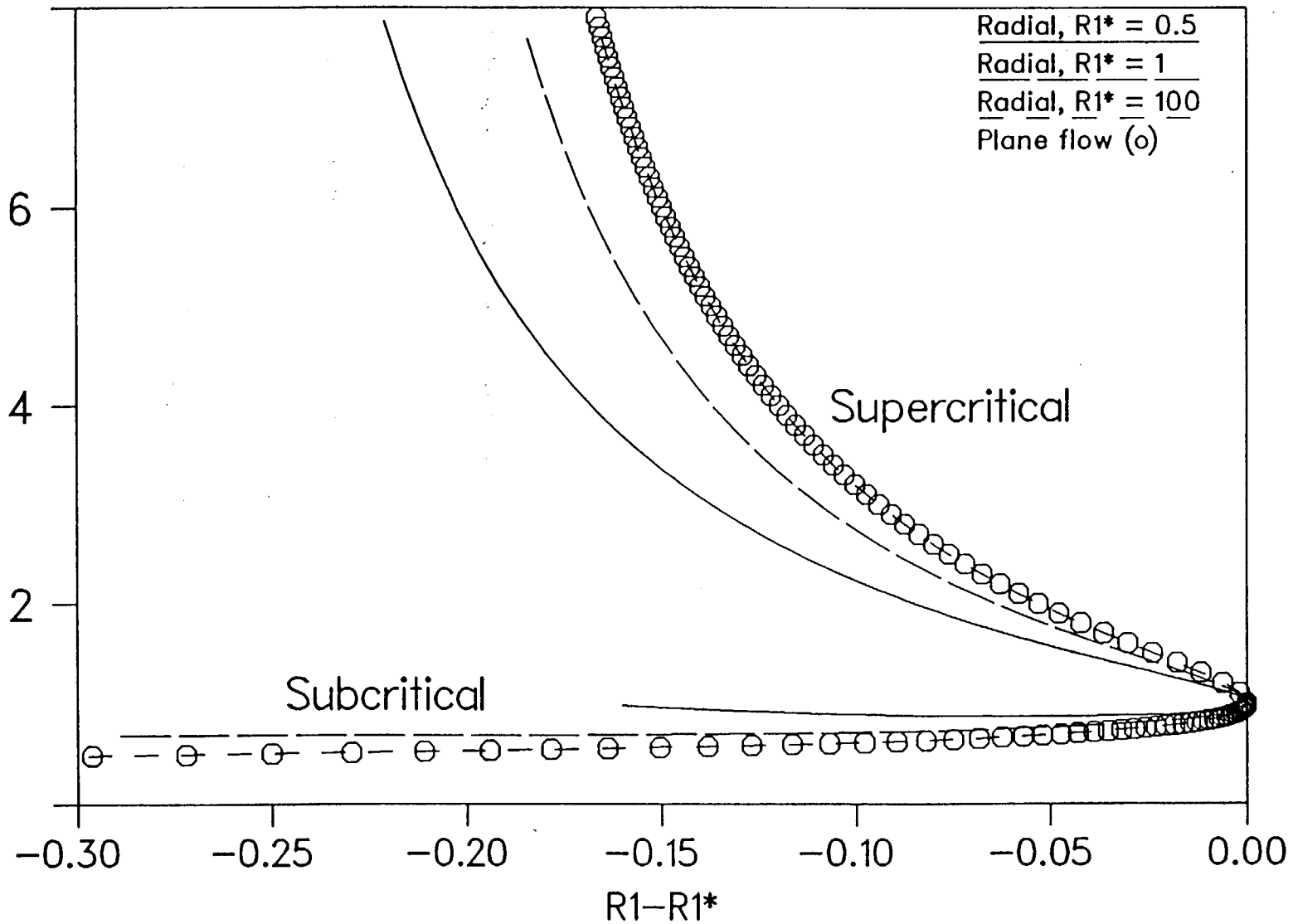

Fig. 6.4 Analytical solution for plane and radial flows over a plate in the presence of gravity (uniform velocity)

starting with Fr>1 may follow the supercritical curve all the way to the exit or may encounter a jump and transform to subcritical flow inside the region under consideration. The location of the jump is determined by the downstream condition of the flow.

(b) Axisymmetric Radial Flow

For radial flow, $\lambda = 1$, eqns. (6.16 and 6.17) may be transformed into the following form

$$(1 - Fr^2) \frac{dFr}{dR1} = \frac{9}{2} Fr^{11/3} - \frac{Fr(2 + Fr^2)}{2\ R1} \qquad (6.25)$$

where

$$R1 = \frac{r}{\frac{6}{c_f} (\nu^2/g)^{1/3} Re^{2/3}} \qquad (6.26)$$

Analogous to plane flow, here the radial distance has been non-dimensionalized using the local Reynolds number and friction coefficient. The variation of friction coefficient with radial distance has been assumed to be negligible. A closed-form solution of equation (6.25) is not possible, so a numerical integration was performed using the Euler method. It can be noticed that the equation is singular at Fr = 1. Therefore, the critical condition cannot be directly applied as a boundary condition in the numerical solution. To avoid this singularity, the equation can be expanded around the singular point and the solution can be found at a short distance from the singular point

from the lowest-order expansion. The numerical integration then can be carried out beginning from a short distance away from the singular point, where the solution is already known. The solution is shown in Fig. 6.4.

It should be noted that the critical radius, $R1^*$, appears as a parameter. For a given flow rate and inlet Froude number, the value of $R1^*$ depends on the inlet radius. A large $R1^*$ indicates that the flow starts up at a larger radial distance, where the effect of curvature is smaller. This is quite evident from the plot since the result for $R1^* = 100$ coincides with the solution for the plane flow. The double-valued nature of the solution is also present in radial flow which also indicates the possibility of a hydraulic jump. The film height before and after the radial jump can be related by the same equation as for plane flow (equation 6.24).

6.4.3 Characteristic Behavior of the Flow

Since the equations of transport for the free surface flow of a thin liquid film are somewhat similar to those for one-dimensional compressible flow, it may be useful to analyze the characteristic behavior of the flow.

The conservation equations in its time-dependent form can be written as

$$\frac{\partial U}{\partial t} + \frac{1}{r^{\lambda}} \frac{\partial}{\partial r} \left(r^{\lambda} E \right) = H$$

where

$$U = \begin{vmatrix} \delta \\ \delta W \end{vmatrix}, \quad E = \begin{vmatrix} \delta W \\ \delta(W^2 + \frac{g\delta}{2}) \end{vmatrix}$$

and $$H = \begin{vmatrix} 0 \\ -\tau_w/\rho \end{vmatrix}$$

where τ_w is the surface shear stress. These are two first-order partial differential equations in t and r with two dependent variables, δ and W.

These two equations may be linearized and written in the following characteristic form:

$$R_t + C R_x = S$$

where

$$R = \begin{vmatrix} W + \sqrt{g\delta_1}\,\frac{\delta}{\delta_1} \\ W - \sqrt{g\delta_1}\,\frac{\delta}{\delta_1} \end{vmatrix} = \text{Riemann invariants}$$

$$C = \begin{vmatrix} W_1 + \sqrt{g\delta_1} \\ W_1 - \sqrt{g\delta_1} \end{vmatrix} = \text{Wave speed}$$

It can be seen that the first invariant always propagates downstream (i.e., $C > 0$). The second invariant, however, propagates downstream for supercritical flow ($Fr = W_1/\sqrt{g\delta_1} > 1$) and propagates upstream for subcritical flow ($Fr < 1$). This implies that both W and δ must be

prescribed upstream for solving supercritical flows while only one is prescribed upstream and one downstream for solving subcritical flows.

6.4.4 Application of Results to Micro-Gravity

The zero-gravity thin film flow considered here can be attained only in a complete absence of the gravitational body force. However, in orbit the gravity is very small, but not precisely zero. Therefore, the range of applicability of the results needs to be investigated. Looking at plane flow results under zero gravity we notice that

$$\delta = \left(\frac{c_f}{2} \right) z + \delta_{in}$$

This suggests a monotonic increase in the film height so long as c_f remains positive. The flow decelerates due to friction and consequently the film height increases. Since the major driving mechanism for this flow is inertia, a film introduced with a finite velocity becomes very slow after traveling a certain distance.

When investigating the expression for the Froude number, it can be noticed that even for a very small gravity force, where the inlet Froude number tends to infinity, the Froude number may become on the order of unity after some distance, since both the deceleration of flow and the increase of film height contribute to reducing the Froude number. The situation here is analogous to hypersonic flow, which in the presence of friction rapidly ceases to be hypersonic after traveling some distance. Therefore, in a microgravity situation, the order of magnitude of the

local Froude number is very important. When the Froude number is extremely large, like near the entrance, the zero gravity results may be applicable. However, away from the entrance, one should resort to the normal gravity results presented here and eventually a hydraulic jump must be encountered.

6.5 ANALYSIS OF FLOW AND HEAT TRANSFER USING PARABOLIC VELOCITY DISTRIBUTION

The one-dimensional analysis presented in the previous section revealed many interesting features of the flow. However, the velocity profile in reality is two-dimensional in nature because of the no-slip condition at the solid wall. As demonstrated by Rahman et al. (1989a), the velocity profile is approximately parabolic in nature in most regions of the flow. The temperature profile may also become parabolic after the thermal boundary layer develops.

We assume the velocity component, w, and temperature, T, to have the following general form where the boundary condition at the solid wall and free surface are satisfied.

$$\frac{w}{W} = 3\eta \left(1 - \frac{\eta}{2}\right) \tag{6.27}$$

$$\frac{T}{T_w} = 1 + B\eta + C\eta^2 \tag{6.28}$$

where η is the dimensionless coordinate across the thickness of the film. The constants B and C will be evaluated later in this section for

different thermal conditions considered here.

Once the velocity and temperature profiles are fixed, the other flow quantities can be readily calculated and are given as follows

$$\tau_w = \frac{3\mu W}{\delta} \tag{6.29}$$

$$q_w = - \frac{KBT_w}{\delta} \tag{6.30}$$

$$q_e = - \frac{KBT_w}{\delta}(B + 2C) \tag{6.31}$$

$$T_e = T_w \ (1 + B + C) \tag{6.32}$$

$$T_b = T_w \ (1 + 5/8 \ B + 9/20 \ C) \tag{6.33}$$

In a thin film flow, the velocity across the thickness of the film is much smaller than the velocity along the plate. Scaling the governing equations (6.1-6.3) using the condition v << w gives

$$\frac{1}{r^\lambda} \frac{\partial}{\partial r} (r^\lambda w) + \frac{\partial v}{\partial y} = 0 \tag{6.34}$$

$$w \frac{\partial w}{\partial r} + v\frac{\partial w}{\partial y} = - \frac{1}{\rho} \frac{\partial p}{\partial r} + \nu\frac{\partial^2 w}{\partial y^2} \tag{6.35}$$

$$\frac{1}{\rho} \frac{\partial p}{\partial y} + g = 0 \tag{6.36}$$

$$u \frac{\partial T}{\partial r} + v \frac{\partial T}{\partial y} = \alpha \frac{\partial^2 T}{\partial y^2} \qquad (6.37)$$

Here $\lambda = 0$ indicates plane flow and $\lambda = 1$ denotes radial flow. Integrating equation (6.36) we get,

$$p = p_e + \rho g (\delta - y) \qquad (6.38)$$

where p_e is the pressure at the edge of the free surface. This indicates that pressure across the thickness of the film is hydrostatic in nature. Also, at zero gravity, $p = p_e$. In the external flow over a flat surface, the ambient pressure usually remains constant. So, in a gravity-free environment, the static pressure is expected to remain constant everywhere in the flow field.

6.5.1 Plane Flow Under Zero Gravity

For plane flow under zero gravity equations (6.34) and (6.35) can be integrated from 0 to δ using the velocity profile given in equation (6.27) and the no-slip condition at the solid wall and zero-shear condition at the free surface. After using the definition of Reynolds number, it results in the relationship

$$\frac{d\delta}{dz} = \frac{2.5}{Re} \qquad (6.39)$$

Integrating this equation, one obtains

$$\frac{\delta}{\delta_{in}} = 1 + \frac{2.5}{Re} \frac{z}{\delta_{in}} \qquad (6.40)$$

For plane flow, the Reynolds number remains constant. Therefore, the film height increases linearly beginning from the entrance location. We also notice that in the limiting case of $Re \rightarrow \infty$, $\delta = \delta_{in}$ everywhere in the flow field. This is quite expected since in an inviscid plane flow, the film height remains constant.

Figure 6.2 shows a comparison of this solution with previous numerical results of Rahman et al. (1989a). The analytical solution tends to predict a somewhat higher film height than the numerical solution, but lower than the solution predicted by assuming a uniform one-dimensional velocity distribution. The assumption of a parabolic velocity profile, even though not exact everywhere in the flow field, produces a reasonable estimate of the film height distribution.

6.5.2 Radial Flow Under Zero Gravity

For radial flow under zero gravity, the integrated equation for the conservation of momentum can be written as

$$\frac{d\delta}{dr} = \frac{2.5}{Re} - \frac{\delta}{r} \qquad (6.41)$$

Analogous to the plane flow case, we have used the continuity equation, the boundary conditions at the solid wall and free surface and the definition of Reynolds number to arrive at this relationship. Note that this equation reduces to the plane flow equation as $r \rightarrow \infty$. We can also observe that $\frac{d\delta}{dr}$ can be positive or negative. So, the film height may increase or decrease in the case of radial flow, in contrast to plane flow, where a linear increase is encountered. The frictional

ORIGINAL PAGE IS
OF POOR QUALITY

resistance at the solid wall reduces the flow velocity and consequently tends to increase the height. However, at the same time, the flow is spreading radially with more area available for the flow as the radius increases. This same behavior was seen in the discussion of one-dimensional analysis (Fig. 6.3), where the parameter 'A' determined the variation of film height downstream from the entrance. 'A' is a function of inlet Reynolds number along with inlet height and radius. Note also that the Reynolds number does not remain constant in radial flows and changes with location.

Integrating eqn. (6.41) gives

$$\frac{\delta}{\delta_{in}} = \frac{r_{in}}{r} + \frac{2.5\ (r^3 - r_{in}^3)}{3\ Re_{in}\ rh_{in}\ r_{in}} \qquad (6.42)$$

The location of the minimum film height may be calculated by differentiating equation (6.42) with respect to r. This results in

$$(r)_{\text{for min } \delta} = r_{in} \left[\frac{3Re_{in}h_{in}}{5} \left(\frac{1}{r_{in}} - \frac{5}{6Re_{in}h_{in}} \right) \right]^{1/3} \qquad (6.43)$$

We can also notice that the minimum will exist when

$$\frac{Re_{in}h_{in}}{r_{in}} \leq \frac{5}{2}$$

The results of the analytical solution for radial flow under zero gravity is also compared with previous numerical results of Rahman et

ORIGINAL PAGE IS
OF POOR QUALITY

al. (1989a) in Fig. 6.2. In this case, we can see a minimum inside the flow domain confirming the observation from the one-dimensional analytical solution using the uniform the velocity profile. Both analytical solutions are close to each other whereas the numerical solution is slightly higher in most parts of the flow.

6.5.3 Plane Flow in the Presence of Gravity

For plane flow where the gravitational body force term is retained, the governing equations of motion (6.34-6.35), can be integrated across the thickness of the film using equation (6.38), the boundary conditions, and the definition of Reynolds number, and can be transformed to the equation

$$\left(\frac{5}{6} - Fr^2\right) \frac{dFr}{dR} = \frac{15}{4} Fr^{11/3} \tag{6.44}$$

where

$$R = \frac{z}{\left[\frac{\nu^2}{g}\right]^{1/3} Re^{5/3}} \tag{6.45}$$

Here the radial coordinate R is normalized in terms of Reynolds number. Note that the definition of R is very similar to the normalized radius R1 used in the one-dimensional analysis using the uniform velocity except that the friction coefficient c_f appears in R1 whereas it does not appear in R. From equation (6.29), the friction coefficient can be easily calculated to be

ORIGINAL PAGE IS
OF POOR QUALITY

$$c_f = \frac{6}{Re} \qquad (6.46)$$

This friction coefficient is correct when the velocity profile is parabolic across the thickness of the film, which obviously assumes that viscous effects are extended all the way to the free surface. When this definition of c_f is assumed, R1 becomes the same as R. In the present investigation we have tried to keep the one-dimensional analysis using the uniform velocity somewhat more general where any known distribution of the friction coefficient may be used.

From equation (6.44) it can be noticed that a critical condition in the flow occurs at Fr = 0.913. Note that this value of Froude number is different from the conventional critical Froude number of Fr = 1, which is strictly valid for a one-dimensional flat velocity distribution. The value of Froude number of 0.913 is therefore the "weighted" value for the parabolic profile. Integrating equation (6.44) with a boundary condition of ($R = R^*$ at Fr = 0.913) we can obtain the solution as

$$-1.195 + \frac{3}{2} Fr^{-2/3} - \frac{5}{16} Fr^{-8/3} = 3.75 (R - R^*) \qquad (6.47)$$

A plot of this equation is shown in Fig. 6.5 (as circles). Analogous to the one-dimensional analysis, the solution is also found here to be double valued in nature. The two stems of the curve denote the supercritical and subcritical flow regimes. The possibility of a hydraulic jump also exists here, which basically depends on the incoming Froude number, length of the plate and flow condition at the outlet. The jump may be present only when the flow initially is supercritical.

ORIGINAL PAGE IS
OF POOR QUALITY

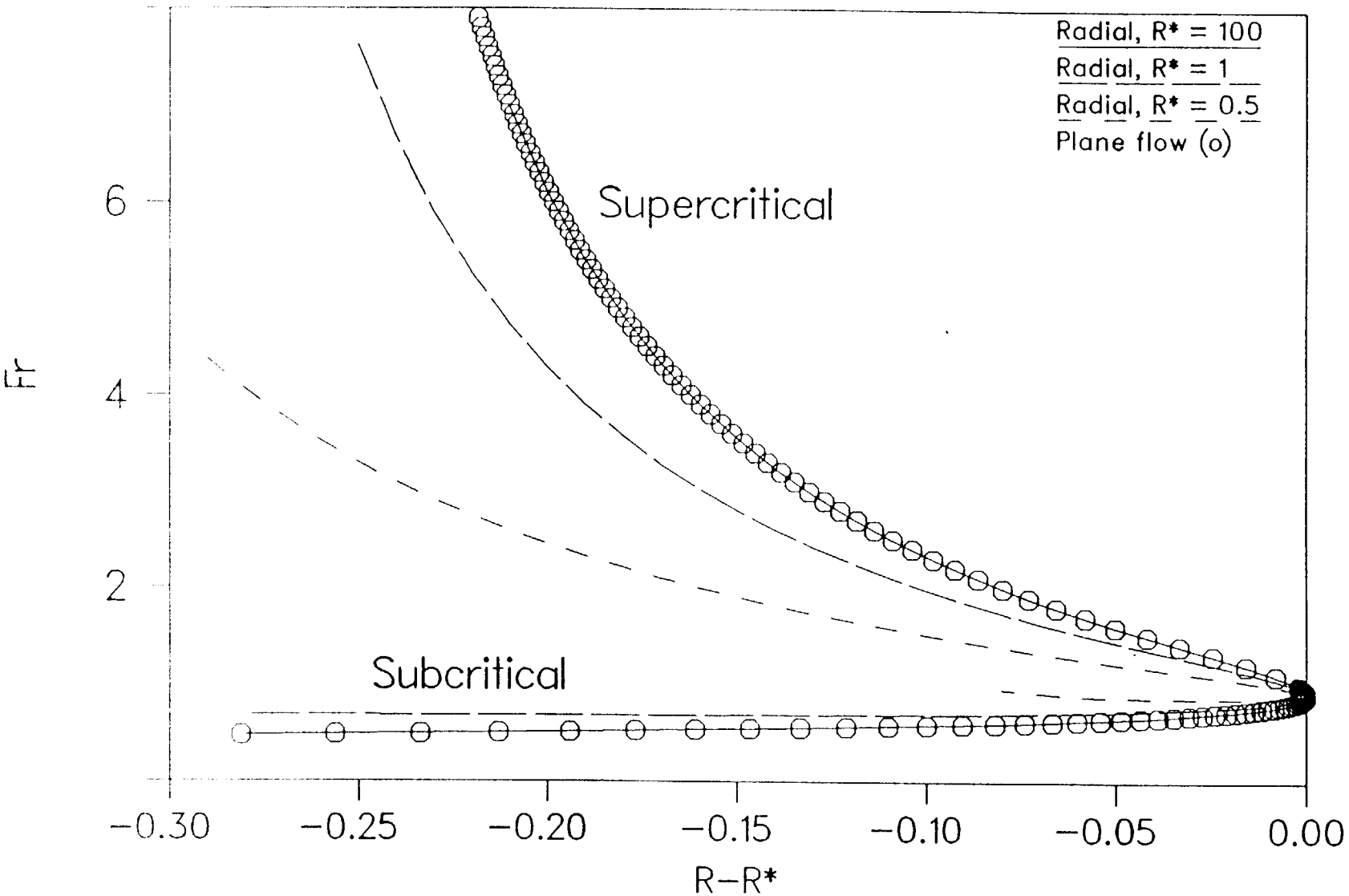

Fig. 6.5 Analytical solution for horizontal flow over a plate in the presence of gravity (parabolic velocity)

The ratio of the film height before and after the jump can be determined from a mass and momentum balance at the jump, which, in this case, turns out to be

$$\frac{\delta_2}{\delta_1} = \frac{1}{2}\left[\sqrt{1 + 9.6\ Fr_1^2} - 1\right] \tag{6.48}$$

where the subscript 1 indicates conditions before the jump and the subscript 2 indicates conditions after the jump. In comparing this relationship with equation (6.24) for uniform flow only the coefficient within the radical changes for the parabolic profile.

Plane flow in the presence of gravity is characterized by two independent dimensionless groups, namely, the Froude number and Reynolds number. Since the Reynolds number is lumped with other parameters in the definition of R, to see its effects more clearly, the plane flow solution is plotted again in Fig. 6.6 for different values of Reynolds number using $(z - z^*)/(\nu^2/g)^{1/3}$ as the abscissa. Note that for a small value of Reynolds number, the supercritical solution cannot be sustained for a large length of the plate. On the other hand, for the same Reynolds number, the subcritical solution may be present for any length of the plate. Also, the length for which a supercritical solution may be present increases with Reynolds number. So, for a given length of the plate and inlet Froude number, the length of the supercritical flow regime is directly dependent on the Reynolds number. For a large Reynolds number, the flow may be supercritical in the entire domain. With a decrease of the Reynolds number, a jump is expected to appear

ORIGINAL PAGE IS
OF POOR QUALITY

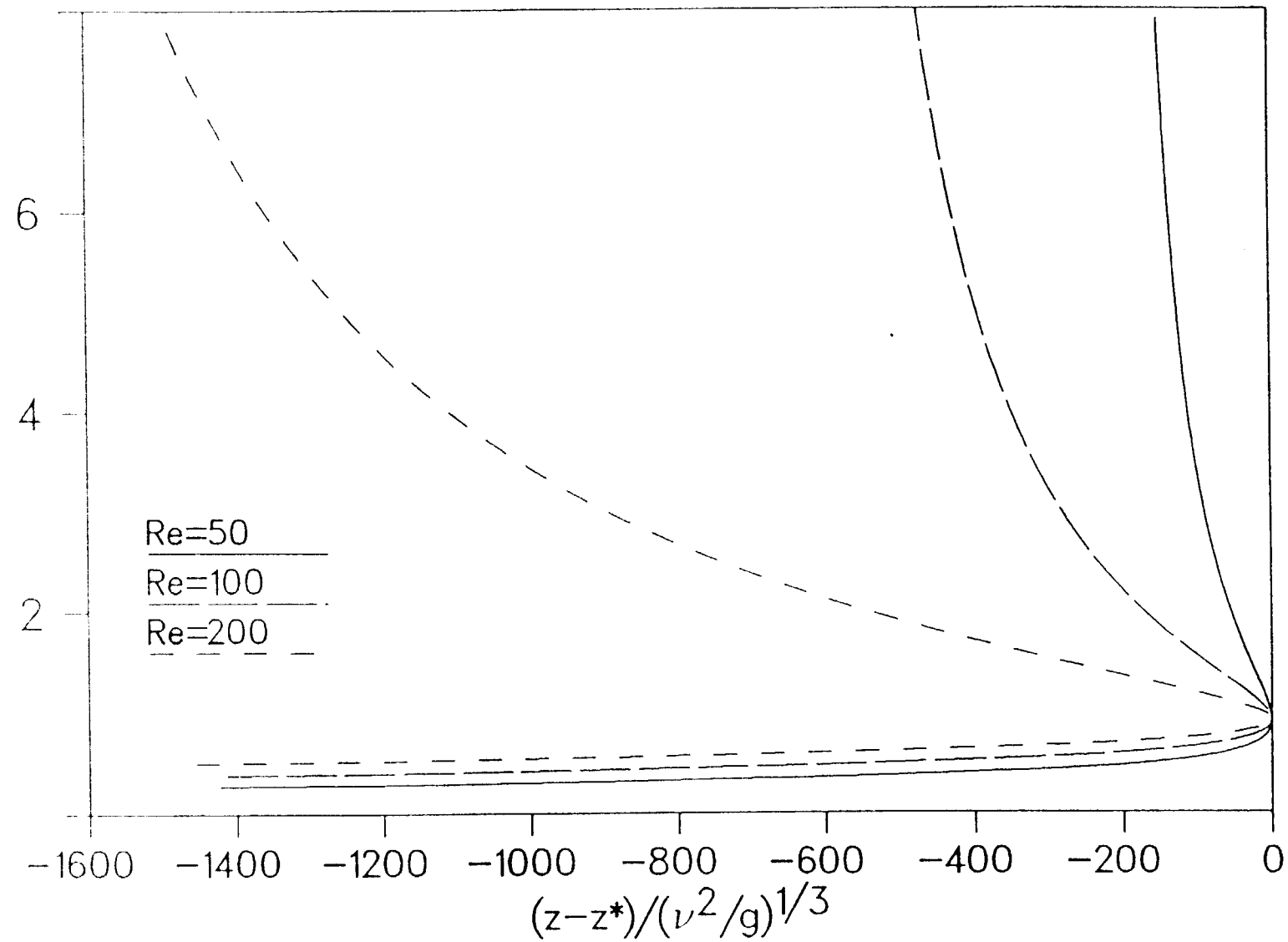

Fig. 6.6 Froude number distribution for plane flow over a plate in the presence of gravity

ORIGINAL PAGE IS
OF POOR QUALITY

with a subcritical regime. As the Reynolds number is reduced further, the jump may move all the way to the inlet, resulting in completely subcritical flow.

The figure also shows that if the flow enters the control volume with a higher Froude number, it may remain supercritical for a larger distance. The effect of gravity can be also analyzed. For a given flow rate and Froude number, $(z - z^*)$ is inversely proportional to $(g)^{1/3}$. So, for a smaller value of g, the length of the supercritical flow regime is expected to be longer. In the limiting case of zero gravity, a subcritical flow regime is not possible and the flow becomes entirely supercritical.

The predicted film height is compared with the previous numerical solution of Rahman et al. (1989a) for Re = 89, Fr_{in} = 8.6, Fr_{out} = 1.0 and L = 0.14 m in Fig. 6.7. The height in the supercritical region is slightly over-predicted, whereas in the subcritical region, the height becomes flatter than the numerical solution. In the numerical computation of Rahman et al. (1989a), a critical outflow condition is assumed to be present at the exit, whereas in the analytical solution this condition was not imposed.

6.5.4 Radial Flow in the Presence of Gravity

For radial flow in the presence of gravity, the equations of motion (6.34-6.36) can be expressed as,

ORIGINAL PAGE IS
OF POOR QUALITY

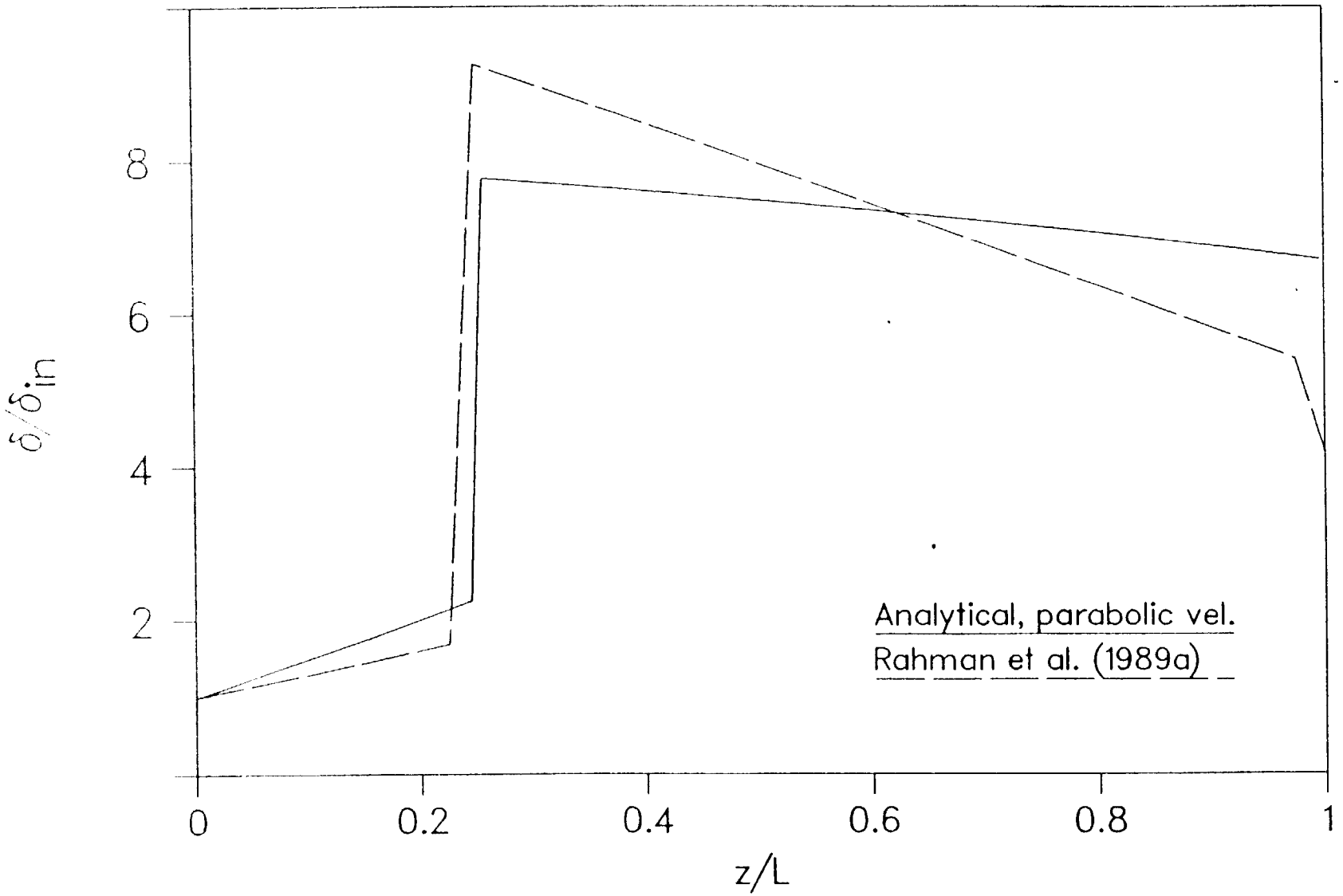

Fig. 6.7 Comparison of predicted film height with a previous result for plane flow in the presence of gravity

$$\left[\frac{5}{6} - Fr^2\right] \frac{dFr}{dR} = - \frac{5Fr + 3Fr^3}{6R} + \frac{15}{4} Fr^{11/3} \qquad (6.49)$$

$$\text{where } R = \frac{r}{\left[\frac{\nu^2}{g}\right]^{1/3} Re^{5/3}} \qquad (6.50)$$

Here, we can also notice that a critical condition is arrived at Fr = 0.913. This confirms that a critical condition in the flow depends on the velocity profile used for the analysis. The double-valued nature of the solution and the possibility of a hydraulic jump still exists. The solution is presented in Fig. 6.5 for different values of R^*. Analogous to plane flow, the critical radius R^* corresponds to Fr = 0.913. As discussed before, a smaller value of R^* indicates that the flow starts up at a smaller radius where the effects of curvature are important. This fact is quite evident in the figure. The curve for R^* = 100 coincides with the plane flow solution. At this situation, the effects of curvature is negligible. Also, at R^* = 0.5 and 1, the Froude number attains a minimum in the subcritical regime. This indicates that if a jump happens before that radial location, the film height may still increase in the subcritical region, attain a maximum and then diminish further downstream. This phenomenon is not present in plane flow and at flows with large values of R^*, where the film height decreases monotonically in the subcritical region. It can also be noticed that equation (6.49) reduces to equation (6.44) as $R \to \infty$. So, the plane flow may be treated as a limiting case of radial flow where $R \to \infty$.

6.5.5 Analysis of Heat Transfer

The heat transfer behavior can be solved by integrating equation

(6.37) with the substitution of equation (6.28) for the temperature profile.

Different thermal boundary conditions are considered in the present study. They are isothermal and uniform flux conditions at the solid wall and evaporation and pure heating without evaporation on the free surface. The heat transfer coefficient for these cases are defined as

$$h = \begin{cases} q_w / (T_w - T_b), \text{ for heating} \\ q_w / (T_w - T_{sat}), \text{ for evaporation} \end{cases} \qquad (6.51)$$

A general expression for the Nusselt number can be evaluated from equations (6.30-6.33).

$$Nu^* = \begin{cases} \dfrac{B}{\frac{5}{8} B + \frac{9}{20} C}, \text{ for heating} \\ \dfrac{B}{B + C}, \text{ for evaporation} \end{cases} \qquad (6.52)$$

A complete analytical solution is possible for the case of heating, when the free surface is assumed to be adiabatic in nature. For this case, $Nu^* = 2.5$ for both isothermal and uniform flux wall conditions.

Note that Nu^* is a function of heat transfer coefficient and film height, both of which change with location on the plate. A comparison of this result with the previous numerical solution of Rahman et al. (1989d) is shown in Fig. 6.8. For radial flow at zero gravity (Re =

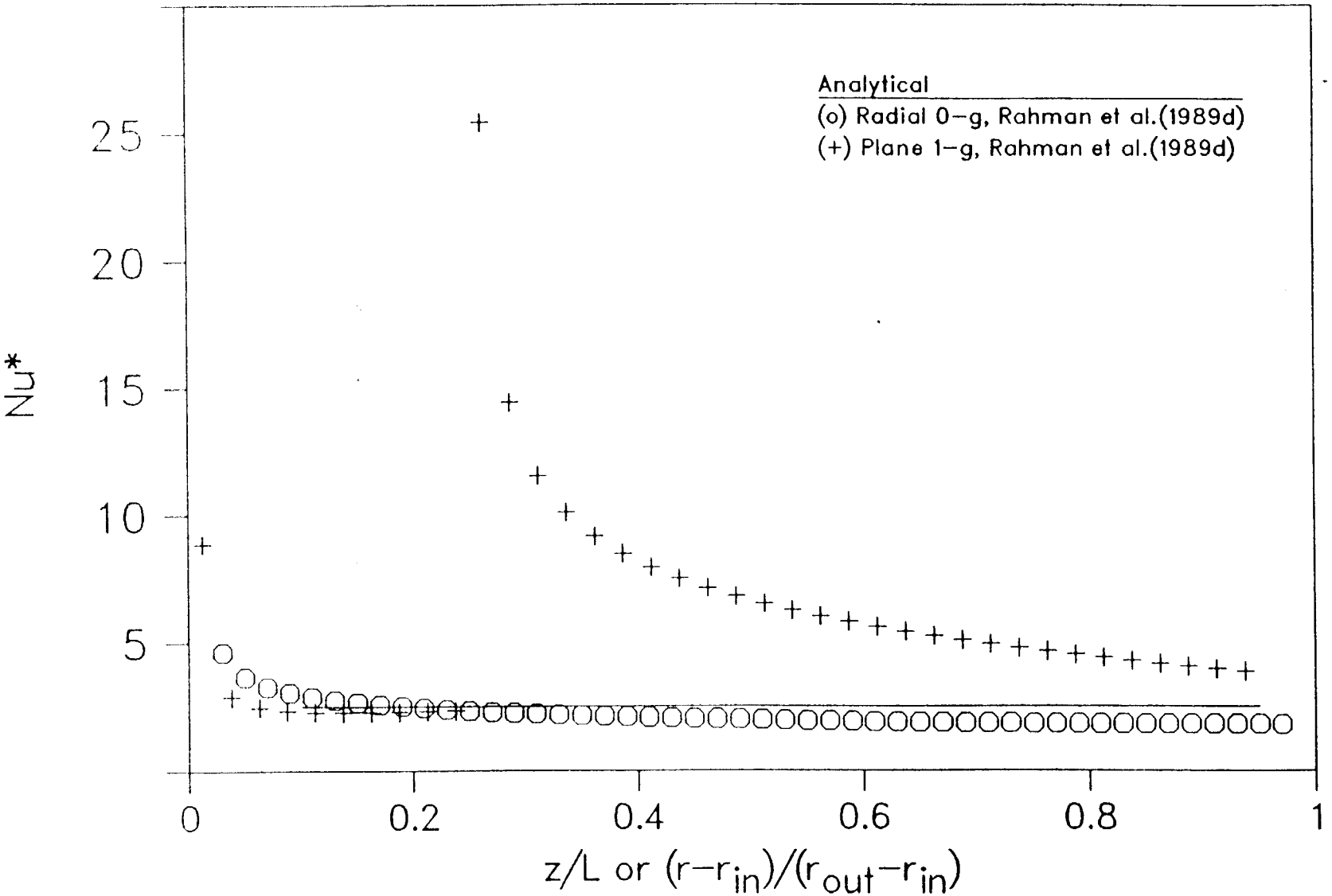

Fig. 6.8 Heat transfer coefficient for heating with no evaporation adjacent to a constant flux wall

404, Pr = 7, r_{in} = 0.05 m, r_{out} = 0.2 m, δ_{in} = 0.005 m, T_{in} = 20°C, q_w = 1000 W/m^2), the numerical Nusselt number starts at a higher value and then approaches an asymptotic limit as the flow moves downstream. This limiting value is somewhat lower that the analytical prediction. This indicates that the true temperature profile is somewhat flatter than the parabola assumed here. For plane flow in the presence of gravity (Re = 89, Fr_{in} = 8.6, Fr_{out} = 1.0, Pr = 7, L = 0.14 m, T_{in} = 20°C, q_w = 1000 W/m^2), the subcritical and supercritical heat transfer coefficients approach the analytically predicted value as the flow moves downstream with the development of the temperature profile.

For an isothermally heated wall with evaporation on the free surface, an expression for the Nusselt number can be derived by integrating equation (6.37) using equation (6.28) for the temperature profile and boundary conditions. The result is

$$Nu^* = 1 - \frac{C_0}{\left[\frac{T_{sat}}{T_w} - 1\right]} e^{\beta(z)} \qquad (6.53)$$

where $$\beta(z) = \frac{80}{7}\,\frac{\alpha}{\bar{q}} \int_0^z \frac{dz}{\delta} \qquad (6.54)$$

Here C_0 is the value of C at one location in the flow, where integration should start.

The expressions for Nu^* are true both for the cases where the gravity is finite and infinitesimally small. The actual heat transfer

ORIGINAL PAGE IS
OF POOR QUALITY

coefficient, however, will be different because of different distributions in the film height.

6.6 CONCLUSIONS

A systematic analysis of thin film flows in a zero gravity and non-zero gravity environment is performed and their implications in a real flow problem under micro-gravity conditions is discussed. The analysis is carried out in two parts. First, the hydrodynamics of the flow is studied for uniform one-dimensional velocity with any given friction factor. Next, the flow field and heat transfer coefficient are determined using the Pohlhausen integral method.

It is found that in the complete absence of gravity, the flow is supercritical, where even for a relatively small, but not negligible gravity, two potential flow regimes - supercritical and subcritical may be present. The two regimes are separated by a jump where large changes of film height take place. In the presence of friction, both supercritical and subcritical flows move towards a critical condition. The flow regime is characterized by the Froude number, whereas the Reynolds number indicates the relative importance of the inertial and viscous effects.

For plane flow, it is found that in the absence of gravity, the film height increases linearly with distance. When gravity is present, the film height increases monotonically in the supercritical region, encounters a jump and then decreases further downstream in the subcritical region. The heat transfer coefficient in this situation is

ORIGINAL PAGE IS
OF POOR QUALITY

characterized by $Nu^{*} = 2.5$, both for isothermal and uniformly heated walls with no evaporation from the free surface.

For radial flow it is found that in addition to the Froude and Reynolds numbers, the inlet radius is an important parameter, which carries the effects of curvature in the flow. At large values of the inlet radius, a plane flow situation is approached. Here, in the presence of gravity, the film height may increase or decrease depending on the flow rate, radial location and Froude number. The comparison of the results with previous numerical solutions shows reasonably good promise that the analytical method presented here can act as a useful tool to easily obtain approximate results for any given flow situation in a normal gravity or microgravity environment.

Section VII

COMPARISON OF THEORETICAL PREDICTION AND EXPERIMENTAL DATA

7.1 SUMMARY

The theoretical models developed in earlier sections are improved and a systematic procedure to compute the free surface flow of a thin liquid film is suggested. The solutions for axisymmetric radial flow on a stationary horizontal disk and that when the disk is rotating around its axis are presented. The theoretical predictions are compared with the experimental data presented in Section II of this report. The details of the flow field are also presented for the stationary disk, which shows flow separation near the location of the jump. The effects of surface tension are found to be important near the outer edge of the disk where the fluid experiences a free fall. At other locations, the surface tension is negligible. For a rotating disk, the frictional resistance in the angular direction is found to be as important as that in the radial direction.

7.2 INTRODUCTION

The appropriate design of a rotating absorber unit for a heat pump, a rotating condenser or evaporator, or the proper method of spin coating deposition on a metal surface all require an understanding of thin film flows over a horizontal rotating surface. Moreover, the impingement of a liquid jet on a solid wall that leads to the formation of a thin film is found in many engineering devices. These free surface flows are sometimes associated with a hydraulic jump where two different flow regimes are encountered at the upstream and downstream sides of the jump. The flow structure around a hydraulic jump is usually complicated in nature, the understanding of which is essential from both theoretical and practical points of view.

The radial spreading of a liquid jet impinging on a flat horizontal surface was studied by Watson (1964). Both analytical and experimental studies of laminar and turbulent flows were made. A hydraulic jump was found to be present under some flow conditions. The analysis covered the supercritical region before the jump where four different flow regimes were identified and analyzed using the Pohlhausen integral method and a similarity transformation. In the subcritical region, the film height was assumed to be constant. For a given location of the jump, the subcritical height could be also predicted.

The heat transfer to a thin film formed by an impinging liquid jet was considered by Chaudhury (1964). His analysis basically followed the ideas introduced by Watson (1964) except that the energy equation was solved. In the region away from the impingement location where a similarity solution

of the momentum equation was possible, the energy equation was solved in a closed form including the effects of viscous dissipation. An approximate solution for the simultaneously developing hydrodynamic and thermal boundary layers were also obtained using the integral method where the temperature profile was approximated by a fourth-order polynomial. Nusselt numbers for different values of the Prandtl number were presented for both the regions.

The laminar flow of a thin film adjacent to a horizontal rotating surface was studied by Rauscher et al. (1973). An asymptotic expansion technique was used to develop an approximate solution where the radial spread of fluid was perturbed to determine the effects of convection, Coriolis acceleration, radial diffusion, surface curvature and surface tension. The physical significance of these higher-order effects were also discussed.

The transient behavior of the film when the rotation is started from an initial stationary condition was examined by Higgins (1986). Both low and high Reynolds number flows were considered. An asymptotic expansion technique was used to develop analytical solutions valid for short and long time scales. His results were valid only when the thickness of the boundary layer is small compared to that of the film. The thin film flow of a non-Newtonian fluid adjacent to a rotating surface was considered in the study of Matsumoto et al. (1982). An integral method was used where the velocity profile across the thickness of the film was approximated by a polynomial.

ORIGINAL PAGE IS
OF POOR QUALITY

The condensation of a saturated vapor onto a rotating horizontal surface was investigated by Sparrow and Gregg (1959). The governing momentum and energy equations were simplified to a set of ordinary differential equations by using a similarity transformation. The equations were then integrated numerically to predict the condensate layer thickness and heat transfer coefficient along with the temperature and velocity profiles. The evaporation of a thin film on a rotating surface was studied by Butuzov and Rifert (1973). Closed-form solutions were derived for the film thickness and heat transfer coefficient.

In all the studies mentioned above, the investigators have developed analytical models for the phenomenon of the radial spread of fluid with or without rotation. Most of these models are for a thin film generated by the impingement of a liquid jet which is characterized by the jet velocity and its diameter. Therefore, they cannot be readily applied to a situation where the film is generated by a discharge from a pressurized container in the center of the disk. Moreover, none of these models handle very well the hydraulic jump associated with these flows. The studies by Watson (1964) and Chaudhury (1964) analyze in detail the supercritical region before the jump, but make a simple assumption that the film height after the jump remains constant, which is not true in reality. A systematic investigation of thin film flows discharged from a pressurized container in the center of the disk has been carried out recently by Thomas et al. (1989) (described in section I of this report), Rahman et al. (1989a) (described in section III of this report) and Rahman et al. (1989c) (described in section V of this report). These studies considered both supercritical and subcritical flow regimes and used numerical techniques to

develop computational procedures for thin film flows.

Thomas et al. (1989) approximated the flow to be one-dimensional in nature by neglecting any variation of velocity across the thickness of the film. The continuity and momentum equations were integrated across the thin film to develop a single equation for the film velocity. The resistance to the flow due to wall shear stress was expressed in terms of a friction coefficient. Suitable expressions for the friction coefficient were developed for regions close to the entrance where the thickness of the momentum boundary layer is small compared to film thickness, and for regions far away from the entrance where viscous effects propagate all of the way across the film. These regions were matched where the two friction coefficients yielded the same results. The equation of motion was solved numerically using the MacCormack predictor-corrector method. Results were obtained for both stationary and rotating disks for a number of inlet Reynolds, Froude and Rossby numbers. In the presence of the jump, the outlet Froude number was always assumed to be unity to simulate a situation where the fluid experiences a free fall over the edge of the disk due to gravity. It was found that jump moves downstream and may get washed away with an increase in the flow rate, angular velocity and inlet Froude number.

The studies by Rahman et al. (1989a and 1989c) solved the flow field numerically using a boundary-fitted coordinate system. No assumption regarding the velocity variation or friction coefficient were required. The studies, however, covered only the case of a stationary disk. Since the height of the free surface is dependent on the flow conditions and is

not known ahead of time, an iterative procedure had to be used to determine the correct location of the free surface. The method presented by Rahman et al. (1989a) in section III of this report is termed as the 'pressure optimization method'. In this method, the shape of the free surface was assumed to be described by an algebraic equation with two or more arbitrary constants. The constants were optimized using an exhaustive search technique that minimized the difference between the computed free surface and ambient pressures. The method was found to be very satisfactory for zero-gravity flows, which was the primary emphasis in that paper. However, in the presence of gravity when a jump existed in the flow field, the method required the supercritical and subcritical flows to be computed separately, and the solutions were matched at the location of the jump. Even though this procedure yielded correct results in regions away from the jump, it could not account for the details of the flow field in the vicinity of the jump. This drawback was removed in the subsequent study by Rahman et al. (1989c).

The method developed by Rahman et al. (1989c) in section V of this report is termed as the 'porous wall method'. In this method, the free surface was assumed to be a permeable wall through which fluid particles may leave or enter the control volume depending on the difference between the fluid and ambient pressures. The shape of the surface was corrected in successive iterations until the free surface conformed to a streamline and the penetration through the surface reduced to zero. This method computed the whole flow field as a single domain preserving the details of the flow in the jump region. The computed flow field, friction and heat transfer coefficients were reported in that paper.

The purpose of the present investigation is twofold. First, to compute the flow field using the methods developed by Thomas et al. (1989) and Rahman et al. (1989a and 1989c) for the experimental conditions reported in Section II of this report. The theoretical and experimental results can then be compared to find the merits and drawbacks of the different prediction methods. The second objective of this work is to improve the existing theoretical models and to suggest a systematic computational procedure for thin film flows adjacent to a stationary or rotating disk.

7.3 EQUATIONS OF MOTION

The body-fitted coordinate system used for the two-dimensional numerical computation is shown in Fig. 7.1. The local coordinates are directed along lines connecting the centers of the adjacent grid cells. The z-axis is directed along the direction of radial spread, i.e., the main direction of flow. The y-axis is directed across the thickness of the film. The height of the free surface from the solid wall is denoted by δ, which varies with radial location on the plate.

The equations governing the conservation of mass and momentum in a thin liquid layer involving a Newtonian, constant-property fluid can be written as

$$\nabla \cdot \vec{V} = 0 \tag{7.1}$$

$$\frac{D\vec{V}}{Dt} = -\frac{1}{\rho}\nabla p + \nu \nabla^2 \vec{V} + \vec{g} \tag{7.2}$$

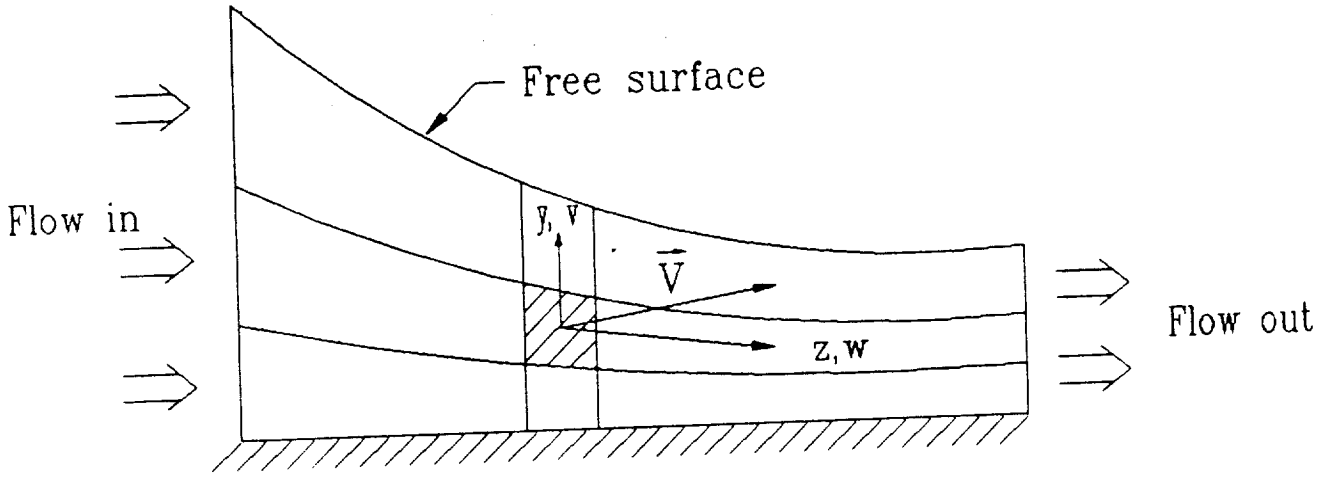

Fig. 7.1. The coordinate system on a grid cell

The boundary conditions are given by:

$$\text{at entrance:} \quad \vec{V} = \vec{V}_{in}, \quad \delta = \delta_{in} \tag{7.3}$$

$$\text{at exit:} \quad \begin{cases} \vec{V} = \vec{V}_{out}, \quad \delta = \delta_{out}, \text{ for stationary disk} \\ \dfrac{\partial \vec{V}}{\partial n} = 0, \quad \text{for rotating disk} \\ p = \rho g \, (\delta - y) \end{cases} \tag{7.4}$$

$$\text{at solid wall:} \quad \vec{V} = \begin{cases} 0, \text{ for stationary disk} \\ \vec{V}_w, \text{ for rotating disk} \end{cases} \tag{7.5}$$

$$\text{at free surface:} \quad \frac{\partial \vec{V}}{\partial n} = 0, \quad p = 0 \tag{7.6}$$

Here n is the coordinate directed normal to the surface under consideration. The p = 0 condition at the free surface is arrived at from a balance of normal stresses where the effects of surface tension and other stresses except for pressure is neglected. This is valid for a thin film flow with large values of the Reynolds and Weber numbers.

7.4 Flow on a Stationary Disk

The situation where the disk is stationary with fluid emanating at the center and spreading out uniformly in the radial direction is considered first. Four sets of experimental data with flow rates ranging from 7 to 15 lpm were taken where the film height was measured in the supercritical and subcritical regions. The measured data for 7 lpm and 11 lpm are plotted in

Figs. 7.2 and 7.3, respectively, where it is compared with the one-dimensional numerical solution by Thomas et al. (1989). It can be noticed that the experimental data compare reasonably well with the numerical solution in the supercritical region, but does not compare well in the subcritical region. The height of the jump is also not correctly predicted. In the numerical algorithm proposed by Thomas et al. (1989), the outflow from the disk was simulated by assigning a Fr = 1 condition at that location. When the fluid flows out of the disk and experiences a free fall, the subcritical flow has to transform to supercritical flow, and a critical condition should exist somewhere in the vicinity of the outlet. However, assigning Fr = 1 at the outlet does not seem to be adequate in this case. From the figure, it can be also noticed that the measured height is higher than the critical height, which suggests that the film is held up by some sort of external force. It can be recalled here that in all previous computations, the surface tension was neglected in all regions of the flow, which may not be correct near the exit since an appreciable curvature of the free surface is encountered due to the rapid turning of the flow.

In the presence of surface tension, the fluid and ambient pressures can be related by the equation

$$p_e - p_a = \frac{2\sigma}{R} \tag{7.7}$$

where $\hat{R}$ is the radius of curvature. If the pressure is assumed to be hydrostatic in nature, this equation can be expressed in terms of film height, as

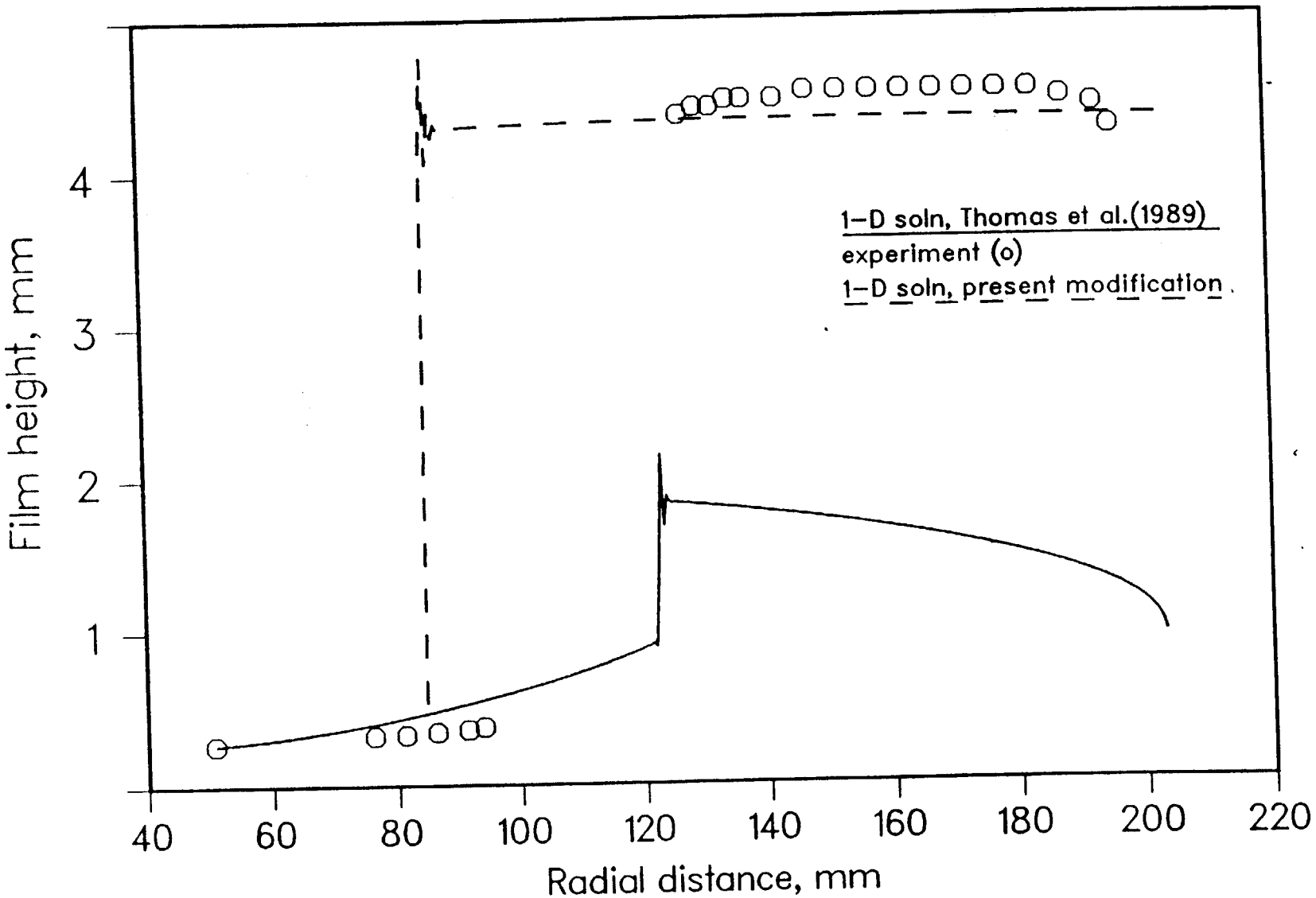

Fig. 7.2 Comparison of experiment with one–dimensional numerical prediction for stationary disk (flow rate = 7 lpm)

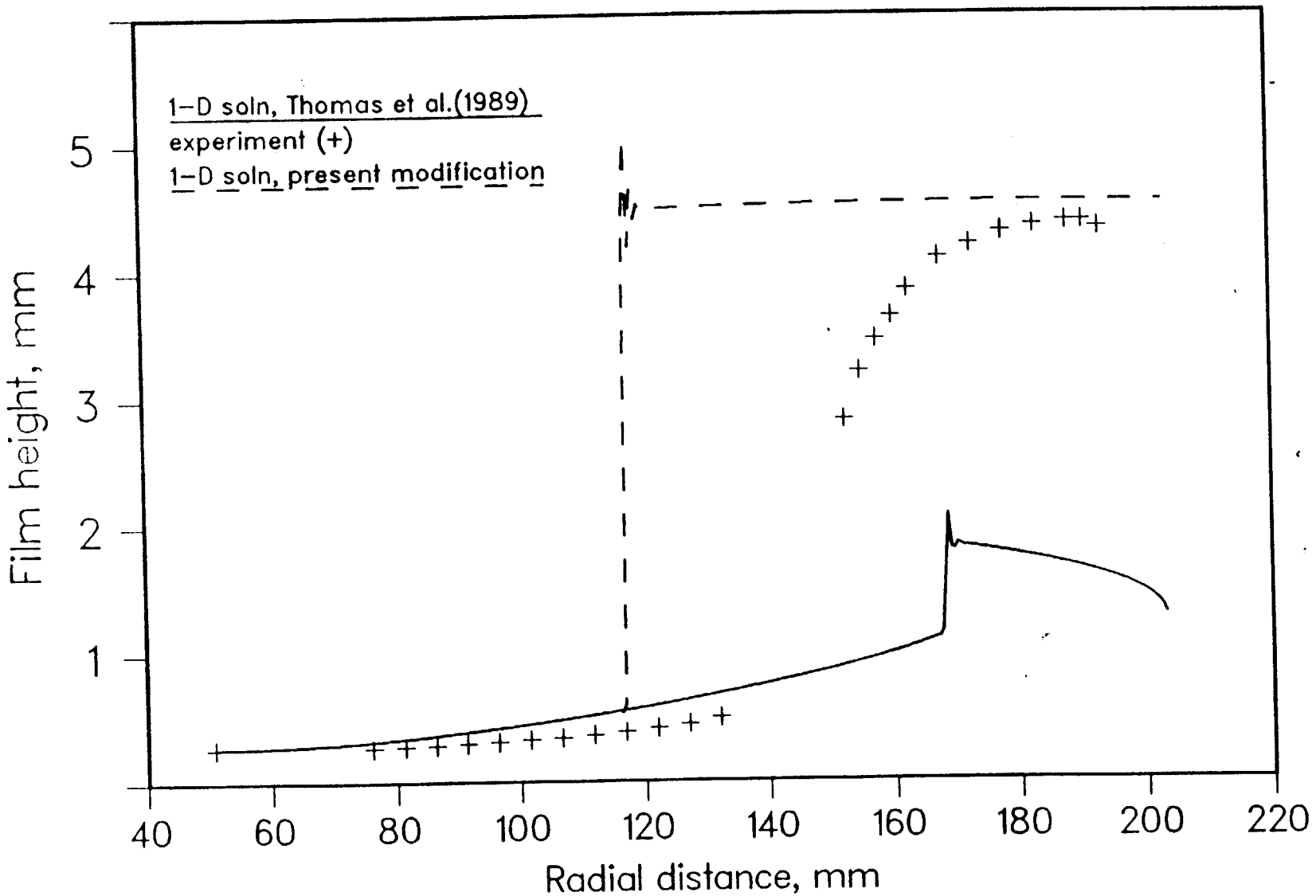

Fig. 7.3 Comparison of experiment with one–dimensional numerical prediction for stationary disk (flow rate = 11 lpm)

$$\delta_e = \delta^* + \frac{2\sigma}{\rho g \hat{R}} \tag{7.8}$$

where δ_e is the actual film height at the exit, and δ^* is the critical height predicted by the Fr = 1 condition at the exit. To solve this equation, an estimate for $\hat{R}$ is required, since that is unknown in general. In the case of the stationary disk, we may assume that the thickness of the film remains approximately constant in the region where the flow changes its direction from horizontal to vertical. This means that the radius of curvature remains of the same order as the film height. Substituting $\hat{R} = \delta_e$ and solving for it, we obtain

$$\delta_e = \frac{\delta^* + \sqrt{\delta^{*2} + \frac{8\sigma}{\rho g}}}{2} \tag{7.9}$$

where $\delta^* = \left[\frac{Q}{2\pi r_{out}\sqrt{g}}\right]^{2/3}$

Equation (7.9), even though quite approximate in nature, seems to give a good estimate of film height at the exit. This is demonstrated in Table 7.1, where the height calculated by equation (7.9) is compared with the measured height at the last data point from the exit where measurement was reliable. The deviation is within 10%. From Table 7.1, it can also be noticed that the deviation has a sign change and increases with the flow rate. When the flow rate is increased, the fluid particles move over the disk with a larger amount of inertia and get swept away further before experiencing the falling motion due to gravity. This increases the radius of curvature of the free surface and thereby decreases the effects of

Table 7.1: Comparison of Calculated and Measured Film Height at Outlet for a Stationary Disk

Flow rate (lpm)	Measured Height (mm)	Calculated Height (mm)	Deviation (%)
7	4.4196	4.3378	-1.85
9	4.318	4.4357	2.73
11	4.369	4.5284	3.65
13	4.216	4.617	9.51

surface tension. So, using $\hat{R} = \delta_e$ overestimates the film height near the exit. The opposite is true for a smaller flow rate. The estimate, however, is reasonable considering the simplicity of the formulation.

The computed result with $\delta = \delta_e$ at the exit with the same inlet condition as the experiment is shown in Figs. 7.2 and 7.3 for flow rates of 7 and 11 lpm, respectively. Now, the subcritical film height compares reasonably well with the experimental data. In the supercritical region, the height remains the same as that computed by the original procedure of Thomas et al. (1989). The location of the jump moves further upstream for both flow rates. The measured location of the jump is found to be somewhere in between the two numerical results. It can also be noticed that the one-dimensional solution simulates the jump as a sudden rise of film height that occurs across a single grid cell. In reality, the jump occurs somewhat more gradually, which in our experiment spanned over a length of 6-25 mm. Even with these drawbacks, the one-dimensional numerical solution developed by Thomas et al. (1989) may be used for a quick estimate of the subcritical and supercritical film height distribution if the modification of the outlet boundary condition proposed here is incorporated.

The experimental data for 7, 9, and 11 lpm are compared with the two-dimensional numerical solutions of Rahman et al. (1989a and 1989c) in Figs. 7.4, 7.5, and 7.6, respectively. Here, we have used the first and last data point as the inlet and outlet conditions for the numerical computation. The computed results by the method of Thomas et al. (1989) are also shown here for a relative comparison. In the two-dimensional numerical solution by Rahman et al. (1989a, 1989c), the velocity profile at

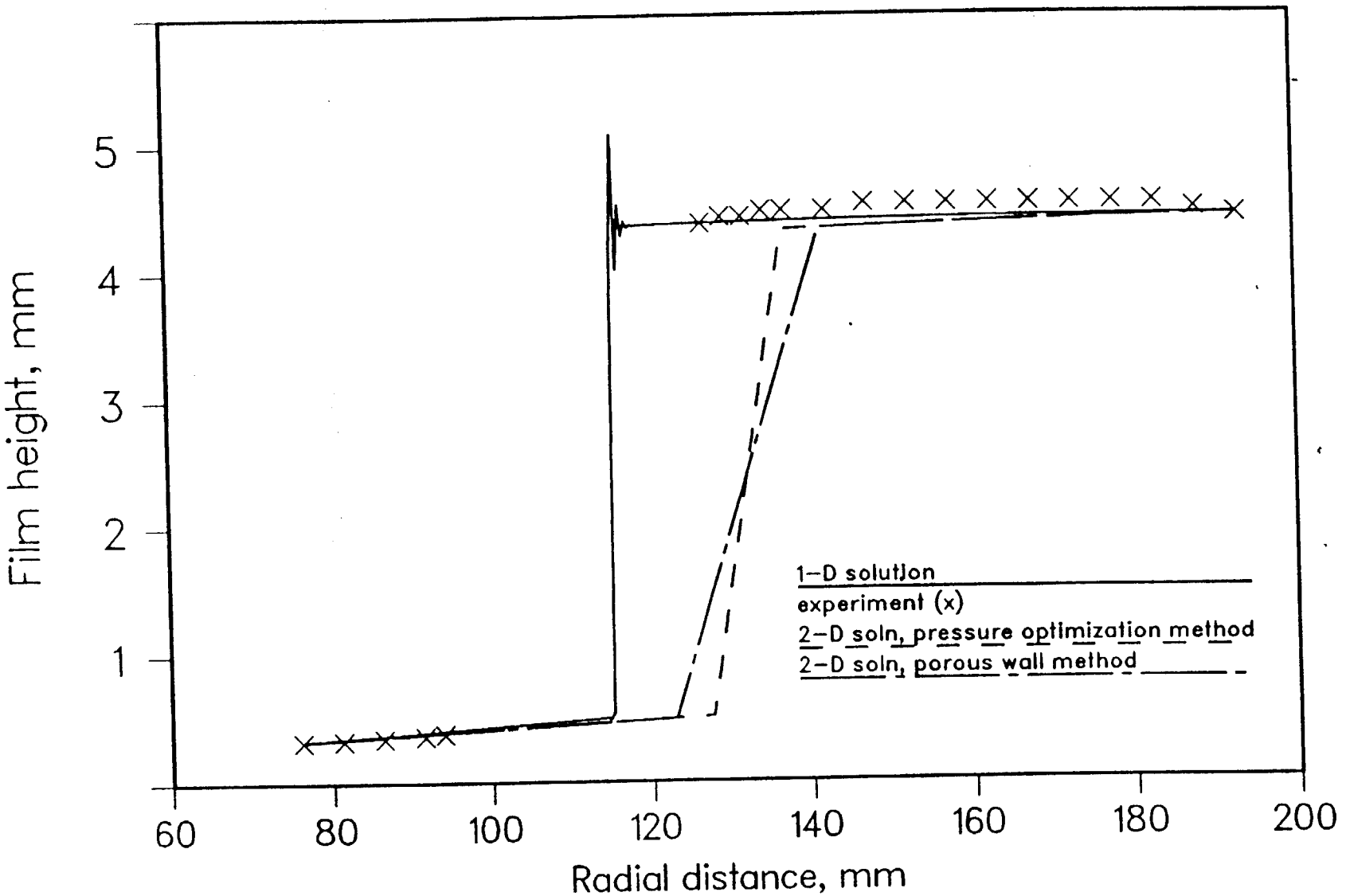

Fig. 7.4 Film height distribution over a stationary disk at flow rate of 7 lpm

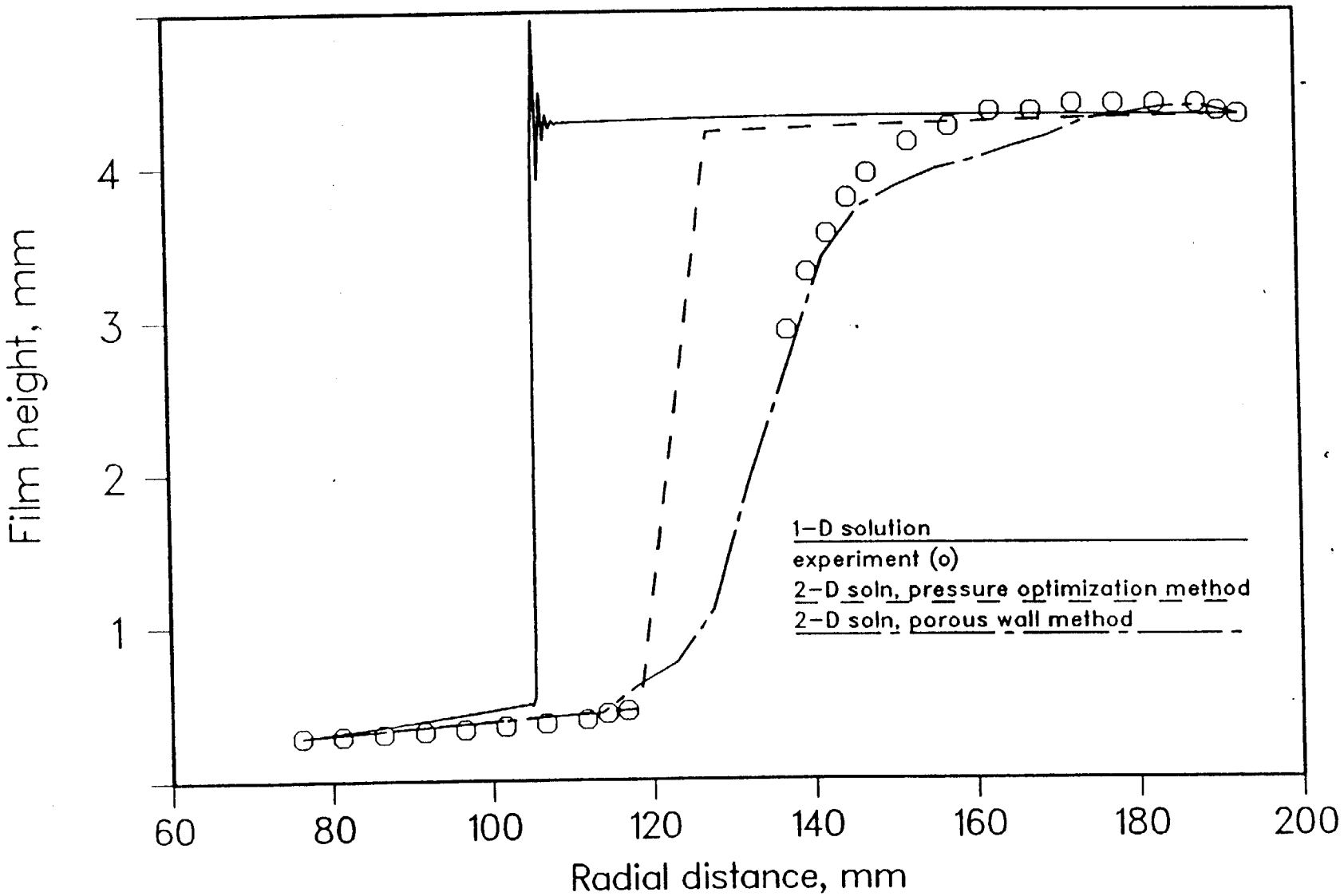

Fig. 7.5 Film height distribution over a stationary disk at flow rate of 9 lpm

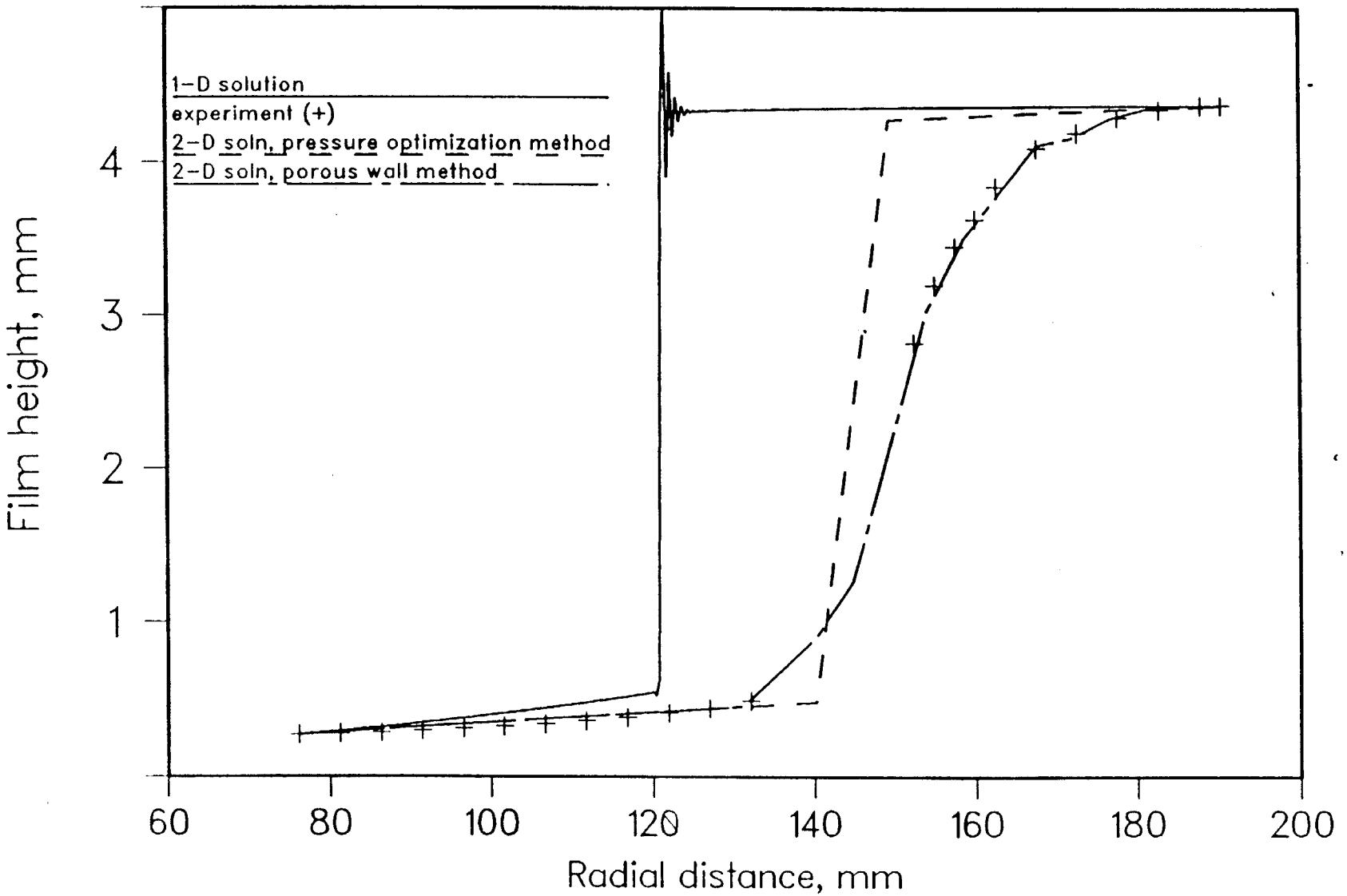

Fig. 7.6 Film height distribution over a stationary disk at flow rate of 11 lpm

the entrance is assumed to be parabolic in nature with a maximum at the free surface. This condition is not present in our experiment since the flow comes through a slot before being discharged onto the disk. So, at the entrance the maximum is expected to be somewhere halfway between the solid walls. After a short distance from the entrance, the flow is expected to evolve to a parabolic profile with the maximum velocity at the free surface, since the no-slip condition exists on the solid wall and the zero-shear condition is present on the free surface. Therefore, using the first measured data point as the entrance instead of the physical inlet is more justified for comparison with the two-dimensional numerical solution. Also, analogous to the one-dimensional solution of Thomas et al. (1989), Rahman et al. (1989a and 1989c) used Fr = 1 to simulate the outflow condition from the disk. As we have already discussed, this is erroneous and the height (or Froude number) at the exit needs to be estimated taking into account the surface tension effects. Equation (7.9) can be applied for this purpose. Since the effects of the surface tension at the outflow location have been already demonstrated in Figs. 7.1-7.2, in these computations the actual experimental measurement has also been used for the exit boundary to eliminate any error associated with the theoretical estimate.

It can be seen that the 'pressure optimization method' developed by Rahman et al. (1989a) predicts the correct location of the jump. The film height in the supercritical and subcritical regimes are also very well predicted. In this method, the supercritical and subcritical flows are computed separately by strictly imposing the inlet and outlet boundary conditions, respectively. The solutions are then matched at the jump

location by preserving the conservation of mass and momentum at the jump. In the original method, the jump happens instantly across one grid cell. In the solution presented here, we have modified it to allow the jump to form across a number of cells that result in a minimum overall pressure difference between the fluid and the ambient. The location for the initiation of the jump was kept the same and only cells at the downstream side were added to it. The quantity optimized was still the RMS error in the free surface pressure normalized by the initial total head (see Rahman et al., 1989a). In this process, both the supercritical and subcritical regimes were considered together along with the jump region. The solutions plotted in Figs. 7.4- 7.6 correspond to the slope of the jump that resulted in the minimum RMS error of the free surface pressure. The figures indicate that the two-dimensional solution predicts the location and slope of the jump somewhat better than the corresponding one-dimensional solution. So far as the location of the jump is concerned, the one-dimensional solution appears to be good for 7 lpm, but it predicts the jump at a radial location closer to the inlet for both 9 and 11 lpm.

Even though the modified 'pressure optimization method' gives the gross structure of the jump, the details of the free surface in the jump region can only be obtained by using the 'porous wall method' developed by Rahman et al. (1989c). In this method, the local free surface height is changed in each iteration depending on the local velocities at the free surface. Moreover, a global variation is taken into account by minimizing the overall rate of penetration through the free surface. The surface evolves by itself as the iteration proceeds and the solution corresponding to the minimum rate of penetration is taken to be final. It can be noted

in Figs. 7.4-7.6 that the film height predicted by the 'porous wall method' most closely matches the experimental data, particularly in the jump region. As mentioned by Rahman et al. (1989c), the 'porous wall method' is quite sensitive to the initial guess of the free surface height distribution and has rather slow convergence characteristics. So, the best prediction approach one can follow is to use the 'pressure optimization method' first to get the gross structure of the jump, and refine that prediction using the 'porous wall method'.

The details of the flow field for the flow rate of 11 lpm is shown in Fig. 7.7. It can be noticed that the velocity profile is parabolic at r = 0.108 m. This location corresponds to the supercritical region. Here the flow is well-structured with the maximum velocity at the free surface. This is the typical velocity profile in most of the supercritical region. However, as the jump is approached and the film height increases, the free surface tends to experience more and more force due to the gravitational head, and the location of the maximum velocity moves down from the free surface to somewhat inside the film. This can be seen in the vector plot centered around r = 0.153 m, where the jump has already started. After initiation of the jump the flow also loses inertia rapidly due to the sudden change in film height. Flow separation is encountered both at the solid wall and on the free surface, which can be noticed in both plots corresponding to r = 0.153 and r = 0.167 m. The separation from the solid wall is due to frictional resistance and was previously seen in the experimental work of Nakovyakov et al. (1978) and the numerical computation of Rahman et al. (1989c). Nakovyakov (1978) actually measured the wall shear stress for a circular hydraulic jump of a thin liquid film and found

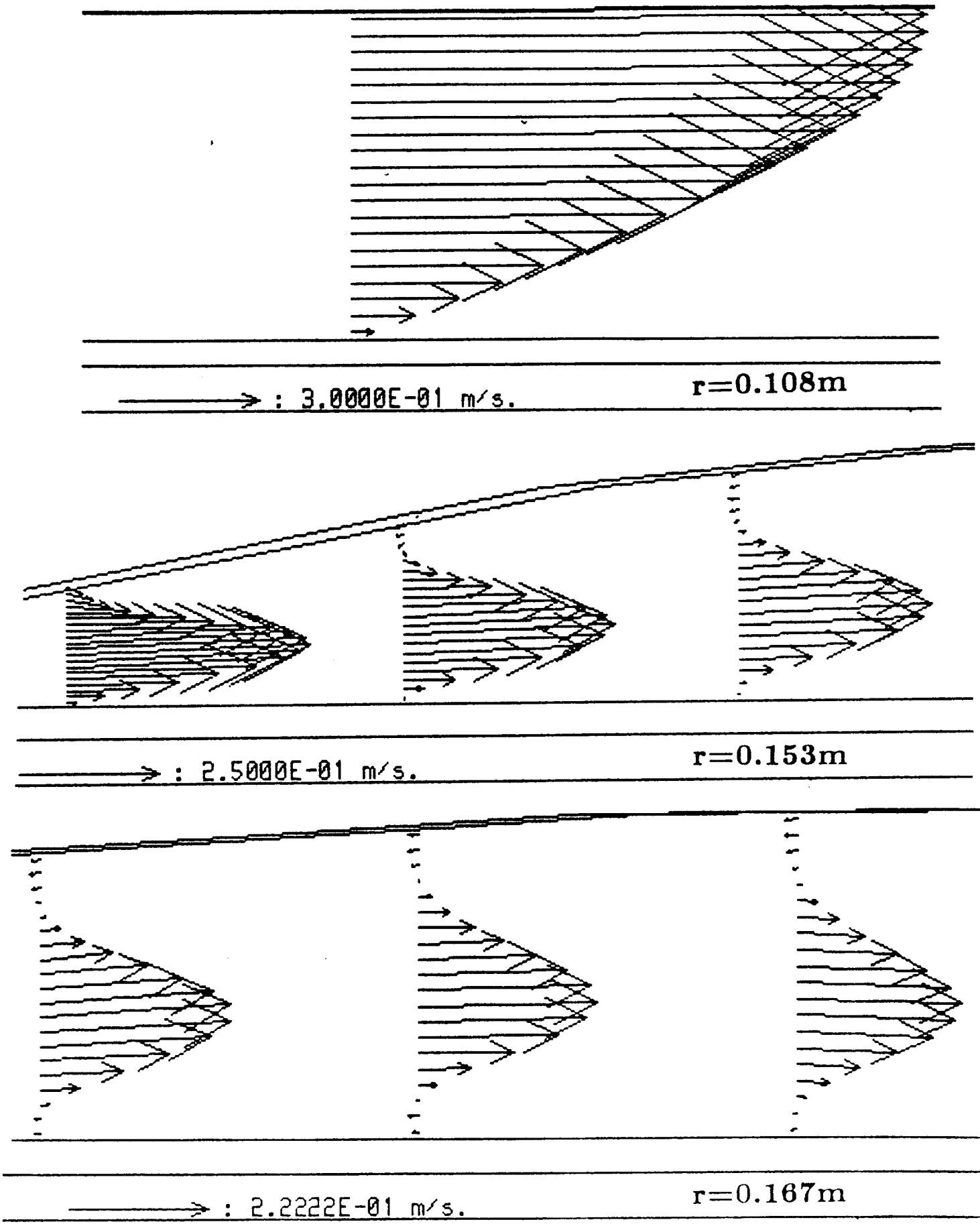

Fig. 7.7 Velocity vectors for thin film flow adjacent to a stationary disk (flow rate = 11 lpm)

it to be negative for a short distance downstream from the location of the jump. Rahman et al. (1989c) reported a numerically computed friction coefficient that was negative in the vicinity of the jump. The flow reattaches to the surface after some distance in the subcritical region. The separation of the flow at the free surface is due to the gravitational pressure gradient and is more commonly termed as a 'surface roller' in the hydraulics literature (Rajaratnam (1967), for example). This roller was not observed previously in other investigations on thin film flows. The reason was that a jump in a thin film flow was believed to be an instantaneous phenomenon and was modeled accordingly, so the details of the flow structure at the jump could not be captured. This phenomenon can be seen when the jump is allowed to develop gradually over a distance. In Fig. 7.7, it can also be noticed that the surface roller starts up at an earlier location and covers a larger region than the separation eddy near the solid wall. As seen in Fig. 7.6, the length of the subcritical region for this flow rate is quite small. If sufficient length is allowed, the flow again develops to a regular parabolic structure with the zero velocity at the solid wall and the maximum velocity at the free surface.

7.5 Flow on a Rotating Disk

When the disk rotates about its axis, in addition to inertial, gravitational and viscous forces, the centrifugal and Coriolis forces shape the flow structure as it moves downstream. For an appreciable rotational velocity (as is considered in our experiment), the subcritical flow region is swept out from the disk and no jump can be present. It may be recalled here that the length of the subcritical flow regime was small even with a stationary disk. If a disk of much larger diameter was considered, a jump

could be possible at a smaller rate of rotation.

We first consider the data corresponding to an intermediate flow rate and angular velocity (11 lpm, 100 rpm), which are plotted in Fig. 7.8 along with the theoretical prediction of Thomas et al. (1989). It can be noticed that the numerically determined film height is reasonable at smaller radii, but seems to deviate from the measurement at larger radii. Both the experimental measurements and the theoretical computation show that the film height increases downstream, attains a peak and then decreases. The experimental data also shows an increment of height near the exit. This increment is believed to be caused by the surface tension as discussed earlier in this section. The effect of surface tension is smaller for a rotating disk than that for a stationary disk since the flow moves over the disk with a higher velocity and results in a larger radius of curvature. In the numerical solution of Thomas et al. (1989), the flow was assumed to be strictly radial in nature with a superimposed solid-body rotation. The resistance to the flow due to friction was taken to be the resistance in the radial direction. In the azimuthal direction, the velocity remained constant all across the thickness of the film with no resistance from the solid wall. In reality, however, the velocity is expected to change due to the finite viscosity of the fluid, so there will be frictional resistance from the wall in the azimuthal direction.

To account for the frictional resistance due to the angular velocity, we may define the total shear stress as

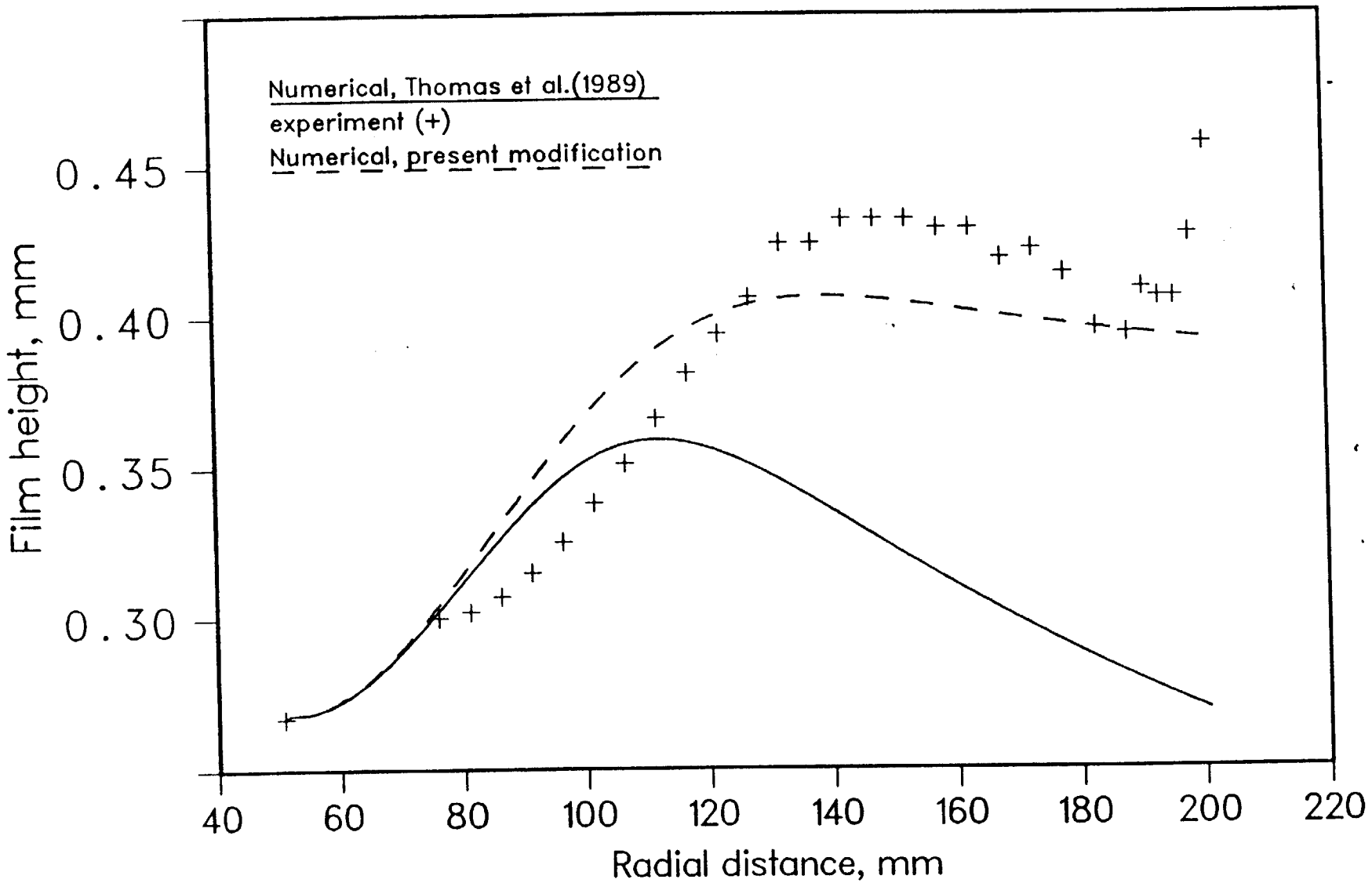

Fig. 7.8 Comparison of experiment with numerical solution of rotating disk (flow rate = 11 lpm, rpm = 100)

$$\tau_w = \sqrt{\tau_\phi^2 + \tau_r^2} \qquad (7.10)$$

Here $\tau_r = c_f\ (1/2\ \rho\ W^2)$, where c_f can be calculated by using the Blasius or parabolic solution given by Thomas et al. (1989). τ_ϕ can be estimated from the exact solution of laminar flow adjacent to a rotating disk in an infinite extent of fluid. As given by Schlichting (1979),

$$\tau_\phi = 0.6\ \rho r\ \nu^{1/2}\ \omega^{3/2} \qquad (7.11)$$

Using τ_w as the shear stress at the solid wall in the formulation by Thomas et al. (1989), the film height distribution was calculated and is shown in Fig. 7.8. The predicted film height compares reasonably well with the experimental data. So, at an intermediate flow rate, both components of frictional resistance are important and one cannot be entirely neglected in favor of the other.

Figures 7.9-7.11 show the comparison of the numerical results with the experimental data for other rotational speeds tested in the experiment. For a smaller rate of rotation (55 rpm), it can be seen that the modified numerical solution predicts the experimental data except for the region close to the outlet where surface tension is large. The original procedure of Thomas et al. (1989) somewhat underestimates the film height in the region away from the center where centrifugal force becomes large. For large rotational rates (200 rpm and 300 rpm), however, the method of Thomas et al. (1989) appears to be reasonably satisfactory and predicts the trend of the experimental data better. The assumption of solid-body rotation

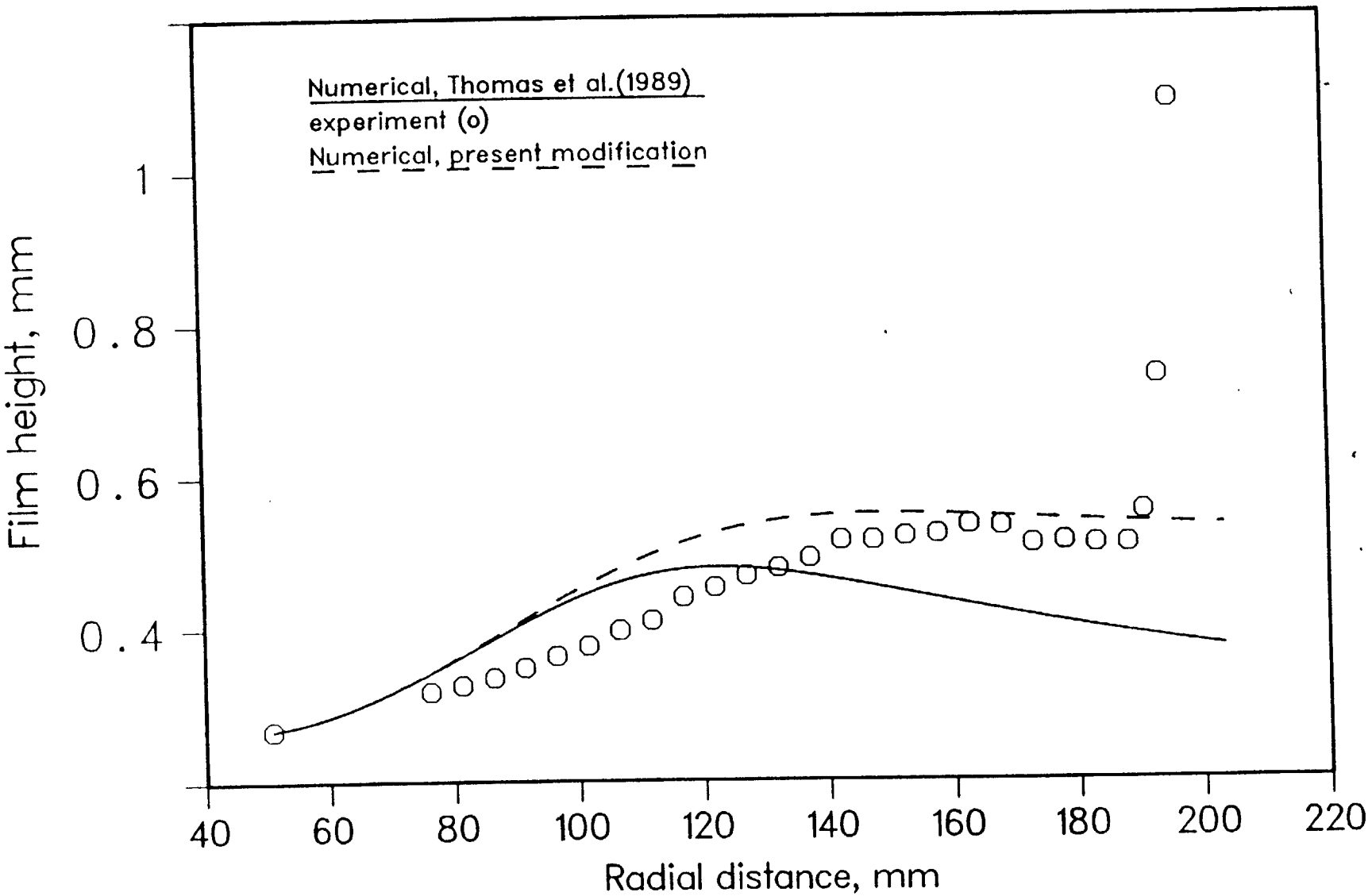

Fig. 7.9 Comparison of experiment with numerical solution of rotating disk (flow rate = 9 lpm, rpm = 55)

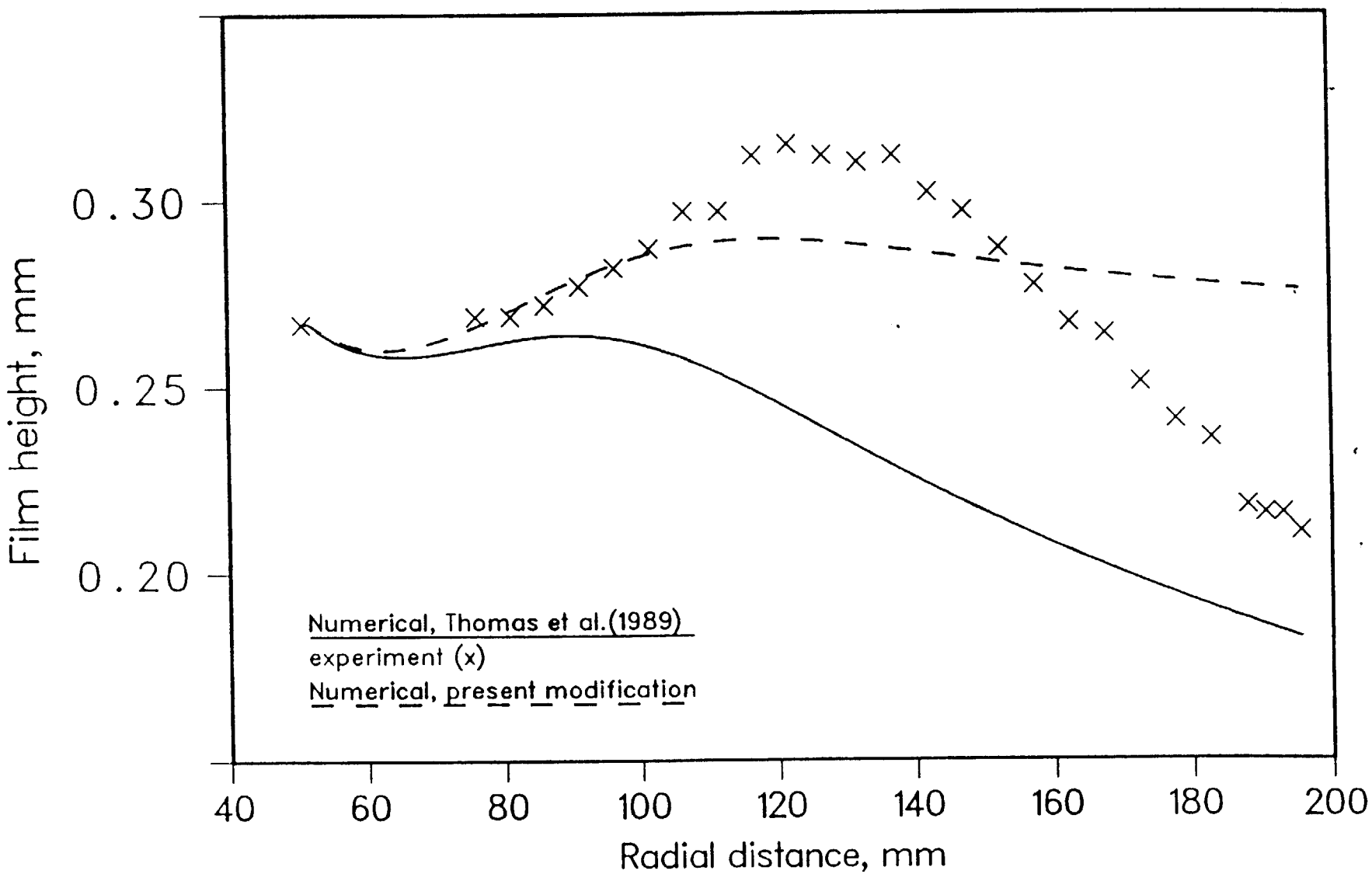

Fig. 7.10 Comparison of experiment with numerical solution of rotating disk (flow rate = 13 lpm, rpm = 200)

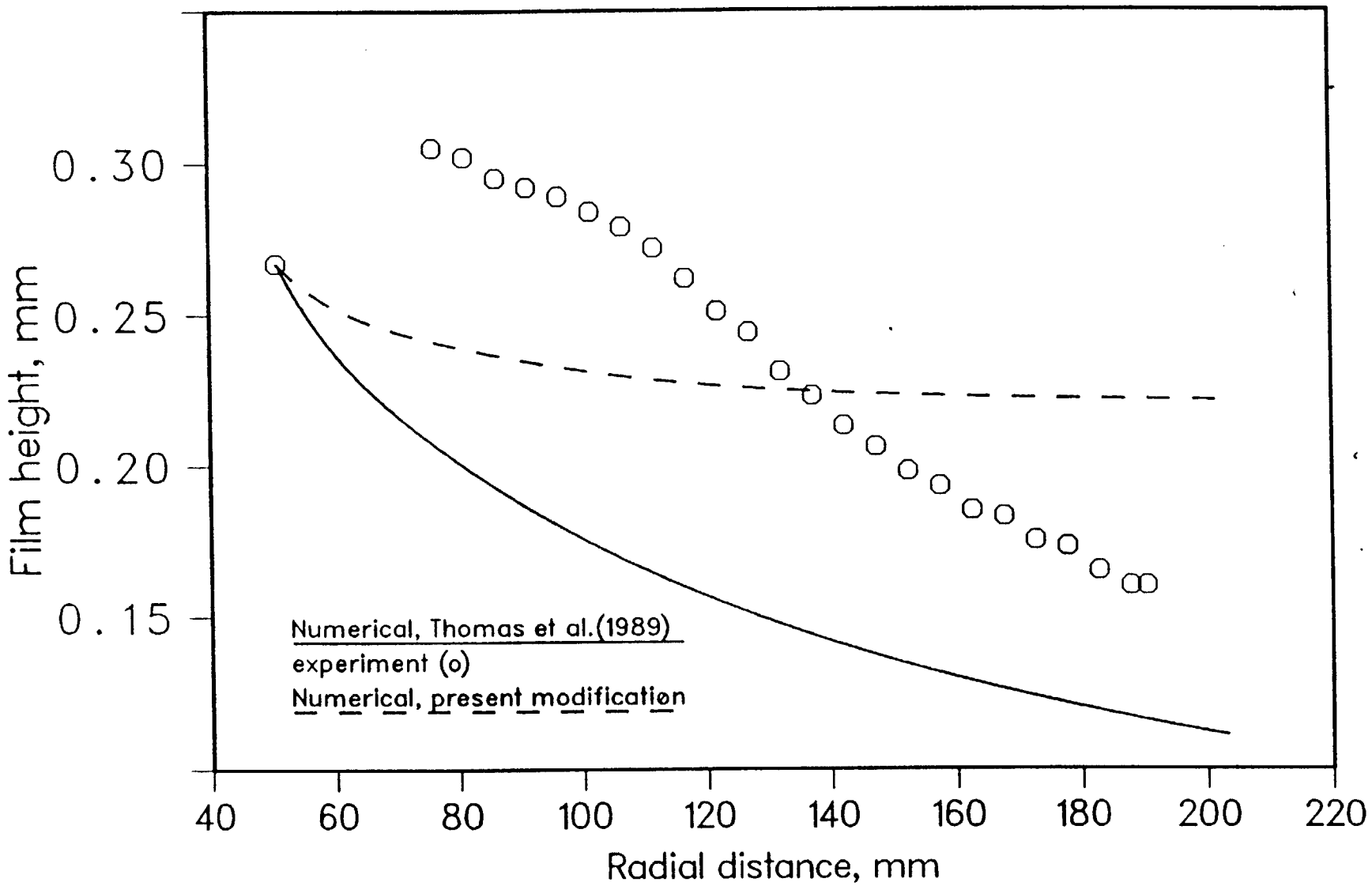

Fig. 7.11 Comparison of experiment with numerical solution of rotating disk (flow rate = 7 lpm, rpm = 300)

inherent in the formulation of Thomas et al. (1989) become more appropriate at smaller values of the Rossby number, i.e., at higher rates of rotation, so the trend seen here may be expected. However, we should also keep in mind the limitations of a simple one-dimensional numerical solution. As seen in the experiment, waves appear on the surface and become more intense at a higher spin rates. The turbulence may also be triggered at a higher rate of flow or rotation. A two-dimensional solution with rotation may address some of these issues, which is beyond the scope of the present paper.

7.6 CONCLUSIONS

The experimental data were compared with the existing numerical solutions of radially spreading thin film flows adjacent to a stationary or rotating disk. Some of the drawbacks of the existing numerical methods are pointed out and corrected. The detailed structure of the flow for a stationary disk is also computed and discussed.

It was found that surface tension is important at the outer edge of the disk. For a stationary disk, a simple model for estimating film height at this location is proposed. At other locations in the flow, the surface tension can be neglected. For a stationary disk, the one-dimensional numerical method of Thomas et al. (1989) or the two-dimensional methods of Rahman et al. (1989a and 1989c) should always be applied with the correctly estimated outlet Froude number, instead of using $Fr = 1$ to simulate a critical (free falling) outflow condition.

In the case of a rotating disk, the frictional resistance due to

angular velocity was found to be important. At a smaller rate of rotation, the resultant frictional resistance was found to be more adequate to predict the film height than using only the radial component.

The increment in film height at the jump was found to be gradual spanning over a number of grid cells. In the two-dimensional 'pressure optimization method' after determining the location of the jump, an additional procedure for adjusting the slope of the jump may be included to arrive at a better structure of the free surface. The two-dimensional 'porous wall method' given by Rahman et al. (1989b) can be used as it is except for imposing the correct Froude number at the outlet. It was also found that recirculating flow is present in the vicinity of the jump, both at the solid wall and on the free surface. The separation of flow at the solid wall is due to the viscous resistance exerted by the wall that overcomes inertia when the film height rises. The separation on the free surface is due to the adverse gravitational pressure gradient.

REFERENCES

Amsden, A.A. and Harlow, F.H., 1970, "A Simplified MAC Technique for Incompressible Fluid Flow Calculations," J. Computational Physics, Vol. 6, pp. 322-325.

Anderson, D.A., Tannehill, J.C. and Pletcher, R.H., 1984, Computational Fluid Mechanics and Heat Transfer, Hemisphere Publishing Corporation, N.Y.

Aroesty, J., et al., 1967, "Blood Oxygenation: A Study in Bioengineering Mass Transfer", Technical Report P-3732, The RAND Corp., Santa Monica, Calif.

Awn, A.G., 1979, "Numerical Modelling of Flows with Moving Interfaces," Ph.D. Thesis, University of London.

Batchelor, G.K., 1967, An Introduction to Fluid Dynamics, Cambridge University Press, Cambridge, England.

Bird R.B., Stewart, W.E. and Lightfoot, E.N., 1960, Transport Phenomena, John Wiley and Sons, N.Y..

Butuzov, A.I. and Rifert, V.F., 1972, "An Experimental Study of Heat Transfer During Condensation of Steam at a Rotating Disk," Heat Transfer-Soviet Research, Vol. 4, No. 6, pp. 150-153.

Butuzov, A.I., and Rifert, V.G., 1973, "Heat Transfer in Evaporation of Liquid From a Film on a Rotating Disk," Heat Transfer-Soviet Research, Vol. 5, No. 1, pp. 57-61.

Carper, H.J., Jr., Saavedra, J.J. and Suwanprateep, T., 1986, "Liquid Jet Impingement Cooling of a Rotating Disk", ASME J. Heat Transfer, Vol. 108, pp. 540-546.

Charwat, A.F., Kelly, R.E. and Gazley, C., 1972, "The Flow and Stability of Thin Liquid Films on a Rotating Disk", J. Fluid Mech., Vol. 53, pp. 227-255.

Chaudhury, Z.H., 1964, "Heat Transfer in a Radial Liquid Jet, J. Fluid Mechanics, Vol. 20, pp. 501-511.

Chun, K.R. and Seban, R.A., 1971, Heat Transfer to Evaporating Liquid Film," ASME J. Heat Transfer, Vol. 93, No. 4, pp. 391-396.

Craik, A.D.D., Latham, R.C., Fawkes, M.J. and Gribbon, P.W.F., 1981, "The Circular Hydraulic Jump", J. Fluid Mech., Vol. 112, pp. 347-362.

Dixon, B.E., Russell, B.A. and Swallow, J.E.L., 1952, "Liquid Films Formed By Means of Rotating Disks", British J. Applied Physics, Vol. 3, p. 115.

Edwards, D.K., Denny, V.E. and Mills, A.F., 1979, Transport Processes: An Introduction to Diffusion, Convection and Radiation, McGraw Hill, N.Y.

Eliseev, V.I., 1983, "Spatial Stability of a Liquid Film on a Rotating Disk", Zhurnal Prikladnoi Mekhanika i Tekhnicheskoi Fizika, Vol. 6, pp. 112-117.

Espig, H. and Hoyle R., 1965, "Waves In a Thin Liquid Layer on a Rotating Disk", J. Fluid Mech., Vol. 22, pp. 671-677.

Faghri, A. and Payvar, P., 1979, "Transport to Thin Falling Liquid Films," Reg. J. Energy Heat Mass Transfer, Vol. 1, No. 2, pp. 153-173.

Faghri, A. and Seban, R.A., 1981, "Heat Transfer in Wavy Liquid Film," Int. J. Heat Mass Transfer, Vol. 28, No. 2, pp. 506-508.

Francis, J.R.D. and Minton, P., 1984, Civil Engineering Hydraulics, Edward Arnold Ltd., London.

Galea, E.R. and Markatos, N.C., 1987, "Prediction of Fire Development in Aircraft," Proc. 2nd Int. PHOENICS User Conference, London.

Harlow, F.H. and Welch, J.E., 1965, "Numerical Calculation of Time-Dependent Viscous Incompressible Flow of Fluid with Free Surface," Physics of Fluids, Vol. 8, pp. 2182-2189.

Higgins, B.G, 1986, "Film Flow on a Rotating Disk," Physics of Fluids, Vol. 29, No. 11, pp. 3522-3529.

Hirshburg, R.I. and Florschuetz, L.W., 1982, "Laminar Wavy-Film Flow: Part I, Hydrodynamic Analysis", ASME J. Heat Transfer, Vol. 104, pp. 452-458.

Hirt, C.W., Nichols, B.D. and Romero, N.C., 1975, "SOLA-A Numerical Solution Algorithm for Transient Fluid Flows," Los Alamos Scientific Laboratory Report LA-5852.

Hirt, C.W. and Nichols, B.D., 1981, "Volume of Fluid (VOF) Method for the Dynamics of Free Boundaries," J. Computational Physics, Vol. 39, pp. 201-225.

Ishigai, S., Nakanishi, S., Mizuno, M. and Imamura, T., 1977, "Heat Transfer of the Impinging Round Water Jet in the Interference Zone of Film Flow Along the Wall", Bulletin of the JSME, Vol. 20, pp. 85-92.

Jenekhe, S.A., 1984, "Effects of Solvent Mass Transfer on Flow of Polymer Solutions on a Flat Rotating Disk", Ind. Eng. Chem. Fundam., Vol. 23, pp. 425-432.

Jun, L., 1985, "Application of Variable Blockage Method to Steady Flows Over Curved Beds," CFDU Report, CFD/85/12, Imperial College, London.

Jun, L., 1986, "Computer Modelling of Flows with a Free Surface," Ph.D. Thesis, University of London.

Katto, Y., and Yokoya, S., 1988, "Critical Heat Flux on a Disk Heater Cooled By a Circular Jet of Saturated Liquid Impinging at the Center", Int. J. Heat Mass Transfer, Vol. 31, pp. 219-227.

Kays, W.M. and Crawford, M.E., 1980, Convective Heat and Mass Transfer, McGraw-Hill, N.Y.

Labus, T.L. and DeWitt, K.J., 1978, "Liquid Jet Impingement Normal to a Disk in Zero Gravity", ASME J. Fluids Engineering, Vol. 100, pp. 204-209.

Matsumoto, S., Saito, K., and Takashima, Y., 1973, "The Thickness of a Viscous Liquid Film on a Rotating Disk", J. Chemical Engineering of Japan Vol. 6, pp. 503-507.

Matsumoto, S., Takashima, Y., Kamiya, T., Kayano, A., and Ohta, Y., 1982, "Film Thickness of a Bingham Liquid on a Rotating Disk," Ind. Eng. Chem. Fundamentals, Vol. 21, No. 3, pp. 198-202.

Miller, R.W., 1989, Flow Measurement Engineering Handbook, 2nd ed., McGraw-Hill, N.Y.

Miyasaka, Y., 1974, "On the Flow of a Viscous Free Boundary Jet on a Rotating Disk, Bulletin of the JSME, Vol. 17, 1974, pp. 1469-1475.

Muzhilko, A.A., Rifert, V.G. and Barabash, P.A., 1983, "Flow of Liquid Film Over the Surface of a Rotating Disk", Heat Transfer - Soviet Research, Vol. 15, pp. 1-6.

Nakovyakov, V.E., Pokusaev, B.G. and Troyan, E.N., 1978, "Impingement of an Axisymmetric Liquid Jet on a Barrier," Int. J. Heat Mass Transfer, Vol. 21, pp. 1175-1184.

Needham, D.J. and Merkin, J.H., "The Development of Nonlinear Waves on the Surface of a Horizontally Rotating Thin Liquid Film", J. Fluid Mech., Vol. 184, pp. 357-379.

Patankar, S.V., 1980, Numerical Heat Transfer and Fluid Flow, Hemisphere Publishing Corporation, N.Y.

Rahman, M.M, Faghri, A., Hankey, W.L. and Swanson, T.D., 1989a, "Computation of the Free Surface Flow of a Thin Liquid Film at Zero and Normal Gravity," to appear in Numerical Heat Transfer.

Rahman, M.M., Faghri, A., Hankey, W.L. and Swanson, T.D., 1989b, "Heat Transfer to a Thin Film with a Free Surface," Numerical Heat Transfer with Personal Computers and Supercomputing, ASME HTD-Vol. 110, pp. 161-168.

Rahman, M.M., Faghri, A. and Hankey, W.L., 1989c, "New Methodology for the Computation of Free Surface Flows Using a Permeable Wall", to appear in Proc. 1989 ASME Winter Annual Meeting, San Francisco.

Rahman, M.M., Faghri, A., Hankey, W.L. and Swanson, T.D., 1989d, "Prediction of Heat Transfer to a Thin Liquid Film in Plane and Radial Flows", ASME J. Heat Transfer, (submitted for review).

Rajaratnam, N., 1967, "Hydraulic Jumps," Advances in Hydroscience, Vol. 4, pp. 197-280.

Rauscher, J.W., Kelly, R.E. and Cole, J.D., 1973, "An Asymptotic Solution for the Laminar Flow of a Thin Film on a Rotating Disk", ASME J. Applied Mechanics, Vol. 40, No. 1, pp. 43-47.

Schlichting, H., 1979, Boundary Layer Theory, Seventh Edition, McGraw Hill, New York.

Seban, R.A. and Faghri, A., 1976, "Evaporation and Heating with Turbulent Falling Liquid Films," ASME J. Heat Transfer, Vol. 98, No. 2, pp. 315-318.

Seban, R.A. and Faghri, A., 1978, "Wave Effects on the Transport to Falling Laminar Liquid Films," ASME J. Heat Transfer, Vol. 100, No. 1, pp. 143-147.

Spalding, D.B., 1980, "Mathematical Modeling of Fluid Mechanics, Heat Transfer and Chemical Reaction Processes," A Lecture Course, CFDU Report, HTS/80/1, Imperial College, London.

Spalding, D.B., Rosten, H.I., Glynn, D.R., Malin, M.R. and Edwards, J.P., 1986, Lecture Panels for Use of the Body-fitted Coordinates in PHOENICS, CHAM TR/126, Concentration Heat and Momentum Ltd., London.

Sparrow, E.M. and Gregg, J.L., 1959, "A Theory of Rotating Condensation," ASME J. Heat Transfer, Vol. 81, No. 2, pp. 113-120.

Thomas, S., Hankey, W., Faghri, A. and Swanson, T., 1989, "One-Dimensional Analysis of Plane and Radial Thin Film Flows Including Solid-Body Rotation," Numerical Heat Transfer with Personal Computers and Supercomputing, ASME HTD-Vol. 110, pp. 103-111, also to appear in ASME J. Heat Transfer.

Watson, E.J., 1964, "The Radial Spread of a Liquid Jet over a Horizontal Plane," J. Fluid Mechanics, Vol. 20, Part 3, pp. 481-499.

Yeung, R.W., 1982, "Numerical Methods in Free Surface Flows," Annual Review of Fluid Mechanics, Vol. 14, pp. 395-442.

Appendix A: EQUIPMENT SPECIFICATIONS

The equipment for the rotating disk unit is divided into four subsystems for the description of the components:

1. Rotating disk assembly
2. Liquid film height measurement system
3. Heat transfer measurement system
4. Liquid circulation system

1. Rotating disk assembly

a) Rotating disk

Material: 6061 aluminum

Diameter: 406.4 mm

Thickness: 6.35 mm

Surface finish: 3.81×10^{-4} mm

Perpendicularity to centerline of spindle: 2.5×10^{-3} mm

Flatness: 2.5×10^{-3} mm

b) Collar

Material: 316 stainless steel

Outer diameter: 102 mm

Perpendicularity to centerline of spindle: 6.0×10^{-4} mm

c) Shim

Material: 316 stainless steel shim stock

Thickness: 0.673 mm

d) Spindle and motor

- Whitnon model 699-0080-000 "piggyback" spindle/motor assembly

Spindle bearings: ABEC #7 angular contact ball bearings

Spindle shaft: 440 stainless steel hardened to 50-55 Rockwell "C" except at shaft extension which will be 38-42 Rockwell "C" due to thin cross section

Electric motor: 0.5 HP at 900 RPM with an input of 230/460 V, 3 phase, 60 Hz (0.75 A @ 460 V)

Driver and driven pulleys are interchanged to obtain speed range change. A frequency inverter will be used to vary the speed within each speed range.

Frequency inverter: 4.5 A @ 460 V

Low speed range: 55 to 374 RPM

High speed range: 423 to 1987 RPM

e) Radial encoder and speedometer

- Airpax solid 60-tooth gear, magnetic pickup, and digital display

Accuracy: ±1 RPM over speed range of 55 to 1987 RPM

2. Liquid film height measurement system

a) Non-contact capacitance sensor

- MTI model ASP-100-CTA

  Accuracy: ±0.002 mm

  Resolution: ±0.002 mm

b) Data logging system

- Fluke model 2280A Data Logger

c) Digital micrometer

- Microcode model 9598

  Accuracy: ±0.002 mm

  Resolution: ±0.002 mm

d) Precision slide

- Microslides model A-6166-LC crossed roller bearing slide assembly

  Accuracy: Run-out over 130 mm = $\pm 2.6 \times 10^{-3}$ mm

3. Heat transfer measurement system

a) Etched foil heater

- Minco mica heater

  Outer diameter: 356 mm

  Inner diameter: 102 mm

  Thickness: 0.635 mm

  (6) - 3.18 mm holes for thermocouples

Maximum operating temperature: 100°C

Electrical specifications: 500 V, 41.67 Ω, 12 A, 6000 W

Maximum heat flux: 6.6 W/cm^2

b) Ceramic insulation

- Aremco 502-600 machinable ceramic

Maximum operating temperature: 590°C

Thermal conductivity: 0.15 W/(m-K)

c) Thermocouples

- Type "T" copper-constantan

Maximum useful range: -200 to 350°C

Maximum error over range: 0.5°C

d) Digital thermometer

- Fluke model 2280A Data Logger

Thermocouple conformity: Better than 0.05°C

e) Slip-ring capsule

- Electro-Tec model ETC P/N 67584

Number of rings/circuits: 20

Current ratings: 3 A at 500 VDC

Contact resistance (noise): 25 mΩ at 100 mA (10 RPM)

Life: 18 million revolutions at 8 RPM

Operating environment: -55 to 125°C

4. Liquid circulation system

a) Rotating union

- Deublin series 1106

b) Digital flow meter

- Cole-Parmer model J-5618-04 Micet semi-micro flow sensor

  Range: 1.51 to 17.0 LPM

  Maximum pressure: 3.76×10^5 Pa at $105^{o}C$

  Linearity: ±1 % full scale

  Repeatability: ±0.25 % full scale

- Cole-Parmer model J-5622-35 Line powered flow meter

  Accuracy: ±1 % full scale

  Repeatability: ±0.5 % full scale

Appendix B: DESIGN OF THE ROTATING DISK ASSEMBLY

The details of the design of the rotating disk assembly will be explained. This includes the rotating disk, spindle, electric motor, rotating fluid coupling, and the electric power supply for the motor and the etched foil heater.

Figure B.1 is an overall view of the rotating disk assembly as it appears in the experimental setup. The electric motor is mounted to the spindle, which in turn is mounted onto the vertical frame plate. The spindle is driven by a poly-groove belt which can be removed by taking a cotter key out and driving a pin down and out of a hole on the plate the electric motor is mounted on. This allows the electric motor to swing toward the spindle. This procedure is also performed to change the speed range of the spindle.

Near the pulley on the spindle in Fig. B.1 is the magnetic pickup for the tachometer. It is mounted through a housing such that it is approximately 0.254 mm (0.010 in.) from a special gear. As the teeth pass by the active sensor, a square wave proportional to the angular speed is generated, which is then read and displayed by the digital readout.

The rotating disk and collar are also shown in Fig. B.1. The collar is mounted onto the spindle shaft with four screws which pass up through a ceramic insulator ring. This is to prevent excessive heat from reaching the high-precision bearings. An O-ring seal is placed between the spindle shaft and the inner diameter of the collar to prevent water from passing

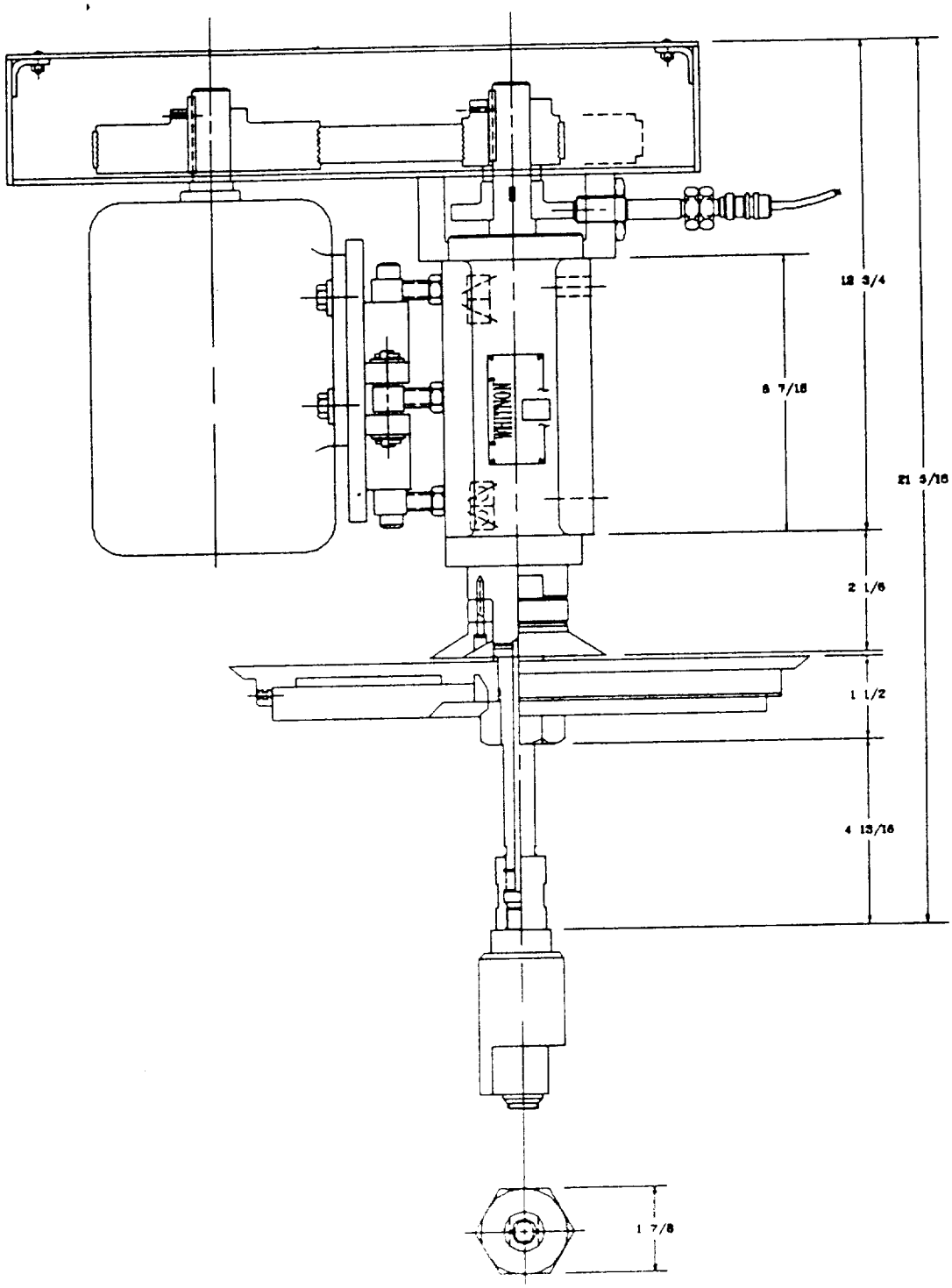

Figure B.1. Side view #1 of motor spindle and disk assembly

ORIGINAL PAGE IS
OF POOR QUALITY

over the top of the collar. A shim is placed between the collar and rotating disk to set the initial gap height. Caution must be used when installing this shim so that the chamfer or bevel on the inner diameter of the shim is directed upward to mate with the small radius where the spindle shaft has a step in diameter. Otherwise, the shim and rotating disk will not seat properly. Also, it was found that the thickness of the shim does not correspond to the initial gap height, as was originally planned. Therefore, feeler gages must be used to directly measure this gap. Like the collar, the rotating disk has an O-ring to prevent water from running directly down the spindle shaft. The large nut below the rotating disk holds the disk against the spindle. In order to achieve repeatability in the stationary film thickness measurements, marks were placed on the collar and the rotating disk for alignment purposes. The two marks were first aligned with each other, and then the marks were aligned with the capacitance probe. With this procedure, repeatability could be achieved.

Some preliminary tests were made with two different collars which are shown in Fig. B.2. The first design was a reducer as shown in Fig. B.2a. The part of the reducer that was closest and parallel to the disk acted as a flow straightener, which directed most of the liquid to flow in the radial direction. However, part of the fluid would rebound off of the disk underneath the flow straightener, which resulted in splashing around the collar at moderate and high flow rates. To eliminate this problem, the collar shown in Fig. B.2b. was tested and it was found that the splashing was not present with the longer flow straightener.

When the disk was rotated, it was found that a significant amount of

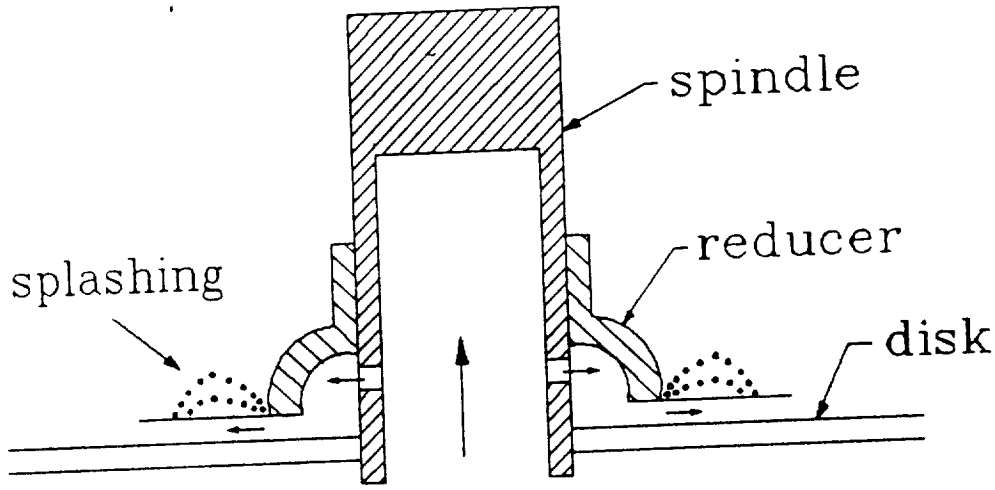

Fig. B.2.a Collar with short flow straightener

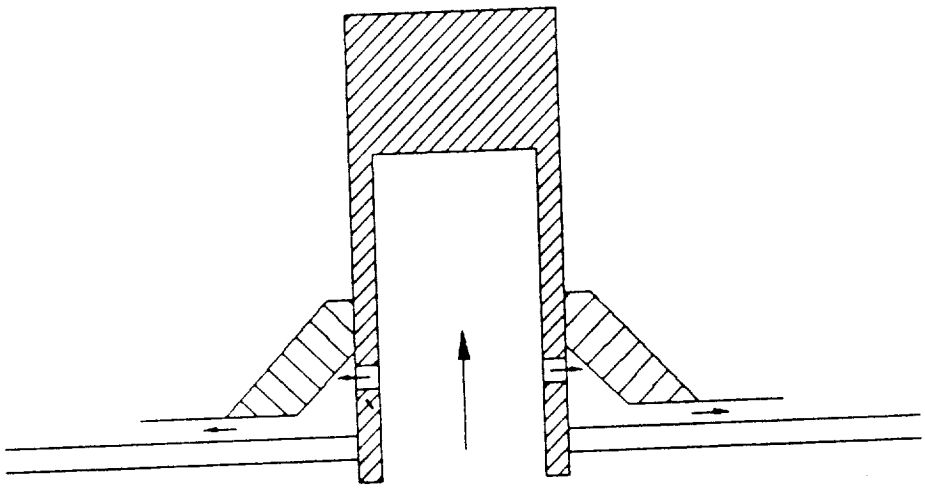

Fig. B.2.b Collar with long flow straightener

Figure B.2. Collar design

water spray was generated by the liquid film leaving the disk and rebounding off of the Lexan water tank. This created problems with water droplets splashing onto the capacitance probe, so a screen mesh was draped on the sides of the tank to absorb the kinetic energy of the droplets and prevent the water spray from rebounding off of the tank.

Below the rotating disk is a cylindrical coupling between the spindle shaft and the rotating fluid union. These items must be removed before the rotating disk can be taken off of the apparatus.

Figure B.3 shows a view of the footprint where the spindle mounting holes are located. Also shown is the top view of the pulley housing on top of the rotating disk assembly. The low speed range is shown in Fig. B.3, whereas the pulleys are reversed to achieve the high speed range.

Figure B.4 presents the side and top views of the aluminum rotating disk. Six holes are drilled from the underside to just below the surface of the disk for the placement of thermocouples along one radius. The top of the disk is coated with an aluminum oxide coating to prevent oxidation on the surface of the disk.

Figure B.5 shows the design of the insulating ceramic disk. A cutout at the top of Fig. B.5 on the ceramic disk is for the electric heater leads. The six holes for thermocouples are drilled completely through the ceramic disk.

The electrical diagram for the rotating disk unit is shown in Fig.

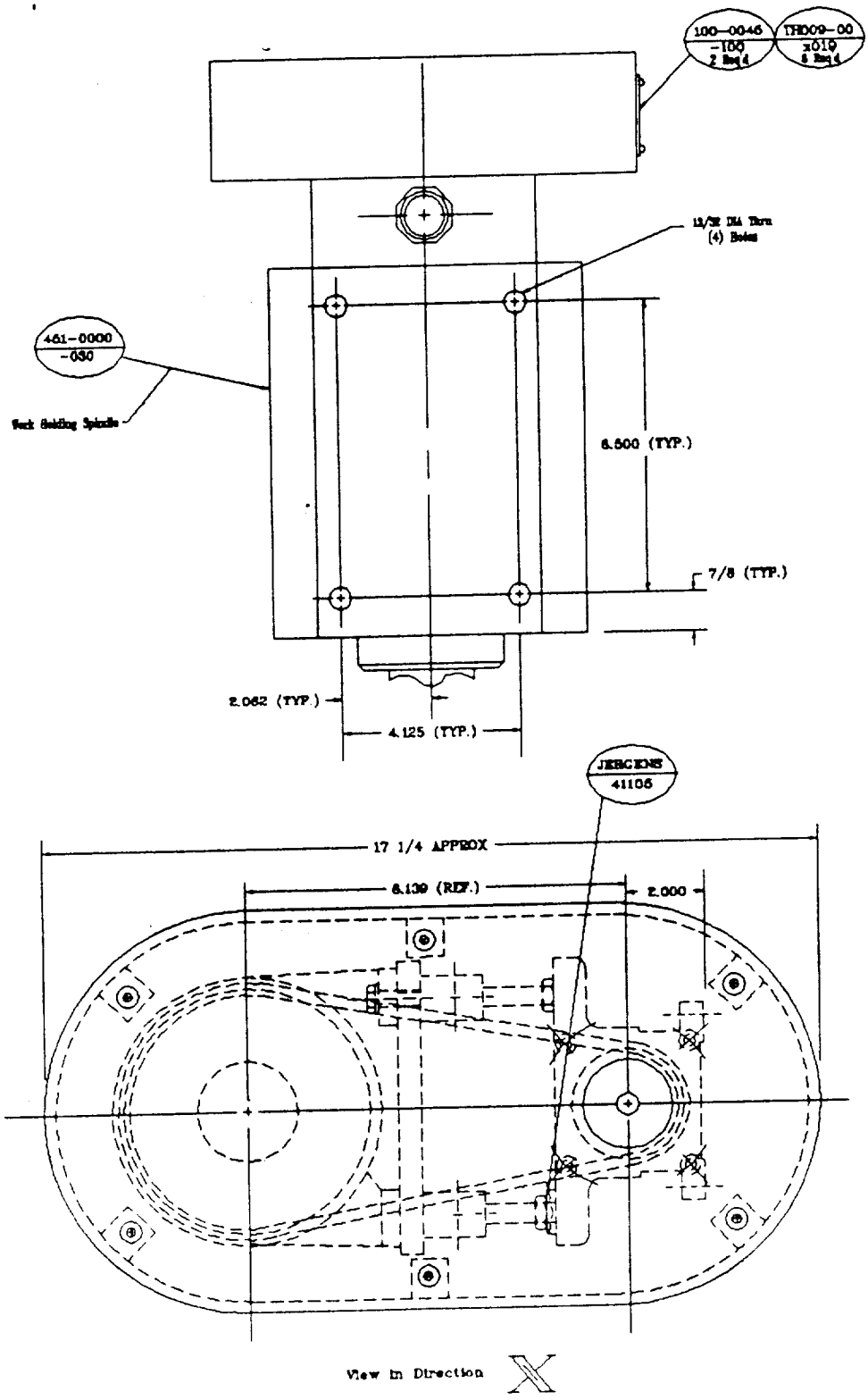

Figure B.3. Side view #2 and top view of motor and spindle

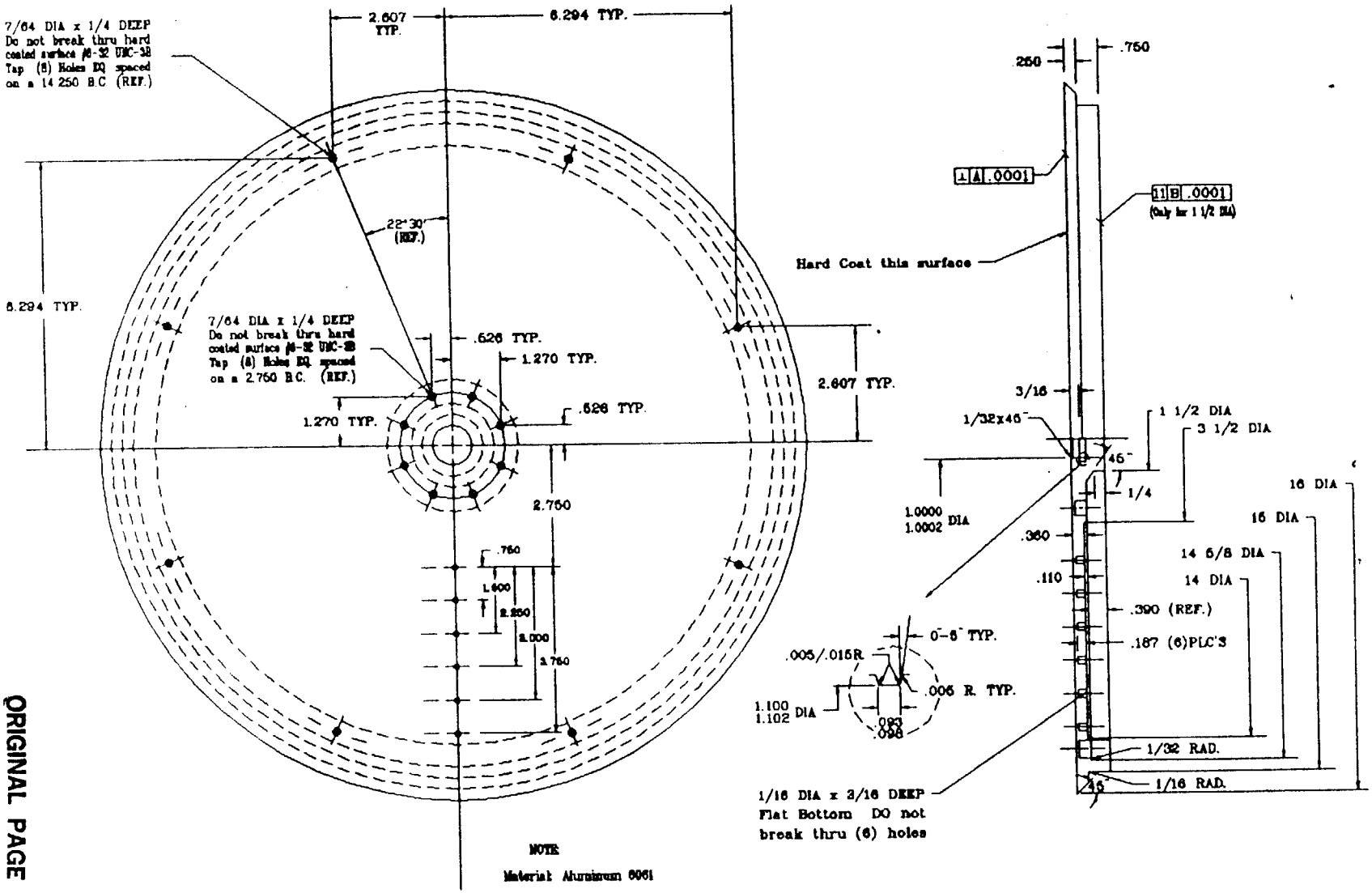

Figure B.4. Aluminum disk

ORIGINAL PAGE IS
OF POOR QUALITY

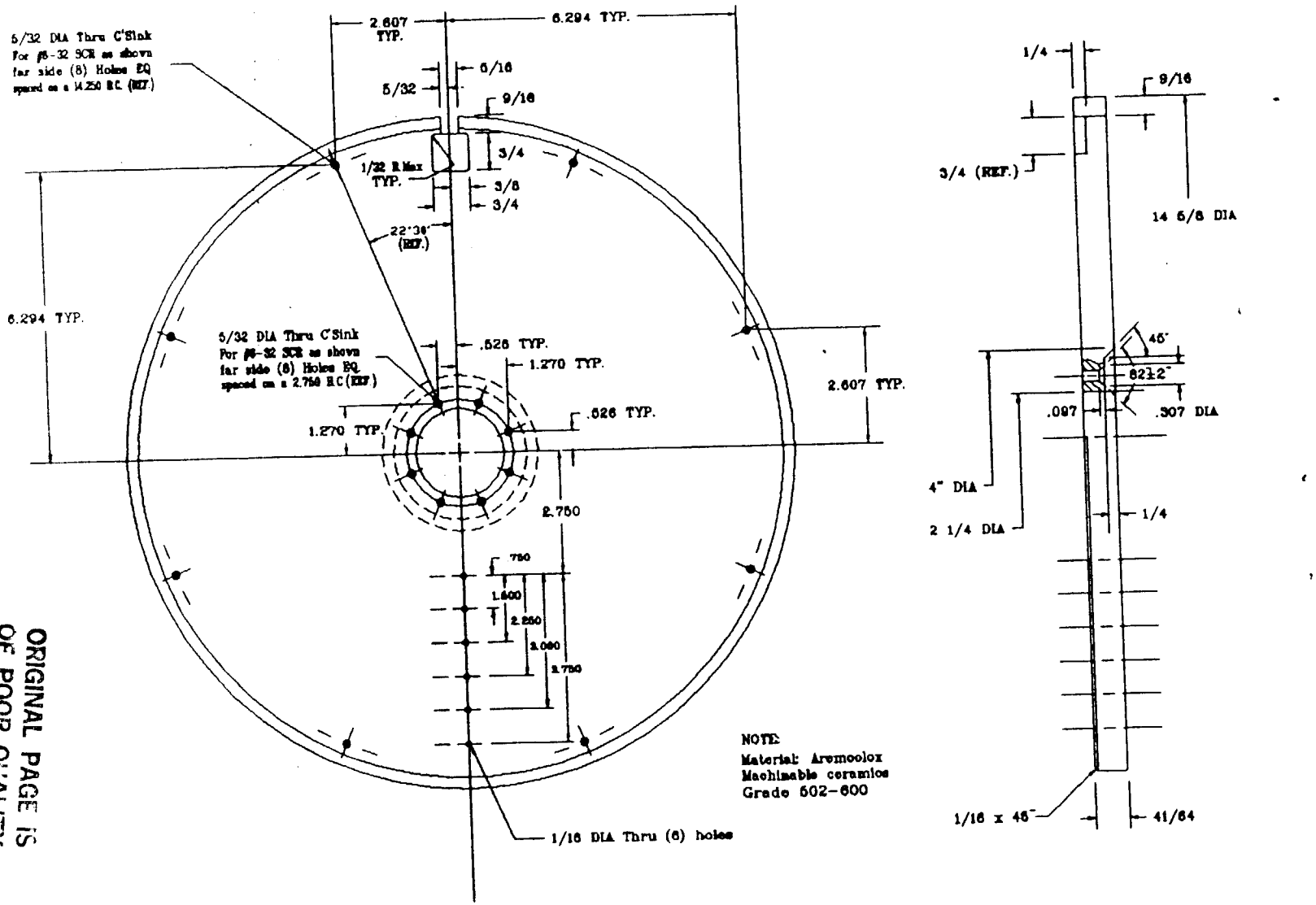

Figure B.5. Ceramic disk

ORIGINAL PAGE IS
OF POOR QUALITY

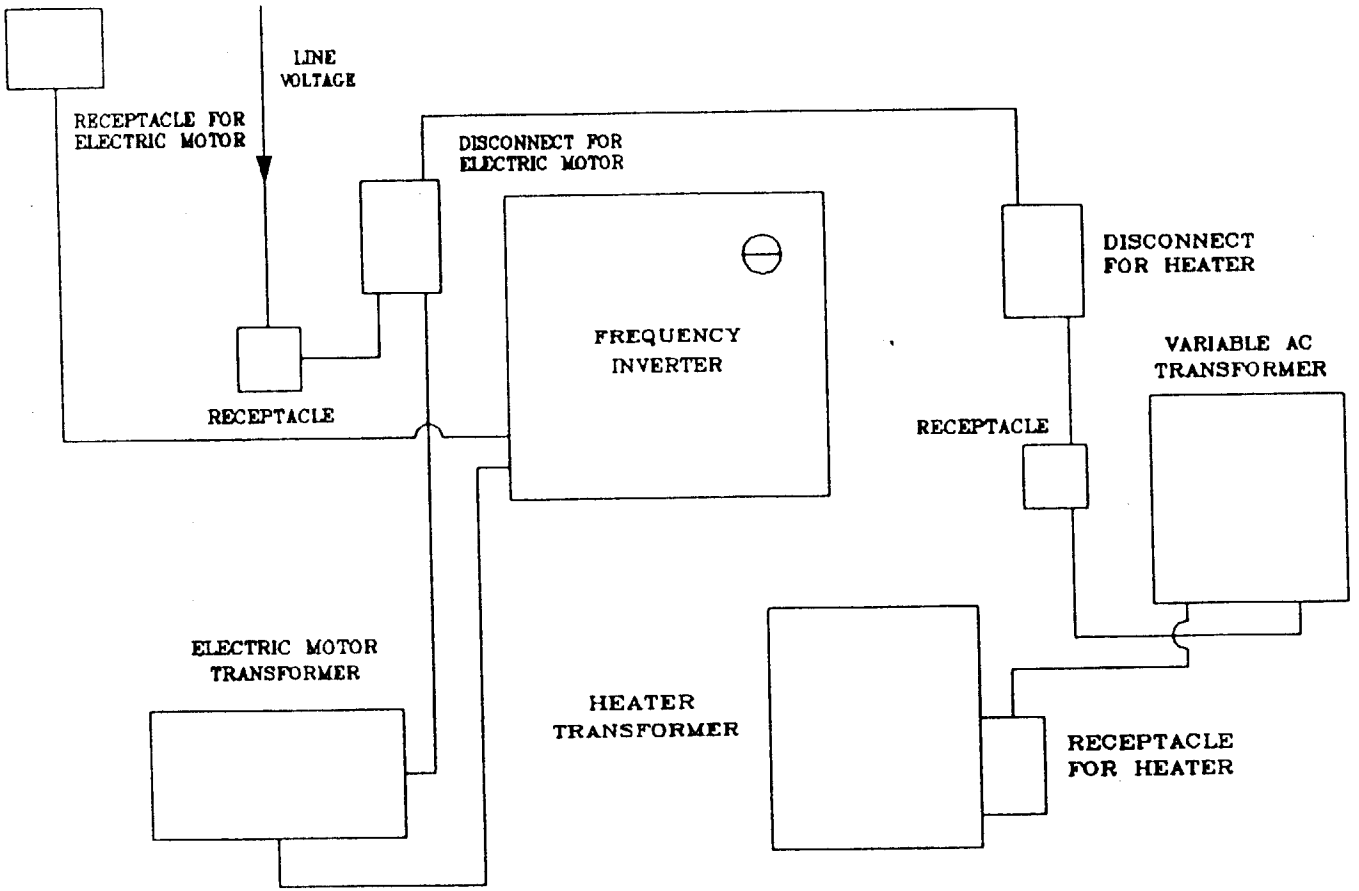

Figure B.6. Electric diagram for the rotating disk unit

B.6. The line voltage comes into the receptacle to the left of the frequency inverter. The plug should never be disconnected from the receptacle when either of the transformers are operating. To energize the electric motor, first switch on the disconnect and then turn on the frequency inverter switch. Turn the system off by reversing the procedure. The electric motor speed is controlled with the remote control panel box supplied with the frequency inverter. After the start button is depressed, the speed dial can be turned to adjust the speed. The disk speed is leveled off when the "at speed" lamp is lit.

To energize the electric heater on the rotating disk, turn down the variable ac transformer and turn on the main and heater disconnects. The variac can then be adjusted for the desired power input. Care must be taken because the output of the receptacle is 0 - 480 V.

Appendix C: ERROR ANALYSIS

In order to properly report any experimental data, an analysis of the errors involved in taking the data must be given. In the present experimental setup, the errors involved in taking two measurements will be described and quantified: the liquid film height, and the liquid flow rate.

Liquid film height

The error in measuring the liquid film height involves three pieces of equipment: the digital micrometer, the capacitance sensor, and the rotating disk. To evaluate the error in the film height measurement, the individual errors of each of these pieces of equipment must be found. A summary of the method to determine the error will now be given. A full discussion on error analysis is given by Miller (1989).

If N is a known function of n independent variables $u_1, u_2, \cdots, u_n$,

$$N = f(u_1, u_2, \cdots, u_n)$$

the absolute error is given by expanding the function f in a Taylor series

$$f(u_1 \pm \Delta u_1, u_2 \pm \Delta u_2, \cdots, u_n \pm \Delta u_n) = f(u_1, u_2, \cdots, u_n)$$

$$+ \frac{\partial f}{\partial u_1} \Delta u_1 + \frac{\partial f}{\partial u_2} \Delta u_2 + \cdots + \frac{\partial f}{\partial u_n} \Delta u_n + \frac{1}{2} \left[\left[\frac{\partial^2 f}{\partial u_1^2} (\Delta u_1)^2 \right] + \cdots \right] + \cdots \tag{C.1}$$

where the partial derivatives are evaluated at the measured values of u_i. If the instrumentation errors Δu_i's are small quantities, the terms which include $(\Delta u_i)^2$ will be negligible. Therefore, equation (C.1) is approximately given by

$$f(u_1 \pm \Delta u_1, u_2 \pm \Delta u_2, \ldots, u_n \pm \Delta u_n) = f(u_1, u_2, \ldots, u_n)$$

$$+ \frac{\partial f}{\partial u_1} \Delta u_1 + \frac{\partial f}{\partial u_2} \Delta u_2 + \ldots + \frac{\partial f}{\partial u_n} \Delta u_n \qquad (C.2)$$

The absolute error of the system is then given by

$$E_a = \Delta N = \left|\frac{\partial f}{\partial u_1} \Delta u_1\right| + \left|\frac{\partial f}{\partial u_2} \Delta u_2\right| + \ldots + \left|\frac{\partial f}{\partial u_n} \Delta u_n\right| \qquad (C.3)$$

where Δu_i is the absolute error associated with the individual measurements. If the Δu's are considered to be statistical bounds on the instrument errors, such as 95 percent confidence levels, the formula for computing the overall error is modified using the root-sum square formula

$$E_{rss} = \sqrt{\left[\frac{\partial f}{\partial u_1} \Delta u_1\right]^2 + \left[\frac{\partial f}{\partial u_2} \Delta u_2\right]^2 + \ldots + \left[\frac{\partial f}{\partial u_n} \Delta u_n\right]^2} \qquad (C.4)$$

The liquid film height is given by the following equation:

$$\delta = h' + (h + \Delta h) - h'' \qquad (C.5)$$

where h' is the digital micrometer reading, $(h + \Delta h)$ is the capacitance

probe reading of the air gap between the probe and the dry disk, and h" is the capacitance probe reading of the air gap between the probe and the surface of the liquid film.

Applying equation (C.4) gives

$$E_{rss} = \sqrt{(\Delta h')^2 + [\Delta(h + \Delta h)]^2 + (\Delta h")^2} \qquad (C.6)$$

The first term in equation (C.6) is the stated accuracy of the digital micrometer, which was calibrated at the factory with an NBS traceable Mark-Tech Laser Gage Model 7980. The maximum deviation over the range of movement reported on the calibration certificate is 0.001 mm. This value is then taken as the maximum error of the instrument. Therefore,

$$\Delta h' = 0.001 \text{ mm}$$

The second term involves the accuracy of the capacitance sensor, which is given by the manufacturer to be ±0.1 percent of the range when calibrated to a known standard. In the present experimental setup, the known standard was taken to be the digital micrometer. The capacitance probe was calibrated at the beginning of each test against the digital micrometer in the following manner:

1. The capacitance probe is lowered until it lightly touches the surface of the disk, which can be seen with a lamp directed behind the probe. The capacitance probe is then zeroed at this point with the offset adjustment.

2. The probe is then raised 0.0254 mm above the disk, where the digital micrometer is zeroed. This is done to eliminate any backlash in the digital micrometer.

3. The capacitance sensor is then raised until it reads the maximum value of its range, which is 2.54 mm.

The value read on the capacitance sensor readout is compared to what is shown on the digital micrometer readout. Any discrepancy can be eliminated by a gain adjustment which is supplied on the capacitance sensor readout. This sets the slope of the linear curve which relates the strength of the electric field to the height of the air gap. By choosing points at 0.0254 and 2.54 mm, the slope can be set over 99 percent of the range for the greatest accuracy. The linearity of the capacitance probe over its range was checked, and the maximum deviation was found to be 0.008 mm. This value will be added to the stated accuracy of the probe.

The second term in equation (C.6) takes on different values when the disk is stationary and when the disk is rotating. When stationary, the second term is the accuracy of the capacitance sensor given by the manufacturer, which is ±0.1 percent of the range when calibrated to a known standard, plus the maximum deviation of the linearity of the probe over its range. Therefore, when the disk is stationary, the second term is

$$\Delta(h + \Delta h) = 0.01 \text{ mm}$$

When the disk is rotating, the error due to the disk not being

perfectly flat and the wobble caused by the bearings must be taken into account. The error when the dry disk is rotating is given by the sum of the standard deviation of the air gap measurement between the probe and the dry disk taken at the outer edge of the disk (where it is maximum) and the combined error of the capacitance sensor reported by the manufacturer and the deviation from linearity of the probe. The standard deviation of the disk with 50 samples is σ = 0.02 mm. Multiple populations with an increasing number of samples were taken to compare the means using a two-tailed z-test to ensure a sample number that is within the 95 percent confidence interval. Therefore, the maximum error in the tare data is

$$\Delta(h + \Delta h) = 0.03 \text{ mm}$$

The last term in equation (C.6) is again the error associated with the capacitance sensor:

$$\Delta h'' = 0.01 \text{ mm}$$

Due to the fact that the mean film thickness is being reported, further comments concerning the third term in equation (C.6) are necessary. At all flow rates and rotational speeds, waves were present on the free surface of the liquid film. Figures (C.1 and C.2) present typical mean h" values and standard deviations as a function of the number of samples taken for the stationary subcritical and supercritical regions, respectively. In each case, the same population was examined for different numbers of samples to minimize the effect of the variation in the flow rate. For subcritical flow, a normal z-test was performed, and it was found that for

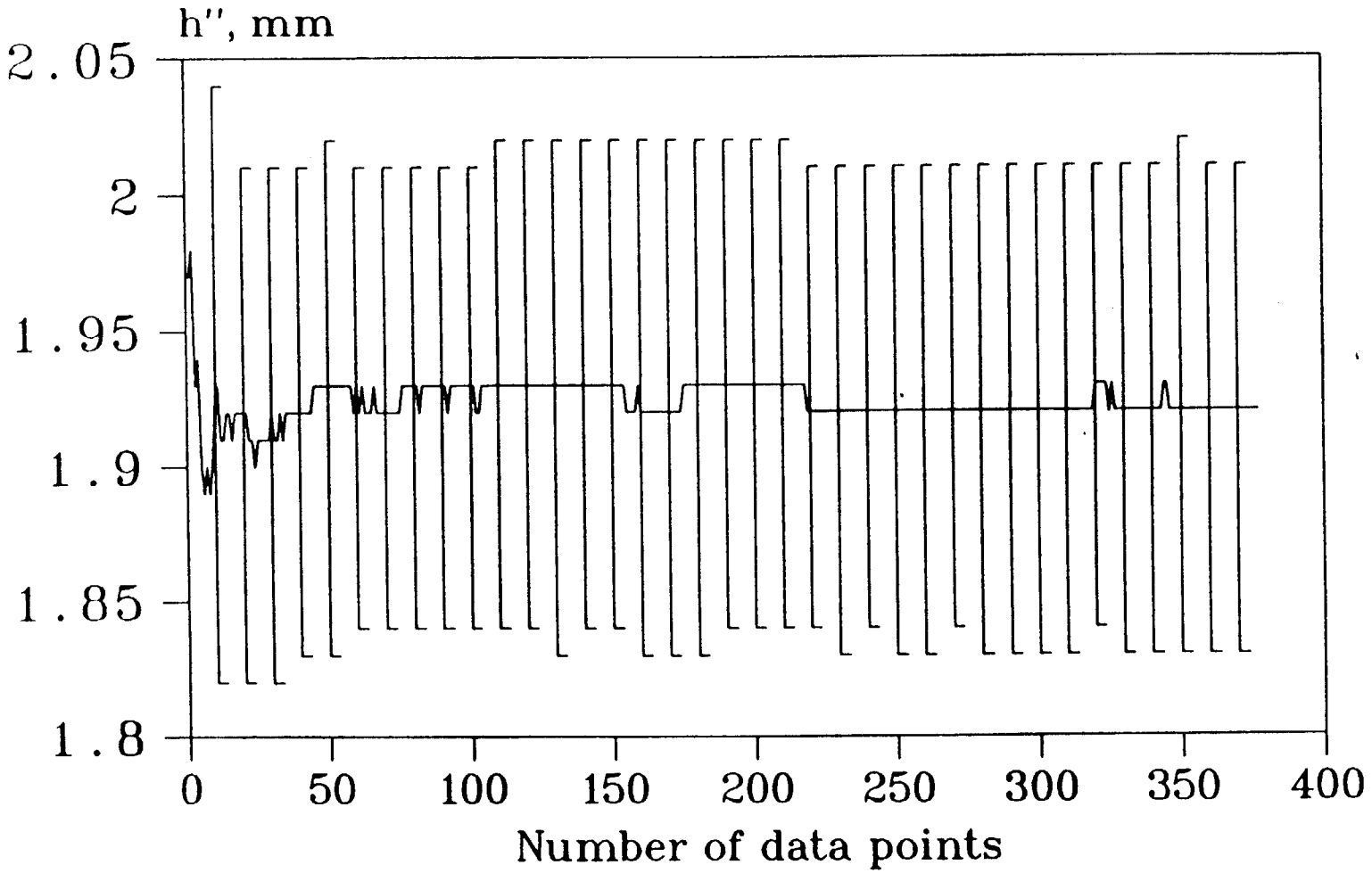

Figure C.1. Typical mean h'' and standard deviation versus number of data points for subcritical flow

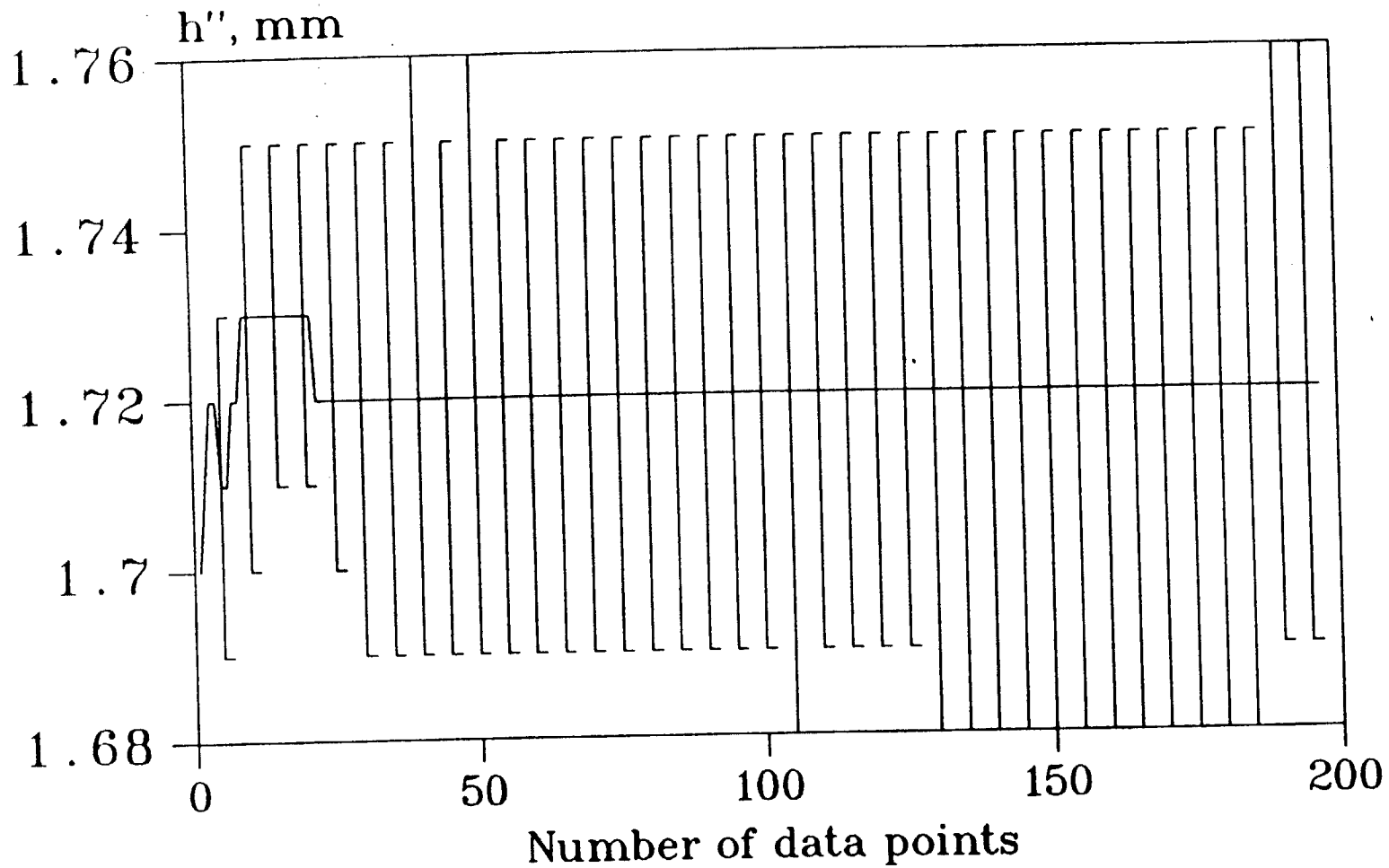

Figure C.2. Typical mean h'' and standard deviation versus number of data points for supercritical flow

125 and 250 samples, the means were equal at the 95 percent confidence level, so 250 samples were taken for each data point reported. Likewise, for supercritical flow 80 samples were taken in order to achieve the same confidence level. It should be noted that the standard deviations from the mean are not errors in the instrumentation but are actual variations in the mean film thickness due to the wavy nature of the free surface of the liquid film. A similar test performed when the disk was rotating showed that the number of samples needed for the 95 percent confidence level was the same as that for the stationary supercritical region. The overall root-sum-square error in the liquid film height measurement is as follows:

Stationary disk -

$\Delta h' = 0.0001$ mm, $\Delta(h + \Delta h) = 0.01$ mm, $\Delta h'' = 0.01$ mm

$E_{rss} = \pm 0.01$ mm

Rotating disk -

$\Delta h' = 0.0001$ mm, $\Delta(h + \Delta h) = 0.03$ mm, $\Delta h'' = 0.01$ mm

$E_{rss} = \pm 0.03$ mm

While the liquid film height at the collar could not be measured with the capacitance probe, the gap between the collar and the disk could be measured with feeler gages. Therefore, for the data point at the collar, the absolute error in the liquid film height was found to be

$E_a = \pm 0.01$ mm

Flow meter

It is desired to determine the accuracy of the flow rate reported in the present experiment. The turbine flow sensor and digital flow meter were calibrated in the following manner:

1. A line was drawn on the inside of a large bucket, and the volume to this line was measured with a 1000 ± 5 ml graduated cylinder. The volume was measured three times and the average of these three readings was 17.23 ± 0.08 L.

2. The flow rate through the flow sensor was allowed to reach the steady state at 12.5 ± 0.05 LPM, which is within the range of the reported flow rates.

3. The timer was started and the water was directed into the calibrated bucket.

4. The amount of time to fill the bucket to the line was noted and the actual flow rate was checked against the reading on the digital flow meter.

5. The gain on the digital flow meter was changed until the flow rate read on the flow meter checked to within ±0.05 LPM of the measured flow rate.

The accuracy of the actual flow rate measured with the bucket and the

stop watch can be determined with the method outlined in the previous section concerning the capacitance sensor. The equation for finding the flow rate is $Q = V/t$, where V is the volume and t is the amount of time. The absolute error is given by the following equation:

$$E_a = \left|\frac{\partial Q}{\partial V}\Delta V\right| + \left|\frac{\partial Q}{\partial t}\Delta t\right| \qquad (C.7)$$

The time and volume measured are as follows:

$t = 1.37 \pm 1/60$ min.

$V = 17.23 \pm 0.08$ L

The partial derivatives are

$$\frac{\partial Q}{\partial V} = \frac{1}{t} = \frac{1}{1.37} = 0.730 \text{ LPM/L}$$

$$\frac{\partial Q}{\partial t} = -\frac{V}{t^2} = -\frac{17.23}{(1.37)^2} = -9.18 \text{ LPM/min}$$

The error in the flow rate measured with the stop watch and the bucket is

$$E_a = \left|(0.730)(0.08)\right| + \left|(-9.18)(1/60)\right| = 0.2 \text{ LPM}$$

The maximum deviation of the flow rate read on the digital flow meter from the actual flow rate was found to be $\pm$ 0.05 LPM. The variation of the flow rate due to the circulation pump for each test where the film

thickness is measured was held to ± 0.05 LPM. Therefore, the total error on the flow rate is the sum of these three readings:

$$E_a = \pm 0.3 \text{ LPM}$$

Appendix D: EXPERIMENTAL DATA

Experimental parameters:

r_{in} = 50.8 mm

r_{out} = 203.2 mm

δ_{in} = 0.267 mm

Fluid temperature = ambient temperature = $22^{o}C$

Working fluid = de-ionized water

Table D.1 . Experimental data for the stationary disk

Radial Location	7 LPM	9 LPM	11 LPM	13 LPM	15 LPM
50.80	0.267	0.267	0.267	0.267	0.267
76.20	0.322	0.282	0.269	0.264	0.250
81.28	0.330	0.289	0.277	0.272	0.254
86.36	0.345	0.300	0.284	0.277	0.259
91.44	0.361	0.315	0.297	0.287	0.266
93.98	0.378	---	---	---	---
96.52	---	0.330	0.310	0.297	0.267
101.6	---	0.350	0.325	0.312	0.288
106.7	---	0.368	0.340	0.330	0.301
111.7	---	0.391	0.361	0.348	0.320
114.3	---	0.429	---	---	---
116.8	---	0.444	0.383	0.371	0.340
121.9	---	---	0.411	0.396	0.359
127.0	4.37	---	0.442	0.424	0.388
129.5	4.42	---	---	---	---
132.1	4.42	---	0.490	0.460	0.412
134.6	4.47	---	---	---	---
137.2	4.47	2.92	---	0.485	0.441
139.7	---	3.30	---	---	---
142.2	4.47	3.55	---	0.516	0.469
144.8	---	3.78	---	0.549	---

Table D.1 Experimental data for the stationary disk, continued

Radial Location	7 LPM	9 LPM	11 LPM	13 LPM	15 LPM
147.3	4.52	3.94	---	---	0.487
152.4	4.52	4.14	2.82	---	0.523
154.9	---	---	3.20	---	---
157.5	4.52	4.24	3.45	---	0.550
160.0	---	---	3.63	---	---
162.5	4.52	4.34	3.84	---	0.568
167.6	4.52	4.34	4.09	2.87	0.596
170.2	---	---	---	3.17	---
172.7	4.52	4.39	4.19	3.48	0.644
175.3	---	---	---	3.63	---
177.8	4.52	4.39	4.29	3.78	---
182.8	4.52	4.39	4.34	4.04	---
187.9	4.47	4.39	4.37	4.16	---
190.5	---	4.34	4.37	4.22	1.90
193.0	4.42	4.32	4.32	4.16	2.22
195.5	4.27	---	4.16	4.06	2.45

Table D.2. Experimental data for the rotating disk: 55 RPM

Radial Location	7 LPM	9 LPM	11 LPM	13 LPM	15 LPM
50.80	0.267	0.267	0.267	0.267	0.267
76.20	0.328	0.317	0.279	0.284	0.274
81.28	0.333	0.325	0.284	0.287	0.279
86.36	0.353	0.335	0.292	0.295	0.287
91.44	0.366	0.348	0.305	0.302	0.292
96.52	0.386	0.363	0.312	0.310	0.300
101.6	0.404	0.376	0.328	0.325	0.315
106.7	0.424	0.396	0.343	0.338	0.330
111.7	0.444	0.409	0.358	0.351	0.345
116.8	0.462	0.439	0.373	0.371	0.363
121.9	0.478	0.452	0.399	0.396	0.389
127.0	0.490	0.467	0.414	0.411	0.401
132.1	0.500	0.477	0.429	0.444	0.429
137.2	0.513	0.490	0.455	0.457	0.442
142.2	0.513	0.513	0.470	0.483	0.460
147.3	0.513	0.513	0.500	0.503	0.475
152.4	0.505	0.518	0.503	0.518	0.505
157.5	0.505	0.521	0.528	0.528	0.518
162.5	0.495	0.533	0.528	0.543	0.531
167.6	0.480	0.531	0.528	0.543	0.541
172.7	0.457	0.508	0.528	0.546	0.551
177.8	0.457	0.511	0.528	0.561	0.551

Table D.2. Experimental data for the rotating disk: 55 RPM, continued

Radial Location	7 LPM	9 LPM	11 LPM	13 LPM	15 LPM
182.8	0.429	0.508	0.528	0.546	0.577
187.9	0.457	0.508	0.551	0.546	0.577
190.5	0.508	0.551	0.551	0.561	0.577
193.0	0.805	0.729	0.635	0.587	0.577
195.5	1.32	1.09	0.808	---	0.630

Table D.3. Experimental data for the rotating disk: 100 RPM

Radial Location	7 LPM	9 LPM	11 LPM	13 LPM	15 LPM
50.80	0.267	0.267	0.267	0.267	0.267
76.20	0.317	0.312	0.300	0.297	0.307
81.28	0.325	0.320	0.302	0.302	0.312
86.36	0.333	0.328	0.307	0.305	0.320
91.44	0.348	0.338	0.315	0.312	0.325
96.52	0.363	0.351	0.325	0.323	0.340
101.6	0.381	0.366	0.338	0.333	0.351
106.7	0.394	0.378	0.351	0.345	0.366
111.7	0.404	0.394	0.366	0.361	0.381
116.8	0.414	0.404	0.381	0.378	0.404
121.9	0.419	0.417	0.394	0.394	0.399
127.0	0.424	0.422	0.406	0.411	0.419
132.1	0.424	0.427	0.424	0.427	0.442
137.2	0.419	0.427	0.424	0.442	0.460
142.2	0.411	0.427	0.432	0.442	0.470
147.3	0.401	0.427	0.432	0.452	0.477
152.4	0.391	0.424	0.432	0.460	0.483
157.5	0.383	0.422	0.429	0.460	0.493
162.5	0.371	0.411	0.429	0.452	0.495
167.6	0.358	0.404	0.419	0.457	0.498
172.7	0.343	0.399	0.422	0.452	0.485
177.8	0.335	0.386	0.414	0.449	0.483

Table D.3. Experimental data for the rotating disk: 100 RPM, continued

Radial Location	7 LPM	9 LPM	11 LPM	13 LPM	15 LPM
182.8	0.328	0.381	0.396	0.445	0.483
187.9	0.315	0.371	0.394	0.432	0.462
190.5	0.312	0.371	0.409	0.442	0.460
193.0	0.310	0.363	0.406	0.442	0.465
195.5	0.330	0.373	0.406	0.432	0.457

Table D.4. Experimental data for the rotating disk: 200 RPM

Radial Location	7 LPM	9 LPM	11 LPM	13 LPM	15 LPM
50.80	0.267	0.267	0.267	0.267	0.267
76.20	0.302	0.290	0.279	0.269	0.272
81.28	0.305	0.297	0.284	0.274	0.279
86.36	0.307	0.300	0.287	0.277	0.284
91.44	0.310	0.305	0.295	0.284	0.292
96.52	0.307	0.307	0.300	0.287	0.300
101.6	0.307	0.312	0.305	0.292	0.310
106.7	0.305	0.315	0.310	0.302	0.322
111.7	0.297	0.315	0.315	0.307	0.330
116.8	0.290	0.312	0.318	0.318	0.343
121.9	0.282	0.305	0.318	0.320	0.350
127.0	0.272	0.302	0.318	0.328	0.356
132.1	0.259	0.292	0.315	0.325	0.358
137.2	0.249	0.282	0.305	0.320	0.358
142.2	0.239	0.272	0.302	0.315	0.356
147.3	0.229	0.269	0.290	0.307	0.353
152.4	0.221	0.254	0.281	0.297	0.348
157.5	0.211	0.246	0.269	0.295	0.340
162.5	0.201	0.231	0.259	0.284	0.333
167.6	0.193	0.226	0.251	0.277	0.325
172.7	0.188	0.216	0.241	0.269	0.320
177.8	0.180	0.213	0.236	0.259	0.307

Table D.4. Experimental data for the rotating disk: 200 RPM, continued

Radial Location	7 LPM	9 LPM	11 LPM	13 LPM	15 LPM
182.8	0.178	0.203	0.223	0.244	0.297
187.9	0.173	0.196	0.223	0.241	0.287
190.5	0.170	0.196	0.218	0.236	0.279
193.0	0.180	0.193	0.213	0.234	0.279

Table D.5. Experimental data for the rotating disk: 300 RPM

Radial Location	7 LPM	9 LPM	11 LPM	13 LPM	15 LPM
50.80	0.267	0.267	0.267	0.267	0.267
76.20	0.305	0.295	0.289	0.282	0.281
81.28	0.302	0.300	0.289	0.287	0.282
86.36	0.295	0.295	0.287	0.292	0.285
91.44	0.292	0.297	0.289	0.295	0.289
96.52	0.289	0.297	0.292	0.301	0.295
101.6	0.284	0.295	0.289	0.303	0.302
106.7	0.279	0.292	0.292	0.305	0.310
111.7	0.272	0.287	0.292	0.304	0.314
116.8	0.262	0.282	0.289	0.305	0.317
121.9	0.251	0.274	0.287	0.303	0.321
127.0	0.244	0.264	0.284	0.303	0.319
132.1	0.231	0.259	0.274	0.297	0.313
137.2	0.223	0.246	0.262	0.288	0.308
142.2	0.213	0.236	0.251	0.280	0.298
147.3	0.206	0.229	0.244	0.279	0.290
152.4	0.198	0.218	0.234	0.264	0.284
157.5	0.193	0.203	0.226	0.250	0.272
162.5	0.185	0.201	0.221	0.250	0.265
167.6	0.183	0.195	0.208	0.239	0.257
172.7	0.175	0.185	0.203	0.230	0.247
177.8	0.173	0.178	0.195	0.227	0.245

Table D.5. Experimental data for the rotating disk: 300 RPM, continued

Radial Location	7 LPM	9 LPM	11 LPM	13 LPM	15 LPM
182.8	0.165	0.175	0.193	0.218	0.233
187.9	0.160	0.168	0.183	0.209	0.219
190.5	0.160	0.168	0.183	0.209	0.227